The Thesis Committee for Joel Phillip Blok
Certifies that this is the approved version of the following thesis:

Stress Monitoring and Sweep Control Studies for Innovative Prestressed Precast Arches

APPROVED BY
SUPERVISING COMMITTEE:

Co-Supervisor: _____
Todd Helwig

Co-Supervisor: _____
Oguzhan Bayrak

Stress Monitoring and Sweep Control Studies for Innovative Prestressed Precast Arches

by

Joel Phillip Blok, B.S.

Thesis

Presented to the Faculty of the Graduate School of

The University of Texas at Austin

in Partial Fulfillment

of the Requirements

for the Degree of

Master of Science in Engineering

The University of Texas at Austin

August 2012

Dedication

To Kate

For giving your love

For helping me through

Acknowledgements

This project was made possible through the generous financial support of the Texas Department of Transportation. I would like to thank Dean Van Landuyt, Charles Walker, and the TxDOT Bridge team. It has been a pleasure getting to work with you. This is an extraordinary bridge, and I am eager to see the finished product.

I owe my supervisors, Dr. Todd Helwig and Dr. Oguzhan Bayrak, a tremendous debt of gratitude. I have thoroughly enjoyed my time at UT, and that is in no small part due to your efforts. I have learned so much from both of you, and strike out in the "real world" knowing I'm the better for it.

I cannot possibly thank my research partner Hossein Yousefpour enough for his support on this research project. His willingness and patience in sharing his knowledge have been invaluable. I am lucky to have worked with him, and am honored to call him a friend. Hossein, I am confident I will never buy a used car from you.

My time at FSEL has been incredible due to the remarkable staff and students. Thanks to Andrew Valentine, Dennis Fillip, and Blake Stasney for their patience as I learned new skills and damaged equipment, to Mike Wason and Eric Schell for their support with all things electrical, and to Barbara Howard and Jessica Harbison for having all the answers. And to all my FSEL friends: It's been great! Thank you, and Hook 'em!

To my family: *hartelijk bedankt*! Your unconditional love and support for Kate and me can never be repaid. While you may never really understand what exactly I was up to "at the lab," please know that any accomplishments of mine were possible only with the knowledge that you believed in me, even if you were shaking your heads at the nerdiness of it all.

Above all, I wish to thank my Creator for the gifts and opportunities He has provided me throughout my life. I am truly blessed.

June 1, 2012

Abstract

Stress Monitoring and Sweep Control Studies for Innovative Prestressed Precast Arches

Joel Phillip Blok, M.S.E.

The University of Texas at Austin, 2012

Co-Supervisors: Todd Helwig, Oguzhan Bayrak

The Texas Department of Transportation (TxDOT) has completed the design of a signature bridge in Fort Worth, TX. The proposed structure is comprised of precast, post-tensioned concrete network arches. The arches will be cast on their sides and then rotated into the vertical orientation. Concerns exist about the durability and stability of the arches during stressing, handling, and transportation. The rotation process in particular represents a critical period in the life of the arches. A monitoring system was proposed to track stresses in the arches throughout the construction operations. The primary goals of the project are to install vibrating wire gages (VWGs) in the arches prior to casting to monitor the performance of the arches until the bridge is completed. The instrumentation will be used to provide real-time feedback to TxDOT and the contractor during stressing, handling, and bridge construction. This thesis focuses on the results of a preliminary laboratory study conducted in support of the instrumentation initiative. The purpose of the study was two-fold: to establish the capabilities and limitations of the VWGs and to study the buckling behavior of slender concrete elements with unbonded post-tensioning. More than sixty axial load tests were performed on two slender concrete specimens

instrumented with VWGs. Observations are made on the accuracy and reliability of the VWGs. In general, the VWGs were found to be both accurate and reliable in measuring structural parameters and reporting trends in behavior, even at low loads. Some apparent errors were identified, but these were attributed to testing inconsistencies and scale factors rather than to gage error. Observations were also made on the buckling behavior of the elements under a variety of axial loading configurations. The effects of the engagement of the tensioned strand with the duct had a significant impact on the behavior. Strand engagement was shown to increase the buckling capacity of the members through stiffening action, but did not necessarily eliminate the risk of instability. Both the gage resolution study and the stability tests are expected to significantly enhance the ability of the research team to support the arch construction operations.

Table of Contents

List of Tables

List of Figures

CHAPTER 1
Introduction

1.1 PROJECT OVERVIEW

The Texas Department of Transportation (TxDOT) has completed the design of a signature bridge on West 7th Street near downtown Fort Worth, TX. The new bridge, connecting downtown Fort Worth with the city's Cultural District, will span the Trinity River and multiple traffic lanes. The proposed structure consists of twelve precast, post-tensioned concrete network arches. The precast network arches will replace an existing bridge that will be removed once the arches are in place. Network arches consist of a tied arch with inclined hangers that serve to reduce the bending moments in the chords of the arch. The West 7th Street arches will be comprised of a precast concrete rib and tie, with inclined stainless steel hanger rods connecting the rib and tie. A TxDOT-provided rendering of the proposed six-span bridge is given in Figure 1-1; Figure 1-2 provides a more detailed perspective of the arches.

Figure 1-1: Street Perspective of Proposed West 7th Street Bridge (Image: TxDOT)

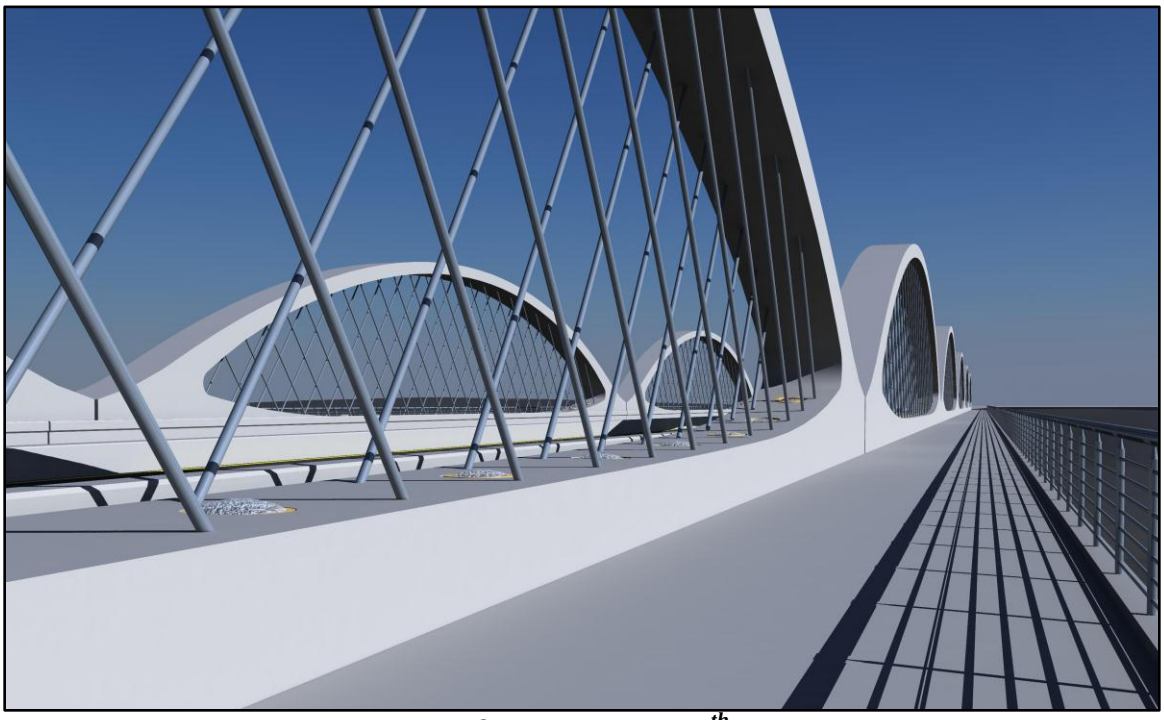

Figure 1-2: Sidewalk Perspective of Proposed West 7th Street Bridge (Image: TxDOT)

Each 300-ton arch will be cast on its side in the horizontal position. After partial post-tensioning and initial installation of the hanger rods, the arch will be rotated 90 degrees about its longitudinal axis into the vertical orientation. The final post-tensioning and tightening of the hanger rods will be completed once the arch is rotated. The arch will then be moved to a nearby storage site until all twelve arches have been fabricated. Once fabrication is complete, each arch will be transported approximately 0.25 miles to the job site and lifted into place. The existing bridge will be removed after the new arches have been erected. Precast floor beams will be hung from the arch ties using post-tensioned bars. The deck will be comprised of precast deck panels and cast-in-place concrete.

As this is the first use of a precast concrete network arch, there are concerns about the durability of the arch during stressing, handling, and transportation. The construction process – principally the lifting and rotation stage – represents a critical period in the life

of the arches. Concerns exist about the impact of cracking on the stability of the arch. Therefore, to minimize the potential for cracking, a monitoring system was proposed to track stresses that develop throughout the fabrication, transportation and bridge construction operations. A research implementation study was established by TxDOT at the University of Texas at Austin to support the monitoring initiative. The primary goals of the project are to install instrumentation in the arches prior to casting and to monitor the performance of the arches until the bridge is completed. The instrumentation will be used to provide real-time feedback to TxDOT and the contractor during stressing, handling, and the construction activities. The instrumentation consists of vibrating wire gages (VWGs) that will be installed at critical sections of the arch to minimize damage to components of the arch during the fabrication, transportation, and installation operations. The primary purpose of the instrumentation is monitoring during construction. However, VWGs have been shown to have excellent durability and long-term reliability. Given the long-term stability of VWGs with respect to strain measurement, the system will allow long-term performance monitoring of the structure.

In addition to real-time monitoring of structural behavior, the instrumentation will provide the capacity to investigate the stress behavior at particularly complex regions, often referred to as *disturbed* or *D*- regions. One such region exists at the intersection of the arch rib and tie, referred to as the *knuckle*. The stress behavior observations from this study will be used to validate a previous TxDOT research study on the design of D-regions.

1.2 SCOPE OF STUDY

The fabrication of the arches is scheduled to begin in May of 2012. The instrumentation is anticipated to play a critical role in providing feedback to TxDOT and the contractors during stressing and handling. Establishing the resolution of the gages is imperative so as to provide confidence in the gage readings. Therefore, a key step prior to construction is establishing the resolution of the gages. As such, a comprehensive gage resolution study was performed at Ferguson Structural Engineering Laboratory (FSEL) at

the University of Texas at Austin. The study sought to establish a fundamental understanding of the capabilities and limitations of the VWGs in a controlled laboratory environment. The results of the study, presented in this thesis, will enhance the efficiency with which the research team can contribute to decisions during arch construction.

In addition to establishing the resolution of the instrumentation, the tests were designed to provide information on the stability behavior of prestressed concrete elements. Slender concrete specimens were fabricated to provide information on the buckling performance of slender concrete elements subjected to axial force from both prestressing and externally applied compression loads. Each specimen was instrumented with the same components that will be used on the arches. Axial loads were applied to each specimen through both unbonded post-tensioning and an external hydraulic actuator. The specimens were not intended to be directly analogous to the arch members. Rather, they provided a means through which to study both the instrumentation and stability behavior in simple structural elements before deploying the instrumentation in the field on the arches. The specimens were also developed to investigate the impact of cracking on the stability of prestressed concrete members.

1.3 THESIS OVERVIEW

The results presented in this thesis were a part of TxDOT implementation project 5253-03. Prior to on-site construction monitoring, the research team's responsibilities on the project included experimental verification of the instrumentation and finite element modeling of the arches. This thesis focuses on the results of the laboratory tests that included more than sixty axial load tests on two slender concrete specimens. Observations are made both on the accuracy and reliability of the VWGs. Similarly, several perceived trends in structural stability under unbonded post-tensioning loads are presented and discussed.

This document is comprised of seven chapters, including this introductory overview. Chapter 2 provides a description of the bridge and the construction process, as well as the proposed instrumentation configurations. Also included is a survey of related

work on both the capabilities of VWGs in field applications and the stability of post-tensioned members.

Chapter 3 provides an overview of the experimental program. Detailed descriptions of the test specimens, the test setup, and the loading schemes employed in the laboratory studies are included. Chapter 4 details several of the experimental procedures employed in the test program. The results of the experimental program are presented with observations and analysis in Chapters 5 and 6. Initial suggestions are made regarding the use of VWGs in the arch construction. In addition, several trends in stability of post tensioned concrete compression elements are noted. Chapter 7 includes a final summary of observations and concludes with several suggestions for future work.

CHAPTER 2
Project Background

2.1 INTRODUCTION

This chapter introduces the background and motivations for the laboratory studies described in this thesis. The experimental program that is described in Chapter 3 is motivated by the construction of a signature network arch bridge for the municipality of Fort Worth, TX. Instrumentation will be installed in each of the arches to monitor structural behavior throughout construction and placement. This chapter details the specific roles the instrumentation will play in stress monitoring, and briefly introduces the laboratory program used to better evaluate the vibrating wire gages' ability to reliably predict structural behavior.

In addition to the development of an enhanced understanding of the capabilities and limitations of the proposed instrumentation, the laboratory studies were performed to investigate the stability and buckling behavior of slender post-tensioned concrete elements. A brief summary of previous studies and background information for the experimental program is also presented in this chapter.

2.2 WEST 7TH STREET BRIDGE CONSTRUCTION PROJECT

The primary motivation for the research program described in this document is the construction of a signature network arch bridge for downtown Fort Worth, TX. An overview of the proposed structure and a detailed discussion of the construction sequence are provided in this section. Figure 2-1 provides a rendering of the proposed structure. Initial site preparation and construction activity began in early 2012. The project, bid at a cost of $24.1 million, is currently slated for completion in late 2013 (Dickson, 2012).

Figure 2-1: Artist's Rendering of Proposed West 7th Street Bridge (Image: TxDOT)

2.2.1 Bridge Overview

The proposed bridge will replace the existing West 7th Street bridge in Fort Worth. The structure will cross the Trinity River, four lanes of traffic on North Forest Park Boulevard, and a number of municipal recreational trails along the west riverbank. West 7th Street is an important traffic corridor; it serves as a primary connection between downtown Fort Worth and the city's Cultural District to the west.

Figure 2-2 identifies the location of the bridge site. Further discussion of the current site and proposed bridge follows below.

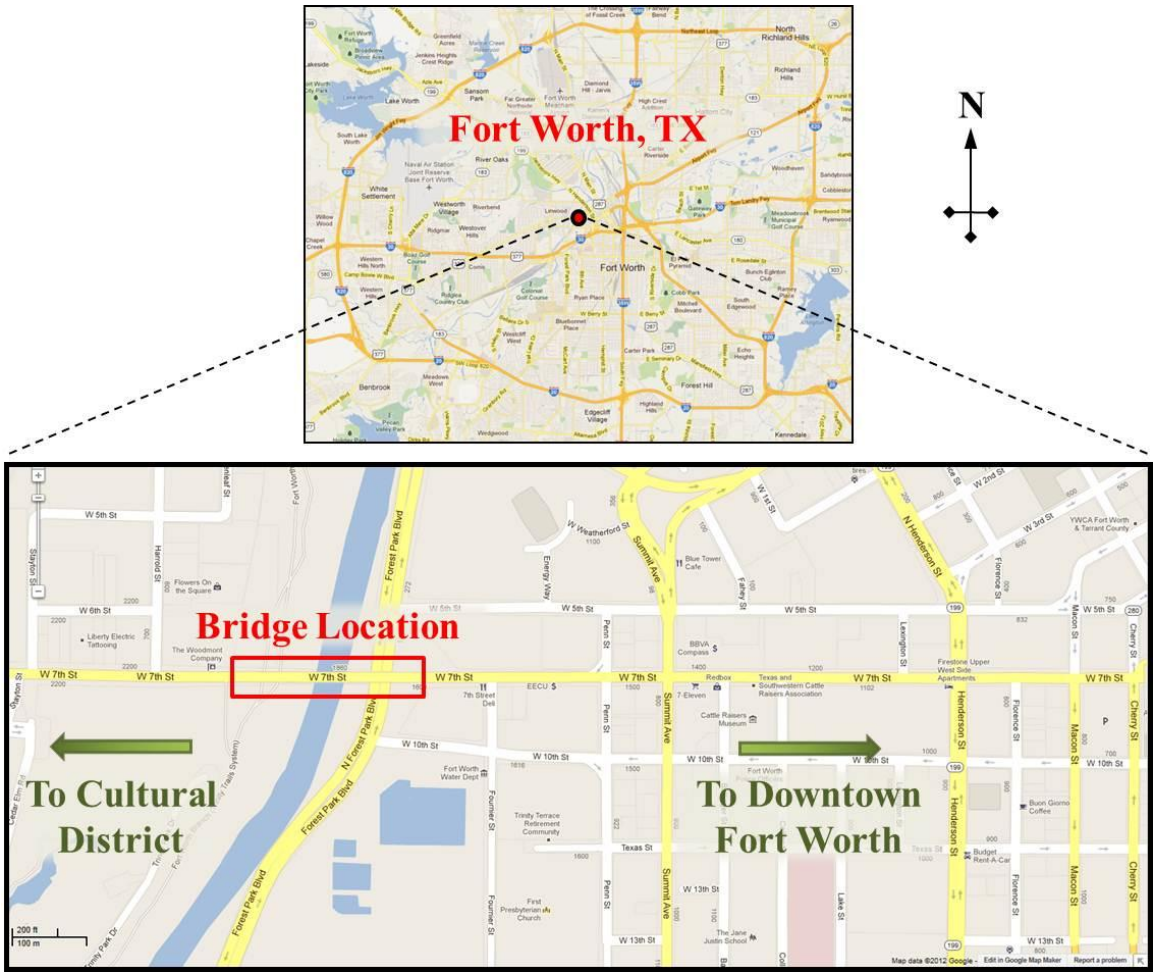

Figure 2-2: Bridge Site (Google Maps)

2.2.1.1 Existing Structure

The current West 7th Street bridge was constructed in 1913, and was lengthened in 1953 when the Trinity River was rerouted. Figure 2-3 provides an aerial image of the current bridge. City officials estimate that the structure has an average daily traffic count of 12,000 motorists (Dickson, 2012).

Significant deterioration, including carbonation, concrete spalling, and exposed reinforcement, has been noted in the existing structure. An inspection of the bridge by the Texas Department of Transportation (TxDOT) resulted in a rating of 38.8/100, warranting a "structural deficiency" classification. In addition to the structural concerns,

city officials wished to enhance pedestrian safety with the addition of wider sidewalks on the bridge. Ultimately, the decision was made to completely replace the current bridge (Dickson, 2012).

Figure 2-3: Existing Bridge (Bing Maps)

Due to the modifications in 1953, the current structure is not considered historically significant, and therefore city officials embraced the opportunity to add a signature bridge to the downtown area. The new precast concrete network arch bridge was conceived and designed by TxDOT. The proposed structure is discussed in detail in the following sections.

2.2.1.2 Proposed Structure

A network arch consists of a curved *rib* and a straight *tie*. The rib supports the tie with a series of inclined *hangers* that run in the plane of the arch between the rib and tie; in return, the tie resists the horizontal thrust generated in the rib. By definition, in a network arch, some hangers are crossed at least twice by other hangers. The region of intersection between the tie and rib is commonly referred to as the *knuckle* (see Figure 2-4). The inclined anchors tend to act like the web of a girder in distributing the shear along the length of the arch, which therefore reduces bending in the arch and tie.

A small but growing number of network arch bridges are in service around the world; these typically consist of a steel rib and a concrete tie or a concrete deck serving as the arch tie (Tveit, 2007). The proposed structure for the West 7th Street bridge is believed to be the first network arch bridge consisting of *precast* concrete arches.

A total of twelve arches will be used in the proposed structure. A geometry of the arches is shown in Figure 2-4 and Figure 2-5. Each arch will measure 163.5 feet in length, 23.5 feet in height, and will be 4.5 feet in width. The hanger rods will be arranged in two parallel planes spaced at 24 inches within the arch. All hangers in a single plane will be parallel, but the hanger angles will be oriented such that each plane's hangers "cross" those of the parallel plane, creating the lattice effect of a typical network arch. Each completed arch is expected to weigh roughly 300 tons.

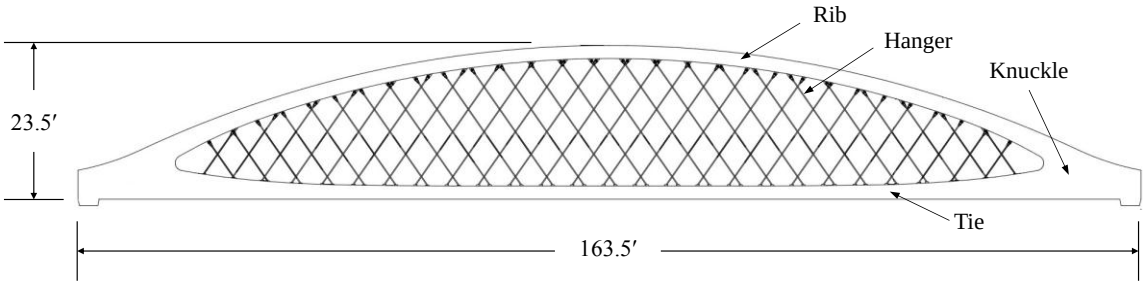

Figure 2-4: Typical Network Arch for West 7th Street Bridge

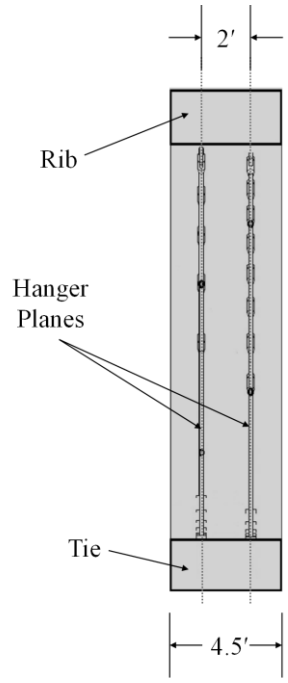

Figure 2-5: Typical Arch Cross Section

The twelve arches will be placed in pairs outside the traffic lanes, resulting in a total of six spans. Precast floor beams will be hung (using post-tensioned bars) between each pair of arches, perpendicular to the direction of traffic. Precast panels will span between adjacent floor beams and support a cast in-place deck for the road surface. A typical span is shown in Figure 2-6.

While the new structure will initially support two lanes of vehicular traffic in each direction, the spans have been designed to accommodate future implementation of a streetcar or light rail system. The total of six spans results in a total approach-to-approach bridge length of approximately 981 feet. Each span will feature a sidewalk and handrail system on the each outside (non-traffic) face of the arch.

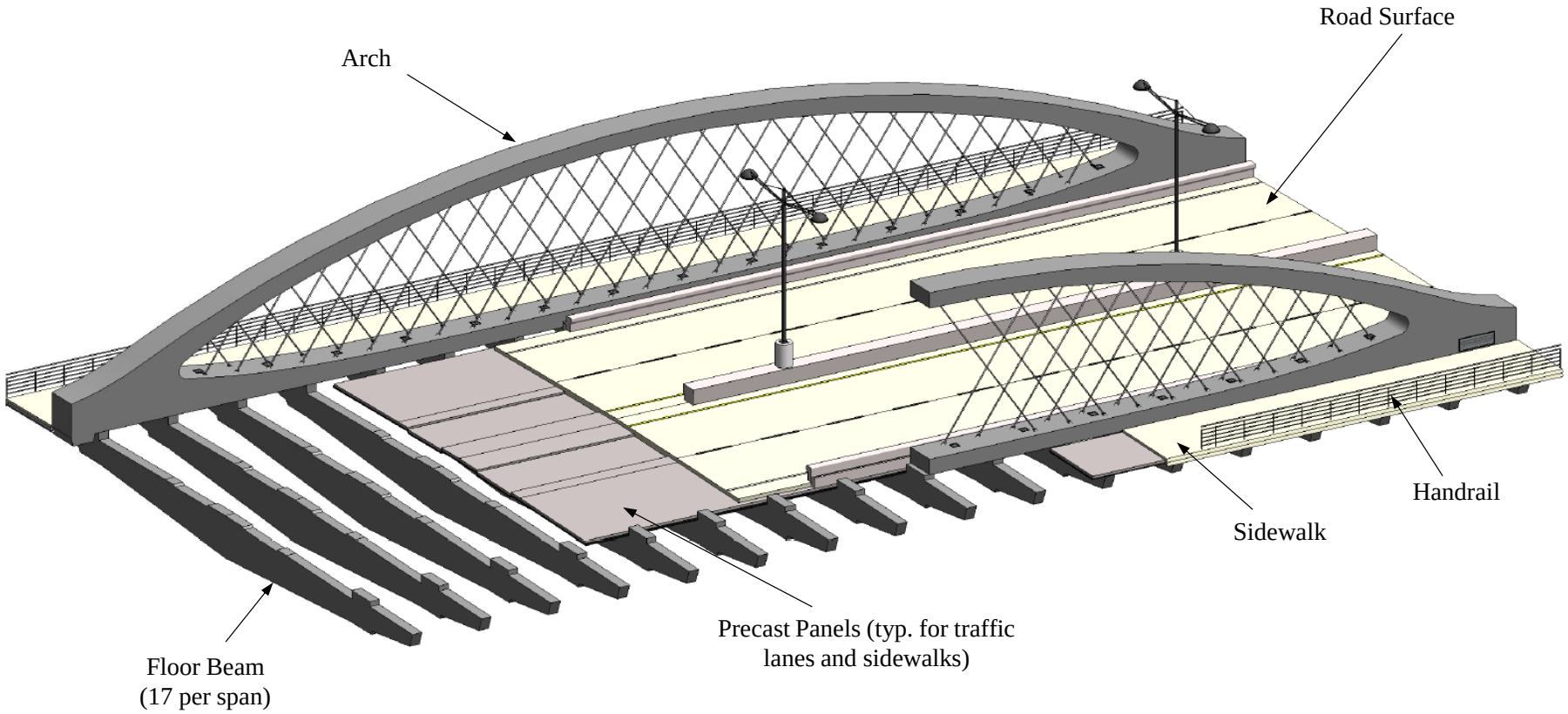

Figure 2-6: Cutaway of Typical Span for Proposed West 7th Street Bridge

While the arches are being constructed in a yard less than one mile to the northwest of the bridge site, the columns or piers for the new structure will be cast next to the existing bridge. When the arches are lifted into place onto these piers, temporary transverse steel bracing for lateral stability will be installed between the tops of the arches. This will eliminate the need to close the current bridge to traffic while the arches are placed.

Once all the arches are set, demolition of the current superstructure will begin. As sections of the original bridge are removed, the floor beams will be hung between the arches. A bedding strip for underlayment will be placed across the floor beams, followed by the precast panels to support the road surface (see Figure 2-6). After the panels are in place, the roadway surface, traffic barriers, sidewalks, and lighting components will be added. The bridge is scheduled to be opened to traffic in November 2013. A timeline for construction is given in Figure 2-7.

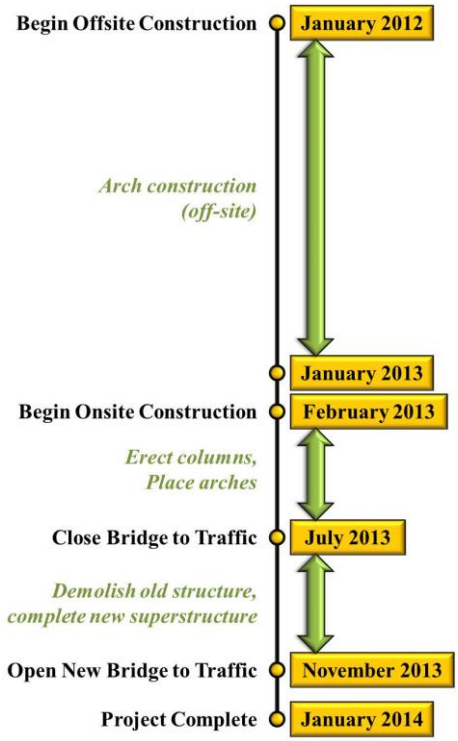

Figure 2-7: Proposed Construction Timeline

A comparison of the existing and proposed bridges (*West 7th Street Fact Sheet*, 2012) is presented in Table 2-1. It can be noted that the proposed structure is nearly exactly the same length as the current structure, but is significantly wider to accommodate vehicular, pedestrian, and potentially rail traffic.

Table 2-1: Comparison of Existing and Proposed Bridges

	Current Bridge	Proposed Bridge
Total Length	982 feet	981 feet
Total Width	57 feet	88 feet
Traffic Lanes	4	4
Sidewalk Width	4.8 feet	10 feet

2.2.2 Arch Construction Sequence

The fabrication of the twelve arches represents the first major construction stage for the bridge project; this is also the stage that is of the most significance for the material discussed in this thesis. Figure 2-8 below depicts the proposed construction sequence for each post-tensioned arch. The specifics of each stage are discussed in this section.

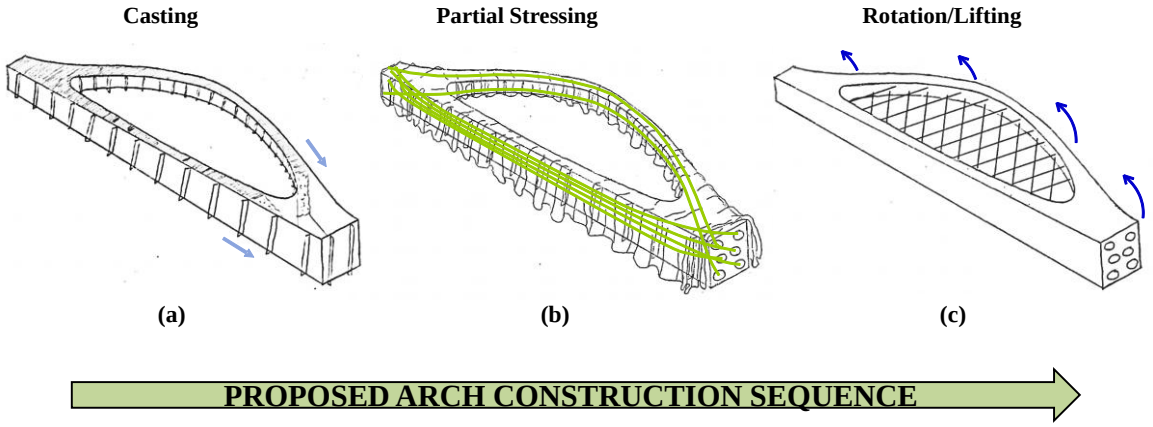

Figure 2-8: Proposed Arch Construction Sequence

2.2.2.1 Casting

Each arch will be cast on its side as shown in Figure 2-8. A set of custom steel side forms will be manufactured prior to casting and positioned on a deck or *soffit*. Once the reinforcing cage has been constructed and placed, concrete will be poured in the forms in the manner depicted in Figure 2-8(a). It should be noted that the casting will progress from one end of the forms to the other, rather than in lifts as might be expected. This will eliminate the occurrence of "cold joints" between lifts, which could increase the risk of arch cracking and would diminish the aesthetic appeal of the finished arches.

In addition to the mild steel reinforcement cage, a series of block-outs or tubes will be cast into the tie of each arch to anchor the diagonal hanger rods and the post-tensioning bars for the floor beams. Stainless steel plates (1.5″ thick) will be cast into the rib to attach clevises which, in turn, will be connected to the hangers.

After the arches are cast and the concrete has achieved sufficient strength, post-tensioning will begin as depicted in Figure 2-8(b). Upon application of a percentage of the final post-tensioning force, the arches will be lifted off the soffit, translated horizontally, and rotated into the vertical orientation, after which the post-tensioning will be completed as depicted in Figure 2-8(c). The specifics of these stages are described below.

2.2.2.2 Post-tensioning

In addition to the mild steel reinforcement cage, each arch will contain a number of plastic conduits or *ducts*. These ducts will be cast into the specimen, creating a void in the concrete through which high-strength steel cables or *strands* can be passed. A group of strands is commonly referred to as a *tendon*. The tendons will be used for post-tensioning the arches. Each arch will contain a total of six primary ducts, each capable of housing a total of nineteen strands. Four of these will run through the arch tie, and two will run through the rib. In addition to the six primary ducts, two supplemental ducts of smaller diameter (twelve-strand capacity) will be added to the reinforcement cage. These

provide the option for additional post-tensioning, should it be deemed necessary for arch performance due to a loss of prestress force over the service life of the structure.

Each strand will ultimately be post-tensioned to a total stress of 208 ksi. However, as previously noted, post-tensioning will be performed in stages. The initial post-tensioning will be completed while the arch is in the horizontal position, with each strand in the rib individually stressed to the full final stress (208 ksi) and the strands in the tie to one-half the final stress (104 ksi). Stressing will occur in increments equaling one-eighth (26 ksi) of the final stress.

It should be noted that the rib is inherently a compression member. It is ostensibly counterintuitive to apply a compressive force (post-tensioning, in this case) to a compression member. However, the development of tensile stresses in the rib is possible during arch lifting and rotation; the additional compressive force will serve to mitigate the risk of cracking the concrete during handling.

Prior to the arch being rotated into the vertical position, the hanger rods will be installed. They will be passed through the hanger tubes in the tie, threaded into the clevises at the rib, and a nut will be tightened below the tie to hold the hanger in place.

Once the target tendon stresses have been achieved, the arch will be lifted and rotated, after which the remainder of the post-tensioning will be applied to the tendons in the arch tie. After post-tensioning is complete, the ducts will be filled with a cementitious grout to provide corrosion protection and to bond the prestressing strands.

2.2.2.3 Rotation and Placement

After the arches have been cast and partially post-tensioned, they will be lifted and rotated with a series of lifting frames and spreader beams. Once clear of the formwork, the arches will be incrementally rotated a total of 90 degrees into the vertical orientation. This will be completed through the fixing of lifting frames at six discrete locations along the arch rib and tie. Each pair of adjacent frames will be connected to a spreader beam, connected in turn via cables to a lifting tower.

Once the arches have been rotated into the upright position, the remainder of the post-tensioning specified for the arch ties will be applied. Additionally, the ties will be raised slightly with hydraulic rams; once lifted sufficiently, the nuts on the hangers will be tightened completely. Thus, when the rams are removed, the hangers will all be loaded approximately equally. After post-tensioning is complete and the hangers have been properly installed and tensioned, the arch will be ready for transport and placement.

It should be noted that a *strong-back* consisting of a standard W36 x 330 wide-flange shape will be fixed to the arch over the knuckle region on each end prior to jacking the tie and fully tensioning the hangers. These strong-backs will provide additional stiffness to critical sections in which cracking is a concern until the arch is in place with the full bridge dead load applied.

Each arch will be placed in a staging area following completion. When all twelve arches have been fabricated, they will be individually loaded onto trucks and transported from the casting site to the bridge location. Each arch will be lifted into place using an overhead crane supported by two modular towers adjacent to the bridge. Once placed on the columns, the arch will be laterally braced for stability.

The rotation and placement sequences are considered a critical interval in the performance life of the arches. The specific concerns associated with development and monitoring of stresses in the arches throughout fabrication, transport, and bridge construction, along with the instrumentation used to address these concerns, are presented in the following sections.

2.3 PROPOSED INSTRUMENTATION

As previously noted, the design and construction of the proposed bridge feature several unprecedented processes and methods. As such, there is reason for concern regarding the structural integrity of the arches. These include the development of excessive stresses in critical arch regions (particularly during the rotation and tie-jacking stages), the lateral stability of the slender arch elements during post-tensioning, and the ability to control out-of-plane *sweep* in the arches during construction.

The goal of this project is to provide measurements of the structural behavior to assist the fabrication and construction of the arches. A key aspect of the project is to calibrate and accurately install the instrumentation in the arches prior to casting. Periodic readings during concrete casting, stressing and transportation of the arches will provide data critical to the evaluation of structural behavior, and will allow the research team to alert the engineers and construction personnel of impending problems. Ultimately, this information will provide a useful tool in aiding the decision-making process regarding modifications to the construction procedures.

The primary components of the proposed instrumentation system are vibrating wire gages (VWGs) that provide a measure of the strain in the concrete. These gages will be monitored using a data logging system that incorporates a wireless instrumentation network. The network allows for real-time monitoring of arch performance throughout the casting, rotation, and placement of the arches. Each instrumentation component is described in the following sections.

2.3.1 Vibrating Wire Gages

The primary instrumentation components for this project are vibrating wire gages (VWGs). The Geokon Model 4200 VWG that will be used on the arches appears in Figure 2-9. Figure 2-9(a) shows the VWG with a typical lead cable. One end of the cable is comprised of a mechanism for reading the gage; the other end is wired into the data logging components. The figure also shows a hand-held readout box that can be used to read the gage values. As every gage in this study will be wired into the data logging system, handheld read-out boxes will not be utilized. Figure 2-9(b) provides a schematic of the VWG's internal components. The data collection process is described in detail in the following pages.

(a)

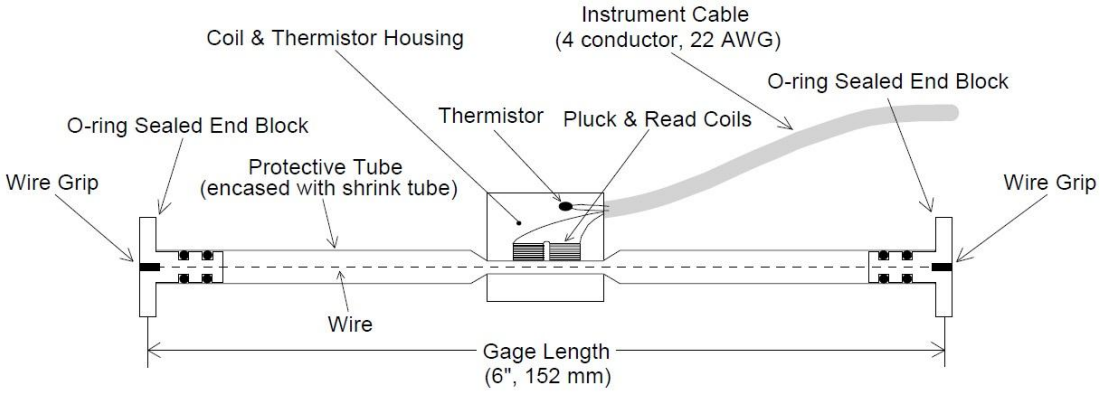

(b)

Figure 2-9: Vibrating Wire Gage; (a) Gage with lead wire and hand-held readout box; (b) Gage schematic (Image: Geokon)

A conference paper describing considerations for the use of VWGs in nuclear structures (Smith, et al., 2001) provides an excellent description of the mechanics of the vibrating wire gage. A VWG is comprised of a steel wire tensioned between two anchorages. An electromagnetic plucking mechanism excites the wire with a pulse of current. The coil in the electromagnet is used to measure the frequency of the vibrating

wire as the wire cuts the flux of the magnet. This device reads the fundamental natural frequency of the wire, described by Equation 2-1.

$$\boldsymbol{f = \frac{1}{2L}\sqrt{\frac{T}{m}}} \qquad \textit{Equation 2-1}$$

$$f = Wire\ frequency\ (Hz)$$
$$L = Length\ of\ wire\ (in)$$
$$T = Tension\ in\ wire\ (lbf)$$
$$m = Mass\ per\ unit\ length\ of\ wire\ (lbm/in)$$

The plucking mechanism converts the frequency to a strain reading through the relationship described in Equation 2-2.

$$\boldsymbol{\varepsilon = \frac{4L^2\rho g}{E}(f^2 - {f_0}^2)} \qquad \textit{Equation 2-2}$$

$$\varepsilon = Strain\ in\ wire\ (in/in)$$
$$\rho = Density\ of\ wire\ material\ (lbm/in^3)$$
$$g = Acceleration\ of\ gravity\ (in/sec^2)$$
$$E = Young's\ Modulus\ of\ elasticty\ of\ wire\ (psi)$$
$$f_0 = Initial\ frequency\ of\ wire\ (Hz)$$

A basic relationship for the frequency-to-strain relationship for the Geokon Model 4200 VWG is provided in the model's manual. The expression is defined in Equation 2-3.

$$\boldsymbol{\varepsilon = 3.304\ x\ 10^{-3} * f^2} \qquad \textit{Equation 2-3}$$

$$\varepsilon = Strain\ measured\ by\ vibrating\ wire\ gage\ (in/in)$$
$$f = Measured\ wire\ frequency\ (Hz)$$

This particular model of gage is designed to be embedded in concrete. Gages are installed prior to casting, typically mounted in some fashion to the mild reinforcement cage such that the gage is positioned at a fixed location in the section. Changes in strain in the concrete surrounding the gage cause a relative displacement in the end blocks of

the gage that cause a change in the natural frequency of the tensioned wire. The strain change can then be calculated using Equation 2-3.

It can be noted from Figure 2-9(b) that each plucking mechanism also houses a thermistor that reports the relative temperatures in the section during readings. Temperatures at the gage location can change from fluctuations in the ambient temperature as well as localized changes from cement hydration in the freshly-placed concrete. The microstrain readings from the VWGs are corrected for temperature effects. Figure 2-9(a) illustrates that the lead wires to each plucking mechanism are encased in a protective cable. This simultaneously allows for data monitoring from a position removed from the gage location and protects the delicate wires during casting.

VWGs have been used successfully in a wide range of structural evaluation and monitoring capacities (refer to discussion in Section 2.5). The specific roles of the gages in the proposed construction project are presented in the following pages.

2.3.2 Data Acquisition System

Once the electromagnetic plucking mechanism has measured the gage wire's frequency, the reading must be passed on to a data logging system whose purpose is to collect the signal from the gages, analyze and process that signal, and store the data. The typical components of the proposed data acquisition system are shown in Figure 2-10. All data logging components were manufactured by Campbell Scientific.

The data acquisition components described in this chapter have been used extensively in research at the University of Texas at Austin. A comprehensive tutorial for instrumentation and monitoring procedures was compiled by graduate student Omar Espinoza (2006); this document was referenced repeatedly throughout this project.

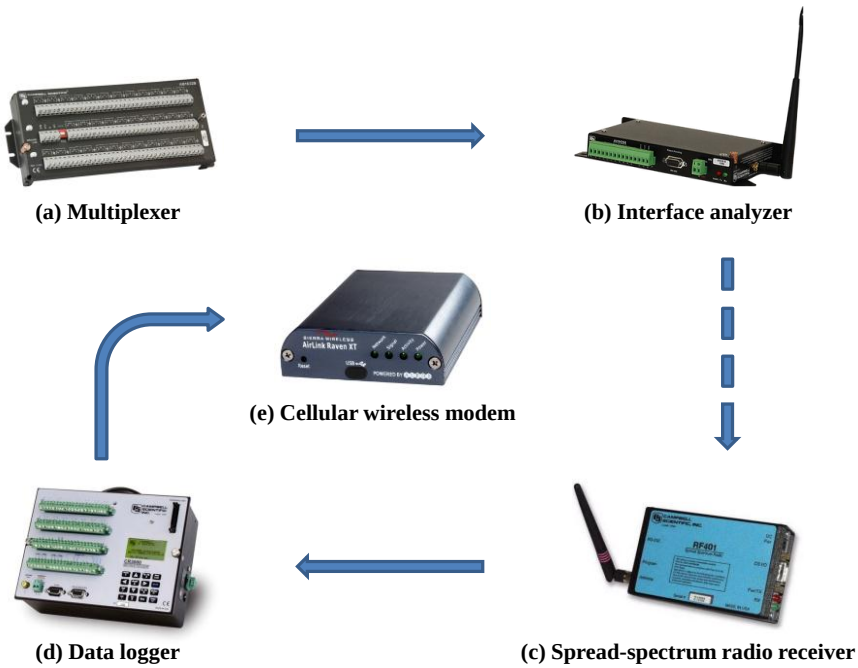

Figure 2-10: Data Logging System Components (Images: Campbell Scientific)

The CR3000 data logger (Figure 2-10(d)) serves as the command center for the system, functioning as a small computer. The user can upload programs to the data logger, enabling it to initiate data readings (referred to as "scans" in the context of the VWGs) and collect and store that data. The Campbell Scientific PC400 interface software was used exclusively in this project for gage and data logger configuration.

Once the data logger initiates a scan, the strain data acquired from the VWGs is passed via the gage lead wires to an AM16/32B multiplexer (Figure 2-10(a)). The multiplexer is in turn wired to an AVW206 interface analyzer (Figure 2-10(b)). The purpose of the analyzer is to convert the raw gage signal into a readable signal for the data logger. It should be noted that gages can be wired directly into an analyzer, but the total number of channel inputs on the analyzer is limited to two. Thus, for projects in which more than two gages are required, the multiplexer is added to the system; the AM16/32B can support a total of sixteen gages. Each analyzer can support two multiplexers, yielding a total gage reading capability of 32 gages for a single analyzer.

After the analyzer has converted the signal, the strain data can be passed on to the data logger. In projects where reasonable proximity to the gages is feasible, an analyzer is often hard-wired directly to the data logger. However, in many cases, logistical or safety considerations dictate the use of a wireless connection for remote monitoring. This project will utilize a wireless analyzer and a RF401 spread-spectrum radio receiver (Figure 2-10(c)) to establish the wireless connection. The radio receiver can be wired directly to the data logger. The wireless connection has an expected useful range of roughly one mile.

When the data from the gages reaches the data logger, it is stored on the CR3000's hard drive. The data logger can be directly connected to a computer via a serial port, which allows the user to manually upload data from the data logger to the PC. While the data logger can be connected to a laptop in the field, long-term monitoring studies may require the use of a cellular modem, such as the RAVENXTV cellular wireless modem (Figure 2-10(e)) used in this study. When the data logger is connected to a modem, the data from gage scans can be uploaded to the wireless network and remotely accessed via the web.

There are, of course, variations on the configuration of the data acquisition network. One such variation was employed in the laboratory studies described in this document, and others will be utilized over the course of the bridge monitoring study. The specifics of the instrumentation for the bridge project are discussed in the following subsection.

2.3.3 Instrumentation Configuration

The components of the data acquisition system described above can be arranged in a variety of configurations, based on the specific monitoring protocol. In the case of the arch construction for the West 7th Street bridge, two main configurations will be used.

The VWGs will be installed throughout the arch at sections where the highest stresses are to be expected during each phase of construction and transportation. Additional gages will be placed in sections where structural behavior may be difficult to

track or predict; these regions are often called “disturbed” or “D” regions. In a typical D-region, the strain profile will not be linear, as conventional Bernoulli beam theory is not applicable. The arch knuckle, where the rib and tie intersect, is a highly congested D-region, and will warrant additional instrumentation.

Instrumentation will be installed at the midspan and quarter-point locations in each arch. Gages will typically be placed in pairs across the axes of the section, allowing for stress and curvature measurements (see Chapters 4 and 5). Figure 2-11 depicts several potential instrumentation sections along the arch rib. The tie will be similarly instrumented. It should be noted that this is not intended to exhaustively define the instrumentation locations, but rather to illustrate a sample of several potential VWG configurations.

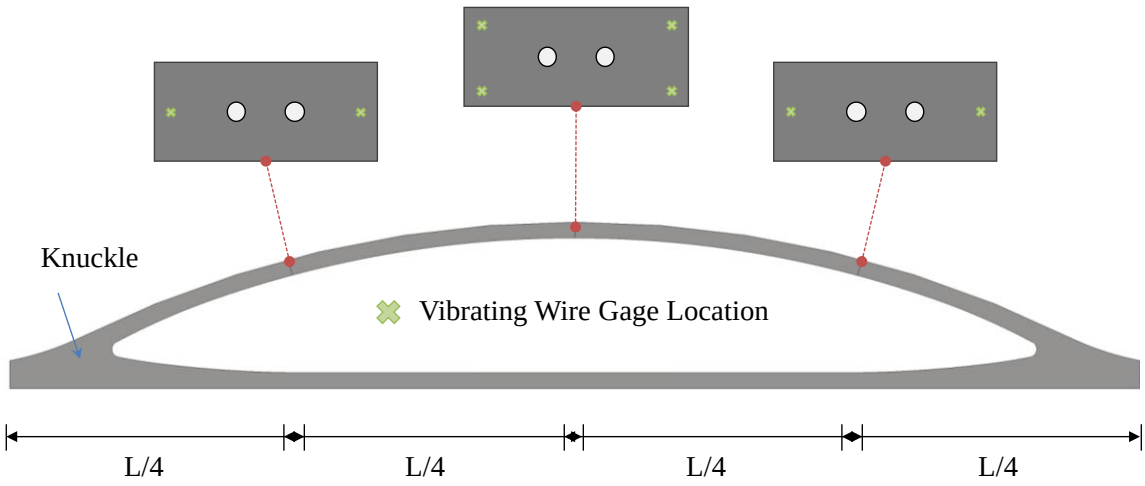

Figure 2-11: Potential Vibrating Wire Gage Locations in Arch Rib

The number and exact configuration of gages will likely change from arch to arch. The total number of gages will be generally be higher in the first few arches compared to subsequent arches, as the critical sections are identified and the instrumentation scheme is refined.

The gages will be mounted on the mild (passive) reinforcement and the lead wires will be bundled and routed through the cage. The bundled cables will emerge from the

arch face at previously selected locations (e.g., near each knuckle region). The lead wires will then be connected to a multiplexer, the first component of the data acquisition network. The data will then be passed to the data logger via either a wired or wireless network as previously described. In the case of arch construction and initial post-tensioning, it may be feasible for the research team to use a hard-wired configuration, but the logistics and safety considerations of the rotation and transportation operations may mandate the use of wireless transmission between the analyzers and data logger.

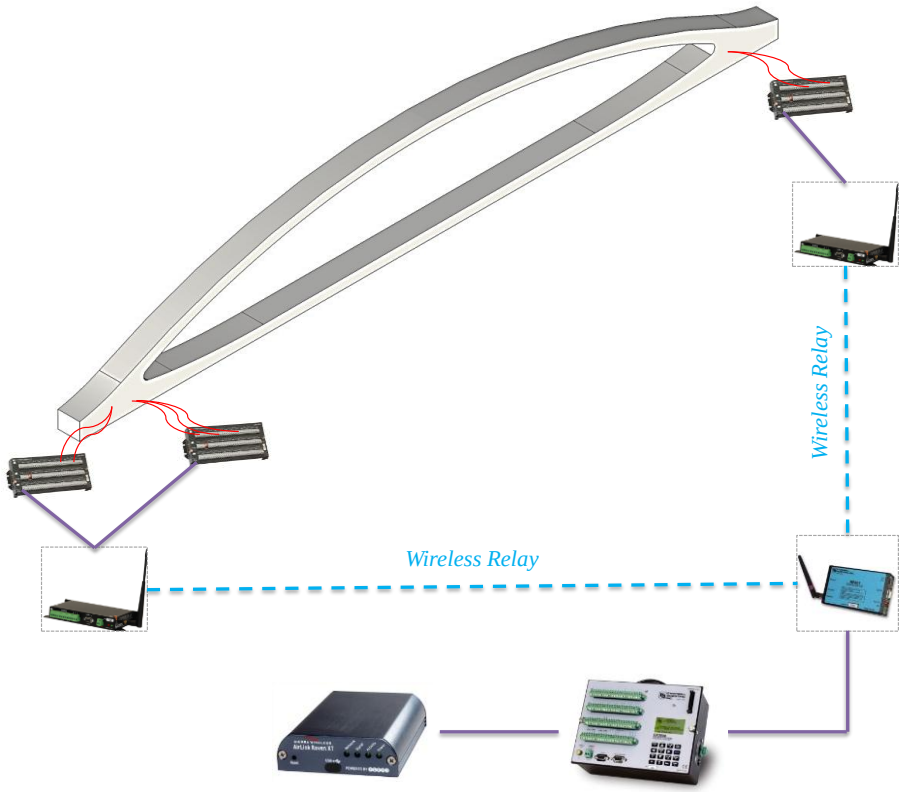

Figure 2-12: Field Monitoring Configuration (Remote Sensing)

For field monitoring during construction and placement of the arches, the research team will connect a laptop computer directly to the data logger and monitor the instrumentation in real-time. However, for long-term stress monitoring through the early performance life of the completed structure, the laptop will be replaced with a cellular

wireless modem to upload the data to the cellular network for remote sensing. A typical remote sensing configuration is depicted in Figure 2-12.

It is important to note that the scan and data relay processes are not instantaneous, but can take several seconds to complete. A gage scan is initiated via a pulse from the data logger; the reading of a single gage takes roughly five seconds. Thus, for sixteen gages in a multiplexer, a single scan could have a duration of up to two minutes. As the construction and rotation procedures are likely to be lengthy processes, this is not expected to be a problem, but is a worthy consideration nonetheless.

The data loggers and computers will be in the possession of the research team throughout field monitoring. As they are hard-wired to the gages, the multiplexers and interface analyzers will be housed in metal lockboxes fixed to the arch. If long-term remote monitoring is to be completed, the radio receivers, data loggers, and cellular modems will be added to the boxes. These components will remain with the arches throughout the duration of the remote monitoring program.

2.3.4 Instrumentation Roles

The instrumentation and data logging systems will be used to monitor several key structural behavior parameters during the construction and placement of the arches. The specific roles of the instrumentation and the design or behavior concerns each addresses are described in this section.

2.3.4.1 Stress Monitoring

The primary instrumentation role is the monitoring of the stresses that develop in the arch members during post-tensioning, lifting, and rotation. Concrete possesses good strength in compression, but the tensile strength is relatively low. As a result, the development of tensile stresses in the arch section is of particular concern. The strength of concrete is often expressed as a function of the 28-day compressive strength, usually denoted by f'_c (ksi). The tensile stress f'_t that causes cracking is often defined as a function of f'_c; the relationship is defined by Equation 2-4.

$$f'_t = \alpha\sqrt{f'_c}$$ ***Equation 2-4***

$$f'_t = Maximum\ concrete\ tensile\ stress\ (psi)$$
$$\alpha = Scalar\ coefficient$$
$$f'_c = Maximum\ concrete\ compressive\ stress\ (psi)$$

It should be noted that Equation 2-4 represents a lower-bound estimate of the maximum tensile stress in concrete. By ACI 318-11, the coefficient α before the radical can be varied between 4 and 7.5, but the conservative lower bound of 4 will be used for the arch instrumentation studies.

The VWGs report strain; stress is calculated in a material's elastic range using Hooke's Law as the product of the strain and the material's elastic modulus (determined as a function of f'_c). The material relationships are described in Equation 2-5 and Equation 2-6.

$$f_c = E * \varepsilon$$ ***Equation 2-5***

$$E = 57000\sqrt{f'_c}$$ ***Equation 2-6***

$$f_c = Concrete\ stress\ (psi)$$
$$E = Concrete\ elastic\ modulus\ (psi)$$
$$\varepsilon = Concrete\ strain\ measured\ by\ gages\ (in/in)$$

The prevention of cracking during stressing and rotation is to be held paramount for the strength and stability of the arches. Thus, reliable monitoring of the stresses in critical arch sections is essential; the VWGs will serve this function during the construction, lifting, and rotation processes. If at any point the stresses approach critical tensile levels, the process will be suspended to prevent cracking. In addition to prevention of cracking, the axial load can be monitored. For purely axial load conditions, averaging the stresses at a given section and multiplying by the section area yields an estimate of the axial load in the section (Equation 2-7). This can be used to monitor the post-

tensioning load and its distribution along the length of the member. If the load is significantly lower at one point along the member, it could indicate a jammed tendon; this data will be used to inform the post-tensioning operations.

$$\boldsymbol{P = A * f_c} \qquad \textit{Equation 2-7}$$

$$P = Axial\ load\ in\ section$$
$$A = Area\ of\ section$$

Stress monitoring will continue during the addition of floor beams and the bridge deck, and into the early service life of the bridge. In addition to preventing cracking in the arch elements, the gage readings will serve to validate the expected stresses used in design.

2.3.4.2 Lateral Stability

Since compression in the arch is one of the primary load-carrying mechanisms, stability of the arch is a concern. The axial stress in the elements of the bridge can result from both post tensioning as well as external loads applied to the arch. The elastic buckling load predicted by the Euler equation is often used as shown in Equation 2-8, where the effective length is utilized. It should be noted that the buckling load is inversely proportional to the square of the member length.

$$\boldsymbol{P_{cr} = \frac{\pi^2 E_c I_{weak}}{(kL)^2}} \qquad \textit{Equation 2-8}$$

$$P_{cr} = Elastic\ buckling\ load\ (lbf)$$
$$E_c = Concrete\ modulus\ of\ elasticity\ (psi)$$
$$I_{weak} = Section\ moment\ of\ inertia\ about\ weak\ axis\ (in^4)$$
$$k = Effective\ length\ factor\ (dimensionless)$$
$$L = Unbraced\ length\ (in)$$

While the axial load in a given section will be determined with the strain gage data as previously defined, the critical buckling load of the arch's rib or tie is difficult to predict since the lateral restraints along the length and at the supports are not well

defined. The end conditions of an axially-loaded member dictate the effective length factor *k*; the interaction of the rib and tie at the knuckle will not be easily defined. In addition, the restraint provided by the prestressing strands on the lateral stability of segments such as the arch and the tie have not been extensively studied in the past. Therefore, the buckling behavior will be qualitatively assessed with the instrumentation.

This qualitative assessment will be accomplished through the monitoring of the curvature in a section. The typical load versus lateral deflection curve of a member subjected to axial compression is depicted in Figure 2-13. For loads that are relatively low compared to the buckling load, the curve is relatively linear and the section has significant stiffness. However, as the buckling load is approached, the member stiffness becomes very low and large lateral deflections occur as the curve approaches the Euler load (P_{cr}) asymptotically.

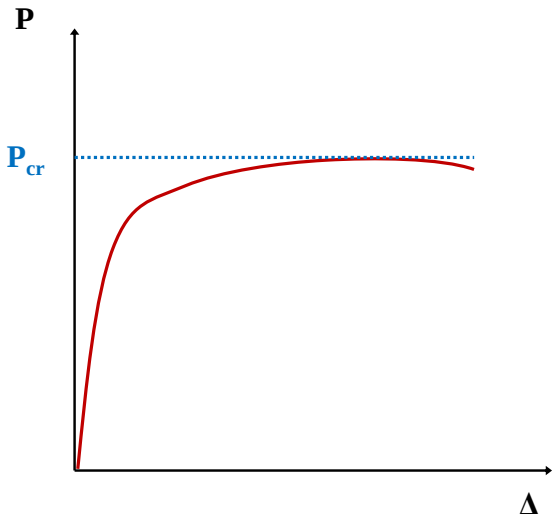

Figure 2-13: Typical Load-Deflection Curve for an Axially-Loaded Member

Real-time monitoring of the load-curvature relationship of the arch will allow the research team to predict impending buckling. This relationship was studied extensively in the laboratory portion of this project, and is discussed at length in Chapters 5 and 6.

2.3.4.3 Sweep Control

The horizontal orientation during casting and the proposed casting procedure introduces an additional concern for the structural behavior. As the arches will be cast in a single lift while in the horizontal orientation, there is likely to be a variation in the concrete properties through the width of the arch (Figure 2-14).

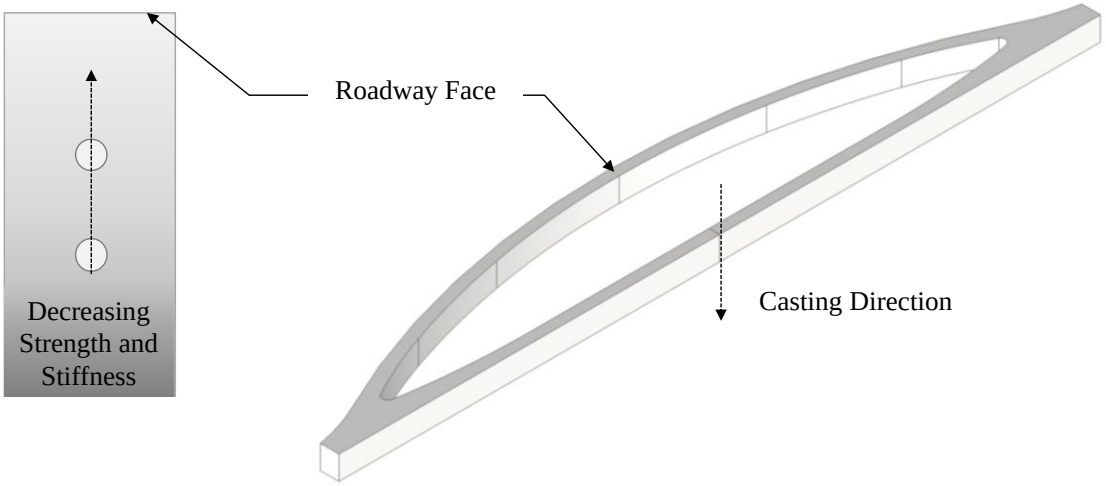

Figure 2-14: Expected Strength/Stiffness Variation over Width of the Arch

As concrete is cast over the 4′-6″ width of the arch, there will be a tendency for the aggregate to settle to the bottom (or sidewalk face), while bleed water will migrate to the top (or roadway face). This will result in a strength and stiffness variation over the width of the arch.

This variation will be of particular concern during the post-tensioning operations. If the same axial load is applied to two sections of different stiffness, the section of lower stiffness will experience a larger axial deformation. Likewise, when the stiffness gradient occurs over a single cross-section, the less stiff concrete will experience a large axial deformation leading to out-of-plane bending deformations that will result in a *sweep* in the arch element. The design team has incorporated post-tensioning ducts that can be used as a "sweep control" mechanism. Varying the level of post-tensioning in each duct

can be used to counter-balance sweep effects due to the stiffness variation in the arch width.

The vibrating wire gages will be used throughout the sweep control operations in a stress-check capacity, ensuring that the variation in post-tensioning across a given section does not create cracking stresses in the element.

2.3.4.4 Long-term Performance

While the primary focus of this research program is to assist the design and construction teams during the implementation stages of the new bridge, the VWGs will be permanently embedded in the arches. Vibrating wire gages have demonstrated excellent durability and reliability over extended periods. The gages can be used to monitor and quantify the effects of concrete creep and shrinkage and long-term prestress losses due to strand relaxation. This provides the capacity for the long-term performance monitoring of the completed structure, which could inform decisions on maintenance or future design considerations.

2.4 LABORATORY PROGRAM

The primary motivation for this project is, of course, the construction of the new West 7th Street bridge in Fort Worth. However, in order to more fully understand the capabilities and limitations of the instrumentation and data acquisition system, and to develop a more thorough understanding of the expected structural behavior of slender post-tensioned elements, an extensive experimental program was developed prior to the start of construction. This multifaceted program served to enhance the confidence and efficiency with which the research team could assess the data acquired from the instrumentation, relate that data to structural performance, and inform on-site construction decisions made regarding observed behavior.

All pre-construction testing was performed at the Ferguson Structural Engineering Laboratory (FSEL) at the University of Texas at Austin. The key components of the laboratory program are briefly introduced here. The design of test specimens and

components, the results of the testing program, and an analysis of the results make up the bulk of this document, and are discussed at length in subsequent chapters.

2.4.1 Vibrating Wire Gage Resolution Study

The primary motivation for the experimental program was the need for a fundamental understanding of the capabilities and limitations of the key instrumentation components. An understanding of the accuracy and precision with which the vibrating wire gages could reliably and repeatedly report strain and infer axial load, stress, and curvature was critical to the success of the instrumentation program.

As such, it was determined that sample gages should be installed in laboratory specimens in which the expected structural behavior was repeatable and well-defined. This provided an efficient platform for the comparison of the theoretical and measured behavior.

Two loading situations were to be considered: (1) axial load from prestressing and (2) externally applied axial loads. A simple rectangular concrete section was chosen. The section is doubly symmetric and the strain profiles of such a section can be reasonably assumed to be linear. The stresses in the section due to axial load and second-order bending effects can be simply and reliably calculated as described in Equation 2-9.

$$\boldsymbol{f_c = \frac{P}{A} + \frac{P\Delta}{S}} \qquad \textit{Equation 2-9}$$

$$f_c = Concrete\ stress\ (psi)$$
$$P = Applied\ axial\ load\ (lbf)$$
$$A = Section\ area\ (in^2)$$
$$\Delta = Measured\ midheight\ deflection (in)$$
$$S = Section\ modulus\ (in^3)$$

The design considerations and final dimensions for the test specimens, the loading schemes, and the placement of the sample instrumentation are presented at length in Chapter 3. It should be noted that the test sections were not designed to exactly model the

behavior of any arch element, but rather to create a simple structural element that demonstrated the resolution of the vibrating wire gages with well-defined support and load conditions. The resulting section had well defined axial and bending behavior and could also be used to study the buckling behavior and influence of cracking on the behavior.

In contrast to the proposed configuration for the arch instrumentation, a much simpler configuration was used in all phases of the laboratory program, as the test setup allowed for relative proximity and access to the instrumentation. A typical laboratory instrumentation configuration is shown in Figure 2-15.

Figure 2-15: Typical Instrumentation Configuration for Laboratory Program

As can be observed from Figure 2-15, no wireless connections was used in the experimental program. Rather, the gages were routed to a multiplexer, which in turn was wired to the interface analyzer and data logger. A direct connection between the data logger and multiplexers initiated the gage scans. This simplified configuration streamlined the data collection process while reducing the length and number of connections needed between components of the data acquisition system.

2.4.2 Stability Studies

The second major facet of the laboratory study was the investigation of the stability behavior of reinforced concrete elements under unbonded post-tensioning. As

previously noted, the lateral stability of the arch elements during post-tensioning is a key construction concern. In an attempt to better understand the elastic buckling behavior, the rectangular test specimen was designed to behave as a slender column. The design considerations and final dimensions for the test specimens are presented in Chapter 3.

While the test specimen was not designed to be specifically representative of any element of the arch, an investigation of its behavior was of significant importance to the proposed field studies. The role that the test specimen will have in presenting a working analogy of arch behavior is evident in Figure 2-16. Structural behavior involving the lateral deflection and potential instability of slender post-tensioned elements is of critical importance to the arch construction process. The simple experimental specimens represented an efficient means of studying the behavior.

In addition to establishing the vibrating wire gages' ability to accurately and reliably predict an impending elastic buckling event, the experimental program sought to study the effects of several interacting factors on the buckling capacity. Perhaps the most significant of these was an investigation of the engagement of a tensioned strand on the edge of the post-tensioning duct, including the effects of this interaction on global system stiffness and overall buckling behavior. It stands to reason that if a tensioned strand contacts the duct wall as the specimen moves laterally, the strand should impart additional stiffness to the system. This should in turn increase the buckling capacity of the member. This is a phenomenon that will likely be encountered during arch fabrication. The laboratory program sought to more fully investigate the structural effects and appropriate additional construction considerations. Background studies on the topic are presented in the following section.

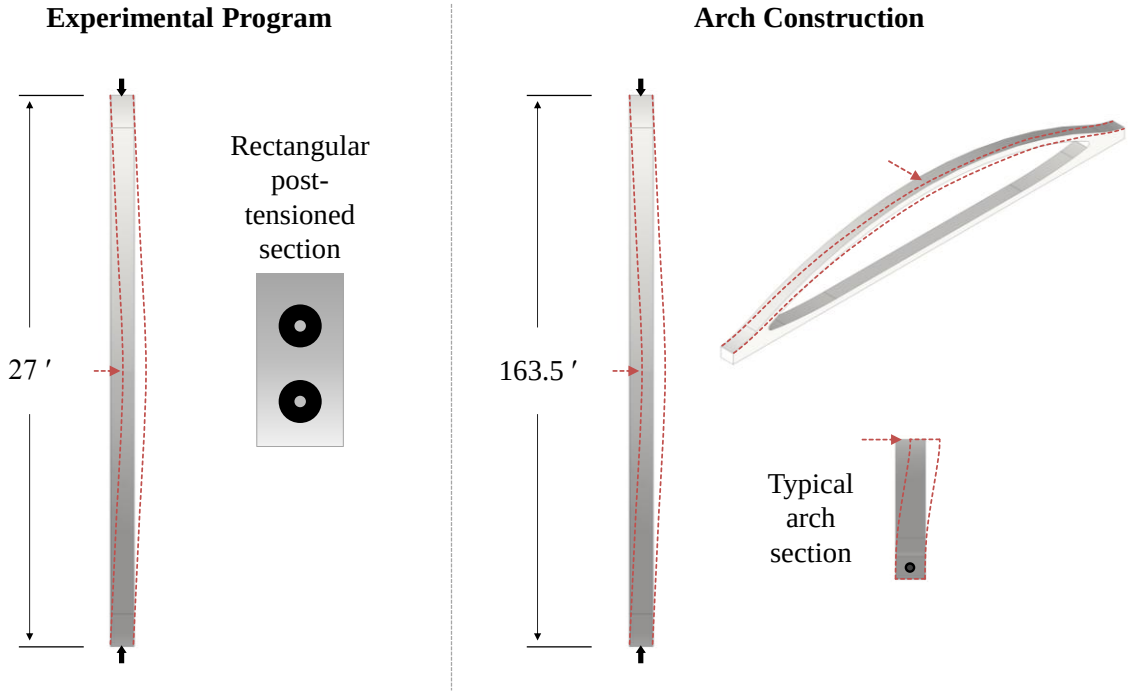

Figure 2-16: Rationale for Lateral Stability Study

Other factors studied included the effects of strand diameter and cracking on the arch behavior. Additionally, the relationship between the level of post-tensioning and ultimate buckling capacity of a slender specimen under external load was studied. In theory, the arches will at no time be under external axial load (as opposed to the axial load applied via post-tensioning) during the fabrication phase. However, an understanding of the interaction between post-tensioning and external loads could serve to inform structural behavior of the arches during external loading. These loads will exist due to the addition of components of the bridge superstructure and on the in-service structure.

2.5 PREVIOUS RESEARCH

A survey of some previous cases employing vibrating wire gages in structural monitoring projects was conducted; several such applications were found and are summarized below. Additionally, an investigation into previous research on the stability

and buckling behavior of post-tensioned elements was conducted. The findings of those studies are briefly presented here.

2.5.1 Vibrating Wire Gages

Vibrating wire gages have been used successfully in structural health monitoring applications throughout the U.S. in both steel and concrete structures. A July 2003 report from Drexel University (Aktan, et al., 2001) to the Federal Highway Administration recommends vibrating wire gages as a viable option for health monitoring of major bridges. While not their only application, VWGs have certainly been used extensively in bridge instrumentation programs. These programs have been well-documented; several are summarized here.

Vibrating wire gages in bridge projects are typically employed in two key roles: to monitor construction procedures, and for long-term performance assessment. The proposed instrumentation for this research project will primarily be used for construction monitoring, but may also be used for additional long-term monitoring when the bridge is in-service. Precedents exist for both roles.

The Veterans' Glass City Skyway, a segmental box-girder bridge in Toledo, OH, was instrumented during its construction in 2001 (Bosworth, 2007). As there was some concern regarding the potential stresses during construction, VWGs were applied externally to the lower slab of several post-tensioned box segments for stress monitoring. Similarly, twelve gages were embedded in sets of four into concrete box girder segments prior to the construction of the Singapore-Malaysia Second Link (Brownjohn & Moyo, 2000). While used primarily during construction, these gages continued to be monitored after the bridge was opened to traffic.

Vibrating wire gages are not always installed with the intent of monitoring stresses during construction. Rather, they may be installed with the intent of monitoring bridge performance under regular live load parameters. Such was the case for Missouri Bridge A6130, a high-performance concrete superstructure near Hayti, MO (Yang & Meyers, 2003). A total of 64 VWGs were embedded in the superstructure to measure in-

service live-load conditions. The gages were found to perform admirably, reporting consistently linear strain profiles, even under minimal loads. The reliable performance of VWGs makes them an excellent alternative to conventional strain gages.

The bridge instrumentation projects described here have been related to concrete bridges. However, the gages have been shown to effectively monitoring stresses in steel structures as well. A 2008 paper (Frangopol, et al., 2008) summarized a comprehensive instrumentation regimen by Connor and Santosuosso (2002) for the Lehigh Bridge SR-33 in Pennsylvania. The authors note the installation of vibrating wire gages on several steel truss members. While simply an element of a much broader instrumentation program, the externally-mounted gages were noted to perform admirably, with reliable and stable data collection capabilities.

Gage durability and reliability is essential to the success of long-term monitoring projects. In addition to the performance observed through field instrumentation, several laboratory studies have been undertaken to establish the long-term consistency of the gages. Bosworth (2007) carefully removed the external gages from the Veterans' Glass City Skyway several years after their installation and performed a laboratory calibration study. He found no significant error in measurement.

A more comprehensive long-term reliability and stability study was performed by Choquet (Choquet, et al., 1999). He identified several key indicators of reliability, including the minimization of zero-drift and sensitivity losses. In the study, gages were applied externally to steel wide-flange sections; readings were taken over 1400 days, demonstrating excellent stability, even with long lead cables. Additional gages were tested against conventional strain gages for a period of two years, with perfect correlation noted. This study led Choquet to the conclusion that vibrating wire gages are a highly reliable and stable option for a wide spectrum of structures, including difficult-access monitoring programs. The results of Choquet's study reaffirm the desirable qualities exhibited by vibrating wire gages for long-term monitoring applications. While care must be taken to properly install and protect the gages from environmental effects, VWGs in the proper configuration demonstrate excellent long-term stability and reliability.

In addition to long-term performance monitoring, vibrating wire gages can be used to evaluate time-dependent material properties. In a MinnDOT study at the University of Minnesota (Ahlborn, et al., 2000), VWGs were embedded in typical prestressed highway bridge girders. The instrumentation was used to monitor creep and shrinkage, as well as prestress losses in the girders. The strain changes measured by the gages were found to be highly consistent with the expected values predicted by conventional material and prestress loss expressions.

It was noted in the discussion of the vibrating wire gage in the previous section that the gages are capable of a variety of measurements. In the proposed instrumentation project, vibrating wire gages will be used to monitor concrete temperature during casting. The temperature-collection capability of VWGs has also been utilized in the field. A new three-span prestressed girder bridge was constructed in Washington (Barr, et al., 2005) to serve as a research specimen. The girders were cast with embedded VWGs; the gages were used to monitor strains and temperatures in the structure during construction and in service. The thermistor data from the gages was used to investigate the effects of temperature on structural performance.

The durability and stability of vibrating wire gages has been studied extensively, with excellent results. These qualities, combined with the gages' multiple data collection capabilities, have made VWGs an excellent choice for short- and long-term performance structural monitoring. This is evidenced by the number of successful bridge instrumentation projects, some of which have been reported here. There is significant precedent to expect similar accuracy and reliability in the West 7th Street bridge project.

2.5.2 Stability Studies

Conventional design theory has long held that a prestressed member cannot buckle under prestressing, so long as the prestressing tendons are bonded to the concrete, or the unbonded tendon is in contact with the duct wall. In theory, in a bonded prestressed member, the concrete in compression will be prone to lateral deflection, but that will be

counteracted exactly by the tendency to straighten in the tensioned steel tendons (Lin & Burns, 1981).

Similarly, in an unbonded post-tensioned member, it is generally accepted that strand engagement with the concrete will impede excessive lateral deflection. It stands to reason that when the tendon and duct wall are in contact, any additional lateral deflection will require lengthening of the tensioned strand. The restoring force provided by resistance to elongation is thought to be easily sufficient to restrain lateral deflection. Several studies investigating these behaviors were conducted around the dawn of prestressed concrete technology in the middle of the 20^{th} century.

In his textbook on prestressed concrete, Magnel (1954) presented an analytical model suggesting that for a post-tensioned element with a single strand in contact with the duct wall at a single point at midspan, the critical buckling load would be four times that predicted by the Euler buckling equation. Magnel cites Keelhoff in stating that for (n-1) contact points between the tendon and the specimen, the critical load could be found as n^2 the Euler buckling load.

Several laboratory tests were performed by Magnel in 1950 and summarized in his textbook (1954) to justify these relationships. In one test, two concrete members with a length of 3 meters and a cross-sectional area of 50 cm^2, with a single duct, were axially loaded. The first, with no prestressing, failed very near the predicted Euler buckling load. The second, with four 5-mm strands, was loaded to nearly two times the Euler buckling load with no observed instability or material failure.

A second test involved a concrete member measuring 20 feet in length with a cross-sectional area of 16 in^2, prestressed with sixteen 5-mm strands. The member was prestressed to a total load measuring nearly three times the Euler buckling load before material failure. While the member had a slenderness ratio of 185, its failure matched that of a member with a slenderness ratio of 14. Magnel asserted that these tests supported his theory that a member with continuous tendon contact will never buckle.

Tests were performed on unbonded post-tensioned specimens by Godden in 1960 and Wilby (1963). In each case, post-tensioning was achieved through the insertion of

Lee-McCall bars into ducts; nuts were tightened on each end of the bar to introduce a compressive force on the specimen. Wilby presented a number of mathematical models predicting significant increases in the critical load for a slender member with tendon engagement. Several laboratory tests were performed to justify these models; Wilby reported a good correlation, but his supporting data is scarce.

The results of Godden's work were similarly difficult to locate; they were summarized by Hurff (2010) in a dissertation investigating lateral-torsional buckling in precast girders. Godden noted a "transition zone" in his load vs. deflection plots during post-tensioning, where the deflection begins to increase at a higher rate. According to Hurff, Godden speculated this indicated the interval when the post-tensioned bar contacted the concrete and the entire system deflected simultaneously. This would appear to be contrary to the conventional thought that tendon engagement should decrease the rate of deflection. Hurff suggested that the presence of a couple in the rigid end anchorages forced additional lateral deflection. Whatever the reasons for the observed relationships, the results presented by Godden seem incomplete with regard to an enhanced understanding of the tendon interaction effects.

In each of the previously described studies, the tendon occupies more than eleven percent of the nominal duct area. In contrast, the proposed study will have a maximum tendon area of less than seven percent of the total duct area. This will allow for significant lateral deflection prior to tendon engagement. A comparison of the tendon areas expressed as a percentage of total duct area for each study is provided in Table 2-2.

Table 2-2: Comparison of Tendon Areas as a Percentage of Duct Area

Study	Minimum Tendon Area (%)	Maximum Tendon Area (%)
Magnel	28.4	41.0
Godden	25.0	76.6
Wilby	11.1	44.4
Current Study	**4.8**	**6.9**

.

While it is generally accepted that a member will not buckle once the strand is engaged, it is recognized that if the tendon area is sufficiently less than the total duct area, stability may be a concern. Bažant (Bažant & Cedolin, 2010) suggested that if post-tensioned strands remain unbonded, the axial reactions at the anchorages could result in some buckling deflections. However, as the deflections increase with additional load, he suggested that the tendon will contact the concrete. This contact results in the development of a radial distributed force, which serves to prevent additional deflections.

While apparently demonstrated in several of the previously-described tests, this may be an overly-conservative representation of the buckling behavior. Benaim (2008) recognized the risk of excessive deflections prior to strand engagement. He described a scenario in which the duct housing the strand was significantly larger than the strand itself. In this case, the compression member could develop significant lateral displacement before the tendon contacted the duct wall. Benaim suggested that if this was the case, the lateral restoring force provided by the strand could be well less than the disturbing force due to the member's deflection, resulting in member instability. The research program described in this document sought to investigate the effects of this interaction on the buckling behavior of concrete compression elements.

An additional factor of interest has been the effect of post-tensioning force on the overall buckling capacity of the column. Lin and Burns (1981) suggest that, for grouted or fully bonded tendons, the compression applied to the concrete is exactly counterbalanced by the tension in the tendons. By equilibrium, the net stress on the section is zero; as such, the buckling capacity of the column is unaffected. However, the same may not hold true for unbonded post-tensioning, where there is no axial stress transfer between the tendon and the concrete section. A 2008 study at Delft University noted a slight increase in the buckling capacity of post-tensioned glass T-beams as the initial post-tensioning increased (Belis, et al., 2006). While apparent, the magnitude of this increase was noted to be relatively insignificant. This relationship is investigated in concrete elements in the experimental program described in this document.

Depending on the circumstances, buckling failures can provide significant warning or can also occur very suddenly with little warning. The behavior can be sensitive to the initial imperfections or out-of-straightness in the member. However, a technique for effective prediction of buckling was critical for this study. While buckling behavior can somewhat arbitrarily be identified by the flattening of the load-deflection or load-curvature curve, a more rigorous method is sought.

One such method was proposed by Southwell (1932). This simple technique involves the plotting of the ratio of the midspan or midheight lateral deflection to the axial load (Δ/P) on the vertical axis, versus the lateral deflection (Δ) on the horizontal axis. Provided that the shape of the initial imperfection is similar to the buckled shape, the relationship of Δ/P versus Δ should be highly linear, with the inverse of the slope equal to the expected elastic buckling load. The x-intercept corresponds to the initial imperfection in the specimen. A typical Southwell plot is depicted in Figure 2-17.

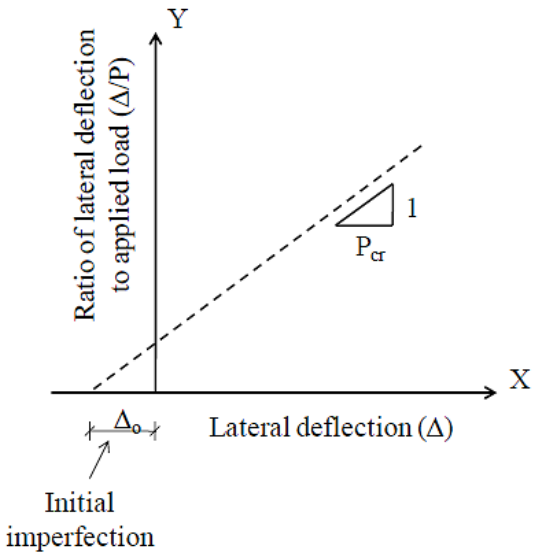

Figure 2-17: Southwell Plot (Image: Wongjeeraphat, 2011)

Early prediction of the expected buckling load using a Southwell plot is particularly helpful if the behavior of a specimen is to be kept in the elastic range. This preserves the specimen for repeated loading cycles without permanent deformation or damage.

Southwell plots have been successfully employed in a number of previous research studies, particularly in steel-related studies. Wongjeeraphat (2011) reported a nearly perfectly linear relationship in his study on the buckling of steel bracing components for truss systems. The method has also proven effective in concrete buckling studies. The Southwell method can also be extended for beam systems as discussed by Meck (1977). For beams, the effects of moment gradient and load position must be considered. Stratford (Stratford & Burgoyne, 1999) discussed the use of Southwell plots in a study of the lateral stability and toppling concerns of long prestressed girders during transportation. He noted that Southwell plots can be used without modification for the prediction of lateral-torsional buckling in concrete elements.

It is important to note that Southwell plots are effective only for concentrically loaded members with a uniform stress distribution along the length. The relationship does not adequately capture bending effects to predict the buckling behavior under an eccentric load. Southwell plots were used to monitor structural behavior in all concentric loading schemes in this experimental program.

2.6 SUMMARY

The background and motivations for this research program were presented in this chapter. This project will assist in the construction of an innovative prestressed, precast network arch bridge for the city of Fort Worth, TX through instrumentation and stress monitoring. The bridge design was completed by TxDOT.

An extensive review of the construction process and timeline was presented. Each of the twelve concrete arches will be cast in a horizontal orientation, partially post-tensioned, and then rotated to the vertical orientation and fully post-tensioned. The arches will then be transported to the bridge site and placed, after which the superstructure components will be added. Project completion is scheduled for late 2013.

This chapter also included a description of the configuration of the instrumentation configuration and data acquisition system for the project. Vibrating wire gages will be installed in each arch; the strain readings from the gages will be collected

and transmitted by the data acquisition system. This data will be used to monitor stresses and curvatures in critical sections of the arches to better assess structural behavior.

The motivation for a pre-construction experimental program was briefly presented, as are the key concerns related to arch fabrication and transportation. A comprehensive review of relevant previous studies was provided. The material presented in this chapter provides valuable information for understanding the outline for the experimental plan discussed in Chapters 3 and 4, followed by the experimental results that are discussed in Chapter 5 and 6.

CHAPTER 3
Experimental Program

3.1 INTRODUCTION

A discussion of the experimental program is provided in this chapter. The test specimens and setup were designed to assess the performance and resolution of the vibrating wire gages in depicting member behavior. In addition to the gage resolution study, the effects of post-tensioning and external load combinations on buckling behavior were investigated. More than sixty load tests were performed on two slender concrete specimens. Gage performance has been carefully monitored, and a primary additional focus has been an investigation of the effects of post-tensioning on member stability. Along with a discussion of the testing program, this chapter includes detailed descriptions of test specimen specifications and construction, instrumentation and data collection, test setup, and test procedure.

3.2 TESTING PROGRAM

The primary motivation of this study was the evaluation of the performance of the vibrating wire gages (VWGs) to be used in the bridge instrumentation project. Given the key role the gages will play in the stress monitoring operations for the TxDOT project, it was imperative that the research team have a fundamental understanding of the precision, accuracy, and reliability of the gages in measuring strain values. The testing program was carefully designed to develop this understanding. It was intended to simultaneously provide confidence in interpreting the strain data and experience in gage installation and data logging techniques.

In addition to the gage resolution study, a key focus of the testing program was to investigate the effects of unbonded post-tensioning on the lateral stability of slender concrete elements. The VWGs played a crucial role in this study as well; the data

acquired from the gages was used to monitor changes in curvature and thus identify buckling in an axially loaded specimen.

3.2.1 Specimen Specifications

The first step in the gage resolution study was the design of the test specimens, which began with the establishment of several key requirements to be met in order to achieve the goals of the lab study. These requirements are summarized as follows:

1- *Simple Rectangular Section*: In an effort to achieve the required confidence in the gages, a simple rectangular section was chosen for the test specimens. Under axial load, the theoretical stresses due to the primary loading and the second-order bending effects at any given rectangular section are easily calculated and compared to the stresses determined from the strain gage readings. The ability to compare the data from the VWGs to a section with well-defined strain behavior enhances the confidence with which the gage data can be used to assess the behavior of the significantly more complex arch sections.

2- *Sweep Control Capabilities*: As previously discussed, the post-tensioning layouts in the arch design were developed so that the contractor has the ability to adjust post-tensioning in the completed arches to control sweep. The embedded gages in the arch will serve as an indicator that the arches are experiencing lateral bending and provide data to assist in achieving proper prestress forces in the arch. To investigate the resolution of the gages in serving this purpose in the arches, the laboratory test specimens were fabricated with ducts that allowed multiple post-tensioned strands. This provided the research team with the ability to investigate the effectiveness of post-tensioning in providing sweep control and the VWGs' ability to monitor the sweep control operations. In the case of the test specimens, it was decided that multiple ducts would be provided, with a single strand in each duct. Additionally, it was hypothesized that strand engagement with the duct wall

would increase the stiffness of the member. With that consideration, the ducts were to be sized significantly larger than the strands to maximize the amount of uninhibited movement before the strand was laterally engaged by the ductwork.

3- *Elastic Buckling Capacity*: An additional motivation for the testing program was to investigate the buckling behavior of the slender concrete compression member. As such, the specimen section had to be minimized to an extent that buckling could be induced. It was decided that the specimen should be sized such that elastic buckling could theoretically be induced under the load provided by the post-tensioning. An additional concern was ensuring that the elastic buckling event occur well before the compressive stress in the concrete approached the maximum compressive stress f'_c. The elastic buckling capacity of the member was described by Euler's elastic column buckling equation (Equation 3-1).

$$\boldsymbol{P_{cr} = \frac{\pi^2 E_c I_{weak}}{(kL)^2}} \qquad \textbf{\textit{Equation 3-1}}$$

$$P_{cr} = Elastic\ buckling\ load\ (lbf)$$
$$E_c = Concrete\ modulus\ of\ elasticity\ (psi)$$
$$I_{weak} = Section\ moment\ of\ inertia\ about\ weak\ axis\ (in^4)$$
$$k = Effective\ length\ factor\ (dimensionless)$$
$$L = Unbraced\ length\ (in)$$

A set of steel side forms measuring 27 feet in length was available at the laboratory; the bottom soffit could be set at a five- or seven-inch width. (The depth of the formwork was 24 inches, but was modified through the construction of a wooden "blockout" to reduce the depth to the desired dimension.) Figure 3-1 shows a sample of several gross section dimensions that were considered, along with the calculated moment of inertia about the weak axis I_{weak} (the direction in which buckling will occur), the critical buckling load P_{cr}, and the ultimate axial capacity of the gross concrete specimen

P_u. It should be noted that these calculations assumed an f'_c value of 4 ksi for the concrete, resulting in an E_c value of roughly 3600 ksi. This was considered a conservative lower bound, as the concrete compressive strength was expected to exceed 4 ksi, thus increasing the elastic buckling capacity P_{cr}. A second simplifying assumption was that the effect of the voids were negligible in the calculation of I_{weak}; only the gross section was considered. While this exclusion actually slightly increased P_{cr}, its effect was less significant than the conservative estimation of E_c.

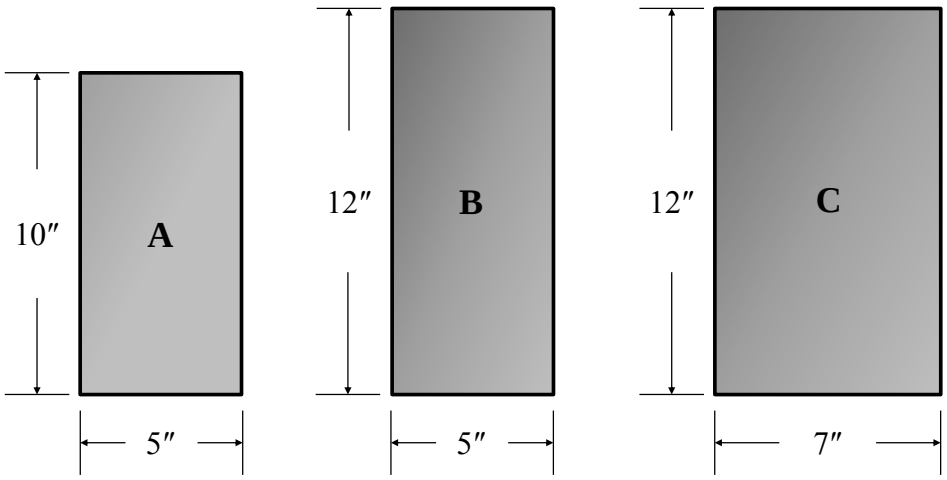

I_{weak} = 104.2 in^4	I_{weak} = 125.0 in^4	I_{weak} = 343.0 in^4
P_{cr} = 35.3 kips	**P_{cr} = 42.4 kips**	**P_{cr} = 116.3 kips**
(P_u = 200 kips)	(P_u = 240 kips)	(P_u = 336 kips)

Figure 3-1: Gross Section Dimensions Considered for Test Specimens

As previously noted, the section was to be designed such that buckling could theoretically be induced through only the axial load provided by the post-tensioning. High-strength seven-wire prestressing strands are commonly available in two diameters: 0.5-inch and 0.6-inch. A single strand is typically stressed to a maximum of 0.75 f_{pu}, where f_{pu} represents the ultimate stress (270 ksi for standard high-strength strands). Thus, a single 0.5-inch strand can be stressed to a load of roughly 31 kips; a single 0.6-inch strand can be stressed to roughly 44 kips.

The relatively small section dimensions, combined with the need to maximize the duct size to accommodate strand translation, limited the number of feasible duct configurations. Plastic duct is typically available in two general shape classifications; round and rectangular. Because the study sought to investigate both sweep control and buckling behavior, the section will translate along both its axes. This made the use of a round duct shape more appealing than a flat rectangular shape. Table 3-1 shows several of the round plastic duct sizes available from General Technologies, Inc. (GTI-USA), a major prestressing products manufacturer.

Table 3-1: GTI-USA Round Plastic Duct Sizes

Nominal Duct Size (in.)	Shape	Inside Diameter (in.)	Outside/Rib Diameter (in.)
0.90	Round	0.91	1.46
1.89	Round	1.89	2.32
2.37	Round	2.28	2.87
3.00	Round	2.99	3.58
3.35	Round	3.35	3.94

Due to the expected congestion in the section, it was decided that only two ducts could be used, placed symmetrically about both the horizontal and vertical axes. With one strand in each duct, the total available axial load provided by post-tensioning was 62 kips for 0.5-inch strands or 88 kips for 0.6-inch strands. This eliminated sections of a seven-inch width from consideration. Figure 3-1 demonstrates that 88 kips is still less than the conservatively estimated elastic buckling capacity for the 7-inch section width.

Ultimately, a gross section with a width of five inches and a depth of ten inches, and an estimated elastic buckling capacity of roughly 35 kips, was selected. This smaller section allowed for significant increases in concrete strength f'_c without the elastic buckling capacity exceeding the available post-tensioning force. As demonstrated in Figure 3-1, buckling will occur well before concrete crushing in the selected configuration. More detailed discussion of individual specimens, components, and construction follows in Section 3.3 of this chapter.

3.2.2 Notable Test Parameters

Once the general specimen specifications were determined, the key measurable parameters to be obtained through instrumentation during the test protocol were established. These parameters and the proposed instrumentation for data collection are detailed in this section.

1- *Strain*: The primary focus of this study was the determination of VWG resolution. A total of six gages were embedded in each specimen; these were used to collect strain values at regular intervals during each load test. The strain data was used to infer the stresses and curvatures in various member sections. This data was then used in parallel with other measured parameters to determine gage resolution and to identify the onset of buckling.

2- *Applied load*: Applied load measurements were taken using a set of three load cells. One center-hole load cell was installed on each of the strands; these were used to measure the post-tensioning load in each strand during testing. A third load cell measured externally applied axial load. A more complete description of the test protocol is included later in this chapter. The applied load data measured by the load cells was used in buckling capacity studies and as a comparison to the axial load inferred from the vibrating wire gages.

3- *Displacement*: As previously discussed, the specimen moved laterally along its strong axis during buckling studies and along its weak axis during sweep control studies. These displacements were measured using linear potentiometers; the data were compared to the deflections inferred from the stain data in the gage resolution study.

4- *Deflected shape*: A final measurement was the monitoring of the deflected shape at regular intervals during load tests. This was accomplished by hand-measuring, at increments along the length of the specimen, the distance between the edge of specimen and taut piano wires stretched parallel to the specimen. This data allowed for the identification of initial imperfections or

out-of-straightness in the specimens, as well as general observation of the deflected shape as the specimen progressed towards buckling.

3.2.3 Progress to Date

At present, more than sixty distinct load tests have been performed on two constructed specimens. Subsequent tests will be carried out on a third specimen with embedded defects to simulate a cracked specimen. Various test protocols have been employed; these are discussed in detail in Section 3.6 of this chapter. The data collected from the VWGs were used extensively in evaluating the reliability and precision of the gages. Both specimens also yielded valuable observations on the buckling behavior of slender concrete elements. The experimental results are presented in detail in Chapter 5. The observations, analysis, and results for the tests of the first two specimens are included in this thesis. Tests are ongoing for the third specimen.

3.3 SPECIMEN FABRICATION

This section provides detailed dimensions, materials specifications, and outlines the fabrication process for the test specimens. Conventional materials and construction methods were used throughout fabrication. Also included in this section is a discussion of some of the challenges encountered during fabrication and casting and the steps taken to minimize the effects of these. As previously noted, a total of three specimens were constructed. The typical specimen section is shown in Figure 3-2. The specifics of the specimen section are discussed in detail in the following pages.

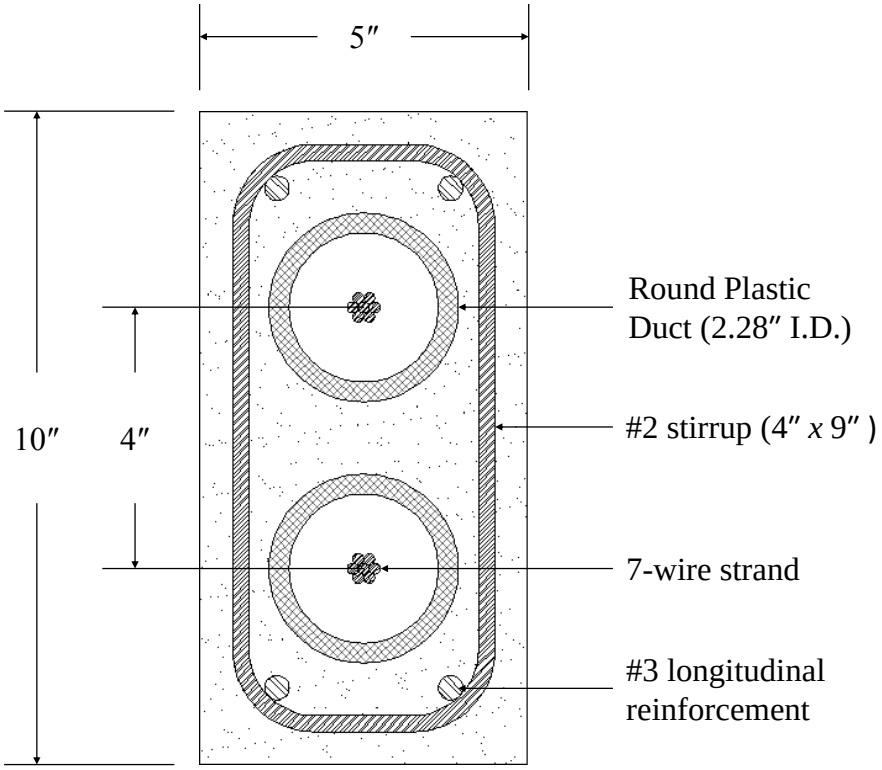

Figure 3-2: Typical Test Specimen Section

3.3.1 Mild Steel Reinforcement

In addition to the high-strength seven-wire strands that were used for post-tensioning, mild steel reinforcement was specified for the specimen. A total of four #3 mild steel bars were specified for passive longitudinal reinforcement. Splices were avoided due to the congestion of the typical section, so these bars were continuous along the length of the specimen. In addition to the longitudinal steel, #2 stirrups at a spacing of twelve inches were provided for shear reinforcement. While the shear demand on the section was minimal, the stirrups provided a measure of insurance and served to support the longitudinal steel and duct in the "reinforcement cage." A schematic of the reinforcement contained in the specimens is shown in Figure 3-3.

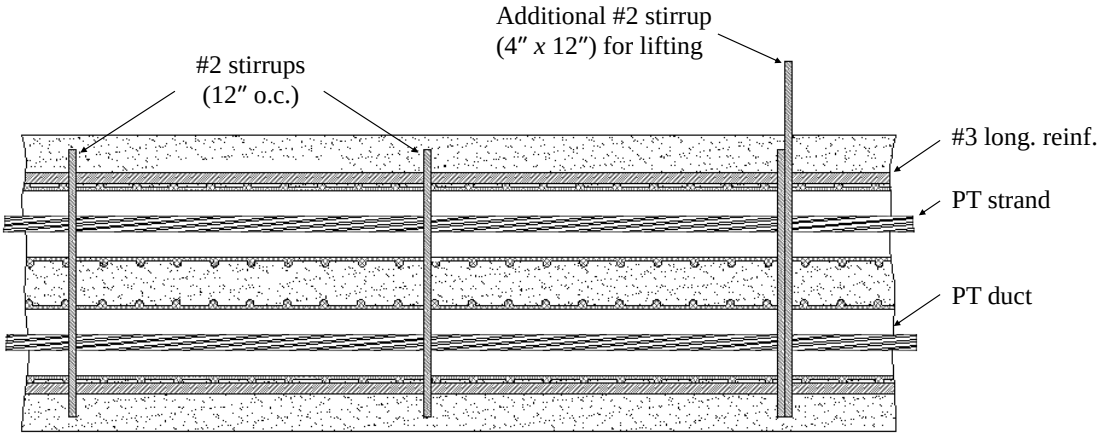

Figure 3-3: Reinforcement Layout for Test Specimen

All specified mild steel was Grade 60 deformed bars. A total of four "coupons" representative of the steel used were included in the shipment. These were tested to establish the actual stress-strain behavior and the yield and ultimate stresses of the mild steel used in the specimen. The values obtained were found to be in accordance with ASTM A615.

3.3.2 Post-Tensioning Strands

In addition to the mild steel reinforcement, two high-strength seven-wire steel strands were specified for the section. One strand was placed in each duct; the primary function of the strands was to provide axial load through post-tensioning. As such, no grouting or bonding was provided. As previously mentioned, two diameters (0.5-inch and 0.6-inch) of strand were used for testing. Strand placement and loading sequence were varied during testing; the specifics of the testing schemes are detailed later in this chapter.

3.3.3 Post-Tensioning Ducts

Two post-tensioning ducts were specified for the section. Integrated into the reinforcement cage before casting, the function of the ducts is to provide a void in the section through which a post-tensioning strand can be passed. In a typical post-tensioning operation, the strands are passed through the ducts and stressed. Next, grout is pumped

into the ducts, bonding the strands and forming a fully composite section. As independent lateral movement of the strands within the ducts was deemed a critical parameter for the buckling study, the strands were not grouted in these specimens.

Post-tensioning ducts are commonly available in two materials: corrugated metal and plastic. Plastic duct was readily available from GTI-USA for this study; typical sizes for round plastic duct are shown in Table 3-1. Given the spacing considerations in the section, the 2.37-inch nominal diameter (2.28-inch inner diameter) was chosen for the test specimens.

The two ducts were placed symmetrically about both section axes, in the configuration shown in Figure 3-2. The ducts were shipped in 20-foot sections, meaning a splice was required in each 27-foot length. As there would be no grouting and no corrosion concerns in the specimen, the duct splice was made using several layers of duct tape. A typical splice is shown in Figure 3-4. The duct spacing was held constant along the length of the member through the insertion of small wood blocks (Figure 3-4) to serve as spacers. More detail on the construction of the specimens and problems encountered with duct placement is included in the following pages.

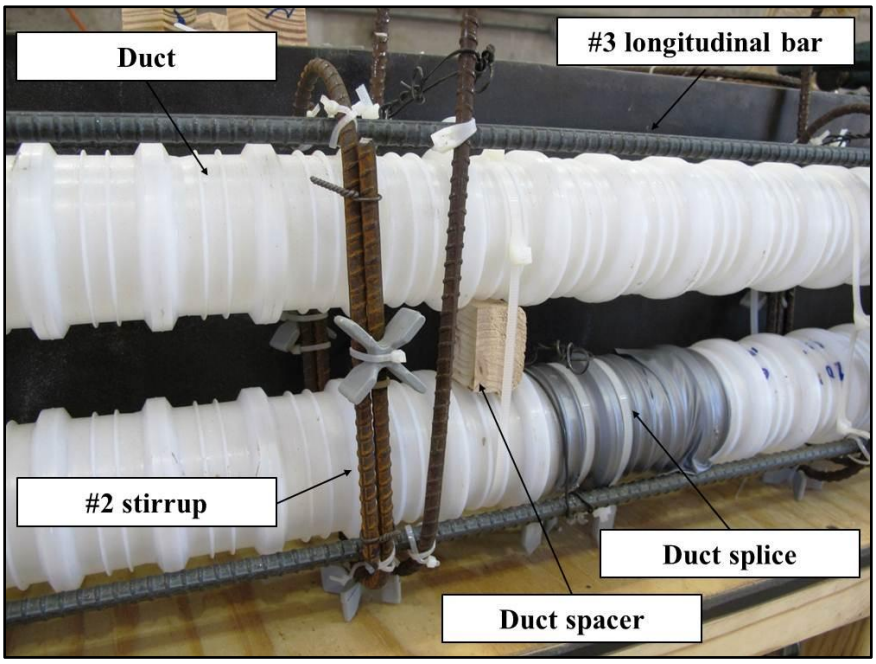

Figure 3-4: Duct Splice in Reinforcement Cage

3.3.4 Concrete Mix

Given the highly congested nature of the section, a high-slump concrete mix with small aggregate size was critical for adequate consolidation and concrete quality. The smallest commonly available aggregate size in Texas is ⅜″. A mix design commonly used for projects at the Ferguson Structural Engineering Laboratory (FSEL) was specified. The typical properties for the mix, 9030DS, are shown in Table 3-2.

The 9030DS mix gains strength very quickly, with expected 28-day compressive strengths well above 8 ksi. Standard 4x8 cylinders were tested for each specimen to establish 7- and test-day strengths. The cylinder breaks indicated a 7-day strength ranging from 8.4 ksi to 9.5 ksi, and initial test-day strengths of 11.0 ksi to 11.3 ksi. Split-cylinder tests for the second specimen yielded tensile strengths ranging from 1.6 to 1.8 ksi. These values exceed the theoretical tensile strength found as 4-7.5 times the square root of the compressive strength, but this is not atypical for high-strength concrete.

Table 3-2: Typical Proportions for 9030DS Concrete Mix

Material	Quantity
Type I Portland Cement	592 lb/yd^3
Fly Ash	200 lb/yd^3
Coarse Aggregate: ⅜″ Gravel	1720 lb/yd^3
Fine Aggregate: Sand	1414 lb/yd^3
Water	18.2 gal/yd^3
HRWR Admixture	47.5 oz/yd^3
Set Retardant Admixture	15.8 oz/yd^3
Water/Cement Ratio	0.26
Slump	8 in

3.3.5 Specimen Construction

The following section details the construction process for the test specimens. The construction consisted of two main stages: the assembly of the reinforcing cage, including the ducts and instrumentation, and casting.

3.3.5.1 Form Preparation

As previously noted, an existing set of 27-foot steel side forms was used for the casting process. These were attached to a plywood soffit, at a width of five inches. The form depth was 24 inches; as the desired section depth was ten inches, a modular wooden "blockout" fourteen inches high and five inches wide was constructed and attached with lag bolts to the soffit between the side forms. It should be noted that during construction, only one side form and the blockout were in place, allowing access to the reinforcement cage. Once the cage was completed and secured atop the blockout, the second side form was moved into place.

Before the cage was placed for the final time, the form sidewalls and the top of the blockout were oiled, and the inside joints between the blockout and side forms were sealed with caulking. In addition to caulk, a double layer of foam weather stripping was fixed to the sides of the blockout; when the side forms were secured, this served to prevent any concrete from leaking out of the section during casting.

3.3.5.2 Cage Assembly

The most significant part of the construction of each test specimen was the assembly of the reinforcement cage. The main stages of the cage assembly are shown in Figure 3-5. The first step was the construction of the shear stirrups; the #2 bars were bent into 4″ x 9″ loops (Figure 3-5(a)) by hand. For the first specimen, two U-shaped bends were produced; the two were tied together with rebar ties into a full loop. For the second and third specimens, a single continuous loop was bent by hand. A ½″ plastic chair was fixed to the bottom and sides of each stirrup, ensuring proper centering of the cage within the section.

After the stirrups were produced, the 20-foot sections of round plastic duct were spliced, using bundling tape as shown in Figure 3-4. These were then laid out next to the formwork and the stirrups were slid over the ducts and spaced roughly at twelve inch increments (Figure 3-5(b)). The four #3 longitudinal bars were then inserted inside the four corner points of the stirrups, parallel to the ducts. The loosely assembled cage was

then lifted onto the wooden blockout. The longitudinal bars were tied to the stirrups (Figure 3-5(c)) in the configuration shown in Figure 3-2 using plastic cable ties. (Plastic ties proved more effective than standard rebar ties on #2 bars.)

The wooden duct spacers (Figure 3-4) were inserted between the ducts; in addition to the spacers between the ducts, 1.5″ plastic chairs were tied to the underside of the lower duct (Figure 3-5(d)) to ensure proper placement in the section. Additionally, the ducts were tied to the stirrups and longitudinal steel to prevent translation of the ducts relative to the reinforcement cage during casting. Once the cage was completed, the ends of the ducts were fitted into wooden end-blocks and caulked prior to casting (Figure 3-5(e)).

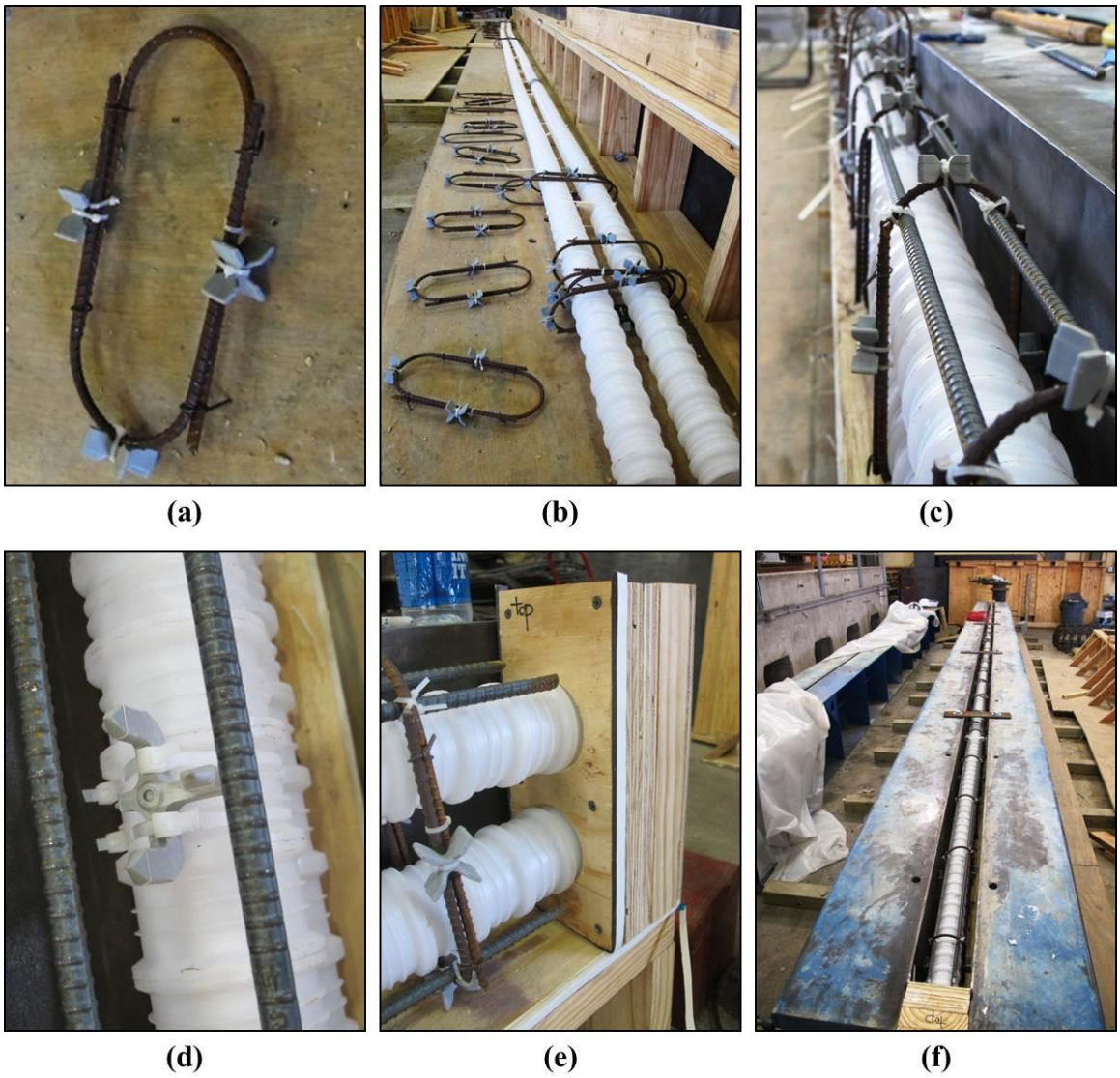

Figure 3-5: Reinforcement Cage Assembly Stages; (a) #2 stirrup; (b) Stirrups placed over ducts; (c) Stirrups tied to longitudinal steel; (d) Plastic chairs tied to bottom of lower duct; (e) Ducts sealed into end blocks; (f) Formwork placed for casting

The final stage of construction before casting was the installation of instrumentation. This process is described in more detail in the following sections. Following instrumentation, the second side form was moved into place for casting (Figure 3-5(f)).

It should be noted that several modifications were made to the specimen construction process after several issues were noted during casting and testing. These are discussed at the end of this section.

3.3.5.3 Casting

The concrete for specimen casting was provided by a local concrete manufacturer. Upon delivery, the concrete was transported from the truck to the formwork in a one-cubic-yard bucket via an overhead crane (Figure 3-6(a)). As previously noted, proper concrete consolidation was critical, considering the highly congested nature of the small section. The steel side forms were not compatible with external vibration, so "pencil vibrators" or "stingers" were used throughout concrete placement (Figure 3-6(b)) to ensure adequate consolidation. After surface finishing, the formwork was covered with plastic for seven days, at which point the specimen was removed from the formwork.

(a) **(b)**

Figure 3-6: Specimen Casting; (a) Concrete transport from truck to formwork via crane bucket; (b) Consolidation via internal vibration

3.3.5.4 Construction Challenges

During cage assembly, casting, and testing, several challenges were encountered. These precipitated a number of changes in the construction procedure detailed in the

earlier section. In the first specimen, the cage was not adequately secured to the blockout, resulting in the cage "floating" during concrete placement. This translated to a slight vertical translation of the rebar cage near midspan. Although it was not possible to measure the exact magnitude of translation, the value was less than the ½″ of cover, but was visible by looking down the length of the prestressing conduit. To ensure this did not reoccur in future specimens, the cage was tied to the blockout at frequent intervals along the length and no further cage translation was observed during casting.

A second significant modification was made from observations during load testing of the first specimen. As the first post-tensioning load was applied to the specimen, cracks formed parallel to its longitudinal axis (Figure 3-7). It was speculated that these cracks were due to stress concentrations arising from slightly raised areas on the end faces of the specimen. If the end face of the specimen is not smooth and planer, the axial force is transferred through the raised imperfections. These represent significantly less area than the entire section, resulting in elevated stresses at those points. It was believed that the cracking was caused by large stresses the occurred due to a poor fit of the end plate against the concrete.

Figure 3-7: End Cracking in First Specimen

In an attempt to eliminate the stress concentrations, the end regions of the reinforcing cages were slightly modified to include a ¼-inch steel plate to serve as the end face of the specimen. These were added as an integral part of the reinforcement cage prior to casting. The 10″-long plates were cut from a length of 5″-wide flat bar, so as to exactly fit the section. Holes adequately sized to fit the ductwork were flame-cut into the plates. Additional 12″-long #3 mild steel bars were cut and welded to the inside face of each plate; these bars were then tied to the primary longitudinal reinforcement to anchor the end plates in place. Bursting stresses were not of significant concern (Collins & Mitchell, 1991) because the load was applied over an area larger than the entire section, due to the sizing of the prestress chair. However, additional #2 stirrups were placed at a spacing of three inches in the end regions as an added measure of insurance against cracking.

Figure 3-8(a) depicts the modified end region as it was tied into the cage prior to casting; Figure 3-8(b) gives a comparison of the end regions of the first and second specimens. The modified end regions proved effective; no end cracking was noted during the load testing of the second specimen.

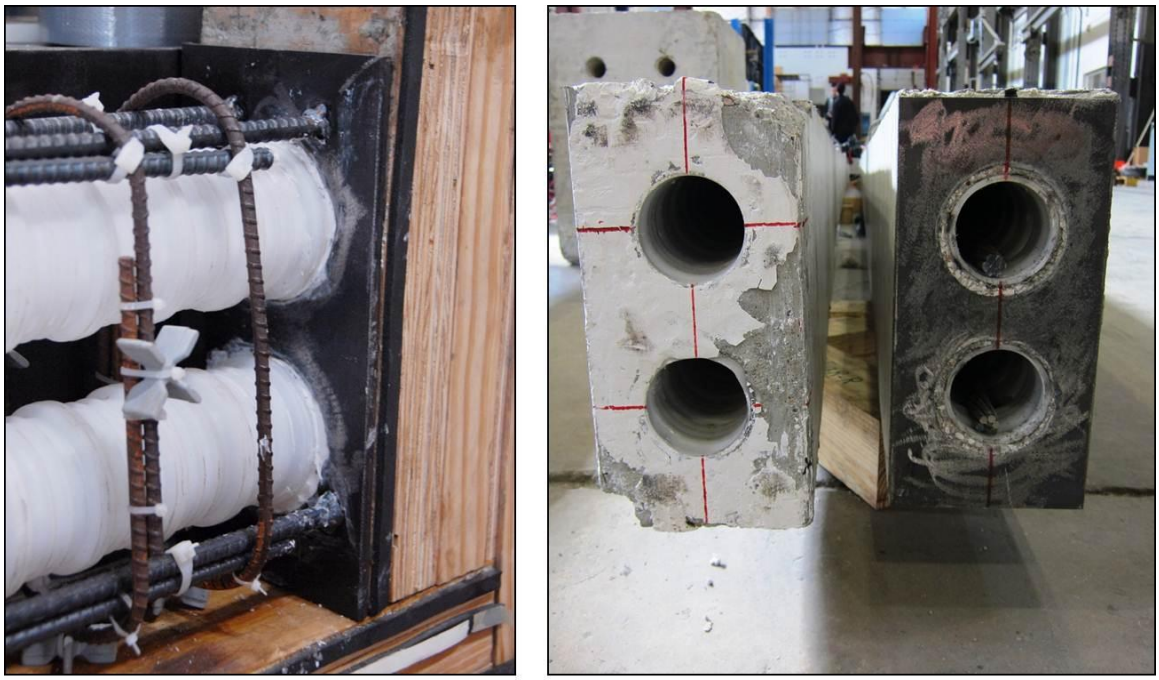

(a) (b)

Figure 3-8: Modified End Regions; (a) End plate prior to casting; (b) Comparison of initial (left) and modified (right) end regions

3.3.5.5 Specimen Lifting and Transport

Given the small section size and the slender nature of the specimen, lifting and transport operations were of special concern. Of particular importance was the prevention of cracking in the member during lifting. In an attempt to eliminate excessive stresses during lifting, it was determined that the specimen would be lifted at three distinct points along its length. During assembly of the reinforcement cage, additional #2 stirrups (4″ x 12″) were provided for lifting (Figure 3-3). These were specified in three groups of four; one group at midspan, and one group at each of the quarter points.

During lifting (which occurred a minimum of seven days after casting), one of the steel side forms was removed and ¾″-diameter steel rods were inserted through the sets of lifting points. These in turn were suspended from a 30′-long steel wide-flange section acting as a spreader beam. The specimen was then slowly lifted from the formwork, with

care being taken to ensure that all three sets of lift points were engaged. The specimen was then transported to the test setup. Figure 3-9 depicts the lifting procedure.

Figure 3-9: Specimen Lifting Technique

While care was taken to ensure that the specimens remained uncracked during lifting, a total of one to four hairline cracks through the section around the midspan lifting points were noted in each of the specimens. Cracking was noted to be most severe in the second specimen. It was speculated that these cracks did not form due to inadequate support during the transport process, but rather in the initial period in which the specimen was lifted out of the formwork. During this interval, the chains supporting the lifting rods had to be readjusted to ensure proper load distribution; this could have resulted in brief periods in which the specimen was somewhat unevenly supported. Additional stresses may have been induced during the immediate lifting out of the formwork. In several cases, the formwork had to be tapped with a hammer to break the specimen free; this

additional restraint may have induced higher local stresses. These cracks were not expected to significantly impact the behavior of the specimen under load.

3.4 TEST SETUP

This section describes the components of the setup used for the load testing of the specimens. A brief overview of the modifications to the setup for the various loading schemes is included; the specific procedures and goals of each loading scheme are described in more detail in Section 3.6.

The test setup had a footprint that measured roughly 45 feet in length and four feet in width; its length was governed in part by the layout of the laboratory strong floor. Key system components were bolted to the 4′-thick concrete strong floor through a series of 1″-diameter rods threaded into anchor points arranged in groups of four spaced at 48 inches. This spacing necessitated the use of HSS 4 x 4 x ⅜ sections to serve as spacers between the loading components and end buttresses.

Figure 3-10 gives a schematic overview of the test setup. It should be noted that the configuration shown represents the test setup as arranged for an external or combined load test. The setup changed slightly for other variations in loading scheme; this is discussed in detail in the following pages.

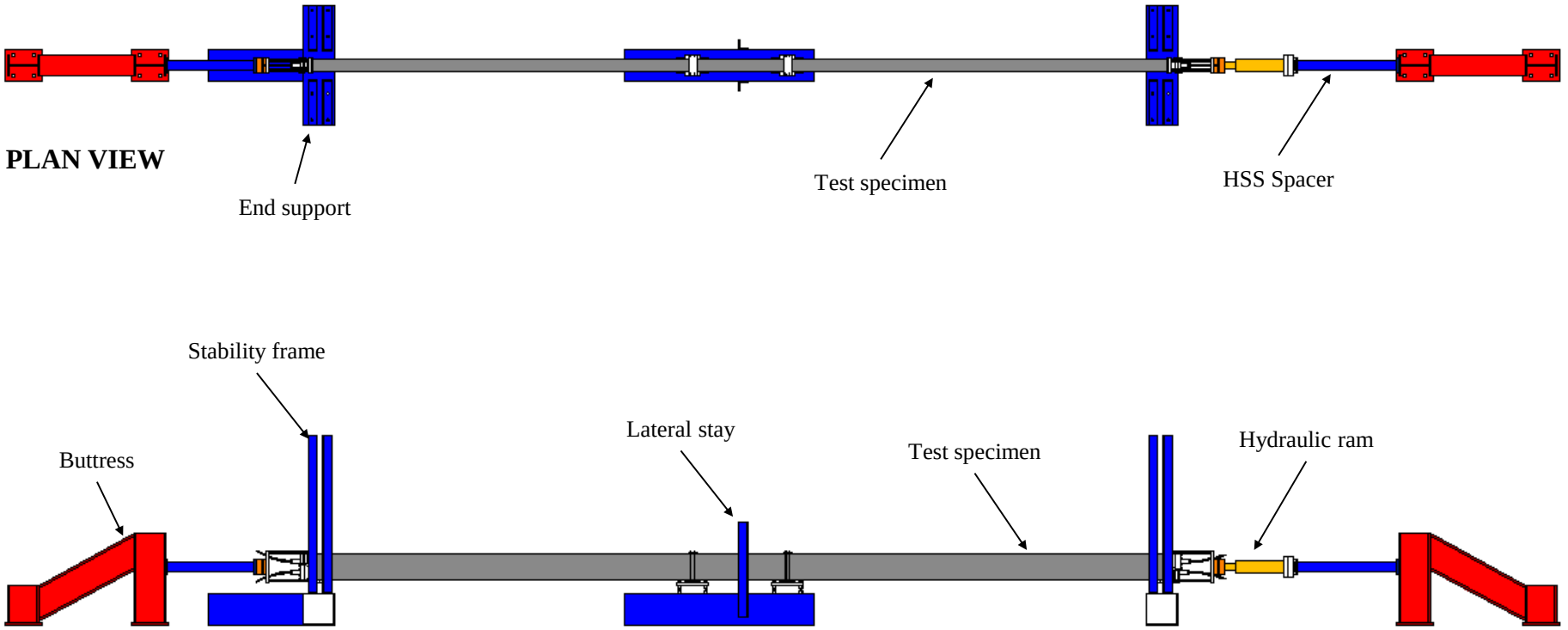

Figure 3-10: Test Setup

3.4.1 Supports

A major design consideration for the setup was to ensure proper support of the specimen to prevent excessive stresses due to self-weight while still minimizing lateral and warping restraint during the tests. The test setup was designed to ensure stability and safety during loading, and to minimize any sources of undesired buckling restraint. The specimen was supported at the ends and at midspan as outlined in the following subsections.

3.4.1.1 End Supports

Each end of the specimen was placed on a HSS 12 x 12 x ½ section. These sections were bolted (snug-tightened) to the strong floor. A thrust bearing was placed atop each end support to minimize the warping restraint at the end of the members. The thrust bearings consisted of a base plate and a series of rings that minimize frictional restraint to warping deformation while still resisting the vertical reaction. A typical thrust bearing is shown in Figure 3-11.

Figure 3-11: Thrust Bearing

3.4.1.2 Midspan Supports

As it was calculated that the specimen would be at risk of cracking under its self-weight, additional supports were specified. Two midspan supports were provided at eighteen inches on either side of midspan. As some irregularity in the level of the floor was expected, the supports were designed to be adjustable. They consisted of a 1″-thick steel plate supported on three ¾″-diameter threaded rods; adjusting the position of the nuts on the threaded rods allowed for the supports to be raised to the desired height to accommodate the specimen. A schematic of the supports is provided in Figure 3-12; the adjustability of the supports is visible in Figure 3-13.

As significant lateral displacement was expected at midspan, the reduction of friction in the supports was critical. A low-friction sliding surface was provided with Teflon pads that served as contact surfaces. The lower pad was epoxied to the base plate of the support; the upper was epoxied to a steel plate that was clamped around the specimen using ¼″ threaded rods. While the Teflon-Teflon bearing surface greatly reduced friction, it could not completely eliminate it. However, once an adequate level of axial compression was provided to prevent cracking, the midspan supports were completely lowered, resulting in up to ½″ of clear distance between the supports and the specimen, eliminating friction at midspan. Of course, the supports were raised prior to complete unloading of the specimen. Figure 3-13 depicts the support adjustment stages.

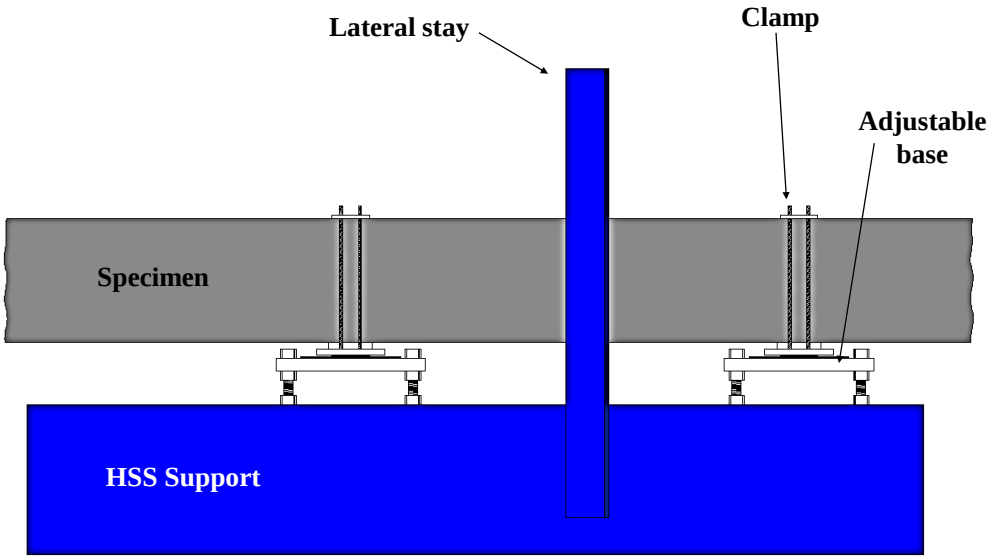

Figure 3-12: Midspan Supports

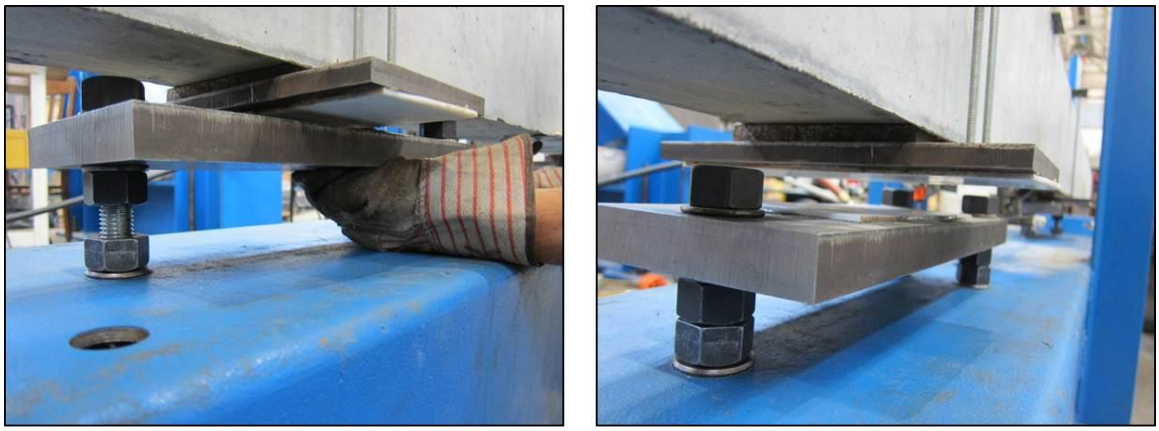

Figure 3-13: Midspan Support Adjustment; (a) Raised position; (b) Lowered position

3.4.2 Stability Components

A second key function of the test setup was to provide adequate support for equilibrium of the specimen and approaching idealized boundary conditions. The idealized boundary conditions consisted of a simply supported member with twist and lateral movement prevented at the ends and no warping restraint at the supports. The

thrust bearings and midspan supports were designed to eliminate unwanted restraint during loading; of particular concern, however, is the development of twist or rocking of the specimen on the supports during loading. In an effort to prevent this, a set of vertical stability frames was bolted to each HSS end support. These housed a set of horizontal threaded rods oriented perpendicular to the longitudinal axis of the specimen. Each end support included four such "contact points" that could be extended into contact with the specimen to prevent rocking or twist at either end. The "contact points" consisted of threaded rods with rounded ends. A schematic of the stability frame orientation is provided in Figure 3-14(a); Figure 3-14(b) gives a detail view of the contact points resisting twist in a test specimen. While the contact points provided critical stability, it was important that they not be tightened beyond initial contact with the specimen. If tightened too much, the end restraint conditions could be significantly altered, resulting in fluctuations in the buckling capacity.

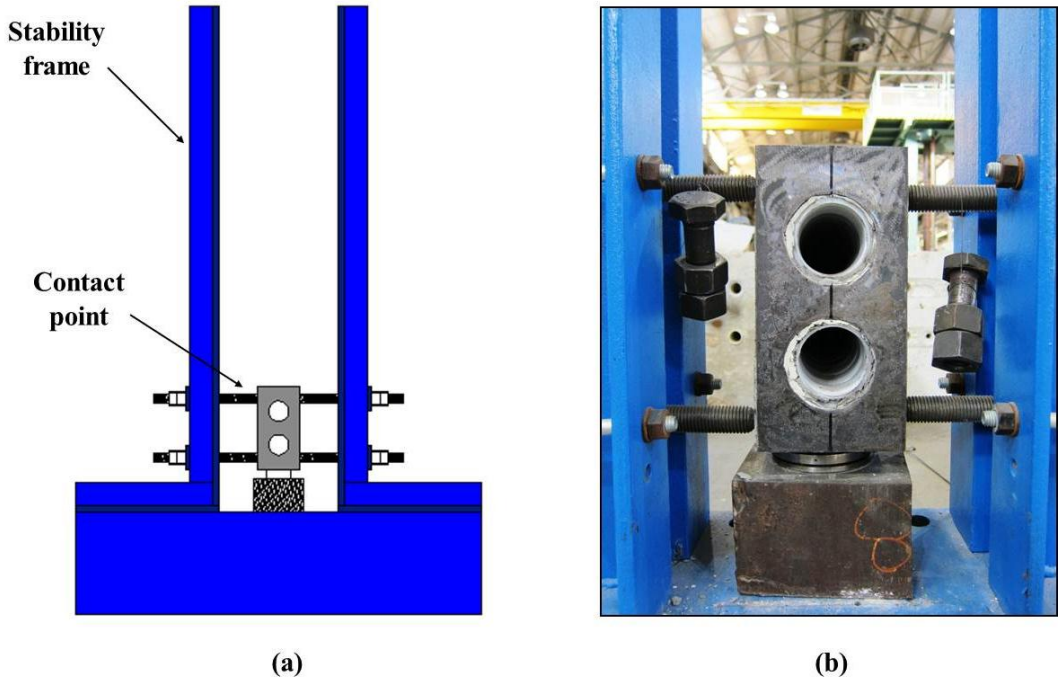

Figure 3-14: Stability Frame; (a) Schematic; (b) Contact points

In addition to vertical stability frames at each end support, vertical steel angles were welded to the HSS support at midspan to act as lateral stays to arrest excessive lateral displacement in the specimen in the event of sudden buckling. In addition to preventing excessive movement, the angles functioned as the zero reference points for lateral displacement measurements with linear potentiometers. The lateral stays are shown in Figure 3-15.

Figure 3-15: Lateral Stays at Midspan

In addition to the stability frames and lateral stays, concrete blocks were placed on each side of the specimen at both the quarter points and each end of the test setup to provide a safety measure during loading operations.

3.4.3 Loading Schemes

Three main schemes were used for the load testing of the specimens: pure post-tensioning (PT), pure external load, and a combination of post-tensioning and external load. Each of these schemes required some modifications to the test setup configuration. The components and configurations involved with each load scheme are described in this subsection. The specific goals and processes for each are discussed in Section 3.6. Figure 3-16 gives a comparison of the test setup configuration for the different loading schemes.

POST-TENSIONING

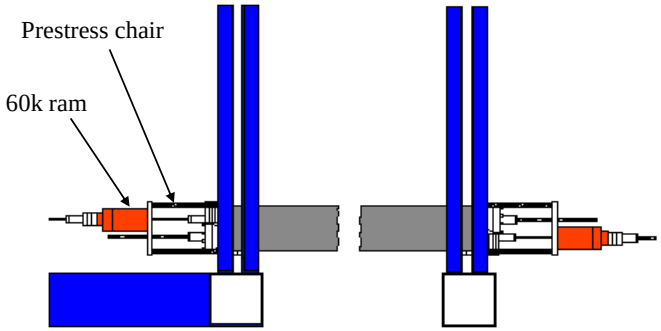

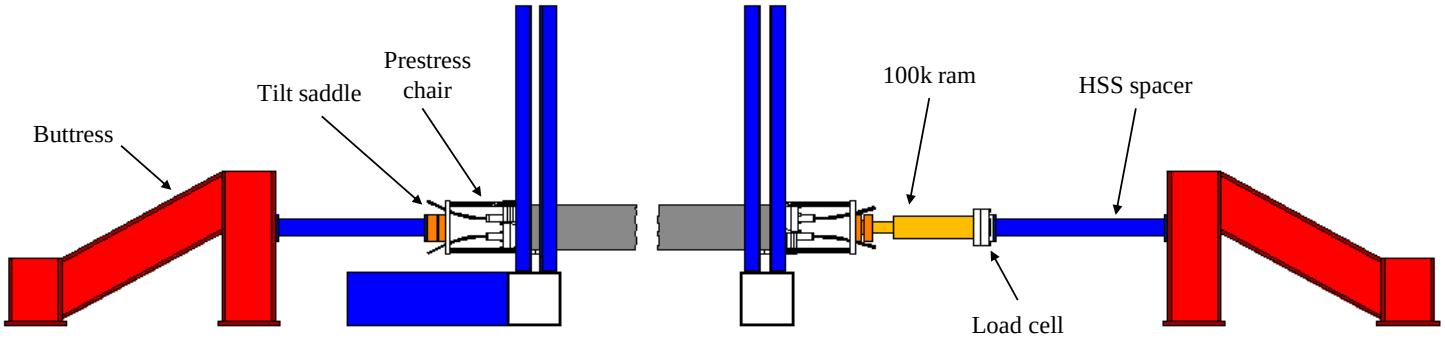

EXTERNAL/COMBINED LOADING

Figure 3-16: Load Setup Comparison

3.4.3.1 Post-Tensioned Tests

The first key loading scheme was pure post-tensioning (PT). In this procedure, axial load was applied to the section through the stressing of the PT strands; this was accomplished with a pair of 60-kip center-hole rams. The typical setup for a PT load test is shown in Figure 3-17. The end of the strand was passed through the ram and a strand chuck was slid into place onto the end of the ram to prevent strand slippage. (A series of spacers were inserted between the ram and chuck to enable chuck removal.)

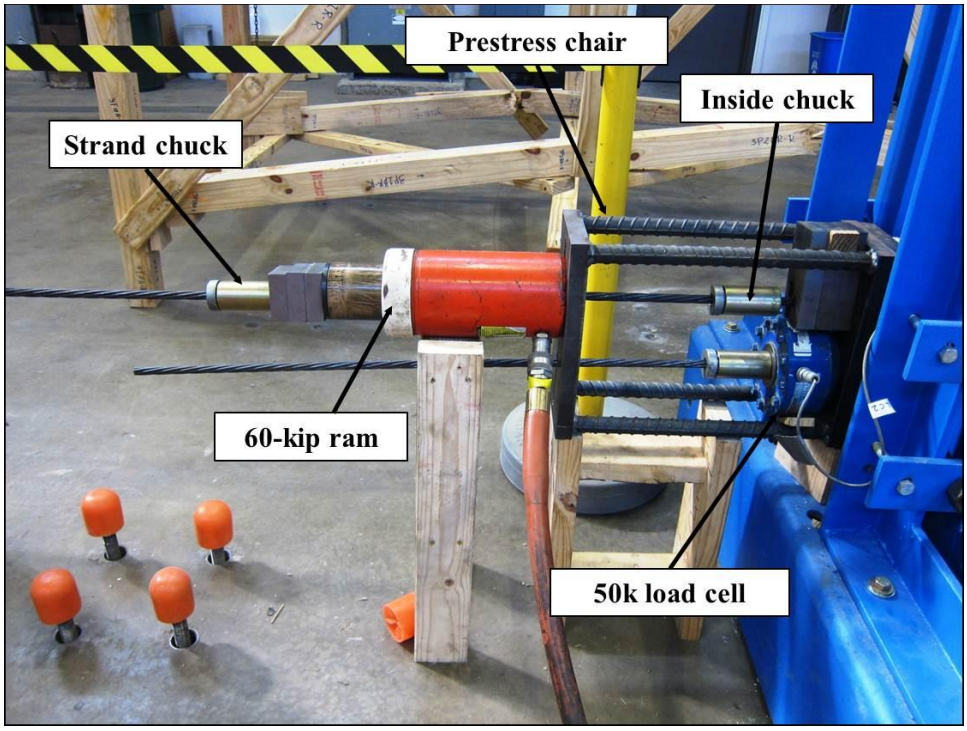

Figure 3-17: Post-Tensioning Load Setup

Loading was performed through a *prestress chair* located at each end of the specimen (Figure 3-17). The purpose of the prestress chair was to facilitate anchorage of the strands after stressing. Two anchorage chucks were used on each strand. One of the chucks (strand chuck) was located behind the prestressing actuator (the 60-kip ram in Figure 3-17) while the other (inside chuck) was located in the prestress chair on the front

side of the actuator. During stressing, the strand chuck was locked behind the actuator and the piston is extended, which stresses the strand. Once the strand has been stressed to the proper level, the inside chuck is engaged and the actuator pressure is released, transferring the force to the inside chuck. Once the inside chucks had been set, the ram could be removed and the PT load is "locked in" on the specimen. This was not used for PT tests (the ram was not removed in this scheme), but was critical in combined loading. In this experimental program, the prestress chair also served to house a load cell centered on each strand. It should be noted that an additional 1″-thick end plate with ⅝″-diameter holes for the strands was placed between the prestress chair and the specimen. The width of this plate and the chair was 5-½″; the height of each was 12″ (slightly larger than the 5″ x 10″ dimensions of the specimen). This oversize ensured that axial loading through the chair and plate would occur over the entirety of the section.

As previously noted, the total axial load that could be applied through the two strands was 62 kips for 0.5-inch strands and 88 kips for 0.6-inch strands.

3.4.3.2 External Tests

The second main loading scheme employed was a pure external load. In this procedure, the 60-kip rams used for post-tensioning were removed and a 100-kip dual action ram was moved into place; the prestress chairs were left in place, but no post-tensioning was applied. The load was applied between the two A-frame buttresses constructed of steel wide-flange sections that were post-tensioned down to the lab's strong floor. As previously noted, the anchorage layout on the strong floor required an HSS spacer to bridge the residual distance between the buttresses and the specimen and ram (see Figure 3-16). Figure 3-18 depicts the external load configuration. In an attempt to decrease the resistance to lateral end rotation during loading, as well as to compensate for slight misalignments in loading components, each HSS spacer was fitted with a spherical head bearing or *tilt saddle*. These are shown in Figure 3-18 and Figure 3-19(b).

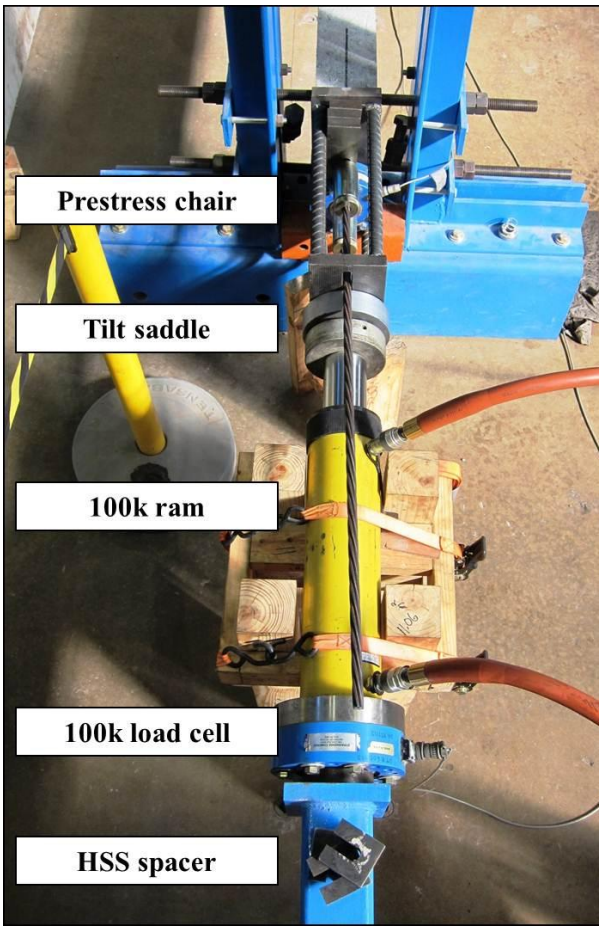

Figure 3-18: External Load Setup

3.4.3.3 Combined Load Tests

The final major load scheme employed was a combination of the post-tensioning and external loading procedures. These tests are referred to throughout this document as *combined load tests*. In this scheme, post-tensioning was applied using the setup shown in; once a desired PT load was achieved, it was "locked in" using the chucks inside the prestress chair. After the 60-kip rams were removed, the external loading components were moved into the configuration as shown in Figure 3-18; external load was subsequently applied.

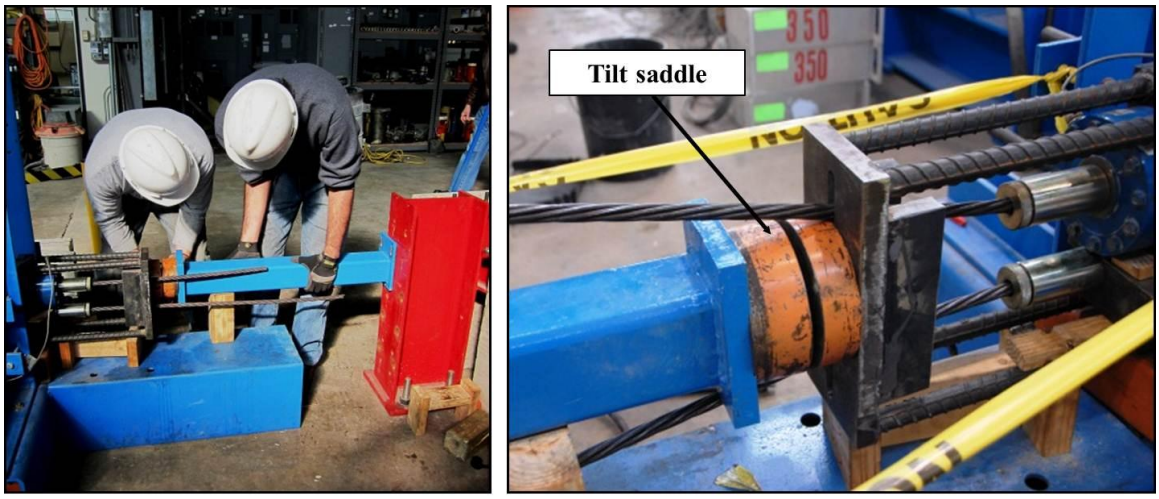

Figure 3-19: Combined Loading; (a) Placing HSS spacers; (b) Tilt saddle with end displacement in strands

Figure 3-19(a) depicts the placement of the HSS spacer after the removal of the PT rams. Note from Figure 3-19(b) that once the PT force had been applied, the ends of the strands had to be moved aside to accommodate the placement of the tilt saddle.

3.5 INSTRUMENTATION

The instrumentation components and configuration have been discussed at length in Chapter 2 of this thesis. This section provides details on the installation procedures and specific usages for the instrumentation as they applied to the experimental protocol.

3.5.1 Vibrating Wire Gages

As previously noted, the primary instrumentation components for the laboratory tests were the vibrating wire gages (VWGs). An extensive discussion of the gages is included in Chapter 2 of this thesis. This section describes the gage configuration and installation procedures for the laboratory specimens.

3.5.1.1 Gage Overview

A total of six VWGs were installed in each test specimen. Four were placed at midspan (13′-6″ from each end), and an additional two were placed at one quarter point (6′-9″ from the end of the specimen). A schematic of the gage layout in each section is provided in Figure 3-20. The spacing between the gages is noted on the figure.

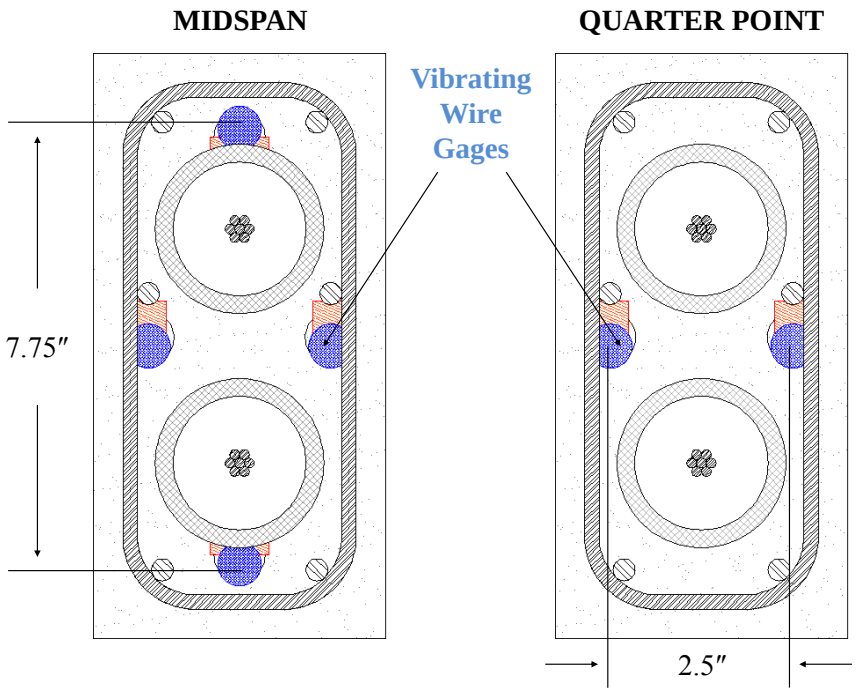

Figure 3-20: Vibrating Wire Gage Placement

Figure 3-21 depicts the numbering system used to identify the gages. As can be seen, the gages were paired across the width of the section at both midspan (Gages 1 and 2) and the quarter point (Gages 5 and 6), and across the depth of the section at midspan (Gages 3 and 4). The strain differentials across each pair of gages were used to infer the curvature in the section. The pairs across the width of the section were used in lateral motion studies, while the pairs across the depth of the section were primarily used to study vertical motion. More detail on the processing and use of gage data is included in Chapters 4 and 5.

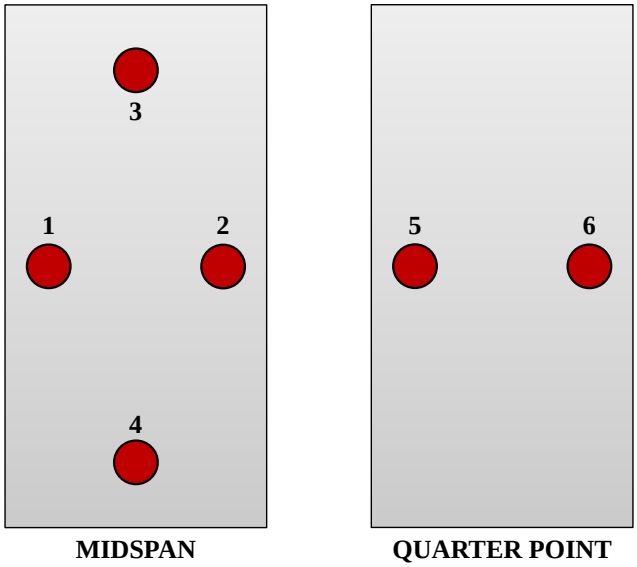

Figure 3-21: Vibrating Wire Gage Nomenclature

3.5.1.2 Gage Installation

The installation of VWGs must be completed with care. There are two key considerations in an effective gage installation. First, the gage must be protected throughout casting, particularly during internal consolidation operations. It is important that the body of the gage is not damaged, the plucking mechanism is not dislodged from the gage body, and the lead wires from the gage are not damaged. Several steps can be taken to avoid these problems. If the gage is mounted parallel to and below a section of longitudinal reinforcement, it is less likely to be directly impacted by a vibrator during consolidation. Similarly, the lead wires should be secured to the underside of longitudinal reinforcement as they are passed through the cage and out of the formwork. Finally, the plucking mechanism should be secured to the gage body (a plastic cable tie is an excellent way to ensure adequate connection). Care was taken to address each of these considerations in the construction of the test specimens.

As no longitudinal reinforcement was located immediately near the desired gage locations, an additional thirteen-inch length of #3 bar was tied between the shear stirrups at the instrumentation sections. A schematic of the typical gage layout is shown in Figure

3-22. The additional length of rebar served to protect the gage during casting. The lead wires for each gage were routed along the undersides of the main longitudinal reinforcement to a point between midpoint and the quarter point. Here, the cables for all six gages emerged from the top of the formwork. It should be noted that the upper and lower gages (Gages 3 and 4) were mounted directly to the ducts (see Figure 3-23(b)).

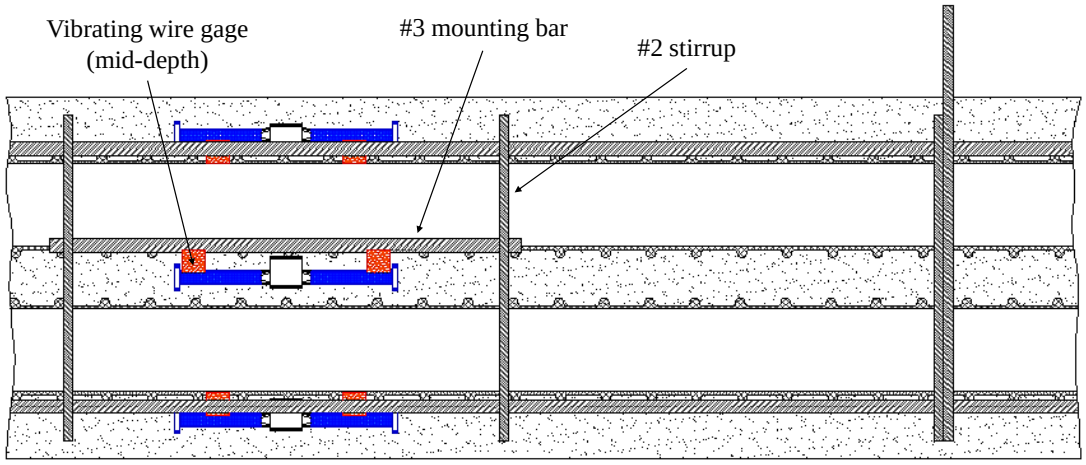

Figure 3-22: Elevation View of Gage Installation Positions

The second key consideration in the installation of vibrating wire gages relates to the maintenance of the position of the installed gages in the section. Ensuring that the gages do not move significantly during casting is critical to accurate derivation of position-related parameters such as curvature. It is important to note that for the extremely small section employed in the test specimens, a small change in gage position will likely result in a relatively large associated in estimating curvature. In the case of the construction of the relatively large arch sections, however, slight changes in gage position will have significantly less impact on the calculation of curvatures in the much larger arch section.

As previously mentioned, some degree of upward translation was noted in the reinforcement cage during the casting of the first specimen. The total translation was estimated as less than ½″, and the spacing of the mid-depth gages (Gages 1 and 2, 5 and

6) was almost certainly unaffected. Nonetheless, it was determined that additional precautionary measures had to be taken in gage installation to ensure the highest possible precision in identifying the final gage locations. In the case of the mid-depth gages, a "mounting frame" was constructed for gage installation (Figure 3-23(a)). The frame consisted of eight short #3 bars; four were cut to five inches (the section width) and four were cut to ten inches (the section depth). The five-inch lengths were tied horizontally across the section, while the ten-inch lengths were tied vertically. These formed an open frame that, when the side forms were placed, held constant the position of reinforcement cage. The thirteen-inch rebar lengths holding the VWGs were tied between the vertical bars. The top and bottom gages (Gages 3 and 4) were fixed directly to the ducts using plastic chairs and cable ties (Figure 3-23(b)). The ducts were subsequently secured to the reinforcement cage. No gage movement was apparent during the casting of the second or third specimens.

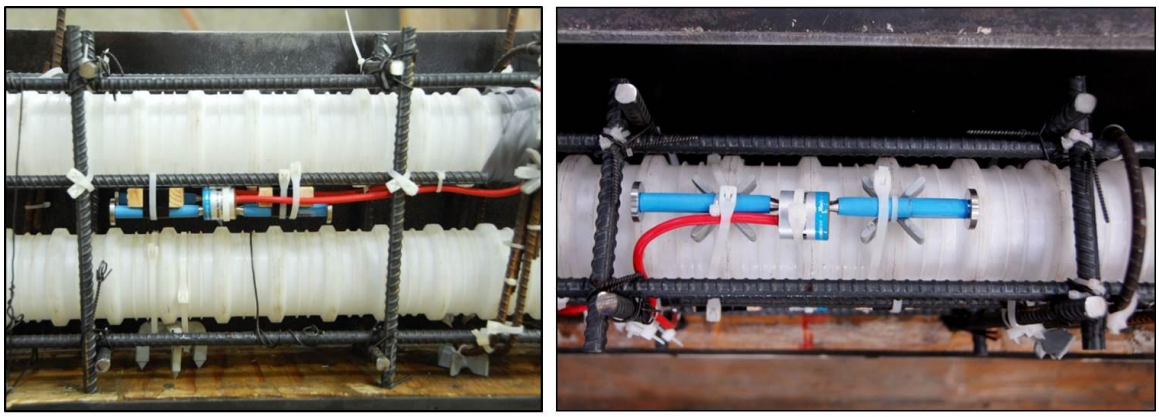

(a) (b)

Figure 3-23: Gage Installation Photos; (a) Additional "mounting frame" for mid-depth gages; (b) Top gage mounted directly on duct

The installation of vibrating wire gages in the test specimens yielded observations and experience that will prove invaluable in the field implementation portion of this project. Many of the same techniques will be employed during arch instrumentation.

3.5.2 Data Logging System

The data logging system components and configurations were discussed at length in Chapter 2. In the interests of simplicity and efficiency, the configuration was modified for the laboratory tests described here. The vibrating wire gages were connected to a single multiplexer, which was in turn connected to an interface analyzer. (This configuration was consistent with the proposed configuration for arch instrumentation.) The analyzer was then connected directly to a CR3000 datalogger, which in turn was wired to a desktop computer. Unlike the proposed arch instrumentation protocol, no wireless connections were utilized in the lab tests. Figure 3-24 shows the data logging equipment used for the tests described in this report.

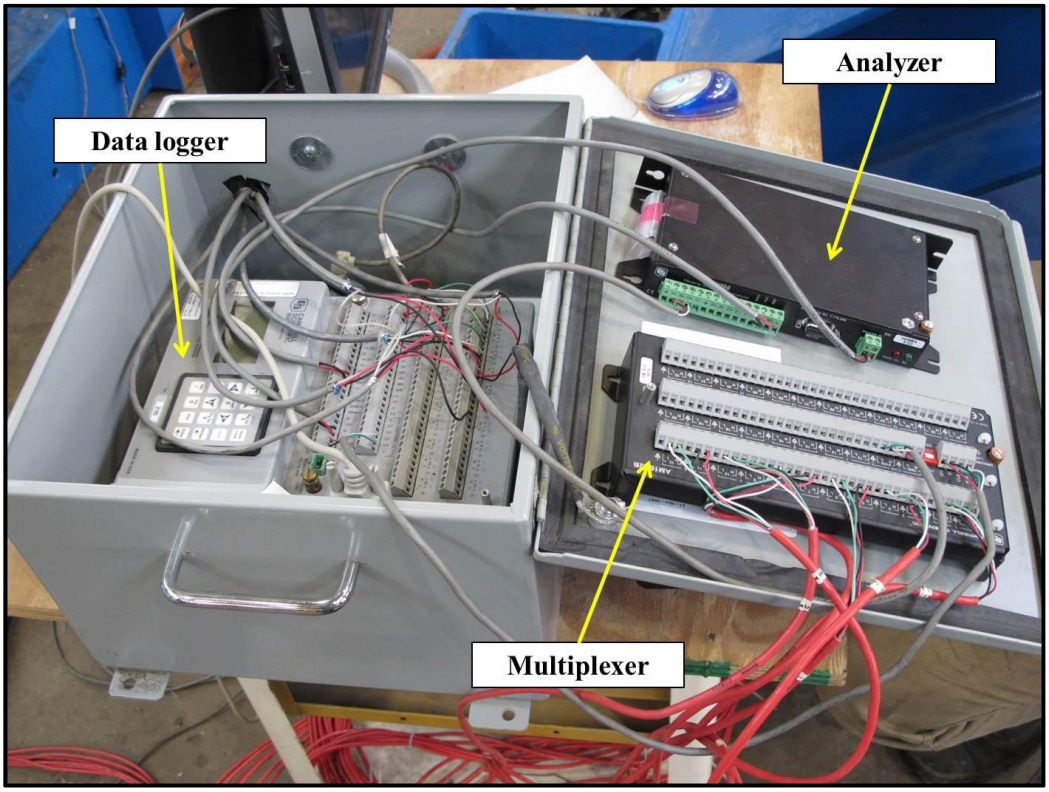

Figure 3-24: Data Logging Equipment for Lab Tests

Periodic data scans were run during each load test. While these scans could be programmed to occur at regular intervals, each scan was manually initiated for the

experimental program. The VWGs were read individually in sequence. The time duration for the scans and collection of all six gages averaged slightly less than one minute. More details on the scan parameters and frequency are included in the test results discussion in Chapter 5.

3.5.3 Load Measurements

Load measurements were taken in real-time during all loading tests. The stressing of the two strands was conducted on opposite ends of the specimens so that the live (stressing) end for one of the strands was the dead end for the other strand. The decision to stress from the opposite ends was made to accommodate a 50-kip center-hole load cell on the dead end of each strand to monitor the individual post-tensioning load. Housed inside the prestress chairs, these load cells remained on the strands for both PT and combined load tests, allowing for the monitoring of both PT load during strand stressing and PT losses during external loading in the combined load tests.

In addition to the 50-kip strand load cells, a single 100-kip load cell was used in tandem with the 100-kip ram during external loading phases. The load cell was placed between the butt of the ram and the HSS spacer at the live end of the external/combined load setup (see Figure 3-16 and Figure 3-18). This load cell monitored the external load applied to the specimen.

All load cells were fully calibrated immediately prior to the testing program. The data from each was compared to the axial load measurements inferred from the VWGs; the results of this comparison are described in Chapter 5.

3.5.4 Displacement Measurements

The third major category of measurements collected during the load tests was displacement. The lateral displacement of the members at midspan was reported in real-time through a pair of linear potentiometers. These were mounted on small angles epoxied to the top and bottom faces of the specimen; the tip of each was placed against the lateral stay at midspan (Figure 3-25(a)). The linear potentiometers were placed in

opposite directions; the lateral deflection was reported as the average value between the two potentiometers. The two potentiometers were also used in tandem to obtain a measure of the amount of twist in the specimen. The magnitude of twist was found to be insignificant throughout testing.

An additional linear potentiometer was mounted to the side of the specimen in the vertical orientation; its purpose was to monitor the vertical deflection of the specimen during loading and support adjustment. A small strip of Teflon was installed under the tip of the potentiometer to ensure unrestrained lateral motion as the specimen moved.

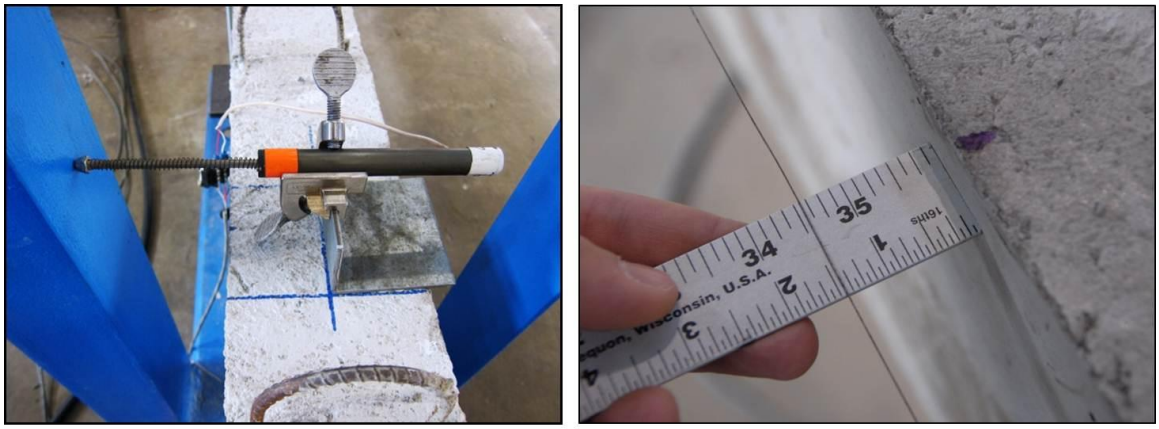

(a) (b)

Figure 3-25: Deflection Measurements; (a) Linear potentiometer for measuring lateral deflection at midspan; (b) Deflected shape measurement

In addition to pure deflection data, a series of measurements were taken at intervals during each test to map the deflected shape of the member. A piano wire was run parallel to each side of the specimen as a reference line. Hand measurements of the distance between this line and the edge of the specimen were taken at one-foot increments along the length of the specimen at intervals during the load tests (Figure 3-25(b)). While not a highly precise measurement, the monitoring of the approximate deflected shape allowed for the identification of general stiffening or softening behavior during loading.

3.6 TEST PROCEDURE

The reconfiguration of components associated with the test setup has been discussed previously. The following section details the specific test procedures and variations for each of the three loading schemes employed in this experimental program.

3.6.1 Post-Tensioning

In the post-tensioned load tests, the 60-kip rams, strand chucks, and PT strands were oriented as described in Section 3.4.3. The strands were stressed, and the strain, load, and deflection behavior was noted as described in the previous section.

Three main variations on the PT test were employed during the experimental program. These are summarized below.

1- *Strand Eccentricity*: In general, the PT strands were positioned such that they coincided with the center of the ducts. Thus, the load applied through the prestress chairs could be classified as concentric. However, in several tests, the strands were shifted laterally ⅝″ to one side of the duct (the height of the strands in the specimen remained unchanged). A typical eccentricity is shown in Figure 3-26. The primary motivation for this variation was to induce bending on the specimen and to investigate the effects of the engagement of a tensioned strand on the side wall of the duct on overall curvature behavior and capacity. More detail on this investigation is included in Chapter 5.

2- *Strand Diameter*: Strands of both 0.5-inch and 0.6-inch diameters were used for post-tensioning. The use of larger strands allowed for the application of a greater overall PT load. The variation of sizes allowed for the investigation of the effects of strand size on potential stiffening or softening behavior, particularly in the presence of strand engagement on the duct wall. Strand sizes were varied in both concentric and eccentric PT loading.

3- *Strand Loading Sequence*: A third key variation in the PT procedure was the variation in the sequence in which the strands were loaded. Initially, the strands were loaded simultaneously, while in other tests, the bottom strand

was loaded to a given level before stressing began on the top strand. Varying the strand loading sequence allowed for a camber to be induced raised the member off the midspan supports and eliminated friction at a lower overall load than if both strands were simultaneously stressed. Additionally, differential loading facilitated the study of curvature across the depth of the section; an understanding of these loading effects is critical to the monitoring of the sweep control mechanism proposed for the arch construction.

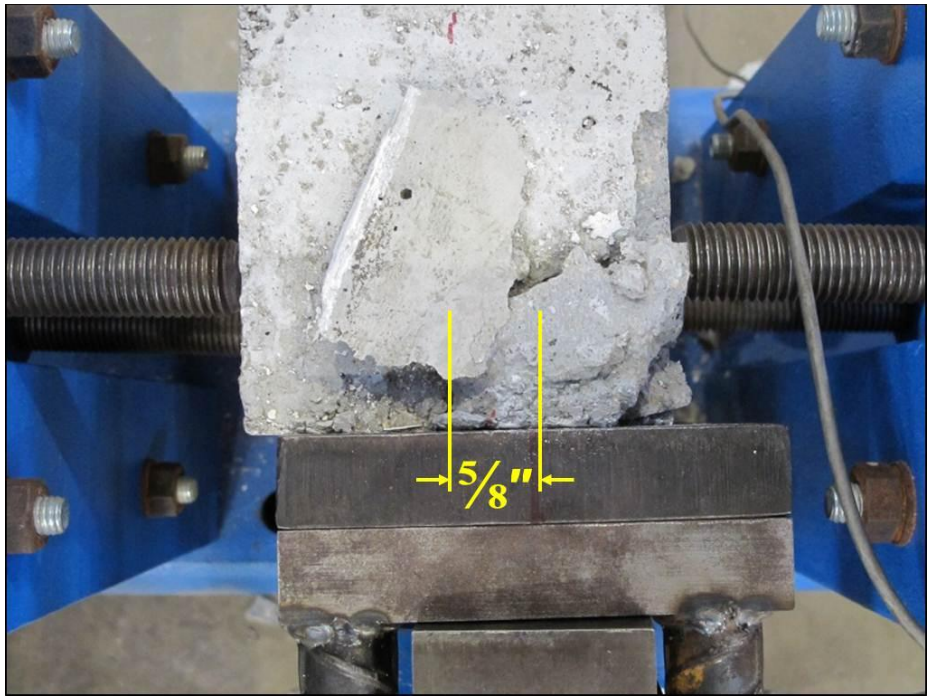

Figure 3-26: Typical Eccentricity (A spalled piece of concrete is visible on top of the specimen; spalling was due to the uneven end faces of Specimen 1.)

In all, over 40 PT tests were performed on the first two specimens. Each variation described here was employed extensively.

3.6.2 External Loading

External load tests were executed using the procedure described in Section 3.4.3. Again, no post-tensioning was used in the external loading scheme. There were no

variations on the external load tests. The primary focus of the pure external loading scheme was to establish the buckling capacity and behavior of the specimen in the absence of post-tensioning. The external load was always applied concentrically.

Five external load tests were performed on the first two specimens. One test on each resulted in a complete buckling failure. These tests are discussed at length in Chapters 5 and 6.

3.6.3 Combined Loading

In the combined loading tests, the 60-kip rams, strand chucks, and PT strands were oriented as described in Section 3.4.3. The strands were stressed, and the strain, load, and deflection behavior was noted as described in the previous section. After the PT load was locked in using the strand chucks, the 60-kip rams were removed. The 100-kip ram and other external load components were moved into position, and load was applied as previously described.

Three main variations on the combined load test were employed. These are summarized below. Note that both the PT and external loads were always applied concentrically in the combined load tests.

1- *Post-tensioning Load*: The primary variation in the combined loading scheme was the level of post-tensioning locked in before the application of external load. Total PT loads of 15, 20, 25, 30, or 35 kips were typically applied prior to external loading. The variation of the initial PT load facilitated a study of the effects of PT levels on overall buckling capacity. Additionally, the effects on the buckling capacity of the stiffening behavior of post-tensioned strands in the presence of strand engagement were noted. The results of this investigation are discussed in Chapters 5 and 6.

2- *Strand Diameter*: Strands of both 0.5-inch and 0.6-inch diameters were used for the initial post-tensioning. Again, the variation of sizes allowed for the investigation of the effects of strand size on potential stiffening or softening behavior, particularly in the presence of strand engagement on the duct wall.

3- *Strand Load Distribution*: A third key variation in the initial PT procedure was the variation in the distribution of post-tensioning between strands. In all combined load tests, the lower strand was loaded first to create camber and allow for the supports to be lowered. However, in some tests, half the overall load was applied to each strand; these were denoted double-strand (DS) tests. In single-strand (SS) tests, over 90% of the total PT load was applied to the bottom strand. A majority of the load in the bottom strand maximized camber and minimized the downward deflection of the specimen, theoretically maximizing the available lateral deflection prior to strand engagement. In addition, the varying the distribution facilitated the study of the effects of individual versus combined strand stiffness on curvature, buckling behavior, and potential twist in the specimen.

A total of thirteen combined load tests were performed on the first two specimens. A single combined load test was performed on the first specimen after it had been completely buckled. Each variation described here has been employed extensively. The results of each test are described in Chapters 5 and 6.

3.7 SUMMARY

The experimental program was outlined in this chapter. The primary motivation for the tests was the establishment of the capabilities and limitations of the vibrating wire gages in reporting material and structural behavior. Additionally, the study sought to investigate the buckling behavior of slender concrete elements under post-tensioning and external loading schemes.

An extensive review of the considerations behind the design of the laboratory test specimens was presented, as is a detailed description of the test specimen construction and instrumentation procedure. A total of three specimens were constructed, each with a total of six vibrating wire gages installed. Two of these specimens have been extensively tested.

A description of the test setup was also included. There were two major requirements for the test setup. It had to adequately support the specimen, providing stability with a minimum of restraint to lateral motion, and it had to be compatible with various loading schemes. The configurations, procedures, and motivations for the three loading schemes (pure post-tensioning, pure external load, and a combination of the two) were described, as were variations in each procedure.

Additional details on the specific experimental procedures are provided in Chapter 4. The results obtained from the experimental program are presented in Chapter 5. The analysis of these results and associated recommendations are presented in Chapter 6.

CHAPTER 4
Experimental Procedures

4.1 INTRODUCTION

A summary of several key data collection processes and test procedures developed during the experimental program is presented in this chapter. As previously noted, the laboratory tests served two primary purposes. The first was to establish a fundamental working knowledge of the capabilities and limitations of vibrating wire gages in a controlled, well-defined environment. The second primary goal was to investigate the elastic buckling behavior of slender reinforced concrete elements under post-tensioning loads. Several data collection and testing techniques are introduced in this chapter.

4.2 OVERVIEW OF TEST PROGRAM

More than sixty distinct load tests were performed on two test specimens. As outlined in Chapter 3, three typical loading schemes were employed: post-tensioning, external loading, and combined (post-tensioning and external) loading. Table 4-1 summarizes the number of tests of each loading scheme performed on each specimen.

Table 4-1: Load Test Summary

Number of Tests Performed			
Loading Scheme	**Specimen 1**	**Specimen 2**	
Post-tensioning	21	22	**PRE-FAILURE**
External Only	2	1	
Combined Loading	0	12	
Post-tensioning	1	0	**POST-FAILURE**
External Only	2	0	
Combined Loading	1	0	
Total	**27**	**35**	

Both specimens ultimately experienced a buckling failure that led to extensive cracking in the section. A small number of tests were conducted on Specimen 1 following

the buckling failure and, as such, tests are categorized as pre- or post-failure. The nomenclature shown in Figure 4-1 and Figure 4-2 is used throughout Chapters 4, 5, and 6 to identify the individual laboratory tests

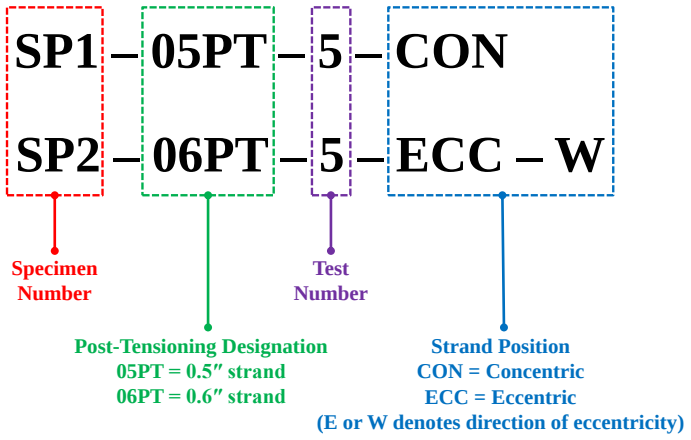

Figure 4-1: Standard Test Nomenclature: Post-Tensioning

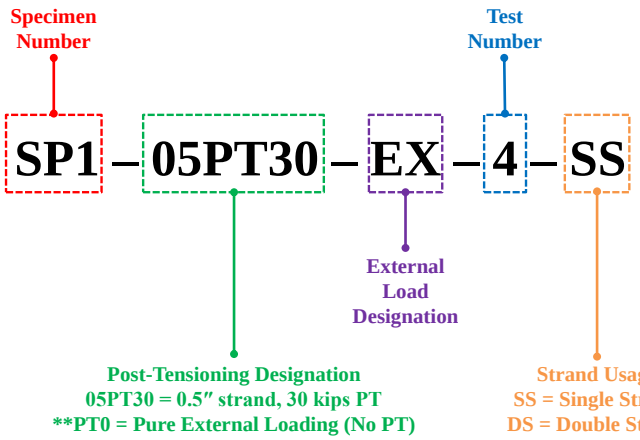

Figure 4-2: Standard Test Nomenclature: External and Combined Loading

Data collected from the vibrating wire gages (VWGs) was processed at intervals throughout the loading sequence. (Each scan of the VWGs was manually initiated.) The raw data were uploaded from the CR3000 data logger via the PC400 interface software and input to a macro-enabled worksheet in Microsoft Excel. The macro program played a

key role in sorting the data, as well as processing and creating several necessary graphs. Axial load (as measured by the load cells) was plotted versus strain, vertical and horizontal curvature, and midspan deflection. For concentric loading schemes, a Southwell plot was also generated. Additionally, estimates of axial load were derived using the data from the VWGs. These estimates were compared to the load data reported by the load cells. Finally, stress estimates were determined from the VWG strain values and compared to theoretical values. The derivation of each plot type is presented with representative data in the following sections.

The vibrating wire gage configuration previously presented in Chapter 3 is shown again for the reader's reference in Figure 4-3 and Figure 4-4. This nomenclature is utilized throughout this document. Note that in the test setup, the longitudinal axis of the specimen was oriented north-south, with Gages 1 and 5 on the west side of the specimen, and Gages 2 and 6 on the east. This also informs the eccentricity designation in the test nomenclature.

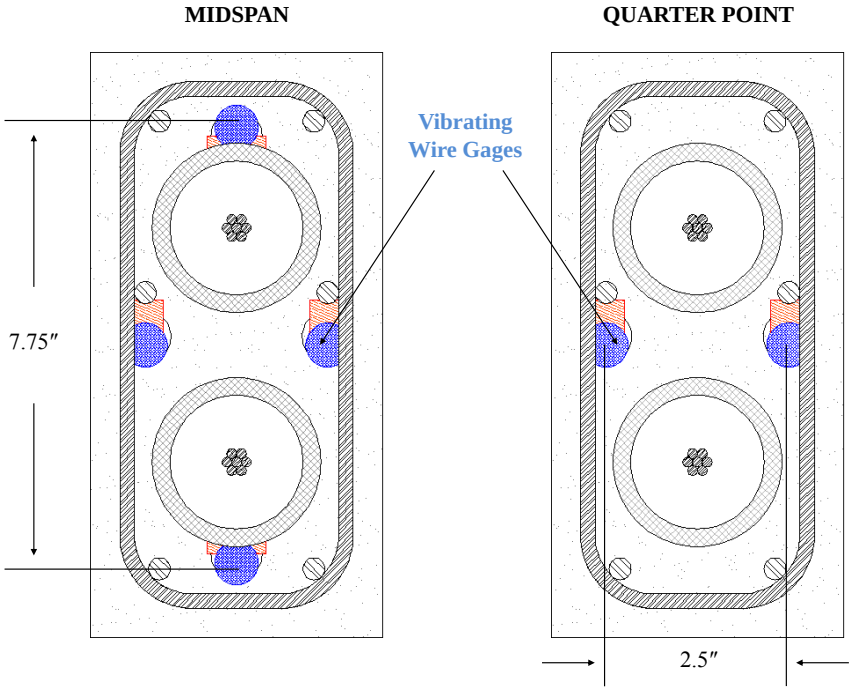

Figure 4-3: Vibrating Wire Gage Placement

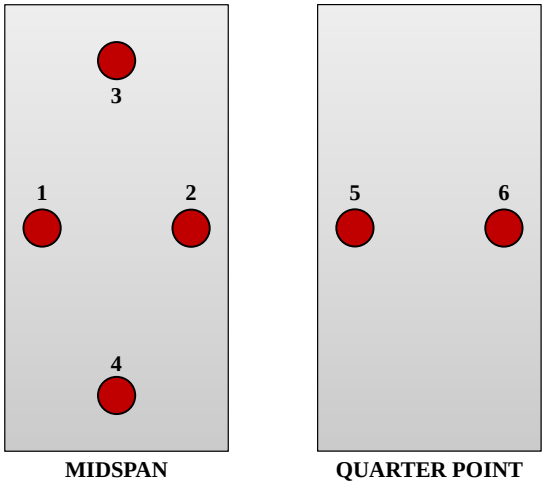

Figure 4-4: Vibrating Wire Gage Nomenclature

4.3 STRAND LOADING SEQUENCES

There was a fundamental difference in the sequence of events during the load tests of the first specimen (SP1) and the second specimen (SP2). In post-tensioned (PT) tests on SP1, the specimen was allowed to camber off of the midspan supports prior to the supports being lowered. After applying a small load (1.0-2.5 kips) to each strand, the bottom strand was loaded to its safe working capacity. The top strand was not loaded, allowing the specimen to camber upwards and off of the midspan supports. Once the specimen was noted to be no longer in contact, the midspan supports were lowered so as to not interfere with the vertical or lateral deflection of the specimen as additional load was applied. Once the safe working capacity of the bottom strand was reached, load was applied to the top strand, causing the specimen to deflect downward.

Graphics depicting the stages of the strand loading procedure for SP1 are shown in Figure 4-5. Figure 4-6 shows a plot of load versus lateral deflection for a typical concentric PT test on SP1. It can be seen from the plot that the lateral deflection is minimal until the specimen cambers off of the supports, at which point the frictional restraint from the intermediate support is eliminated and deflection increases.

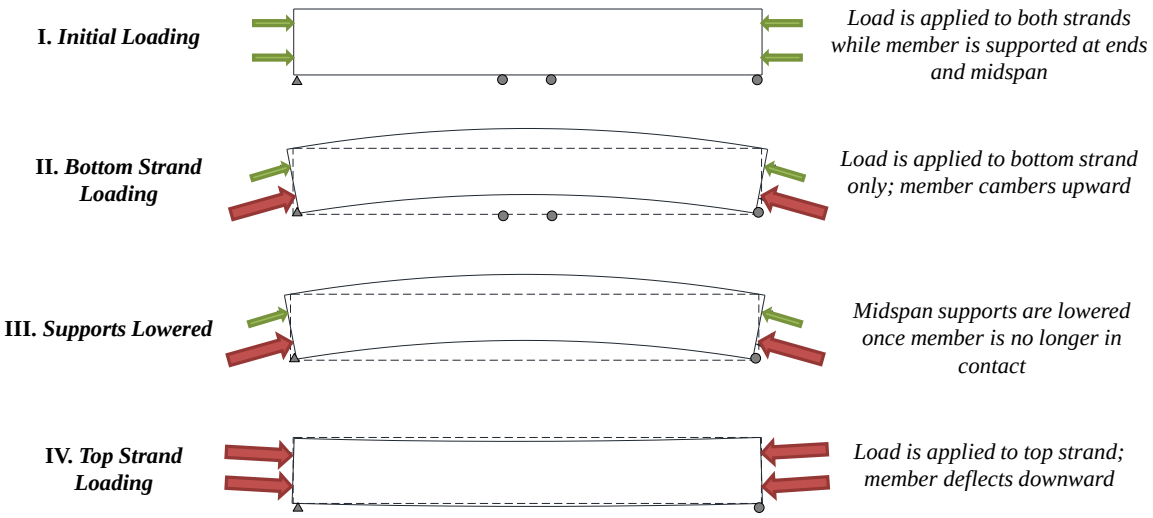

Figure 4-5: Typical Strand Loading Sequence for SP1 (Elevation View of Test Setup)

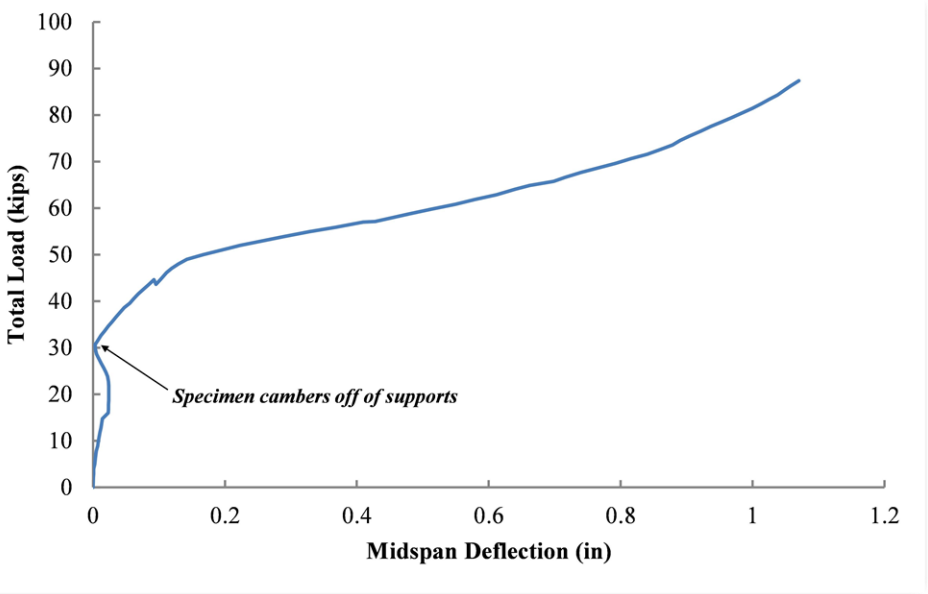

Figure 4-6: Load vs. Lateral Deflection for Concentric PT Test SP1-06PT-2-CON

In SP2, the supports were lowered at a predetermined axial load, regardless if the specimen had cambered enough to fully clear the midspan supports. This predetermined load was chosen as a conservative estimate of the axial load required to prevent cracking under self-weight. Because significant bending had been noted in the prestress chairs during the external load tests of SP1, stiffeners were added to the chairs. As such, the

camber of the specimen by loading a single strand was less effective. The stages of the strand loading sequence are depicted in Figure 4-7.

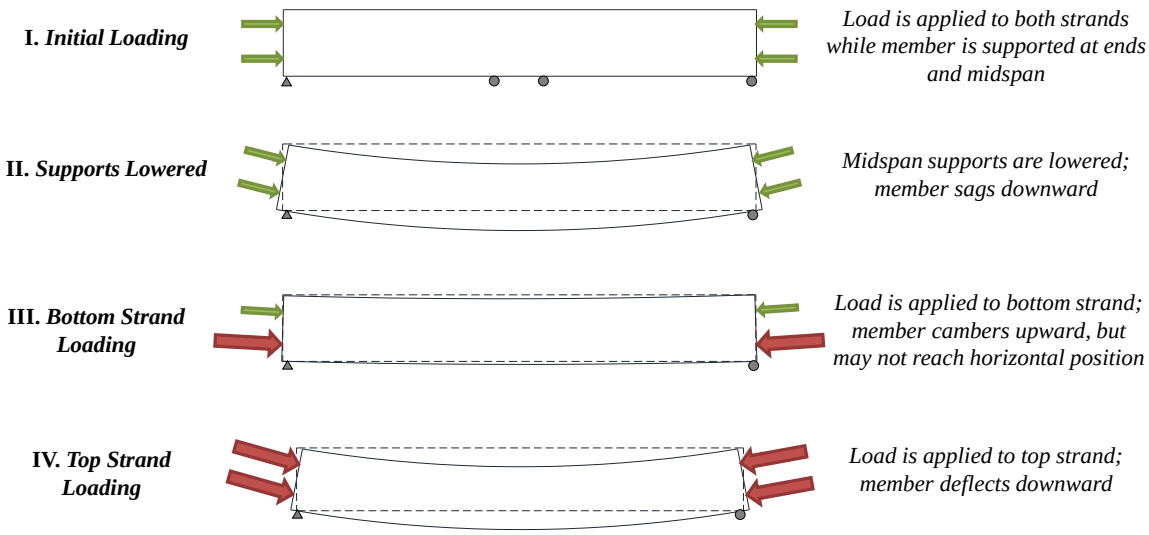

Figure 4-7: Typical Strand Loading Sequence for SP2 (Elevation View of Test Setup)

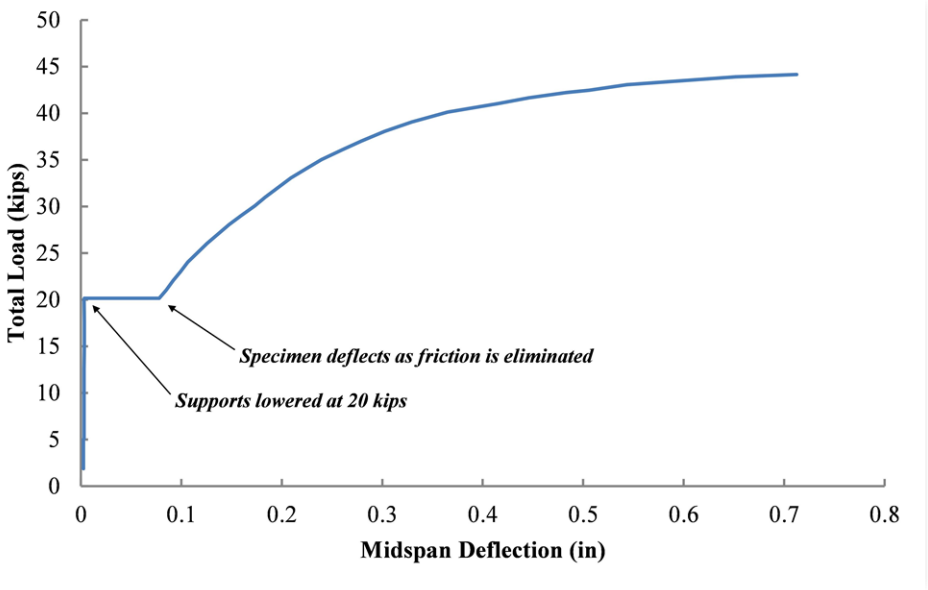

Figure 4-8: Load vs. Lateral Deflection for Concentric PT Test SP2-05PT-6-CON

In tests in which the supports were lowered prior to the specimen cambering off of the supports, the lowering of the supports represented a rapid elimination of the

frictional restraint provided by the supports. As such, a sudden increase in the lateral deflection was noted in the plot of load versus lateral deflection (Figure 4-8) for tests in SP2. This "jump" was also noted in load-curvature plots.

Specific considerations for each specimen necessitated a difference in loading sequence between the two specimens. Nonetheless, the data collected from both specimens was found to be reliable and useful, both in establishing the resolution of the VWGs and in studying the buckling behavior of the members under unbonded PT loads.

4.4 GAGE MONITORING

The primary focus of this research program was the establishment of a fundamental understanding of the capabilities and limitations of the VWGs. This section describes several of the key structural behavior parameters that were either directly read from the gages or inferred from the gage data. Some representative data is presented where applicable; a more comprehensive overview of results is provided in Chapters 5 and 6.

4.4.1 Strain Monitoring

The raw strain values read from the VWGs served as the fundamental data for this research program. The strain values for each gage were monitored throughout loading. These values were used primarily to infer other behavior parameters such as curvature, stress, and axial load. Still, the raw strain data for each gage was plotted against the applied axial load and monitored throughout testing. These plots were used to observe behavioral trends and gage consistency.

4.4.2 Curvature Monitoring

Curvature was a vital parameter throughout the study. The strain data from the VWGs was used to monitor the curvatures in the midspan and quarter point sections. Horizontal or lateral curvatures were monitored at both midspan and the quarter point using the pairings of Gages 1 and 2 and Gages 5 and 6, respectively. In addition, the

vertical curvature was monitored at midspan using Gages 3 and 4. Curvature was estimated as the ratio of the strain differential to the distance between a pair of gages (Equation 4-1, Equation 4-2, and Equation 4-3). The gage nomenclature and the distances between gage pairs were shown in Figure 4-3 and Figure 4-4. Horizontal curvature resulting in westward lateral movement (tension in gage 1) was defined as positive. A schematic of the sign convention for horizontal curvature is given in Figure 4-9.

$$\boldsymbol{\phi_{h\_mid} = \frac{(\varepsilon_1 - \varepsilon_2)}{d_{12}}} \qquad \textit{Equation 4-1}$$

$$\boldsymbol{\phi_{h\_qp} = \frac{(\varepsilon_5 - \varepsilon_6)}{d_{56}}} \qquad \textit{Equation 4-2}$$

$$\boldsymbol{\phi_{v\_mid} = \frac{(\varepsilon_3 - \varepsilon_4)}{d_{34}}} \qquad \textit{Equation 4-3}$$

$\phi_{h\_mid} = Horizontal\ curvature\ at\ midspan\ (in^{-1})$
$\phi_{h\_qp} = Horizontal\ curvature\ at\ quarter\ point\ (in^{-1})$
$\phi_{v\_mid} = Vertical\ curvature\ at\ midspan\ (in^{-1})$
$\varepsilon_1 \dots \varepsilon_6 = Strain\ report\ by\ gages\ (in/in)$
$d_{12} \dots d_{56} = Distance\ between\ gage\ pair\ (in)$

In addition to the linear potentiometer deflection data, horizontal curvature served as a key indicator of buckling behavior. The horizontal curvature was plotted against the axial load for all load tests and was closely monitored throughout loading. Trends in the slope of the load-curvature plots could typically be interpreted as softening as the specimen approached buckling or stiffening as the tensioned strand moved into contact with the duct wall. A typical load-curvature plot exhibiting both softening and stiffening behavior is shown in Figure 4-10.

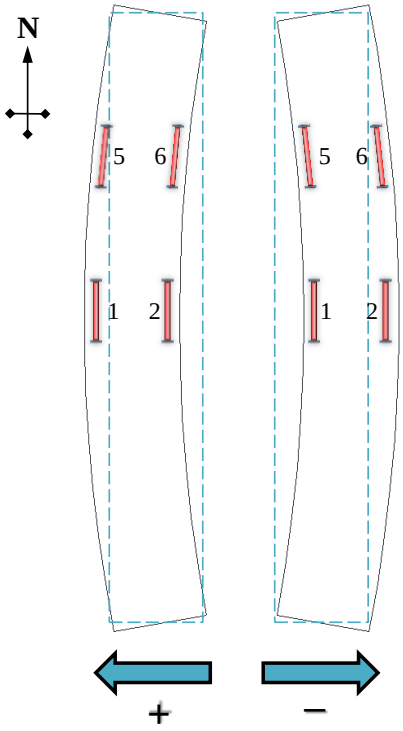

Figure 4-9: Horizontal/Lateral Curvature Sign Convention (Plan View of Test Setup)

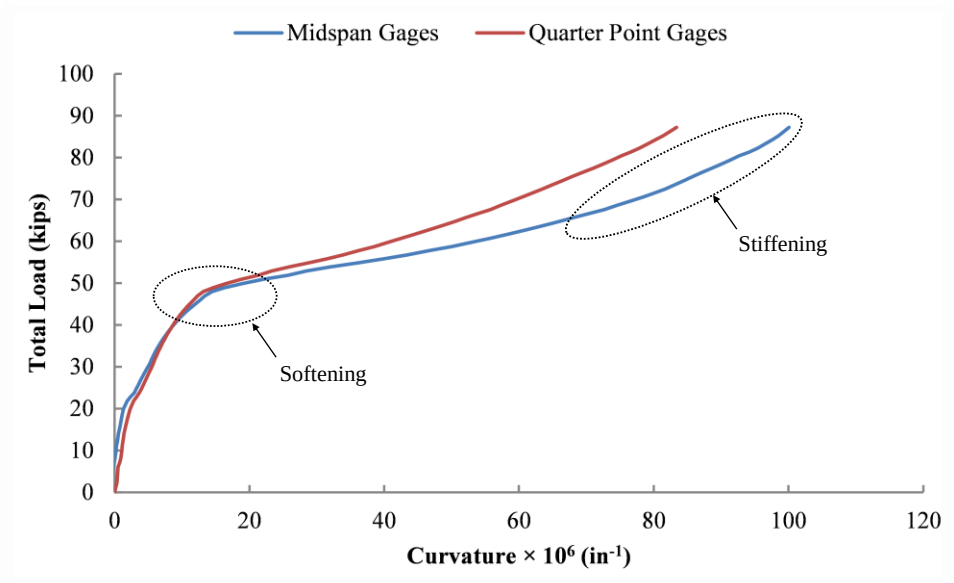

Figure 4-10: Load vs. Lateral Curvature for Concentric Load Test SP2-06PT-1-CON

The sign convention for vertical curvature is shown in Figure 4-11. Upward camber (creating tension on the member's bottom face) is defined as positive curvature; downward sag is defined as negative curvature.

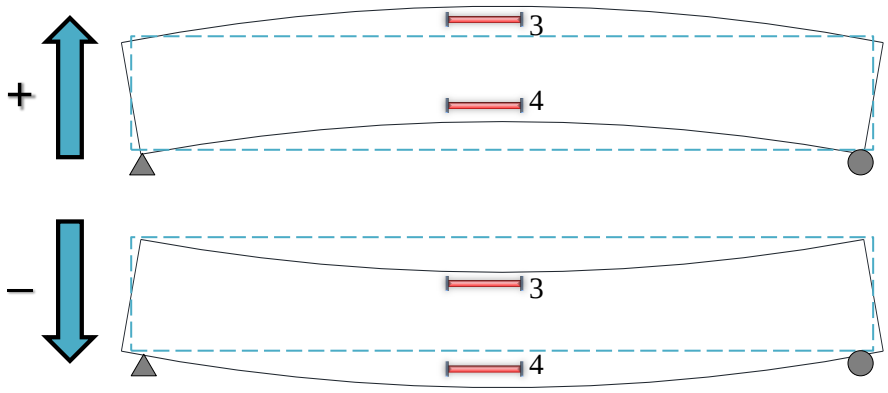

Figure 4-11: Vertical Curvature Sign Convention (Elevation View of Test Setup)

Because Gages 3 and 4 are situated about the section's strong axis, vertical curvature was not used to monitor buckling behavior. However, the vertical curvature data proved very useful in the observation of the effects of various strand loading techniques. For example, trends in vertical curvature were monitored as the specimen was cambered upward due to the loading of the bottom strand. Similar trends were noted as the member sagged downward due to top-strand loading or after the midspan supports were lowered. These studies are analogous to the sweep control studies for the arch construction project.

4.5 STABILITY MONITORING

In addition to the calibration of the VWGs, the strain and curvature data were used in evaluating elastic buckling behavior. The specific techniques used to identify buckling are discussed in this section.

4.5.1 Identification of Buckling

As previously discussed, buckling of a structural element can be an inherently sudden event; however, depending on the initial imperfections and bracing present, buckling can also be a gradual loss of stiffness. Initial imperfections or out-of-straightness add uncertainty to the prediction of the critical load. As such, a reliable method of predicting buckling behavior is desired. This is particularly important in this study, as the behavior was to be constrained to the elastic range for most of the tests. This was done so multiple load tests could be performed without significant change in material properties or damage to the specimen. Two methods were used for identification of buckling behavior. These are discussed below.

4.5.1.1 Stiffness Trend Monitoring

Theoretically, when buckling occurs (and the critical axial load is reached), the unrestrained length of the specimen tends to deflect laterally without bound. However, before this occurs, a loss in stiffness should be noted. This would be manifested as a decreasing slope or "flattening" in a load versus deflection or load versus curvature plot. A typical curve demonstrating this flattening is shown in Figure 4-12.

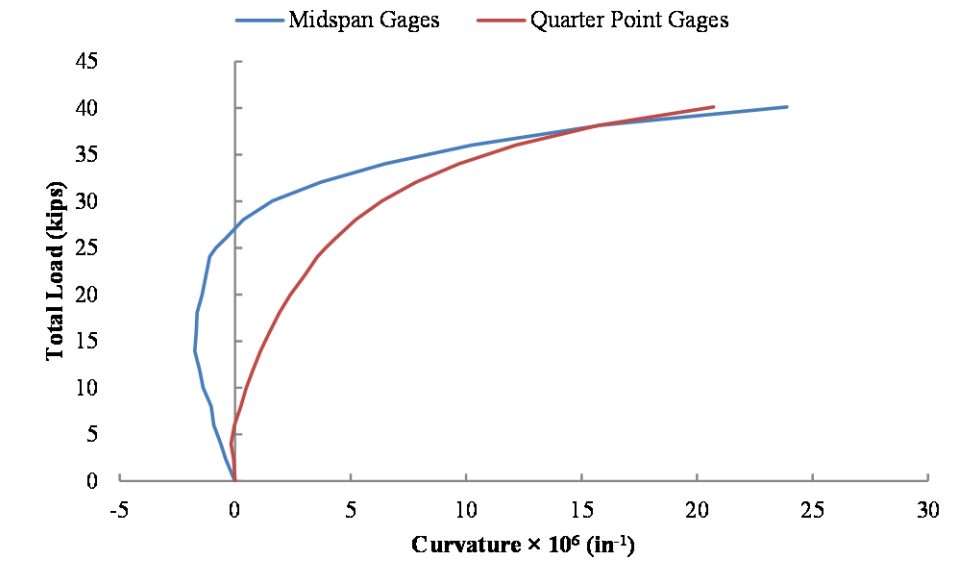

Figure 4-12: Buckling Indicated as a Loss of Stiffness in a Load vs. Lateral Curvature Plot for Concentric PT Test SP2-06PT-1-CON

While somewhat arbitrary, this technique allows for the early detection of buckling behavior through the real-time observation of stiffness trends. Because the relationship is certainly nonlinear, and the loss of stiffness takes place over some time, it is difficult to identify a well-defined buckling point without taking the specimen to failure. However, the technique represents a simple and effective tool for qualitatively identifying the onset of buckling. An additional advantage of this method is that these trends hold for any of the axial loading schemes, including eccentric loading. (In eccentric loading, lateral deflections are primarily due to pure bending; while the curvature increases at a higher rate than in concentric loading, the relationship is relatively linear before buckling.)

4.5.1.2 Southwell Plots

The Southwell plot was introduced in Chapter 2 as a means of predicting the critical axial buckling load. A Southwell plot graphs the ratio of the lateral deflection to the axial load on the vertical axis versus the lateral deflection on the horizontal axis. The

inverse of the slope is the predicted critical load for column instability. The x-intercept provides an estimate of the initial imperfection or out-of-straightness in the specimen.

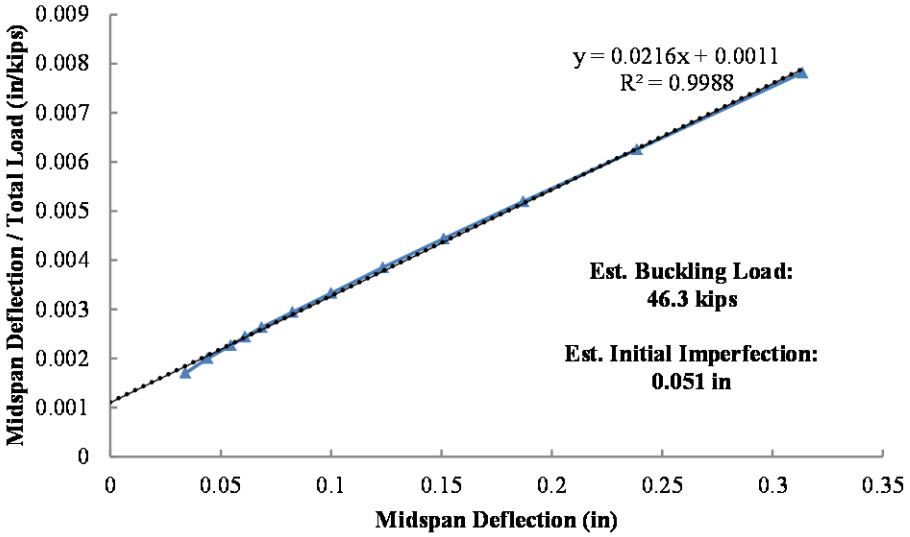

Figure 4-13: Southwell Plot for Concentric PT Test SP2-06PT-1-CON

As previously noted, the Southwell plots are not as meaningful for the eccentric loading cases. (For eccentric load schemes, buckling was identified only through the observation of stiffness trends.) Southwell plots were created for all concentric load tests in this experimental program. A typical plot is presented in Figure 4-13. This plot represents the same test as depicted in the load-curvature plot in Figure 4-12. The critical buckling load for this test was predicted as 46.3 kips by the Southwell plot. To prevent damaging the specimen, the test was stopped before the total load reached 46 kips, but a significant loss of stiffness was noted (Figure 4-12).

The Southwell plots provided an effective means of predicting the critical buckling load in the test specimens without inducing severe damage. As the specimens were to be preserved for multiple load tests, the predicted critical load was not reached until the last test. However, as is shown in the subsequent chapters, the Southwell plots displayed excellent correspondence with the observed stiffness trends, and informed the cessation of loading for each test. Southwell plots for each test are presented where appropriate in the following section and in the appendix of this document.

4.5.2 Deflected Shape Monitoring

In addition to the stiffness trend monitoring and Southwell plot construction, the general deflected shape of the specimen under loading was recorded. This was accomplished by measurement of the lateral deflection of the specimen at specific load increments. The deflections were measured at stations spaced at one-foot intervals along the length of the specimen. As previously noted, the deflection at each point was taken to the nearest one-sixteenth of an inch. The deflected shape data are not highly precise, but afford a reasonable illustration of the deflection behavior of the specimen along its length. It should be noted that this third technique was not introduced until the testing of the second specimen.

A typical set of deflected shape curves for a load test is shown in Figure 4-14. The plot yields several important observations. First, the general symmetry of deflection is readily visible; this indicates a relative equality in the fixity of each end of the specimen. As expected, it can be seen that the magnitude of deflections increase rapidly as the specimen approaches buckling. The test shown was stopped at a total PT load of 44 kips due to prevent damaging the specimen from overstressing.

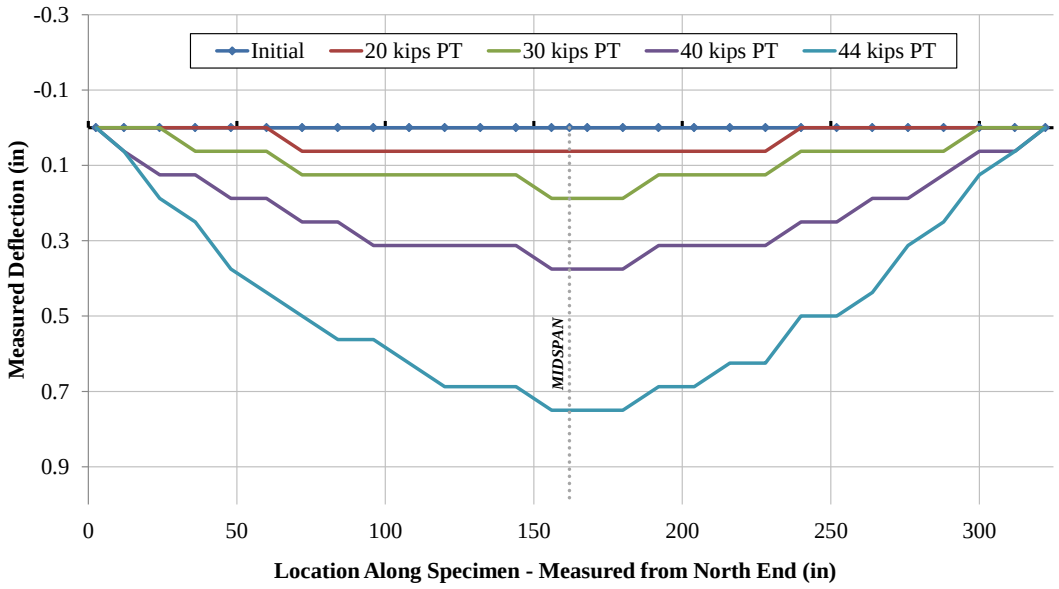

Figure 4-14: Deflected Shape Progression to Buckling (SP2-05PT-6-CON)

While not highly precise, this third check serves not only as an indication of impending buckling, but also as a validation of the linear potentiometer data. In general, the deflection measurements at midspan and the quarter point were in excellent correspondence to the deflection reported by the linear potentiometers. The combination of this technique with both general stiffness observation and Southwell plot construction resulted in a comprehensive monitoring program for elastic instability trends.

4.6 SUMMARY

A summary of several key experimental procedures was provided in this chapter. The laboratory program sought to establish the reliability of the vibrating wire gages and associated instrumentation as related to specific structural parameters. In addition, the stability of slender post-tensioned elements was studied at length. The test nomenclature and several experimental variations were introduced; these will be referenced throughout the following chapters.

An extensive review of the material and structural parameters assessed by the vibrating wire gages were presented. The raw strain data from the gages was used to infer curvature at the sections of interest. The conventions for positive and negative curvature were outlined in this chapter.

A key component of the stability study was the identification of buckling or the onset of structural instability. An impending buckling event was predicted through the qualitative monitoring of the changes in stiffness and curvature, the estimation of the deflected shape, and the quantitative prediction of the critical buckling load using the Southwell plot. These techniques were explained in detail in this chapter.

Selected results were presented in this chapter to explain the experimental testing procedures. The results are covered in more detail in the following chapters as well as in the appendix.

CHAPTER 5
Experimental Results

5.1 INTRODUCTION

A comprehensive summary of the data collected during the experimental program is presented in this chapter. The laboratory tests served to establish a fundamental working knowledge of the capabilities and limitations of vibrating wire gages and to investigate elastic buckling behavior of slender post-tensioned elements. Data selected as typical of the experimental results are presented in the body of this chapter, while the remaining data are provided in the appendix.

5.2 SCOPE OF EXPERIMENTAL PROGRAM

More than sixty distinct load tests were performed on two test specimens. Table 5-1 summarizes the number of tests of each loading scheme performed on each specimen. Both specimens ultimately experienced a buckling failure that led to extensive cracking in the section. A small number of tests were conducted on Specimen 1 following the buckling failure and, as such, tests are categorized as pre- or post-failure. This data was presented in Chapter 4, but is repeated here for the reader's reference.

Table 5-1: Load Test Summary

Number of Tests Performed			
Loading Scheme	**Specimen 1**	**Specimen 2**	
Post-tensioning	21	22	**PRE-FAILURE**
External Only	2	1	
Combined Loading	0	12	
Post-tensioning	1	0	**POST-FAILURE**
External Only	2	0	
Combined Loading	1	0	
Total	**27**	**35**	

5.3 GAGE MONITORING

The primary focus of this research program was the establishment of a fundamental understanding of the capabilities and limitations of the VWGs. This section describes each of the structural behavior parameters that were either directly read from the gages or inferred from the gage data. Representative data is also presented.

5.3.1 Strain Monitoring

As discussed in Chapter 4, the raw strain values read from the VWGs served as the fundamental data for this research program. The strain values for each gage were monitored throughout loading. As described in each of the following subsections, these values were used primarily to infer other behavior parameters such as curvature, stress, and axial load. However, the raw strain data for each gage was plotted against axial load and monitored throughout testing. These plots were used to observe behavioral trends and gage consistency. An example of a typical load-strain curve is given in Figure 5-1. Additional load-strain curves are provided where appropriate to support observations of the inferred parameters.

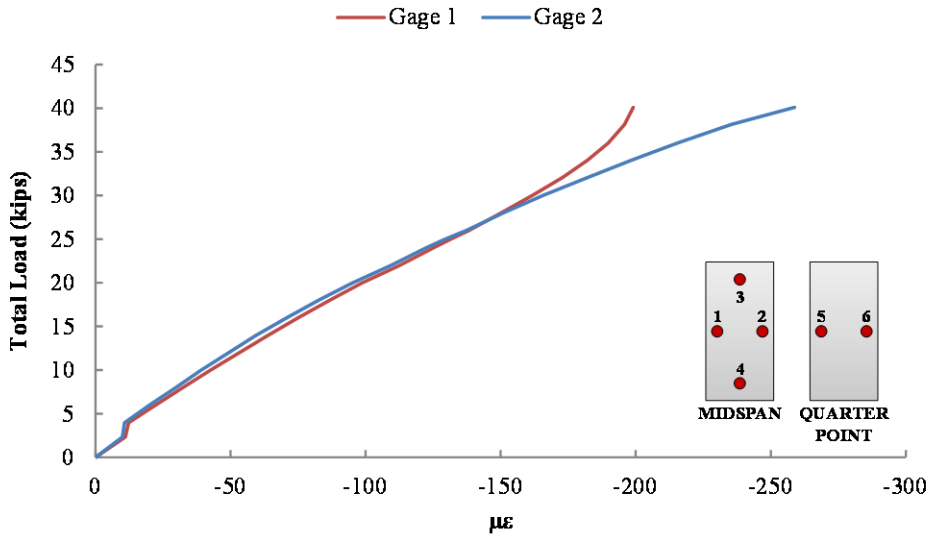

Figure 5-1: Load vs. Strain (Gages 1-2) for Concentric PT Test SP2-06PT-1-CON

The plot in Figure 5-1, depicting a test stopped for stability concerns, illustrates the consistency of the strain data with observed structural behavior. As the axial load was increased, the member deflected to the west. At the onset of buckling, the deflection began to increase rapidly. The state of stress in the cross section is comprised of stresses from the axial compression from the prestressing superimposed on the stresses from bending. The bending associated with buckling-type deformations leads to tensile stresses on the west side (Gage 1) of the specimen and compressive stresses on the east side (Gage 2). This is represented in the increasing compressive strain in Gage 2 on the east and the "trend reversal" of Gage 1 on the west. As is demonstrated throughout this chapter, the VWGs were consistently able to track strain shifts and reversals such as that depicted in Figure 5-1.

5.3.2 Curvature Estimation

As detailed in Chapter 4, curvature was a critical structural parameter, both for understanding the ability of the gages to report observed structural trends, and in the stability studies. Lateral curvature was monitored throughout loading; it was able to show softening as the specimen approached buckling or stiffening as the strand engaged the conduit. A typical load-curvature plot exhibiting both softening and stiffening behavior is shown in Figure 5-2.

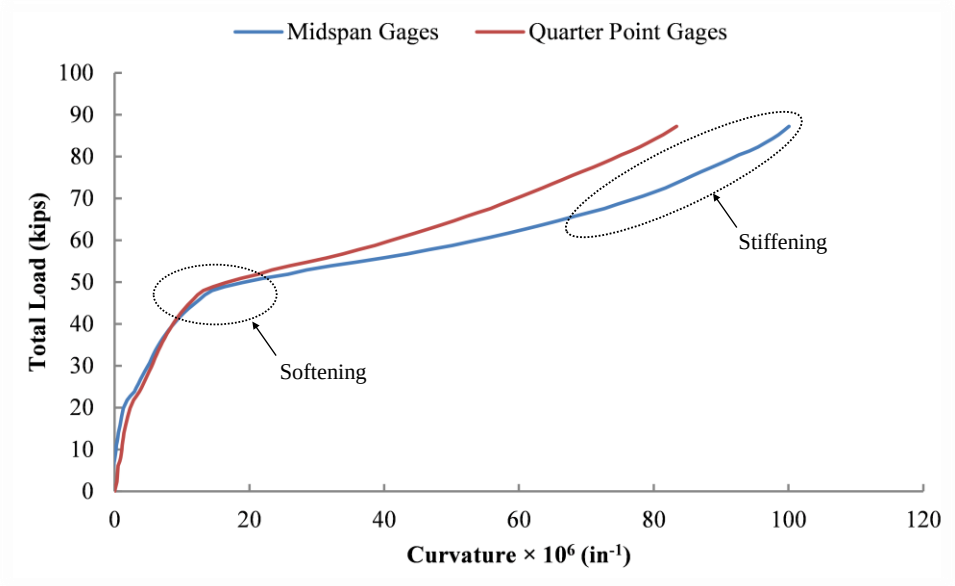

Figure 5-2: Load vs. Lateral Curvature for Concentric Load Test SP2-06PT-1-CON

Vertical curvature was also monitored. The excellent ability of the VWGs to report trends consistent with the loading sequences is evident in the plots of load versus vertical curvature. As outlined in Chapter 4, the practice of lowering the supports at a predetermined PT load was used exclusively in the second specimen (SP2). The loading stages of these tests are outlined again in Figure 5-3.

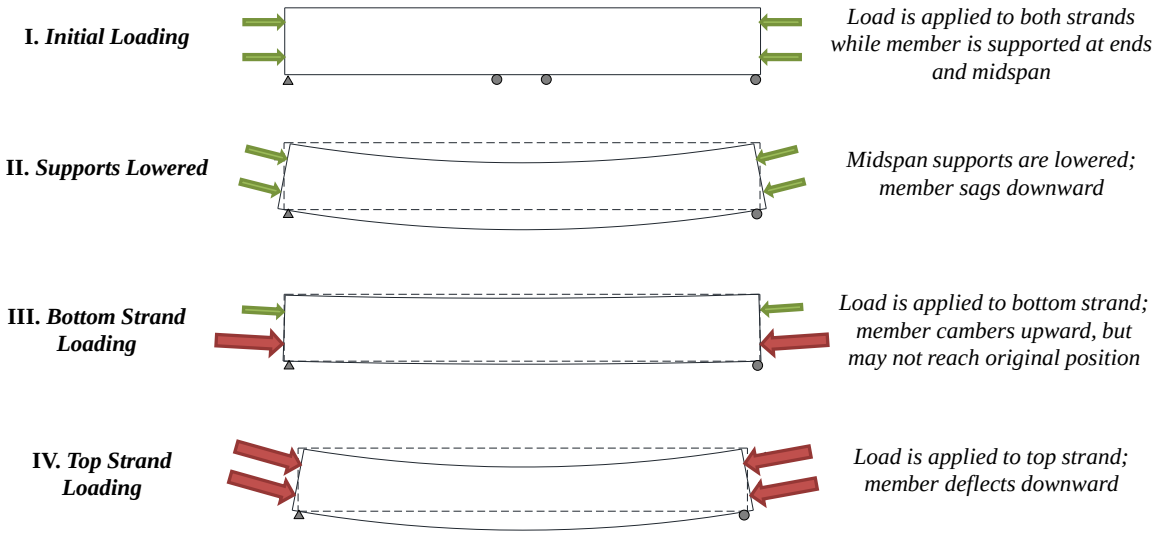

Figure 5-3: Typical Strand Loading Sequence for SP2 (Elevation View of Test Setup)

A typical plot of the observed trends in vertical curvature is presented in Figure 5-4. For the test shown in Figure 5-4, both strands were loaded simultaneously to a total load of 3 kips (1.5 kips per strand). Next, the load on the bottom strand was increased to 13.5 kips, for a total load of 15 kips. The supports were then lowered, creating a jump in negative vertical curvature as the specimen deflected downwards. The bottom-strand loading was continued until the safe working load was reached (approximately 30 kips for a 0.5-inch diameter strand). Stressing the bottom strand led to camber in the beam that is indicated by the reduction in the absolute magnitude of the vertical curvature during the Stage III region on the curve. The subsequent bottom-strand loading did not create sufficient camber for the member to return to its original position; the curvature was still negative when top-strand loading began. As expected, stressing the top strand led to an increase in the negative curvature. As can be seen in the plot in Figure 5-4, the vertical curvature trends can be closely correlated to the loading. The ability of the gages to track the changes in curvature is a positive indication of the VWGs' ability to serve as an indicator in the proposed sweep control operations in the arches.

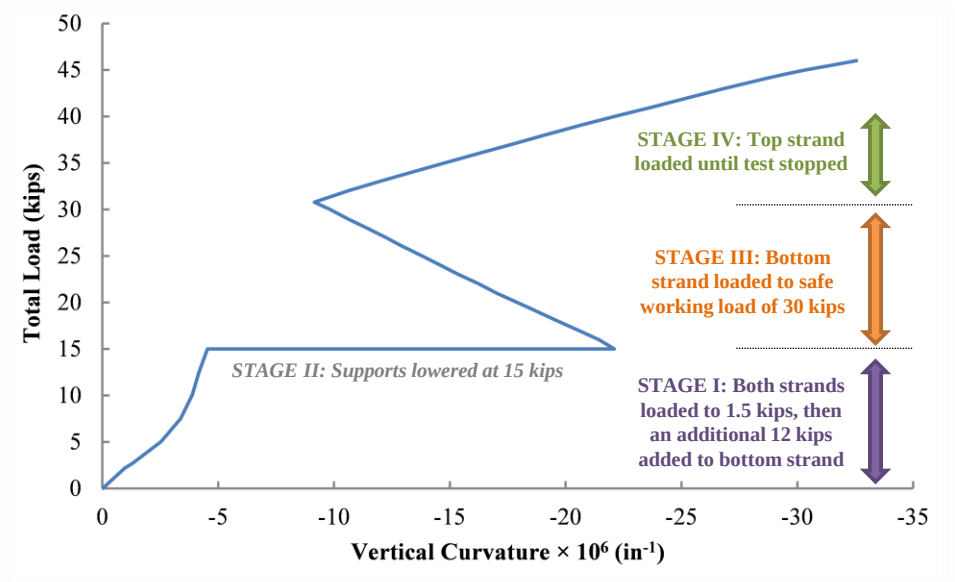

Figure 5-4: Load vs. Vertical Curvature for Concentric Load Test SP2-05PT-3-CON

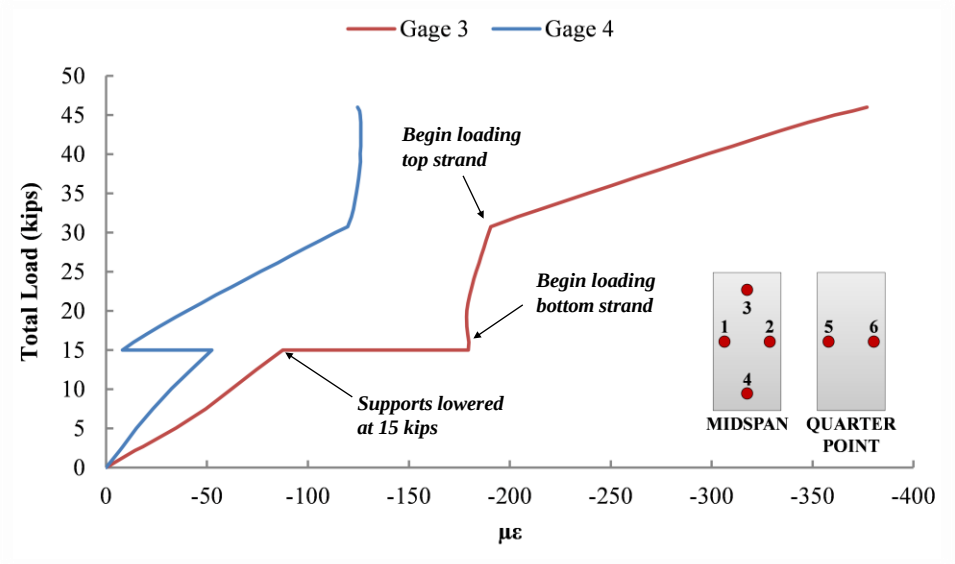

Figure 5-5: Load vs. Vertical Strain for Concentric Load Test SP2-06PT-3-CON

It is also beneficial to examine the load-strain data for this test. A comparison of the load-strain behavior of Gages 3 and 4 is presented in Figure 5-5. At 15 kips of PT, the midspan supports were lowered. The member sagged downward, reducing the compressive strain in Gage 4 and increasing the compressive strain in Gage 3. As the bottom strand was then stressed, the strain in Gage 4 increased rapidly in compression. Stressing of the bottom strand produces axial compression and tensile bending stresses in the top of the beam and as a result, Gage 3 experienced very little change. It can be seen that the Gage 3 strain never matched that of Gage 4, indicating that the camber did not fully cancel the sag in the member. After the maximum load was reached on the bottom strand, top-strand loading began. A rapid increase in compressive strain in Gage 3 was noted, coupled with a lesser increase in Gage 4, as the negative curvature increased. As with vertical curvature, the strain data is an excellent indicator of strong-axis sweep in the member.

5.3.3 Stress Estimation

The vibrating wire gages were also used to determine the stress in the section. The stresses as reported by the VWGs were found at each gage location by multiplying the

strain by the assumed modulus of elasticity. This is the technique that will be employed in the field during monitoring of the network arches. This data was compared to the theoretical stresses at each point due to the combination of axial load, self-weight, and lateral bending. The expressions for the theoretical stress at each gage are defined in Equation 5-1, Equation 5-2, Equation 5-3, and Equation 5-4. It should be noted that theoretical stresses were not calculated until the midspan supports had been lowered.

$$\sigma_1 = \frac{-P_{tot}}{A_{tr}} - \frac{P_{tot} * sign(\Delta_{lp2}) * \Delta_{lat} * x_1}{I_{tr,weak}} \qquad \textit{Equation 5-1}$$

$$\sigma_2 = \frac{-P_{tot}}{A_{tr}} + \frac{P_{tot} * sign(\Delta_{lp2}) * \Delta_{lat} * x_2}{I_{tr,strong}} \qquad \textit{Equation 5-2}$$

$$\sigma_3 = \frac{-M_{sw} * x_3}{I_{tr,strong}} - \frac{P_{tot}}{A_{tr}} + \frac{P_{tot} * \Delta_{vert} * x_3}{I_{tr,strong}} - \frac{(P_{top} - P_{bot}) * 4" * x_3}{I_{tr,strong}} \qquad \textit{Equation 5-3}$$

$$\sigma_4 = \frac{M_{sw} * x_4}{I_{tr,strong}} - \frac{P_{tot}}{A_{tr}} - \frac{P_{tot} * \Delta_{vert} * x_4}{I_{tr,strong}} + \frac{(P_{top} - P_{bot}) * 4" * x_4}{I_{tr,strong}} \qquad \textit{Equation 5-4}$$

$$\sigma_1 \dots \sigma_4 = Stress\ at\ midspan\ (psi)$$
$$P_{tot} = Total\ axial\ load\ in\ specimen\ (lbf)$$
$$P_{top}, P_{bot} = Axial\ load\ in\ top\ or\ bottom\ strand\ (lbf)$$
$$A_{tr} = Transformed\ section\ area\ (in^2)$$
$$I_{tr,strong}, I_{tr,weak} = Transformed\ strong\ or\ weak\ moment\ of\ inertia\ (in^4)$$
$$x_1 \dots x_4 = Distance\ to\ gage\ from\ axis\ (in)$$
$$M_{sw} = Moment\ due\ to\ self-weight\ (lbf-in)$$
$$\Delta_{lp2} = Lateral\ deflection\ of\ member\ measured\ by\ linear\ pot\ 2\ (in)$$
$$\Delta_{lat} = Lateral\ deflection\ of\ member\ at\ midspan\ (in)$$
$$\Delta_{vert} = Vertical\ deflection\ of\ member\ at\ midspan\ (in)$$

The correlation between the measured stresses (the product of the strain and concrete modulus) and the theoretical stresses (found using the above equations) was highly dependent on gage location. For Gages 1 and 2 (located on the horizontal neutral axis of the section at midspan), the correlation was good for tests in which significant

strand engagement with the conduit was not present. In general, the ratio of calculated to measured stresses for Gages 1 and 2 in these tests was between 0.8 and 1.2. These tests included the majority of concentric PT tests for both specimens. Figure 5-6 shows a typical plot of the estimated stress ratio for one such test. The errors in these tests are likely significantly impacted by the assumed value for the elastic modulus.

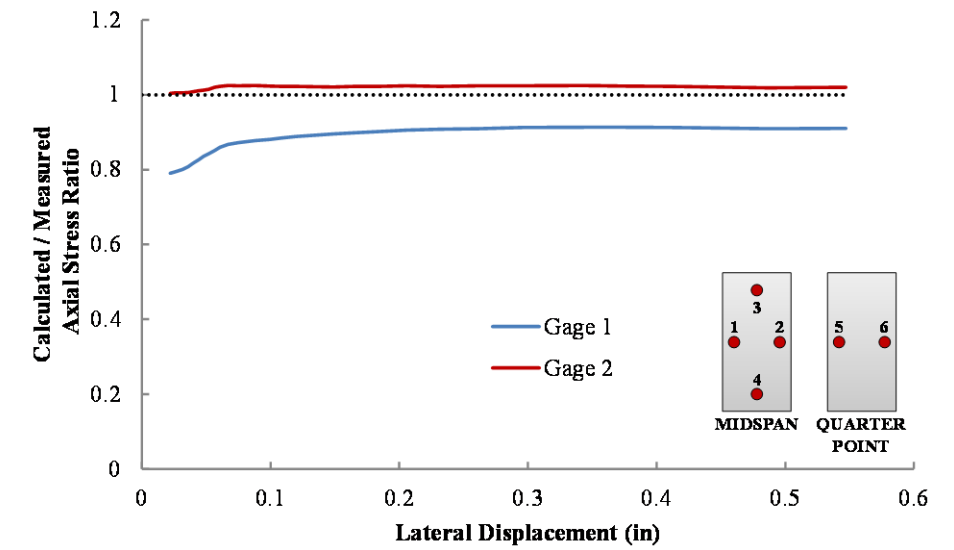

Figure 5-6: Comparison of Calculated Stress to Measured Stress (Gages 1 and 2) for Concentric PT Test SP2-05PT-3-CON

In contrast, the correlation between calculated and measured stresses was poor for Gages 1 and 2 when significant stiffening due to strand engagement with the conduit was noted. One such test is shown in Figure 5-7. The corresponding stress estimates for Gages 1 and 2 are shown in Figure 5-8. The decreasing accuracy of the stress estimates can clearly be seen as the stiffness of the system increases when the strand contacts the duct wall.

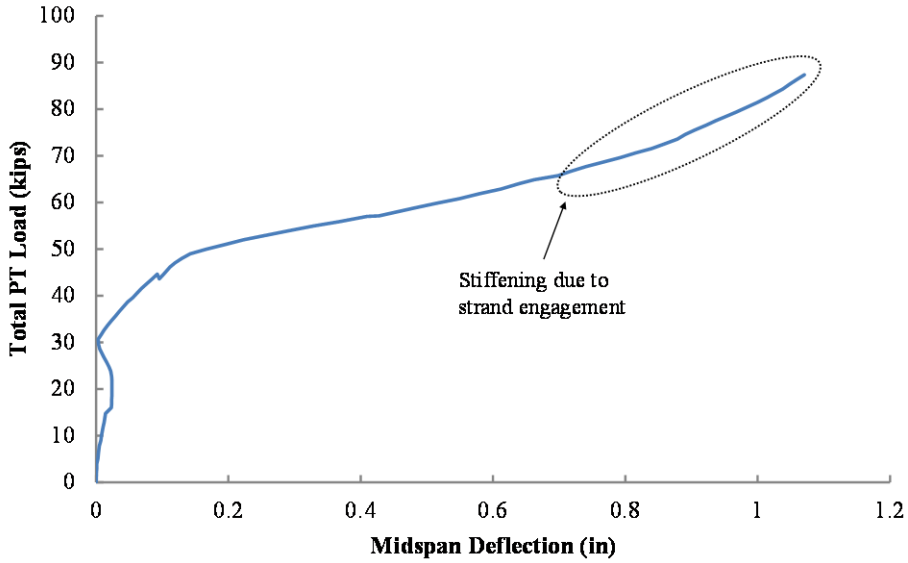

Figure 5-7: Load vs. Midspan Deflection for Concentric PT Test Exhibiting Stiffening (SP1-06PT-2-CON)

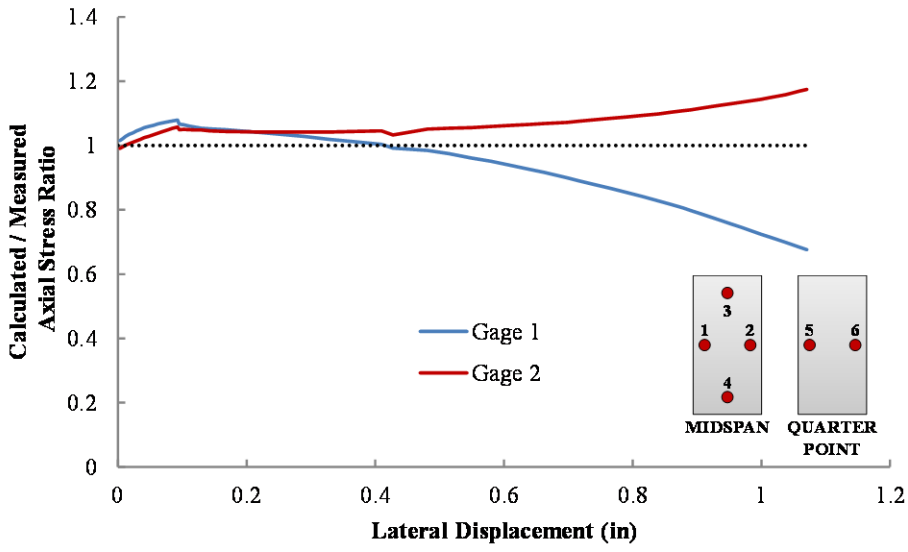

Figure 5-8: Comparison of Calculated Stress to Measured Stress (Gages 1 and 2) for Concentric PT Test with Stiffening Action (SP1-06PT-2-CON)

The correlation between calculated and measured stresses was consistently very poor for Gages 3 and 4 (on the vertical neutral axis at midspan). A typical plot of the ratio of calculated to measured stresses is given in Figure 5-9. The lack of accuracy in Gages 3 and 4 may be due to variation in the strain profile around the ducts on which these VWGs were mounted. In addition, the loading and restraint conditions that evolved during strand engagement likely created a more complicated state of stress than was represented by Equation 5-1 — Equation 5-4. Further discussion of potential sources of error is provided in Chapter 6.

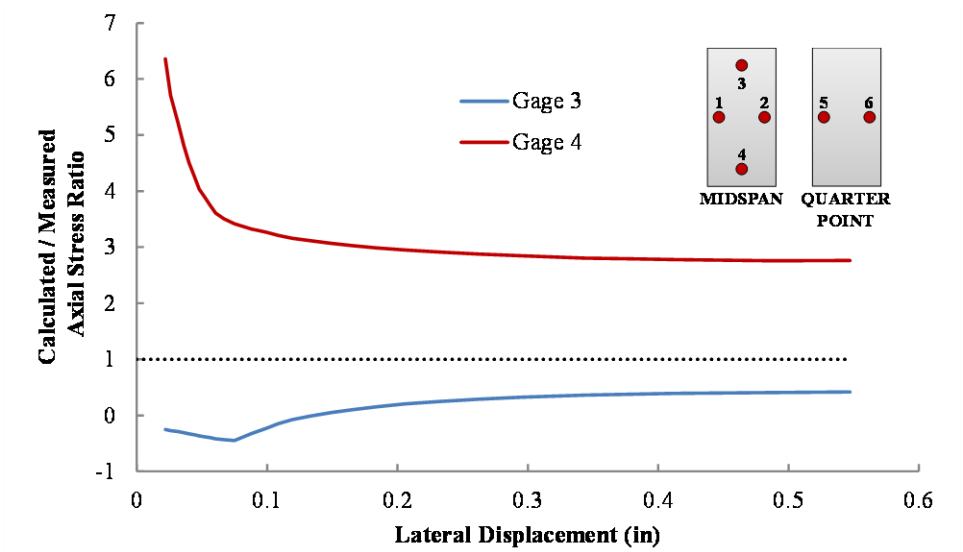

Figure 5-9: Comparison of Calculated Stress to Measured Stress (Gages 3 and 4) for Concentric PT Test SP2-05PT-3-CON

The individual stresses inferred from each gage were also used for the calculation of the maximum stresses in the section. The stress gradient between gage pairs was extrapolated to estimate the stress at the extreme fibers of the section. The most critical point (where the section experienced tension due to bending about both axes) was closely monitored. While this data was not recorded, it was used as an indicator in real-time

during the loading to reduce the risk of cracking in the section. Several tests were stopped due to the risk of cracking, in an attempt to preserve the integrity of the specimens.

5.3.4 Axial Load Estimation

Effective prediction of the internal axial load will be important in the field monitoring protocol. The research team should have a reasonable estimate of the applied load from the construction team's monitoring of the tendon jacking force. However, the research team must have the ability to estimate the loads based upon the VWG readings as well. Careful analysis of the construction process was completed by the design team in an attempt to ensure that the arch does not crack or become overstressed at the various stages of construction. However, several assumptions were made in the analysis. These assumptions will be verified in the field. The VWGs will represent the only method of evaluating internal stresses. Similarly, the loads estimated by the VWGs will be used to generate the load-curvature trends that will be essential to monitoring structural stability. As such, calibration of the gages was a key goal for the gage resolution study.

Axial load in a section was estimated using the relationships detailed in Equation 5-5, Equation 5-6, and Equation 5-7. The strains reported by the each pair of gages at a section were averaged. (The gages across from each other in each section were paired: Gages 1-2 and Gages 3-4 at midspan, and Gages 5-6 at the quarter point.) This average strain value was used for the estimation of the pure axial stress (P/A) at each section.

$$\boldsymbol{P = A * f_c} \qquad \textit{Equation 5-5}$$

$$\boldsymbol{f_c = E * \varepsilon_{avg}} \qquad \textit{Equation 5-6}$$

$$\boldsymbol{E} = \begin{cases} \mathbf{57}\sqrt{\boldsymbol{f_c'}}\ for\ f_c' \leq 7\ ksi \\ \mathbf{1000 + 40}\sqrt{\boldsymbol{f_c'}}\ for\ f_c' > 7\ ksi \end{cases} \qquad \textit{Equation 5-7}$$

$$P = Axial\ load\ in\ section\ (kips)$$
$$A = Section\ area\ (in^2)$$
$$f_c = Concrete\ stress\ (ksi)$$
$$E = Concrete\ elastic\ modulus\ (ksi)$$
$$\varepsilon_{avg} = Average\ concrete\ strain\ measured\ across\ pair\ of\ gages\ (in/in)$$
$$f_c' = Concrete\ compressive\ strength\ (psi)$$

The elastic modulus of the concrete in the first specimen (SP1) was found as approximately 5.5 ksi using Equation 5-7. This value was consistent with the ratios of calculated to measured stresses. As such, it was assumed valid and was not adjusted. This was not the case for the second specimen (SP2), however. The elastic modulus of the concrete in SP2 was originally calculated using Equation 5-7 as approximately 5.0 ksi. However, as previously mentioned, some cracking was noted around midspan; this was thought to have occurred during lifting of the specimens. The cracking in SP2 was more extensive than in SP1. As such, the elastic modulus was reduced to roughly 4.4 ksi. This new value was based on an analysis of the strain data from the pre-failure external load test on SP2. The average ratio of calculated stresses to measured stresses (described in Section 5.3.3) for the external load test was used to define the adjustment factor. The adjusted modulus estimate appears reasonable in the context of axial load and stress estimates. The research team is currently conducting tests on the concrete mix design that will be used in the arches, in an effort to determine the elastic modulus as a function of concrete maturity. As a result, the researchers will have modulus values to be used with the gages based upon the specific age of the concrete in the field tests. This data will improve the accuracy of the field measurements.

As described in Chapter 3, the test instrumentation included a load cell on each strand, with a third load cell for external loading. These served as a benchmark for the axial load estimation provided by the gages. The estimated axial load was plotted against the total load measured by the load cells.

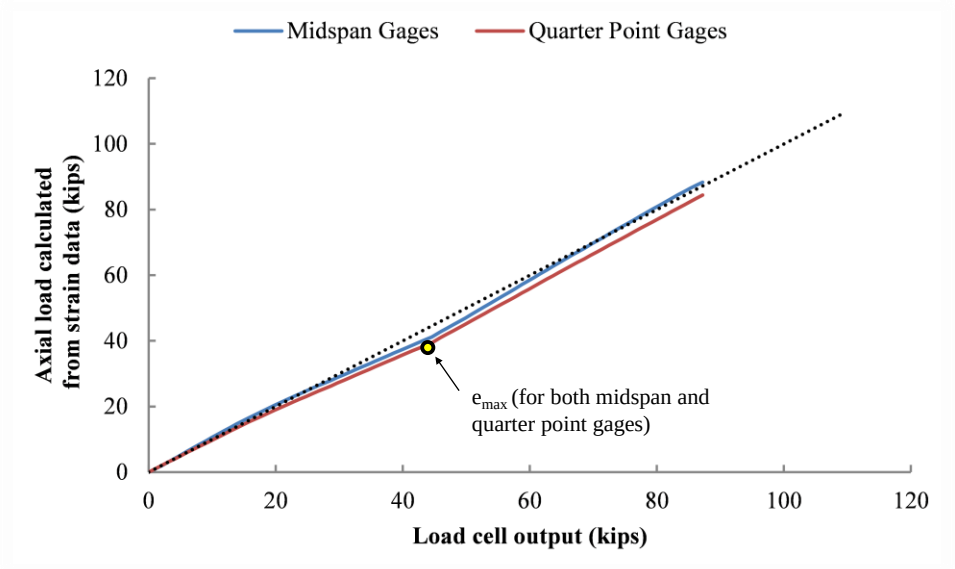

Figure 5-10: Axial Load Estimation for Concentric PT Test SP1-06PT-3-CON

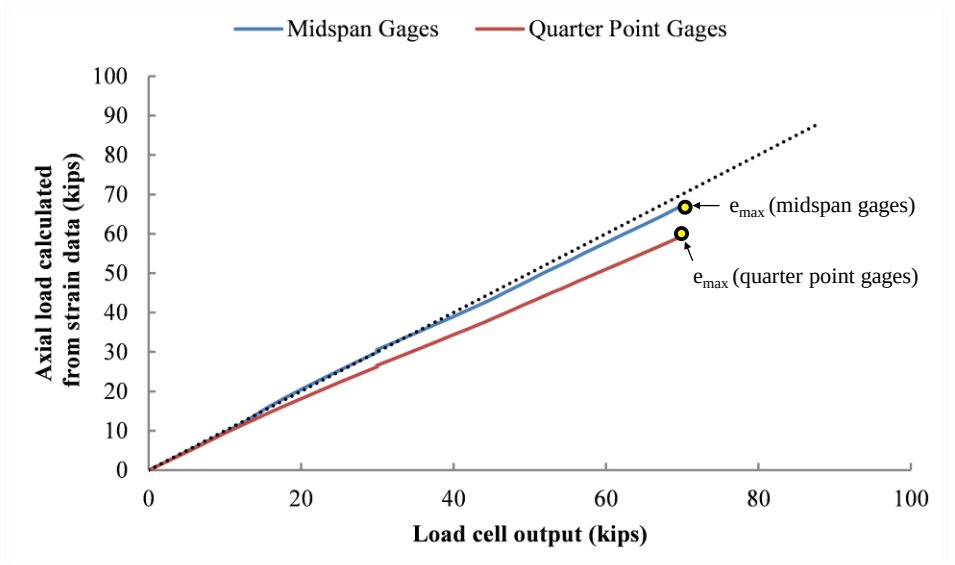

Figure 5-11: Axial Load Estimation for Eccentric PT Test SP2-06PT-11-ECC-E

Typical plots for the comparison of axial load are given for a concentric and eccentric post-tensioned (PT) test in Figure 5-10 and Figure 5-11, respectively. An additional comparison plot for a concentric PT test is given in Figure 5-12. The dotted line indicates perfect correlation between the load cell output and the axial load

calculated from the VWG data. Additional axial load estimation plots are included in the appendix of this document.

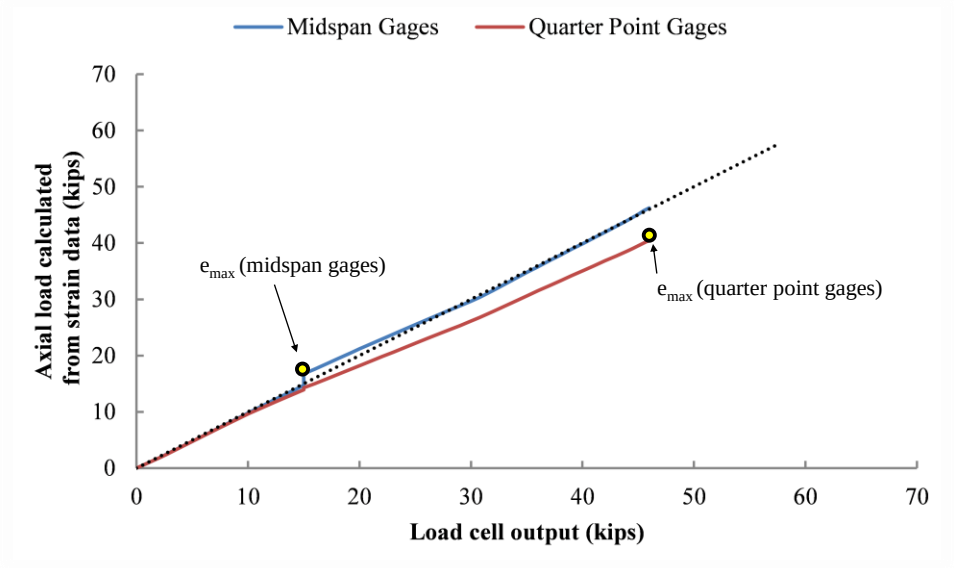

Figure 5-12: Axial Load Estimation for Concentric PT Test SP2-05PT-3-CON

In PT tests in the second specimen (SP2), the supports were lowered as described in Chapter 4. A slight jump in the axial load estimate was noted at the point of the supports being lowered. After this initial jump, however, the axial load estimates typically were highly consistent with the load cell data. Figure 5-12 shows an eccentric load test on SP2, in which the midspan supports were lowered at a PT load of 15 kips. The jump in axial load is evident. This jump in the axial load estimate was thought to be due to the rapid elimination of the axial force component taken by the midspan supports due to friction. These observations are discussed in more detail in Chapter 6.

The percent error for each test was generated for each data collection point, starting once the load reached 20 kips. At low loads, small errors in load estimation could result in a large reported error; this was thought to be somewhat misleading and was thus eliminated. The point of maximum percent error is denoted as e_{max} on each of the previous figures. A maximum error was found for the estimates from both the midspan and quarter point gages.

Table 5-2: Comparison of Axial Load Estimates in Pre-Failure PT Tests

(i) Axial Load Estimation - PRE-FAILURE PT TESTS (SP1 and SP2)					
Quarter Point Gages			**Midspan Gages**		
Max Estimation Error	No. of Tests	% of Tests	Max Estimation Error	No. of Tests	% of Tests
> 10%	32	74.4%	> 10%	5	11.6%
7-10%	6	14.0%	7-10%	12	27.9%
5-7%	2	4.7%	5-7%	15	34.9%
0-5%	3	7.0%	0-5%	11	25.6%
Maximum Error = 15.5%			**Maximum Error = 12.6%**		

(ii) Axial Load Estimation - PRE-FAILURE PT TESTS (SP1 only)					
Quarter Point Gages			**Midspan Gages**		
Max Estimation Error	No. of Tests	% of Tests	Max Estimation Error	No. of Tests	% of Tests
> 10%	10	47.6%	> 10%	0	0.0%
7-10%	6	28.6%	7-10%	8	38.1%
5-7%	2	9.5%	5-7%	9	42.9%
0-5%	3	14.3%	0-5%	4	19.0%
Maximum Error = 13.1%			**Maximum Error = 9.8%**		

(iii) Axial Load Estimation - PRE-FAILURE PT TESTS (SP2 only)					
Quarter Point Gages			**Midspan Gages**		
Max Estimation Error	No. of Tests	% of Tests	Max Estimation Error	No. of Tests	% of Tests
> 10%	22	100.0%	> 10%	5	22.7%
7-10%	0	0.0%	7-10%	4	18.2%
5-7%	0	0.0%	5-7%	6	27.3%
0-5%	0	0.0%	0-5%	7	31.8%
Maximum Error = 15.5%			**Maximum Error = 12.6%**		

Table 5-2 summarizes the maximum errors in axial load estimates for the VWGs in pre-failure load tests. This table includes data for all PT tests *before* significant cracking occurred in each specimen due to buckling failure. (Errors in estimation were found to be much higher after failure. This is to be expected, as the assumed modulus of elasticity was likely to be inaccurate for the cracked section.) Only PT tests are compared here; the combined PT and external loading schemes were performed post-failure in SP1

and pre-failure in SP2, so were not easily comparable. In addition, loading on the arches will be primarily post-tensioning, so monitoring the gage behavior under PT loads is critical. The values reported in Table 5-2 are the *maximum* error calculated for all the data points; the *average* error in estimation for each test is lower.

In general, reasonable correspondence was observed between the load measured by the load cells and that calculated from the gage data was noted throughout testing. The error between the estimated and measured axial load was less than 10 percent for the midspan gages in the vast majority of tests. The estimates from the quarter point gages were only slightly less consistent. Further analyses of these values and potential sources of error are presented in Chapter 6.

5.4 BUCKLING RESULTS

The second goal of the experimental study was the investigation of buckling behavior. Some general observations on the buckling behavior of the two test specimens are presented in this section. Buckling trends were noted under each of the three loading configurations. Each specimen was ultimately loaded to a complete and irreversible stability failure under external load. General data and trends are provided here with a more extensive discussion and analysis of the stability studies presented in Chapter 6.

5.4.1 Study Motivation

The stability monitoring portion of this research program seeks to establish a fundamental understanding of the elastic buckling behavior of slender compression elements with unbonded post-tensioning. The key relationships and initial observations are detailed below.

1- *Buckling behavior under post-tensioning*: As noted in Chapter 2, conventional theory holds that post-tensioned concrete elements cannot buckle under the prestressing load alone. This assumes that the tendons are continuously bonded to or are in contact with the concrete. The experimental program described in this thesis sought to investigate the general buckling behavior of

unbonded post-tensioned elements. This was accomplished by applying combinations of post-tensioning (PT) loads in various configurations. Behavior trends consistent with elastic buckling were noted under post-tensioning. These observations are presented in the following pages.

2- *Effects of strand engagement on buckling capacity*: Previous studies (presented in Chapter 2) have noted that the interaction of the post-tensioning tendon and the concrete has a profound impact on the buckling behavior of a member. This relationship was confirmed by the lab tests in this study. Eccentric loads were applied to induce bending and ensure strand engagement (the contact of the tensioned strand against the duct sidewall). Strand engagement and stiffening action was noted in the load-deflection and load-curvature behavior. Apparent increases in the elastic buckling capacity of the member were noted.

3- *Effects of initial post-tensioning on buckling capacity under external load*: Design convention holds that for bonded prestressing tendons, the internal equilibrium between the steel in tension and concrete in compression results in a zero net stress on the section. This implies that the magnitude of the external load that can be applied to the column prior to instability will be unchanged by the level of prestressing (Bazant & Cedolin, 2010). This study sought to investigate if the same held true for unbonded post-tensioning. The tests specimens in this study were designed so that the prestressing tendons were not in contact with the duct until the member experienced sufficient lateral movement to engage the strand. As such, it would stand to reason that the post-tensioning would simply transfer a compressive stress to the section, inducing a compressive pre-load. This pre-load would be included in the critical buckling load, reducing the amount of additional external load that can be applied to the column.

4- *Effects of strand diameter on buckling response*: The load tests were conducted on each test specimen with two different tendon sizes. It was

theorized that the increased stiffness of a larger tendon should impart additional lateral restraint to the member at the onset of buckling. In addition, more prestress force can be applied to a larger tendon, increasing the available axial load to be applied to the concrete member. Some notable increases in stiffness were observed. Additionally, the increased axial loads allowed for further investigation of the effects of strand engagement.

Each of these relationships is investigated in more detail in the following pages. Following a presentation of data and initial conclusions on each, further analysis is provided in Chapter 6.

5.4.2 Buckling Under Post-Tensioning

In the loading scheme involving only post-tensioning (PT), the onset of buckling was noted in some tests. In several tests on the first specimen (SP1), loss of stiffness was noted in both the load-curvature and load-deflection curves, as can be seen in the tests shown in Figure 5-13. This softening indicates that buckling under PT loads was a concern in SP1 in its intact, uncracked (pre-failure) state. However, buckling under PT loads was never achieved in SP1. In some cases, the safe working loads of the strands were not adequate to reach the buckling loads. In other tests, the system regained stiffness at higher loads due to contact between the strands and the duct wall.

Stiffening behavior was noted in only a few tests under concentric PT loads up to 88 kips. Of all concentric PT tests on SP1, an increase of stiffness was noted in only the last two tests with 0.5-inch diameter strands and the only two pre-failure tests (prior to the cracking of the specimen under the external load test) with 0.6-inch diameter strands. A comparison of two concentric tests, one with stiffening and one without, is presented in Figure 5-13. The maximum lateral deflection in each of the SP1 tests in which stiffening was noted is in excess of 0.85 inches. The deflections in the other concentric PT tests did not exceed 0.65 inches and no definitive stiffening was noted. Therefore, it seems that once a critical deflection was reached, the energy required to displace the strand further was great enough that additional stiffening was noted in the system.

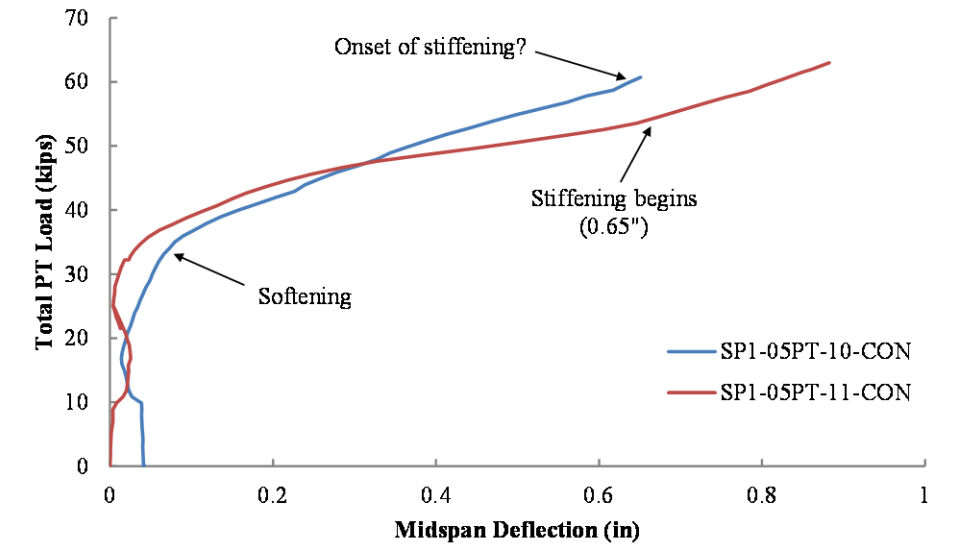

Figure 5-13: Comparison of Load-Deflection Data for Two Concentric PT Tests in SP1

It is likely that the reduction of some end fixity allowed for additional deflection to be achieved in the later tests. The reduction in end fixity may have come from adjustments that were made in the contact points used to resist twist and lateral movement at the ends of the sections. In Figure 5-13, the maximum deflection in SP1-05PT-10-CON was 0.65 inches. It appeared that some stiffness was being introduced into the system at this deflection, but the test had to be stopped because the safe working load of the strands had been reached. The following test (SP1-05PT-11-CON) began to exhibit stiffening at the same deflection.

There were a number of early test difficulties in SP1 that had to be resolved. Initially, the supports were not lowered at any point during the tests, and the strands were loaded simultaneously. Since the simultaneous stressing generates a concentric prestress that does not lead to a camber at any point during the testing, the supports were in contact for the duration of the test. Although the Teflon reduced the frictional resistance, the coefficient of friction was still 4-5% and therefore the supports did provide some restraint. The resulting frictional forces restrained lateral motion of the specimen under

concentric PT loads. The total lateral deflections in these cases were negligible and, as such, meaningful Southwell plots could not be produced for these tests. Once the issues were resolved through sequential strand loading and support lowering as described in Chapter 4, the Southwell plot estimates were in good agreement with the observed behavior.

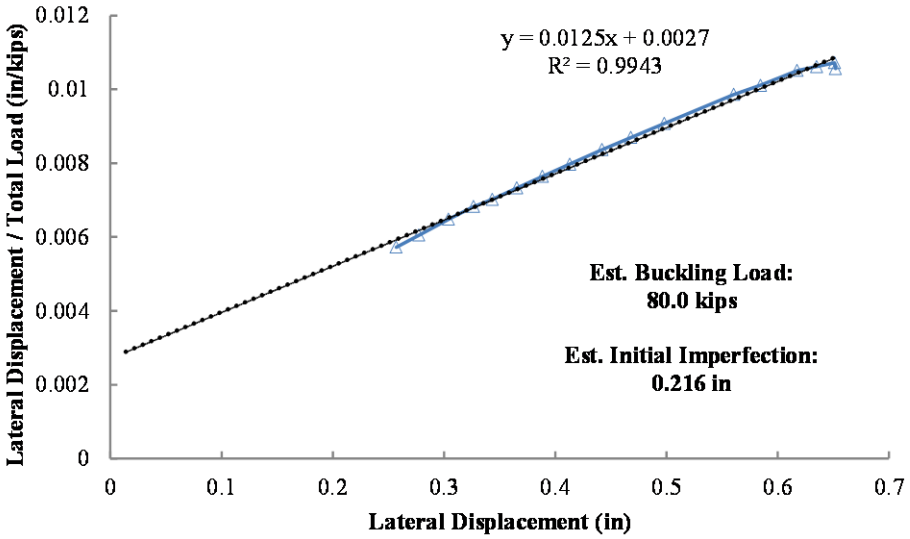

Figure 5-14: Comparison of Load-Deflection Data for Two Concentric PT Tests in SP1

A Southwell plot for SP1-05PT-10-CON (one of the tests depicted in Figure 5-13) is shown in Figure 5-14. The predicted buckling load is well above the calculated Euler buckling capacity of approximately 50 kips, demonstrating the stiffening effects. A more detailed investigation of the effects of strand engagement as manifested in the Southwell plots is provided in Chapter 6.

In contrast to SP1, the onset of definitive buckling behavior was clearly noted in most concentric PT load tests for the second specimen (SP2). A clear loss of stiffness was noted in the load versus lateral curvature plots (Figure 5-15). Similarly, the Southwell plots indicated lower buckling loads in SP2 than in SP1. Figure 5-16 depicts the Southwell plot for the same concentric PT test and predicts a critical load of 50.3 kips. This is consistent with the observed load versus lateral curvature curve in Figure 5-15.

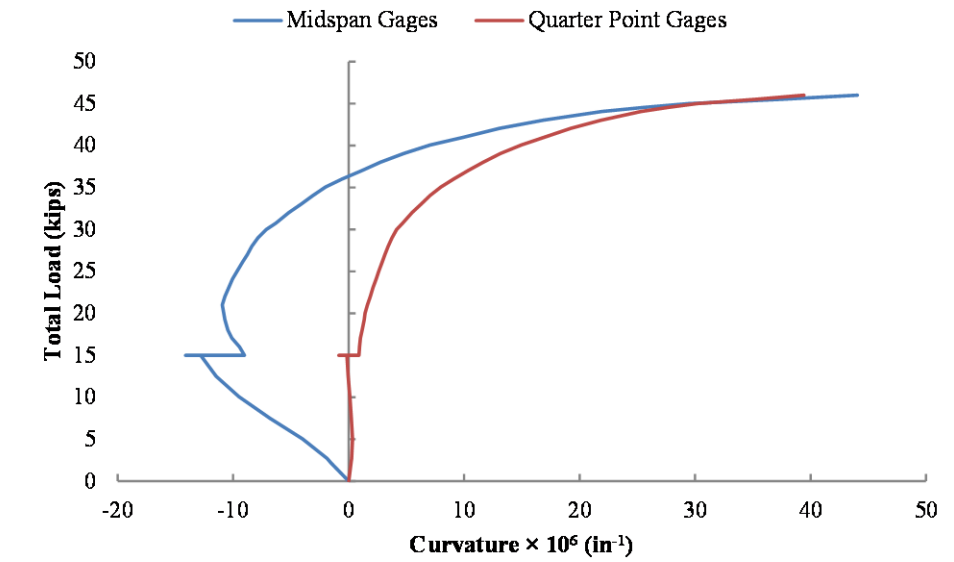

Figure 5-15: Load vs. Lateral Curvature for Concentric PT Test in SP2-05PT-6-CON

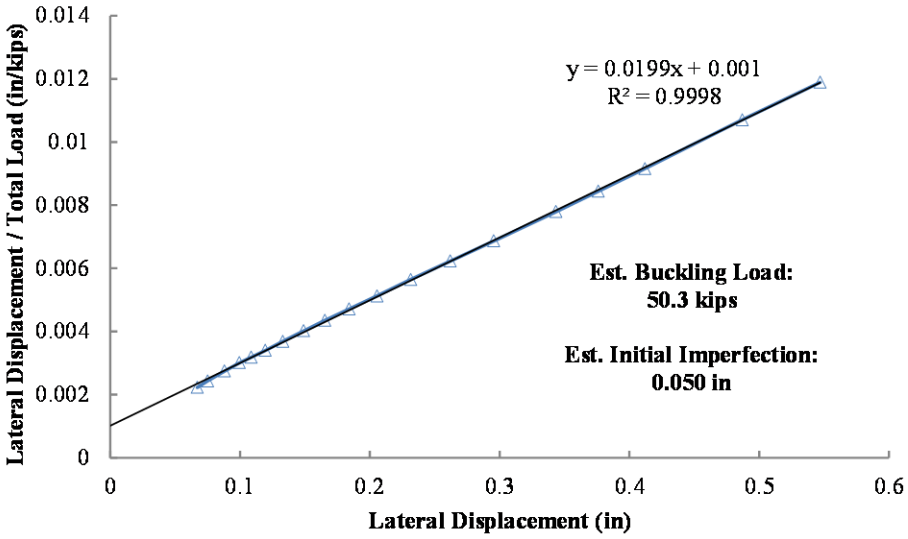

Figure 5-16: Southwell Plot for Concentric PT Test SP2-05PT-6-CON

It can be noted from Figure 5-15 that the curvature started as negative and then moved in the opposite direction once the supports are lowered. This is likely due to the frictional restraint provided by the midspan supports. The specimen routinely displayed

this trend reversal. It was thought that the midspan supports provided a form of bracing influencing the specimen's tendency to bend in a manner such that the midspan was in negative lateral curvature. Once the friction was eliminated, the unbraced specimen reversed its curvature and deflections increased. The behavior may also indicate the relatively small initial imperfections in the members. The metal formwork used was highly precise and as a result, the members were quite straight. Because the specimens were relatively straight, a small amount of restraint was sufficient to cause the sections at midspan to begin bending in one direction and then flip to the other direction once the intermediate supports were removed.

The concentric PT tests were typically stopped due to buckling concerns, well before the capacity of the strands was reached. The eccentrically-loaded PT tests for SP2 were similar to SP1 in that no significant loss of stiffness was noted under PT loads (Figure 5-17). Eccentric tests were generally not stopped until the allowable working load of the strands was reached, or until the risk of cracking was deemed too great.

A clear buckling risk was noted under concentric post-tensioning in SP2; this was not the case in SP1. The differences between the buckling behavior of SP1 and SP2 under concentric PT loads may also be related to strand engagement. As was previously noted, the midsection of the reinforcement cage and ducts "floated" upward during the placement of concrete in SP1. (Due to proper precautions, no such duct displacement was noted in the construction of SP2.) In SP1, while the ducts remained nearly symmetric about the vertical axis, they translated upward, so were not symmetric about the horizontal axis of the section. Thus, while the strands may have appeared to be concentric at the ends of the specimen, they were more likely located much nearer the bottom wall of the ducts at midspan. As such, significant strand engagement at midspan in SP1 would be induced by minimal vertical or lateral displacement at midspan due to PT loads. In short, it is likely that the strands in SP1 were in contact with the duct walls very early in the loading cycle, if not at the start of the test. As mentioned before, the total length of contact between the strand and duct may also have affected the stiffening behavior in the specimen.

In contrast, the strands in SP2 were likely to have been nearly concentric throughout the length of the member. Therefore, the vertical deflection due to camber or sag and the lateral deflection due to load would have to have been more significant for the strands to contact the duct walls. Strand engagement is thought to be the primary reason for the differences in behavior between SP1 and SP2. The effects of strand engagement on structural behavior are discussed at more length in Chapter 6.

While strand engagement was more or less incidental in the concentric load tests, it was intentionally induced in eccentric tests. The strands were oriented with a ⅝″ eccentricity as described in Chapter 3. In both specimens, tests with eccentrically oriented strands did not demonstrate buckling behavior. This would seem to indicate that when sufficient bending was induced by the eccentricity, the midspan deflection increased to a point where a significant length of the tensioned tendon was in contact with the duct wall. At this point, the tensioned strand imparts stiffness to the overall system, increasing the critical buckling load.

As stated above, eccentric load tests in SP1 and SP2 (Figure 5-17) never exhibited definitive softening behavior. Figure 5-17 shows a set of three eccentric tests; two are from SP1 (with different strand diameters), and one is from SP2 (0.6-inch diameter strand). The clear lack of buckling risk is thought to be due to strand engagement with the duct wall. Both specimens exhibited some early stiffening behavior, as seen in Figure 5-17, but the load versus deflection behavior was nearly linear as the tests progressed. It can be seen from the load-deflection plots that no significant loss of stiffness is noted, even as the total load extends well beyond the theoretical Euler buckling load of approximately 50 kips.

The clear contrast between the softening behavior noted in the concentric tests and the lack of softening in the eccentric tests was thought to be related to the total length of contact between the duct wall and the tensioned strand. In the concentric configuration, only a relatively short length of the tendon may have been in direct contact with the duct. It was not until the specimen reached a critical lateral deflection that enough of the strand was engaged to provide a restoring force resulting in noticeable

stiffening (Figure 5-13). Due to the large flexural deformations in the eccentric load cases, a larger length of the strand was likely to be in contact from relatively early in the stressing. Stiffening was noted early in the stressing process, where the strand quickly picks up stiffness as it is tensioned. After the well-defined early stiffening, the behavior becomes nearly linear. While additional stiffening was almost certainly present, it was unlikely to be discernible over the relatively small load range. (The total load was limited to the capacity of only two tendons.) As such, the behavior appeared mostly linear for eccentric PT loads at higher loads.

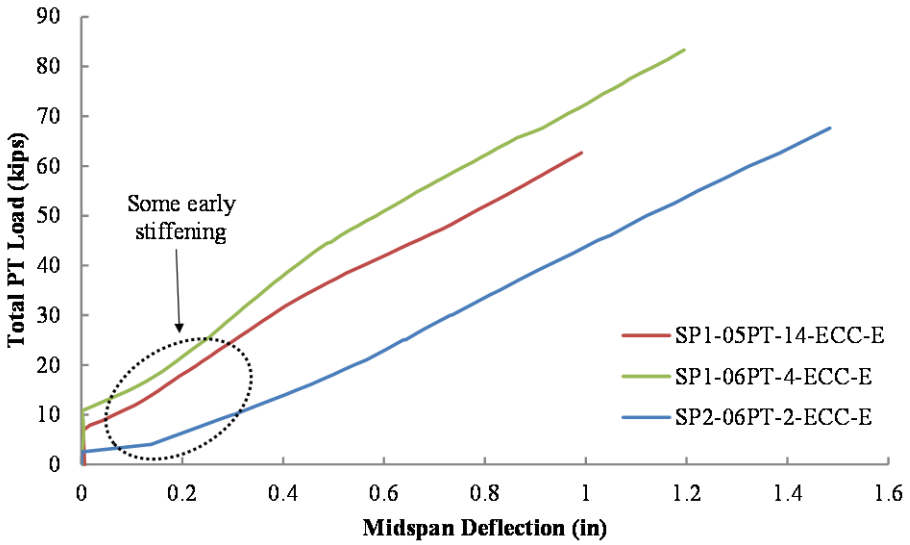

Figure 5-17: Load-Deflection Data for ⅝" Eccentric PT Tests in SP1 and SP2

It should also be noted that the early stiffening is slightly less pronounced in SP2 than in SP1. This is likely related to the stage at which strand engagement is thought to occur. Construction errors due to duct translation during casting were noted in SP1 (discussed in Chapter 3). As such, the length of strand engaged with the duct wall at the start of the test was almost certainly greater in SP1 than in SP2. As the strands quickly gained stiffness under early loads, this stiffness was imparted to the system and noted at

early stages in SP1. In SP2, the strands likely did not engage to a significant degree until later, at which point the stiffening effects were less pronounced. The strand engagement relationships are described in more detail in the following chapter.

5.4.3 Buckling Under External Loading

Both test specimens underwent at least one test in which the load was purely external, applied via the 100-kip ram. While the tendons remained in the ducts, they were not stressed. The details of the configuration were described in Chapter 3.

The first external load test in SP1 was ended due to excessive deflections noted in the end plates of the prestress chairs. Stiffeners were welded to the plates, and the loading was repeated. It should be noted that during external load testing of SP1, the real-time monitoring had not yet been updated to include Southwell plot abilities. Thus, the tests were performed without a quantitative estimate of the buckling capacity. (Southwell plots have since been utilized for all relevant tests.)

The majority of PT tests were performed on SP1 prior to the external load tests. As previously noted, no definitive buckling behavior was noted during the application of PT load, up to a total of 88 kips. As such, the total allowable external load was mistakenly expected to be in excess of 80 kips as well. However, the specimen buckled suddenly at a load of 51 kips. The specimen immediately after the buckling failure is pictured in Figure 5-18. Significant cracking was noted along the tensile face of the member. These cracks were marked and are depicted in Figure 5-19.

It should be noted that the buckled shape was not symmetric about the midspan. Rather, the buckling occurred near the north quarter point. While this could have been due to a weaker section at that point, it is also likely that there existed a higher degree of fixity for this specific test at the south end than at the north. While this is not ideal, the individual thrust bearings and tilt saddles at each end may have exhibited different freedom of rotation. In addition, the configuration of load components at each end was not symmetric. The south (live) end included both an HSS spacer and the ram, whereas the north (dead) end included the spacer only. These factors, sought to be minimized in

subsequent tests, may have contributed to the lack of symmetry in the buckled shape of the first specimen.

Figure 5-18: SP1 after Buckling Failure (Test SP1-PT0-EX-2)

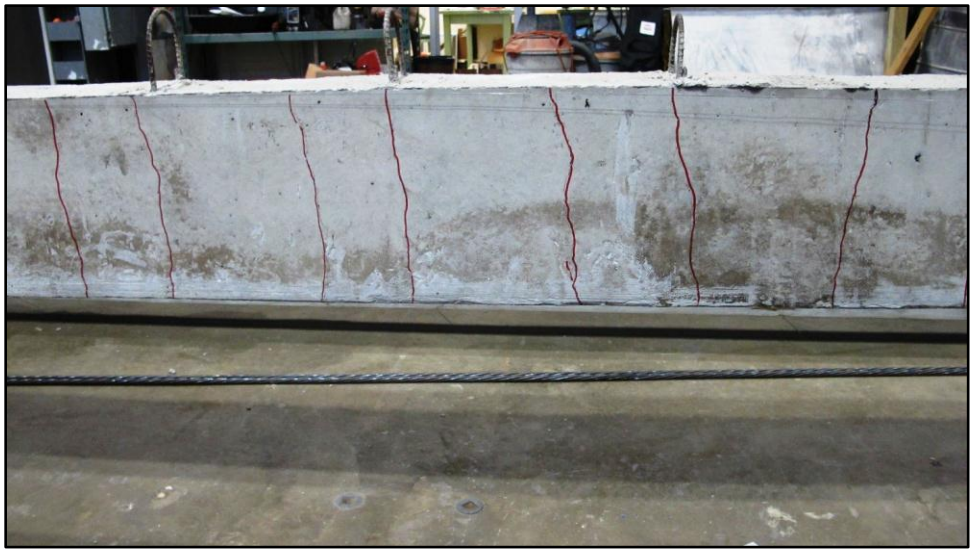

Figure 5-19: Cracking in SP1 after Buckling Failure (Test SP1-PT0-EX-2)

Although the buckling was somewhat unexpected due to the results of previous tests, the VWG data excellently displayed the loss of stiffness indicative of imminent buckling. Had the data been carefully monitored in real-time during the test (the macro for doing so was not fully developed for the first specimen), it would have been obvious to the research team that the risk of buckling was high. The load-curvature plot for this test is shown in Figure 5-20. A Southwell plot was constructed after the test; it predicted a buckling load of 52.9 kips, very close to the actual buckling load of 51.0 kips. (As the failure was unexpected, the last pre-failure scan of the VWGs was made at 49.5 kips. The real-time load cell data indicated a peak load of 51.0 kips.) This plot is shown in Figure 5-21. The results of this test confirm the ability of the VWGs to accurately and reliably indicate structural stability.

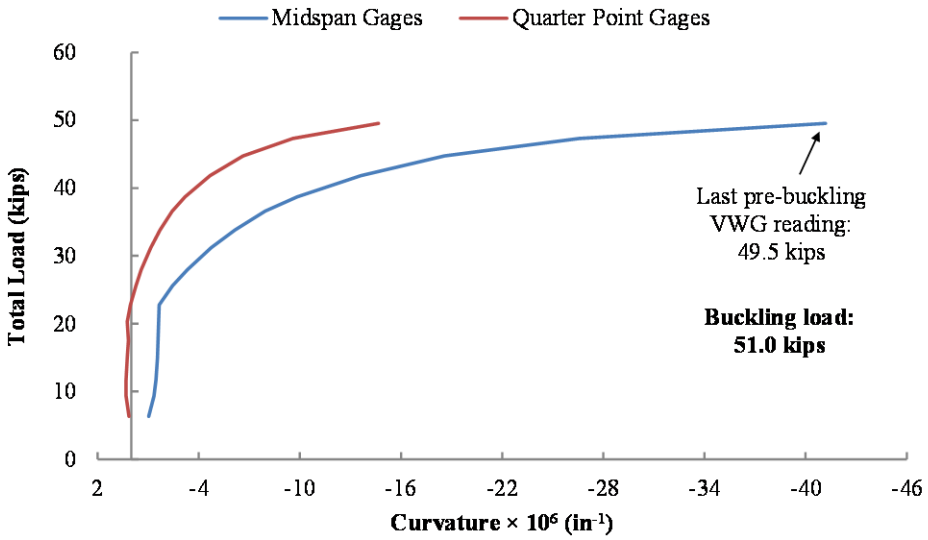

Figure 5-20: Load vs. Lateral Curvature for External Test SP1-PT0-EX-2

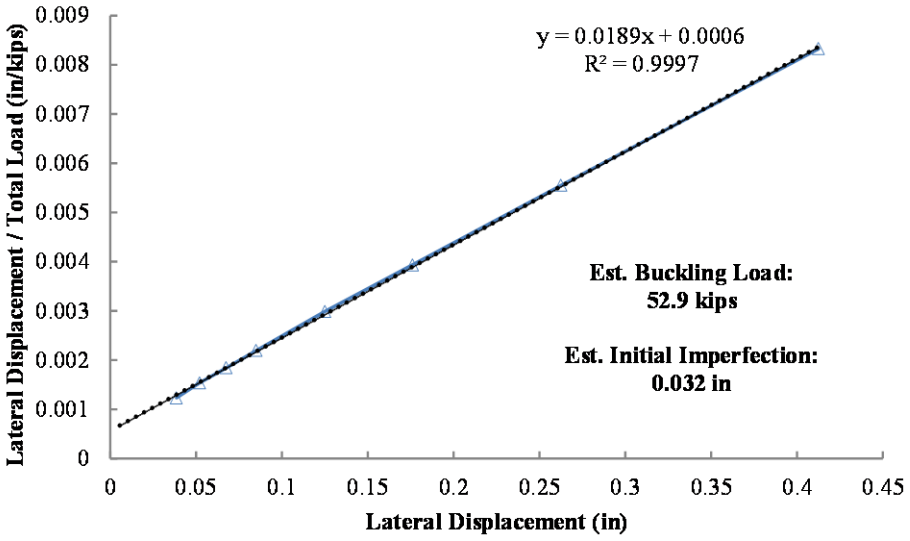

Figure 5-21: Southwell Plot for External Test SP1-PT0-EX-2

The second specimen (SP2) was also loaded externally to failure. Again, failure was sudden and somewhat unexpected, but not due to insufficient monitoring of the VWG data. In the first external load test of SP2, external load was applied to 48.5 kips. As buckling appeared imminent from the graphs, it was decided that the test should be stopped. As the research team prepared to remove the load, the specimen buckled suddenly under the load (48.5 kips) at which it had been held for roughly five minutes. In this case, the buckled shape was symmetric about midspan, indicating homogeneity of the specimen and that the effects of differential end fixity were minimal.

As in the tests of SP1, the VWGs effectively predicted the buckling behavior. However, some test difficulties rendered the Southwell plot inconclusive. A load-curvature plot and Southwell plot for the external loading of SP2 are provided in Figure 5-22 and Figure 5-23, respectively.

It can be seen that the Southwell plot prediction for SP2 is well above the actual buckling load. This is due to a problem in the test setup. A mid-test visual inspection of the test setup revealed that one of the contact points on the north end of the specimen was jammed against the specimen, providing undesired fixity to that end. The problem was corrected, but the fixity introduced errors into the Southwell plot prediction. Only the

data points after the correction were used for the Southwell plot construction, but it can be seen that the initial imperfection estimate is faulty. As the assumed initial deflected shape and load sequence were not ideal, the Southwell plot was considered invalid, and the test was monitored primarily through the observation of the load-curvature data.

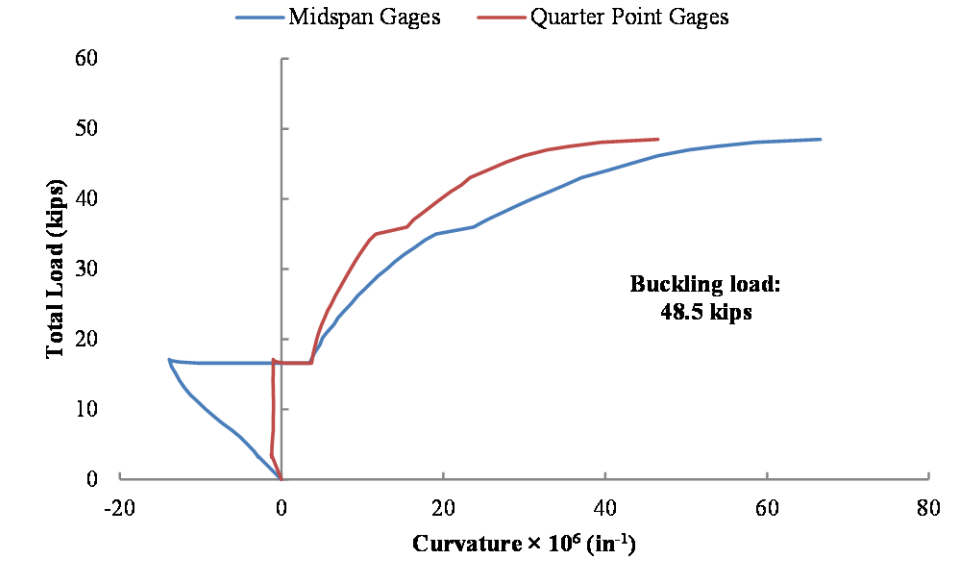

Figure 5-22: Load vs. Lateral Curvature for External Test SP2-PT0-EX-1

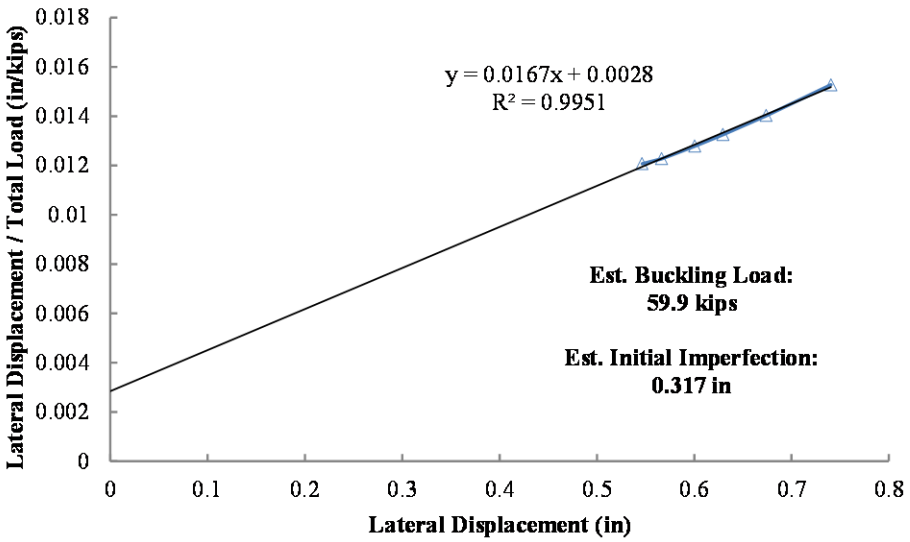

Figure 5-23: Southwell Plot for External Test SP2-PT0-EX-1

In each of the external load tests, the onset of buckling was easily identifiable in both load-deflection and load-curvature data. Additionally, the observed deflected shape trends coincided well with the stability behavior, with deflections increasing rapidly as the load reached the critical buckling load. The ultimate load (at which failure occurred) was in excellent agreement with the Southwell plots' prediction for each specimen.

5.4.4 Buckling Under Combined Loading

Load tests employing first post-tensioning (PT) and then external loads, referred to here as combined load tests (described in Chapter 3), were performed on both specimens. These were, however, performed at different stages in the life of each specimen. In the first specimen (SP1), the buckling under external load (Figure 5-18) was unexpected. As such, no combined load tests were performed on the specimen prior to buckling. A single combined load was applied to SP1 after the buckling failure. A total of 60 kips of concentric PT load were applied prior to external load. This value is well above the critical buckling load of 51 kips for the *undamaged* specimen, again indicating the important role of strand engagement. After the PT force, an additional 16 kips of external load were applied to the specimen before the test was stopped due to buckling risk. While it is difficult to draw definitive conclusions from this single test, the effects of strand engagement in increasing the lateral stability of the member are clearly evident.

In the second specimen (SP2), a total of twelve combined load tests were performed prior to failure under external loading. In each test, concentric PT load was applied to a specified level and "locked in" prior to the application of external load. Tests were performed using both 0.5-inch and 0.6-inch diameter strands. In an additional variation, two distinct strand loading sequences were employed for each strand diameter. In the double strand (DS) designation, the bottom strand was loaded first, to roughly half the total PT load. After the supports were lowered, the remainder of the PT load was applied to the top strand. In the single-strand (SS) designation, over 90% of the PT load was applied to the bottom strand, with minimal load on the top strand. While it was thought that some twist in the specimen might be noted due to the difference in stiffness

between the top and bottom strands, no significant differences were observed between the DS and SS load schemes.

Some differences were noted, however, in the buckling behavior of SP2 for tests utilizing 0.5-inch (05PT) and 0.6-inch (06PT) strands. In the initial application of PT for all combined load tests, significant stiffness loss was noted. This represented a trend consistent with the other concentric PT tests performed on the specimen. As in the PT tests, the displacement did not increase enough to observe any stiffening behavior due to strand engagement. Once the external load was applied, however, an apparent increase in stiffness was noted. The stiffening curve was not visible in real-time in any plots for 0.5-inch strands; rather, the slope of the external-load portion of the load-curvature plot was greater than the PT-load portion, indicating an increase in stiffness. The specimen then quickly lost stiffness until loading was stopped for buckling risk. A typical load-curvature plot for a combined load test with 0.5-inch strands for SP2 is given in Figure 5-24.

When 0.6-inch strands were used, the behavior was somewhat different. In these tests, some initial buckling under PT loads was again evident but seemed less severe than in the 0.5-inch strands. After the application of external load, some stiffening was noted at the point of strand engagement. In contrast to the tests with 0.5-inch strands, the stiffening behavior could actually be noted in the external-load portion of the load-curvature plot. A typical load-curvature plot for a combined load test with 0.6-inch strands for SP2 is given in Figure 5-25. Again, softening behavior was noted as the external load was increased; the tests were stopped when the risk of buckling became too great.

The apparent difference between the stiffening observed in “real-time” in the 06PT combined tests and the “implied” stiffening in the 05PT combined tests may have been somewhat artificial. The resolution of the stiffening slope is highly dependent on the number of data points; this is directly related to the frequency of the VWG scans. It is possible that the scan frequency was simply not high enough to note the stiffening behavior in the 05PT tests. There are, however, some other apparent differences between the two tests.

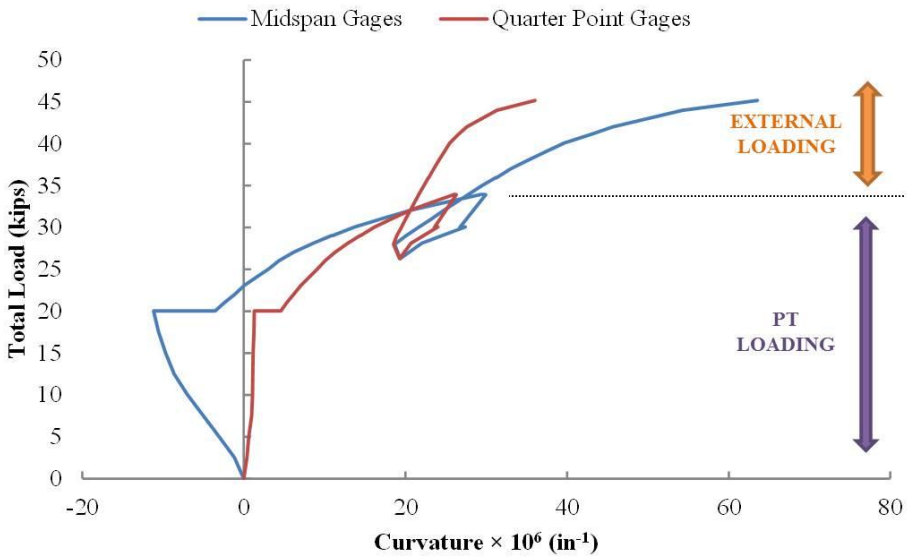

Figure 5-24: Load vs. Lateral Curvature for a Combined Load Test with 0.5-Inch Diameter Strands (SP2-05PT25-EX-2-DS)

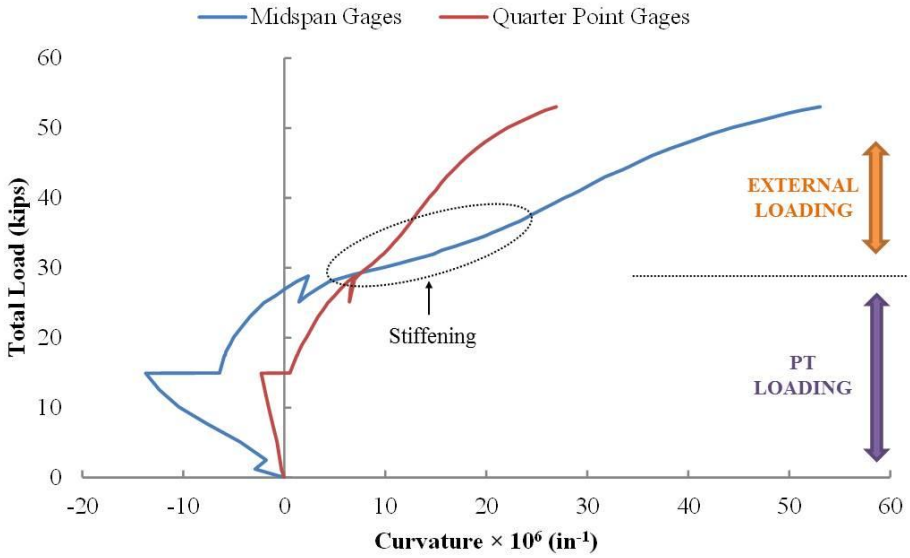

Figure 5-25: Load vs. Lateral Curvature for a Combined Load Test with 0.6-Inch Diameter Strands (SP2-06PT25-EX-1-DS)

It should be noted that some of the immediate change in stiffness (particularly evident in Figure 5-24) after the transition between load types could be contributed to

increased system stiffness. As previously discussed, additional end fixity may result from the external load components. However, the effects of strand engagement are clearly evident in the gradual increase in slope in the load-curvature behavior. The 0.5-inch strands seem to impart less stiffness to the system than do the 0.6-inch strands. This is to be expected, but is worth noting. The majority of 05PT combined tests were stopped due to buckling concerns at loads below 47 kips (very close to the observed elastic buckling capacity of 48.5 kips). However, the majority of 06PT combined tests progressed to loads in excess of 55 kips. The differences in structural behavior between combined load tests of each strand diameter illustrated the strand engagement effects due to the relative stiffnesses of each strand size.

This data also appears to indicate that there is a difference in structural response and the effects of strand engagement under external load as compared to post-tensioning. This relationship is discussed in more detail in Chapter 6.

It should be noted that no combined load tests were taken to failure. In SP1, the only combined test was run after failure had occurred, and in SP2, all tests were run prior to the application of pure external load. The preservation of SP2 in its uncracked state was deemed important, so all tests were stopped when the risk of cracking reached a predetermined critical level, or when the risk of buckling was high. It seems likely that, had the external load been increased until failure, a sudden buckling event could have occurred. However, the tensioned strand likely would have arrested the lateral motion before it increased without bound. It would be beneficial to allow a combined load test on a future specimen to progress to failure, in an attempt to monitor the effects of strand engagement on structural stability at critical buckling loads.

Again, the data obtained from the VWGs was in excellent agreement with the observed structural behavior. The majority of the external loads on the arches during construction will be the loads from self-weight and the loads from the floor beams. The tests with the VWGs have efficiently and reliably reported structural behavior under a variety of load conditions and parameters. This significantly enhances the confidence

with which the gages can be used to assess the conditions in the arches during construction.

5.5 SUMMARY

A summary of experimental findings was provided in this chapter. The laboratory program sought to establish the reliability of the vibrating wire gages and associated instrumentation as related to specific structural parameters. In addition, the stability of slender post-tensioned elements was investigated. The primary motivations for the stability study were briefly outlined.

An extensive review of the material and structural parameters measured by the vibrating wire gages was presented. The raw strain data from the gages was used to infer curvature, stresses, and axial load. The methods of using the strain data to determine these parameters were discussed here. In general, the strain and curvature data from the vibrating wire gages was very useful in identifying trends in structural behavior. The data also provide a reasonably accurate measure of axial load, although some errors were noted. The accuracy of the stresses inferred from the gages was highly variable, but this was thought to be due to overly simplifying assumptions in calculation and not to gage inconsistencies.

A key component of the stability study was the identification of buckling or the onset of structural instability. An impending buckling event was predicted through the qualitative monitoring of the changes in stiffness and curvature, the estimation of the deflected shape, and the quantitative prediction of the critical buckling load using the Southwell plot. These techniques were explained in detail in this chapter. Several observations regarding stability trends were made.

General results were presented in this chapter, along with data deemed representative of the tests. A more comprehensive presentation of data from each test is provided in the appendix. Initial observations were made in the chapter, but more complete analysis of these results and associated recommendations are presented in Chapter 6.

CHAPTER 6
Analysis and Conclusions

6.1 INTRODUCTION

This chapter provides final analysis on the test results detailed in the previous chapter. The performance of the vibrating wire gages in the laboratory program is summarized, and conclusions are presented regarding the gages' strengths and limitations in field applications. While no additional data is presented, further analysis is provided through plots of representative results. As previously noted, comprehensive plots of all load tests are included in the appendix of this document.

6.2 GAGE PERFORMANCE

The fundamental motivation for the experimental program was the determination of the capabilities, limitations, and reliability of the vibrating wire gages. The techniques of converting the raw strain data to curvature, stress, and axial load values were discussed and presented with representative results in Chapter 5. Final conclusions regarding gage performance in reporting these structural behavior parameters are provided in this section.

6.2.1 Gage Accuracy and Precision

The data from the vibrating wire gages (VWGs) were used to infer several key structural behavior parameters. Representative plots for each parameter were presented in Chapter 5. A brief discussion of the VWGs' performance in reporting each parameter follows. A summary of potential sources of error is provided at the end of this section.

6.2.1.1 Strain

The VWGs report strain data in microstrains; this data was used to generate each of the plots discussed previously. As discussed in Chapter 2, VWGs have been

demonstrated in the past to report strain values with high resolution. Strain increases in the laboratory were easily observed in all gages under the application of only a few hundred pounds of axial load. The gages also demonstrated an excellent capacity to report strain trends consistent with those expected from the observed structural behavior. The strain resolution of the VWGs was shown to be fully adequate in reporting both strain values and trends for the purposes of the arch construction and implementation.

6.2.1.2 Curvature

Horizontal and vertical curvatures were calculated as the ratio of the strain differential between two gages to the distance between those gages. In general, the curvatures calculated from the VWG data displayed excellent trends consistent with the observed structural response. As discussed in Chapters 4 and 5, the trends were highly effective in identifying the onset of buckling in the loaded specimens.

It should be noted that the curvatures were highly sensitive to the gage locations in the test specimens. As the specimens were very small, slight errors in estimating the as-built locations of the gages would result in significant errors in the curvature estimation. In the much larger arch sections, the curvature estimations will be significantly less sensitive to these errors. In general, the derivation of curvature from the VWG strain data was found to be a highly effective method of monitoring structural response under axial loading. The excellent sensitivity of the gages to small changes in strain under axial load ensures that the gages will serve as an effective means to measure curvature in the arches. This will be critical in the monitoring of member stability during the post-tensioning and arch rotation operations.

6.2.1.3 Stress Estimation

The strain values from the VWGs were used to estimate the stresses in the section. In addition to being compared to theoretical or calculated stresses, these values were used to inform the research team of the risk of cracking in the loaded specimen. As discussed in Chapter 5, there were some errors in the stress estimates from the VWGs

when compared to the theoretical values. The correlation was generally good for some gages, but significant errors were noted in the other gages.

Gages 3 and 4, offset relative to the strong axis (located along the week axis) of the section, were found to produce consistently poor stress estimates. These errors were likely due to the calculation of the theoretical stresses. The theoretical stresses were calculated as an interaction of axial compression and biaxial bending; plane sections were assumed to remain plane. However, the equations used in this calculation may not have fully represented the state of stress in the section. The plastic ducts represent significant negative areas in the section (accounting for roughly 20% of the gross area). As noted in Chapter 3, Gages 3 and 4 were mounted directly to the surface of the ducts. The localized stresses around the ducts may have been highly complex and not analogous to the general state of stress in the section. A more complex analysis would be required to better calculate the theoretical stress values. Because the ducts in the arch sections will represent a much smaller percentage of the total area, the impact on the accuracy of the VWGs will be much smaller than in the test specimen.

In addition to the simplification of the assumed stresses, some errors may have been introduced from the assumed loading conditions. While the loads in each strand were known from the load cells, the load was transferred to the section through the prestress chair and endplate. Thus, the distribution of stresses over the depth of the section is difficult to define. Gages 1 and 2 are located on the neutral axis for vertical bending and thus were unaffected by the vertical bending stress assumptions. Because the stresses due to horizontal bending are much less complex, the calculated stress estimates for Gages 1 and 2 are much more consistent with the measured values. Gages 3 and 4 are directly related to the vertical bending stresses, and thus might be much less consistent with the calculated values.

It was noted in Chapter 5 that the correlation significantly weakens for Gages 1 and 2 when strand engagement is noted (e.g., in eccentric tests). This too can be explained through the complex state of stress that is thought to develop when the strand engages with the duct wall. Most importantly, the strand engagement provides a type of

bracing to the specimen at midspan. As such, the assumed interaction of bending and compression would not be valid, and the accuracy of the stress estimates should deteriorate. Similarly, the transfer of force between the tendon and specimen is complex, and certainly affects the validity of the relationships used to calculate the theoretical stresses.

In short, the theoretical stresses were found to be generally consistent with the measured values only when the loading was well-defined and easily understood. As soon as the load paths and specimen fixities became more complex, the correlation deteriorated rapidly. No corresponding changes were noted in the load-strain plots, meaning that the measured stresses were not affected to the same extent. (Again, the measured stress values were found as the product of concrete strain and modulus.) This can be taken to indicate that the errors were related to an insufficient or overly simplistic theoretical framework. The actual material modulus will also vary compared to the empirical modulus equation that was used for much of the data. Extensive testing of the concrete mix that is to be used for the arch is currently underway. The material is being tested for modulus on days 1, 2, 3, 4, 5, 7, 10, 14, 21, 24, 28, 32, 35, 42, 49, and 56 so that a relationship between the modulus as a function of time can be developed. The modulus will be used during stressing, transportation, and other stages of construction will be based upon the time dependent expression to improve the accuracy of the stress estimates in the field.

Based upon the results from the laboratory tests, the VWGs should be highly effective in monitoring stresses in the arches. The stress estimates from the VWGs are thought to be accurate, with the discrepancies arising from errors in assumptions and scale factors on the test specimen. The strain data from the gages was found to be highly reliable and consistent with the observed behavior. While the calculation of theoretical stresses is highly dependent on the assumed behavior, derivation of measured stress as the product of measured strain and the elastic modulus is always valid. The ductwork in the arch will represent a much smaller area of the section and the VWGs will not be mounted near the ducts. As such, the local stress effects will be less significant. In

addition, as outlined above, cylinder tests are being performed for a test batch of the concrete mix selected for the arches, in order to determine the modulus of elasticity as a function of concrete age. This will provide a reasonable estimate of the actual modulus, enhancing the accuracy of the stress calculations.

6.2.1.4 Axial Load Estimation

Axial load was also calculated from the strain data at each of the gage sections (midspan and quarter point). The technique for deriving the axial load from the strain data was introduced in Chapter 5. As noted there, the axial load estimates were found to generally be consistent with the load cell data for both specimens.

The maximum error for midspan gages in all tests was 12.9 percent, with the majority of tests being well below ten-percent error. Table 6-1 summarizes the accuracy of the load estimates for each specimen. This data was presented in Chapter 5, but is repeated here for the reader's convenience.

Table 6-1: Comparison of Axial Load Estimates in Pre-failure PT Tests

(i) Axial Load Estimation - PRE-FAILURE PT TESTS (SP1 and SP2)					
Quarter Point Gages			**Midspan Gages**		
Max Estimation Error	No. of Tests	% of Tests	Max Estimation Error	No. of Tests	% of Tests
> 10%	32	74.4%	> 10%	5	11.6%
7-10%	6	14.0%	7-10%	12	27.9%
5-7%	2	4.7%	5-7%	15	34.9%
0-5%	3	7.0%	0-5%	11	25.6%
Maximum Error = 15.5%			**Maximum Error = 12.6%**		

(ii) Axial Load Estimation - PRE-FAILURE PT TESTS (SP1 only)					
Quarter Point Gages			**Midspan Gages**		
Max Estimation Error	No. of Tests	% of Tests	Max Estimation Error	No. of Tests	% of Tests
> 10%	10	47.6%	> 10%	0	0.0%
7-10%	6	28.6%	7-10%	8	38.1%
5-7%	2	9.5%	5-7%	9	42.9%
0-5%	3	14.3%	0-5%	4	19.0%
Maximum Error = 13.1%			**Maximum Error = 9.8%**		

(iii) Axial Load Estimation - PRE-FAILURE PT TESTS (SP2 only)					
Quarter Point Gages			**Midspan Gages**		
Max Estimation Error	No. of Tests	% of Tests	Max Estimation Error	No. of Tests	% of Tests
> 10%	22	100.0%	> 10%	5	22.7%
7-10%	0	0.0%	7-10%	4	18.2%
5-7%	0	0.0%	5-7%	6	27.3%
0-5%	0	0.0%	0-5%	7	31.8%
Maximum Error = 15.5%			**Maximum Error = 12.6%**		

As discussed in Chapter 5, differences up to 15.5 percent were noted between the axial load estimates from the quarter point gages and the load cell data. The larger error at the quarter point locations was thought to be due to a number of factors. Most importantly, the difference between the measured and calculated load could have been due to material inconsistencies. In each specimen, a single modulus of elasticity was assumed for the entire specimen. However, it is certainly likely that the modulus had some variability over the length of the specimen. As such, it could have been slightly

different at the quarter point section from the midspan section. This difference could have resulted from concrete variability during casting or from minor cracking during specimen transport and testing. Even moderate differences in elastic modulus could have significantly affected the accuracy of the axial load estimates. This may have contributed to the steady increase in error in the quarter point gages (Figure 6-1).

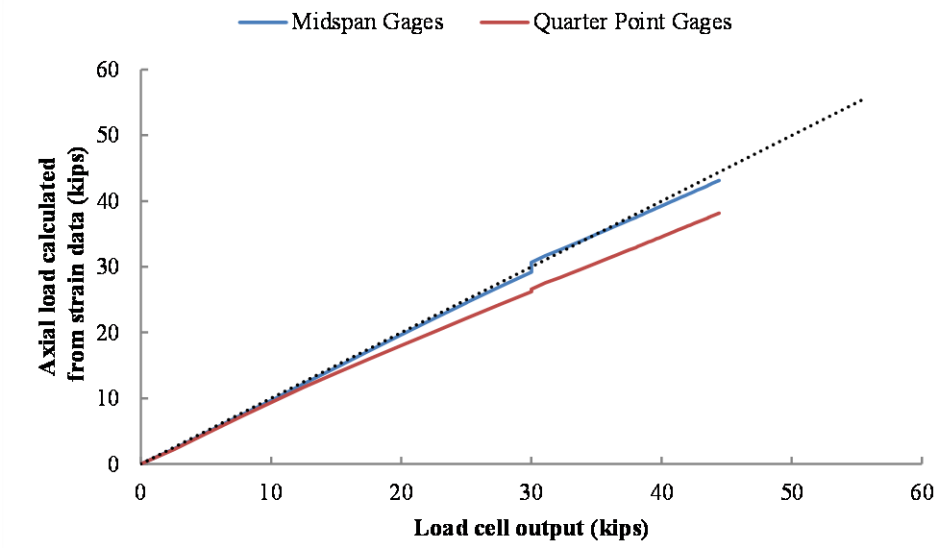

Figure 6-1: Axial Load Estimation for Concentric PT Test SP2-06PT-10-CON

While expected to be less significant, several other factors could have contributed to the errors in axial load estimation. Figure 6-2 shows a top view of the specimen as it deflects under axial load. The deflected shape is assumed to be sinusoidal. Because of the free space in the duct, the strand remains straight, prior to engaging the duct wall. The post-tensioning load applied to the strand is captured by the load cell at the end face of the specimen. However, because the strand remains straight in the duct while the curvature of the member increases, the axial component of the load decreases. The difference between the load in the strand and the axial load in the member results in a shear component in the section.

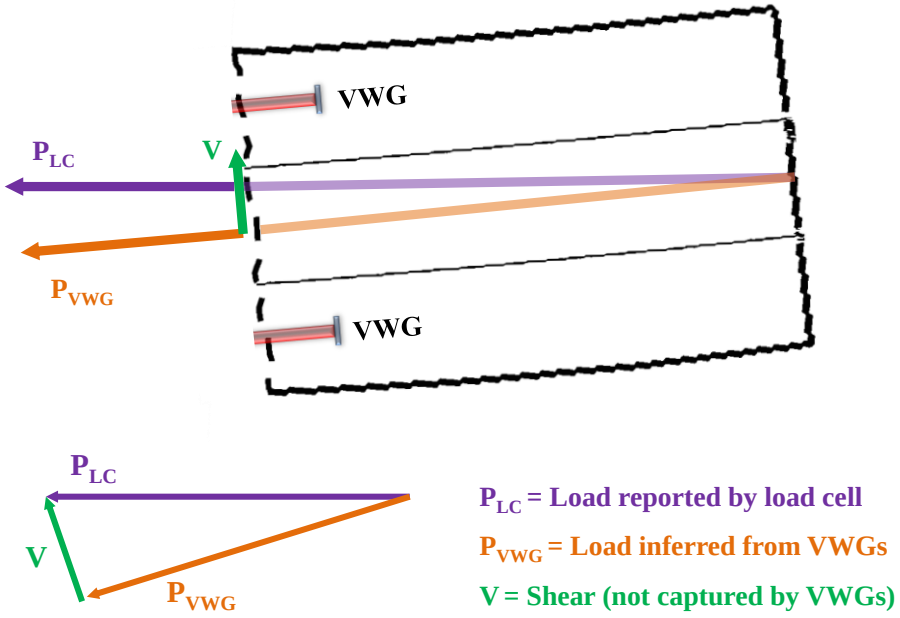

Figure 6-2: Drift in Axial Load Estimation Due to Shear at Quarter Point

The VWGs are oriented along the longitudinal axis of the member, and thus report only the axial load component parallel to their orientation. The magnitude of this component, as illustrated in Figure 6-2, is less than that of the total strand force. As such, the gages report an axial load lower than what is reported by the load cell. As the load on the strand increases, so too does the curvature in the specimen. This in turn increases the shear in the section. This could have contributed to the steady escalation of the discrepancy between the VWGs' load estimate and the load cell data (Figure 6-1). As the angle of rotation about the vertical axis at the midspan is theoretically zero for a half-sinusoidal deflected shape, no shear component exists there. As such, the midspan gages are virtually unaffected by this same source of error. While the shear component was expected to have been very small, it may have introduced small additional errors in measurement of the axial load.

While the axial load estimates for the midspan gages were found to be very consistent with the load cell data, some small errors were noted. Of course, this too was likely due to errors in estimation of the elastic modulus of the concrete or to slight errors

in estimating the net cross-sectional area. A second possible source of error for the midspan gages is presented in Figure 6-3. As the specimen deflects into the half-sinusoidal shape, the strand remains straight inside the duct. However, the load cell may exhibit a tendency to rotate slightly with the end face of the member. This differential rotation between the load cell and the strand chuck creates a non-uniform loading on the load cell. The graphic in Figure 6-3 greatly exaggerates the magnitude of the rotation, but illustrates how the non-uniformity in loading can develop. The effects of this differential rotation were also expected to be small in magnitude. Consideration of this behavior, however, is important in the rationalization of the sources of error in the axial load estimates.

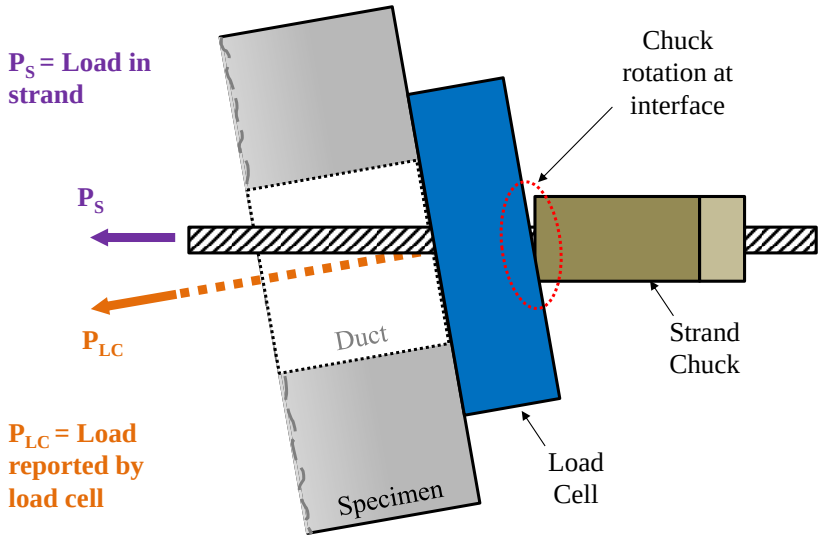

Figure 6-3: Error in Axial Load Estimation Due to Differential End Rotations

Additional errors in the axial load estimates may have been related to the test sequence. As mentioned in Chapter 5, it was thought that the observed jump in the axial load estimates at midspan could have been due to the sudden elimination of the axial load component taken as friction in the supports. This seems reasonable, but is difficult to verify quantitatively.

In short, while some errors were noted, strain data from the VWGs in each specimen were used to estimate axial load with reasonable accuracy and reliability. As with each of the structural parameters monitored by the VWGs in this study, errors in the test setup or specimens are amplified tremendously by the small size of the specimens and the limited load range. It is important to note that the maximum errors in midspan load estimates were generally on the order of a few kips. While slightly more significant for the small test specimen loads, this value is essentially negligible in comparison to the loads proposed for the arch sections.

While it is indeed possible that minor errors may arise with a number of the gages in the field, it is highly unlikely that they will be as significant over the much larger load range and in the much larger specimens. Several arch sections, including the midspan of both the rib and the tie, will be instrumented. This redundancy will allow for the careful comparison of the loads at each section. A key function of this monitoring of the axial load at discrete sections will be to identify any losses in PT force due to friction. It might seem that the errors encountered in the laboratory tests might compromise this ability. However, the errors discussed here should be largely negligible compared to the magnitude of any significant prestress losses. Similarly, the magnitude of the errors in axial load estimation will not be sufficient to significantly compromise the research team's ability to effectively monitor structural stability trends.

Given the excellent results of the experimental program and the proposed instrumentation protocol, it can be expected that the gages will provide a reliable means to monitor axial load. The resulting load-curvature trends will provide a means to monitor member stability.

6.2.2 Gage Consistency and Durability

While the accuracy of the gages is of critical importance, the significance of gage durability and consistency cannot be overlooked. The gages will be used in the field over the course of several months and a variety of loadings. It is important that the gages not only be consistent with one another, but also report values consistent between distinct

loading cycles. Similarly, it is crucial that the gages have sufficient durability characteristics, so as not to be critically damaged during placement, casting, or loading.

As discussed above, the VWGs were found to deliver reasonable results over the course of the experimental program. In addition to the noted accuracy in measurement, the gages were found to be consistent with each other. For instance, the readings of a single gage were never found to be unreasonably different from the readings of the other five gages in either specimen. Similarly, the values reported by each gage were reasonably consistent among the more than sixty load tests performed. As noted in Chapter 2, VWGs have an excellent history of reliability for long-term monitoring. Nothing in the results of this study has been shown to contradict those conclusions.

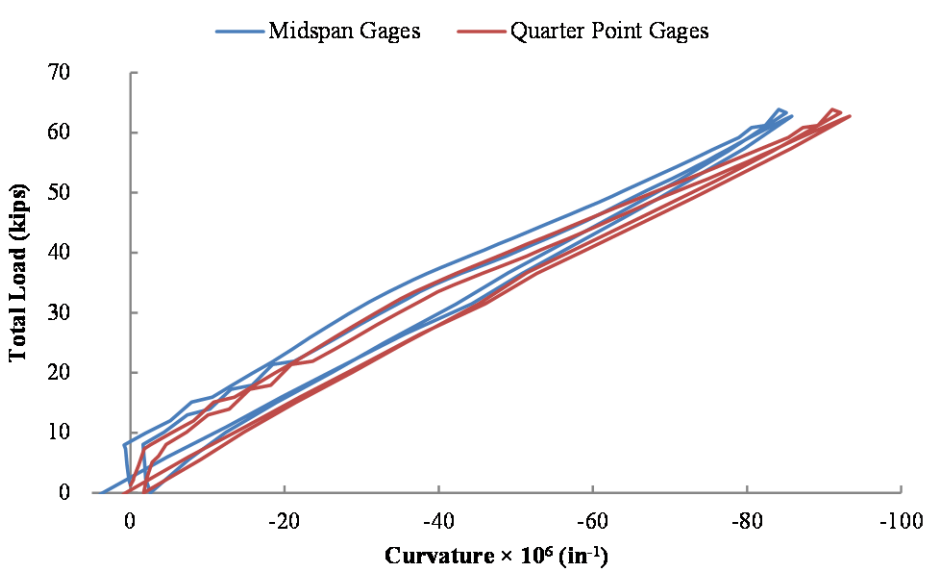

Figure 6-4: Gage Consistency in Load vs. Lateral Curvature Plots for an Eccentric PT Test (SP1-05PT-16-ECC-W)

It can be seen from a perusal of the experimental results presented here and in the appendix that the results of similar tests are not always numerically equivalent. For instance, there exists a fair range in the maximum curvature achieved in concentric PT tests for the same specimen. Again, this is not thought to be due to gage inconsistencies,

but to incidental changes in the end fixity of the specimen. This theory is supported by the range of maximum deflections reported by the linear potentiometers, in excellent agreement with the range of curvature**s.** Figure 6-4 presents an eccentric PT test in SP1 in which the PT load was immediately reapplied upon removal. Because the end fixities were not changed, the results between loading cycles were highly consistent.

The durability of the gages is also notable. Over the course of the experimental program, the VWGs were subjected to significant axial and bending stresses, including sudden stability failures. Despite the various loadings, the data reported from the gages were found to be generally consistent throughout the testing regimen.

6.2.3 Gage Limitations

While they have been demonstrated to be generally accurate and highly reliable, the gages are not without their limitations. It is evident from the preceding discussion that some test results were relatively accurate; however, there were errors in some gage readings when compared to the theoretical solutions. It is important to note that this is not thought to be due to compromised gage performance, but to the variables in the experiments. The transfer of axial load from the strands to the section and the complexities this introduced has already been discussed at length. Other sources of error may have been related to the specific configuration of components for each loading scheme.

One common source of uncertainty that could have affected any of the measured parameters is the lack of consistent definition in the end conditions of the specimen. While consistency was sought in maintaining the relative fixity of each end for all tests, this was very difficult to achieve. Incidental changes in end fixity and load alignment may have resulted from slight shifts in the specimen during loading or unloading, or while reconfiguring the test setup between post-tensioned and external loadings. Similarly, complete elimination of friction between the specimen and supports, as well as in the thrust bearings themselves, was impossible. While every attempt was made to eliminate these sources of uncertainty, the results were certainly affected to some degree.

As such, what appear as inconsistencies or errors in the VWG readings are likely inconsistencies in the test setup, and should not compromise the researchers' confidence in the capabilities of the VWGs.

In addition to the limitations of the gages themselves, the data acquisition system has an important limitation in its configuration that is important for the field studies. Because each gage is mechanically read, VWGs have a relatively low scan rate. An individual gage can require two to five seconds of scan time; each data logger will be connected to a maximum of sixteen gages. As such, it is not unreasonable to expect a total duration of roughly two minutes for each scan of the gages in an arch. While the rotation of arch is expected to take hours, it is important to note that proper stress monitoring requires adequate budgeting of time for data collection.

6.2.4 Summary of Gage Performance

The gages were found to deliver reasonable accuracy and consistency in measuring strain, stress, curvature, and axial load. The resolution of the gages was excellent, generating useful, noise-free data even at low axial loads. Some inconsistencies between measured and theoretical values were noted in both axial load and stress estimates. These errors were believed to be due to errors in assumption and not to gage inaccuracies.

In addition to the measurement of individual structural parameters, the VWGs were demonstrated to be an excellent means of reporting structural trends. Both the load-strain and load-curvature curves were highly consistent with the observed behavior. The load-curvature plots also were highly effective in the indication of impending buckling through the stiffening and softening behavior indicated by the gages. This capacity of the VWGs will be important in monitoring member stability in the arches.

In general, the results of the experimental study have shown VWGs to be sufficiently precise, accurate, and consistent for the proposed instrumentation program. The accuracy and reliability in both measured parameters and behavioral trends represent the gages' excellent capacity for monitoring the arch construction operations.

6.3 BUCKLING CAPACITY FACTORS

A secondary focus of the experimental program was the study of the lateral stability of slender concrete members with unbonded post-tensioning. The techniques of using the load-deflection and load-curvature trends in conjunction with Southwell plots were provided with representative results and discussed in Chapter 5. Final conclusions regarding the factors that were observed to affect the buckling capacity of the members are presented in this section.

6.3.1 Lateral Restraint Factors

Significant variations were observed in the buckling capacity of both specimens under the load cases consisting of post-tensioning (PT) and combined (PT and external) loading schemes. In many cases, clear increases in the apparent buckling capacity were noted during the test through stiffening action. These stiffening effects are thought to be due to two closely-related factors involving the contact of the tensioned strand with the duct wall. Each of these factors and its related effects are discussed below.

6.3.1.1 Strand Engagement Effects

Strand engagement has been defined throughout this thesis to describe the action that occurs when the axially-loaded specimen deflects enough that the duct wall is brought into contact with the tensioned strand. This was observed throughout the testing to result in significant stiffening action that served to increase the buckling capacity of the member. This effect is illustrated in the following series of figures depicting clear stiffening action observed in a PT load test on the first specimen (SP1). In this test, 0.6-inch strands were used in a concentric configuration. Figure 6-5 depicts the load-curvature behavior of the test; clear stiffening is noted as the strands engage. The curve is divided into load increments, defined as series I-VI. A Southwell plot is constructed for the loading cycle and is shown in Figure 6-6. The same load series apply to the Southwell plot. The Southwell plot parameters are defined in Table 6-2.

It can be noted that the buckling capacity indicated by the Southwell plot is in good agreement with the behavior demonstrated in the load-curvature data. The slope of the load-curvature (and load-deflection) plot increases as the stiffening action occurs. This indicates that the buckling capacity of the column increases as the strand engages and imparts stiffness. This is clearly evident in the Southwell plot, where the predicted buckling capacity of the member is equal to the inverse of the slope of the Southwell plot. The values in Table 6-2 indicate a rapid increase in the buckling capacity.

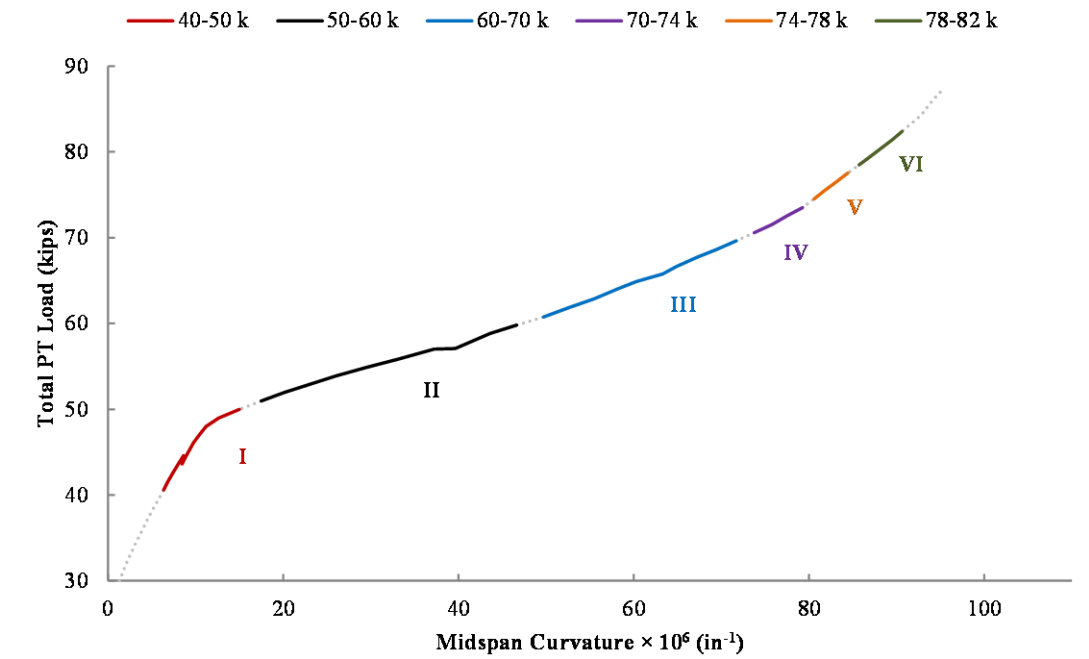

Figure 6-5: Load-Curvature Plot for PT Test Exhibiting Stiffening (SP1-05PT-2-CON)

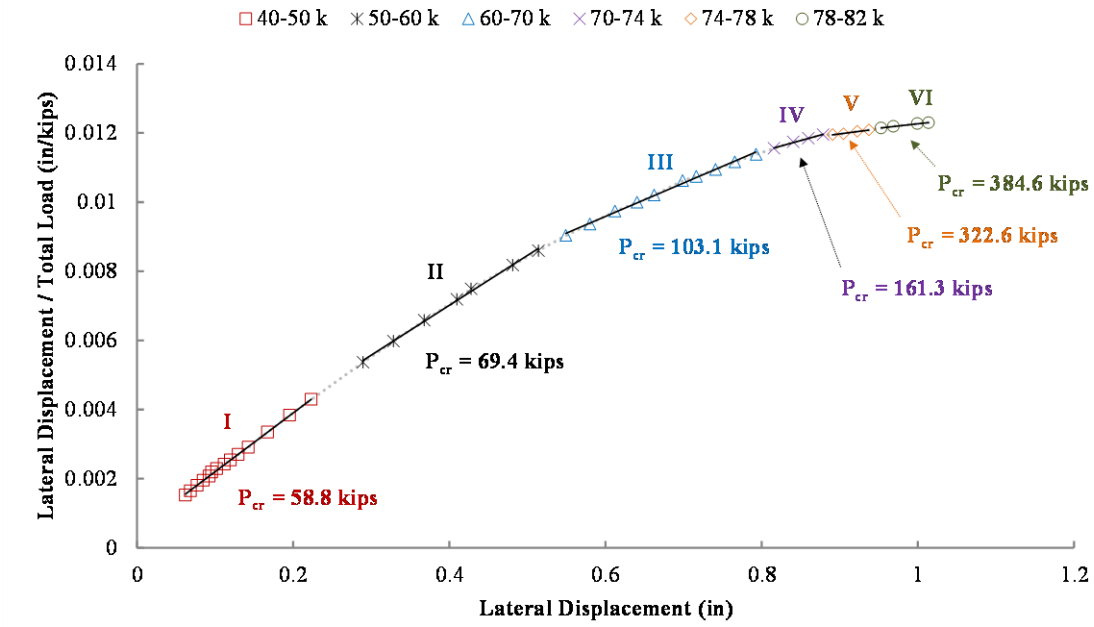

Figure 6-6: Southwell Plot for PT Test Exhibiting Stiffening (SP1-05PT-2-CON)

Table 6-2: Southwell Plot Parameters for SP1-05PT-2-CON

Series	Load Increment (k)	Slope	Y-Intercept	R^2 value	Buckling Load P_{cr} (k)	Initial Imperfection (in)
I	40-50	0.017	0.0005	0.9990	**58.8**	0.029
II	50-60	0.0144	0.0013	0.9982	**69.4**	0.090
III	60-70	0.0097	0.0038	0.9966	**103.1**	0.392
IV	70-78	0.0062	0.0065	0.9913	**161.3**	1.048
V	74-78	0.0031	0.0092	0.9912	**322.6**	2.968
VI	78-82	0.0026	0.0097	0.9930	**384.6**	3.731

It is important to note that the predicted buckling capacity for each phase is not necessarily the load at which the specimen would buckle. The validity of the Southwell plot prediction is compromised when broken into series as this. For tests exhibiting stiffening behavior, the initial assumptions of the Southwell plot are violated. The stiffening action essentially provides a bracing mechanism that changes the assumed shape, so the original theory does not hold. Similarly, the calculated initial deflections are shown to become large; this too is inconsistent with Southwell's theory. Therefore, the Southwell plot overestimates the buckling load for these cases, and the values shown should not be taken as the actual capacity of the system. The plot does, however, give a valuable illustration of the increased capacity provided through strand engagement.

The additional capacity afforded the member through strand engagement effects is clearly evident for PT loads. This appears to be consistent with the findings of Magnel (1954) and Wilby (1963), both of whom observed significant gains in capacity due the interaction of the PT bar with the duct wall. Magnel suggested that for $(n - 1)$ discrete points of contact between the strand and the duct, the buckling capacity of the member should increase by a factor of n^2. The tests in this study were not designed to be capable of identifying the specific engagement characteristics such as the total engaged strand length or the number of points of contact. As such, the estimate of n^2 could not be verified, but is not contradicted. As discussed in Chapter 5, the total length of contact between the strand and duct wall appeared to have a significant effect on the extent of the stiffening action.

While buckling was never noted in PT tests where strand engagement was evident, the results were different for the combined load tests. Buckling behavior under external load was noted after evidence of strand engagement and associated stiffening. This effect is illustrated in the following series of figures depicting a combined load test on the second specimen (SP2). In the test (SP2-06PT25-EX-6-DS), 25 kips of PT load were applied to the strands before external load was applied. Some softening was noted under PT loads, as was typical for SP2. Figure 6-7 depicts the load-curvature plot for the test. The external loading portion of the curve is divided into load increments, defined as series I-III. In Figure 6-7, Series I represents some continued softening under the initial external load, Series II indicates stiffening during strand engagement, and Series III represents final softening behavior under external loads.

A Southwell plot is constructed for the loading cycle and is shown in Figure 6-8. The same load series apply to the Southwell plot. The Southwell plot parameters are defined in Table 6-3. Again, it should be noted that the Southwell plot predictions are invalid for this test, as the assumed conditions for Southwell plot construction are violated. Nonetheless, the plots again provide an excellent representation of the effects on buckling capacity of the observed stiffening and softening action.

Inspection of the plots for this test yields a number of interesting observations. It is apparent that, while some additional stiffness is clearly imparted to the system due to strand engagement, the effect is not boundless in this loading scheme. Similarly, the stability behavior of the member is very different for pure post-tensioning and for external loads applied after post-tensioning. In short, the buckling behavior of slender post-tensioned members under external loads appears to be significantly different from the capacity during the post-tensioning operations.

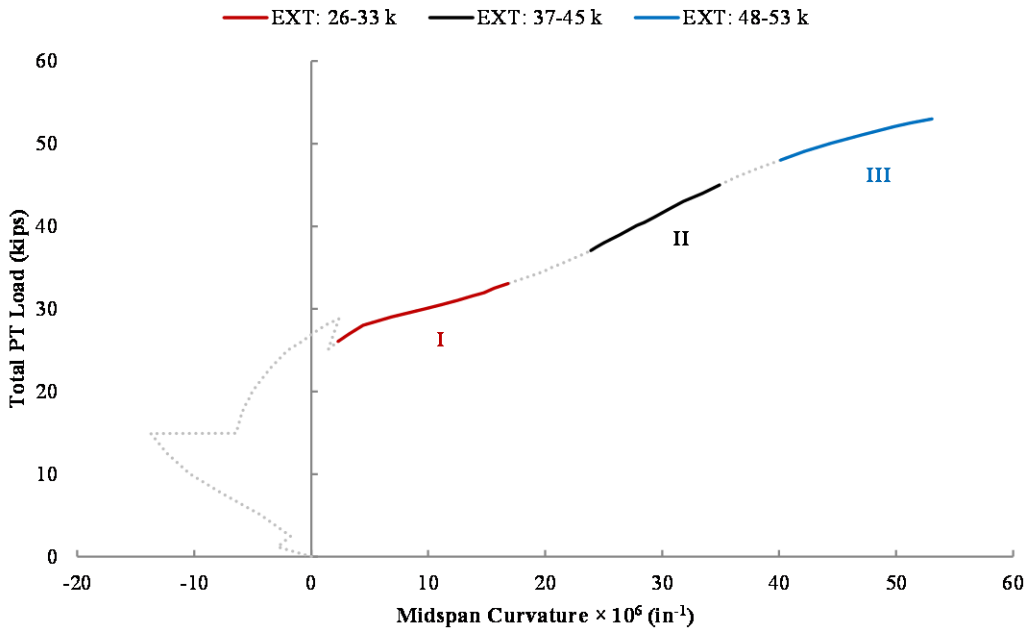

Figure 6-7: Load-Curvature Plot for Combined Test Exhibiting Stiffening and Softening (SP2-06PT25-EX-6-DS)

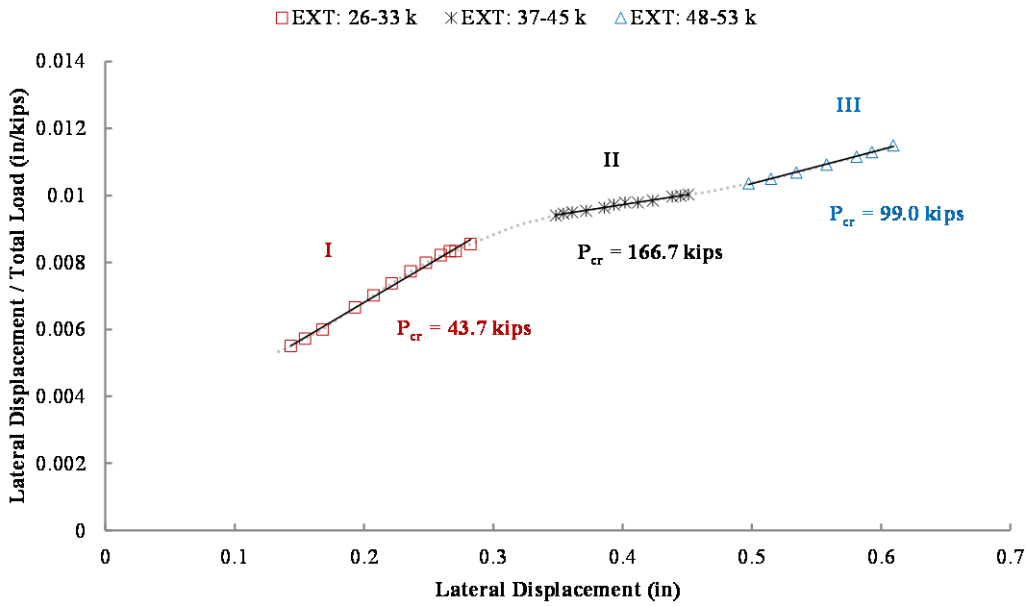

Figure 6-8: Southwell Plot for Combined Test Exhibiting Stiffening and Softening (SP2-06PT25-EX-6-DS)

Table 6-3: Southwell Plot Parameters for SP2-06PT25-EX-6-DS

Series	Load Increment (k)	Slope	Y-Intercept	R^2 value	Buckling Load P_{cr} (k)	Initial Imperfection (in)
I	EXT: 26-33	0.0229	0.0022	0.9951	**43.7**	0.096
II	EXT: 37-45	0.006	0.0071	0.9904	**166.7**	1.183
III	EXT: 48-53	0.0101	0.0053	0.9968	**99.0**	0.525

These observations are intuitive. Under post-tensioning, the tension applied to the tendon steadily increases. As suggested by Bažant (2010), some buckling deflections can occur due to the reactions at the tendon anchorages. However, as the strand engages with the duct wall, these deflections will be controlled. As the tension continues to increase in the strand, so too will the stiffness in the system. As long as the capacity of the strands is not reached, it appears as though buckling will not occur under post-tensioning. Of course, this assumes an ideal system with significant strand engagement. The laboratory tests in this study have indicated the significance of duct and strand configuration on member stability.

In contrast to continuous post-tensioning, the combined load tests applied an external load to a member previously post-tensioned to a given load. The data in Figure 6-7 indicate that, after some stiffening, buckling is imminent as the external load increases. In the external load stage, a compressive load is applied to the self-balanced system. The tendons are in tension, but as the compressive load increases, the member shortens. This results in a loss of tensile force in the tendon. The shortening of the concrete member is significantly less than the elongation introduced to the tendons through post-tensioning. As such, with the practical member lengths for which buckling would be a concern, the tendons will always be in tension. However, as the tension in the strands decreases, so too does the stiffening action provided through strand engagement, increasing the risk of buckling. This is observed in the buckling risk evident in SP2 in Figure 6-7. The n^2 increase in buckling capacity suggested by Magnel (1954) was based only on continuous PT loads. The research presented in this thesis indicates that the stiffening effects of strand engagement are significantly reduced under external loading.

As mentioned in Chapter 2, there has also been some interest in the effects of initial post-tensioning on the buckling capacity of slender members under external load. While not a focal point of this study, some observations can be made from the combined load tests. In SP1, a single combined load test was run after failure of the specimen. Post-failure external load tests indicated a post-failure buckling capacity of approximately 15 kips for SP1 (shown in Figure 6-9 as SP1-PT0-EX-4). In the subsequent combined load test, a total PT load of 60 kips was applied, with no noted risk of instability. The subsequent external load, however, reached a total of 16 additional kips before the test was stopped for buckling concerns. This load is in good agreement with the buckling capacity of the damaged member under pure external load. This test (SP1-06PT60-EX-1) is also shown in Figure 6-9. This exercise indicated the difference between the load types and the role of strand engagement. The PT load greatly exceeded the expected buckling capacity (indicating stiffening due to strand engagement), but provided little additional benefit under external loading. This interaction was more fully explored in SP2.

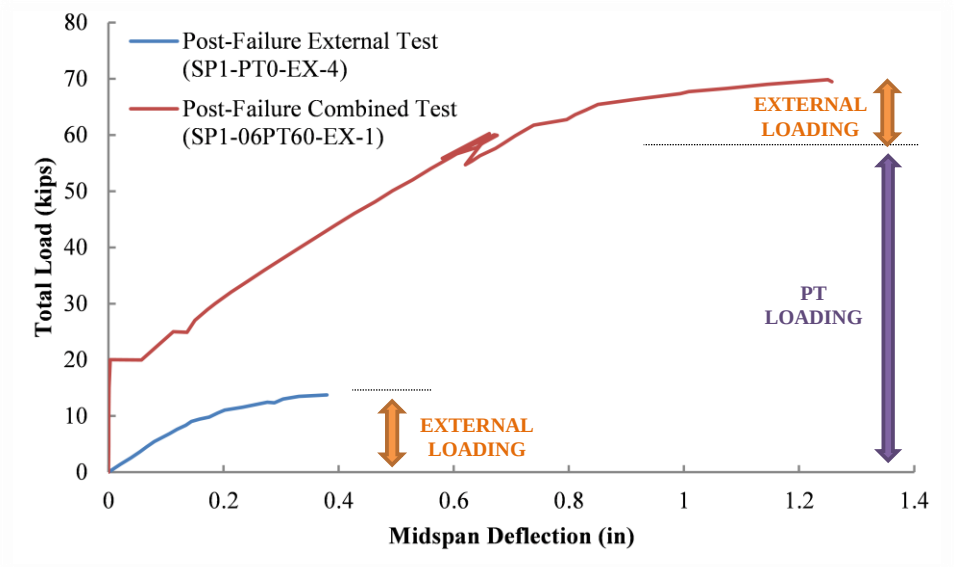

Figure 6-9: Comparison of Post-Failure Tests for SP1

In SP2, all combined load tests were performed prior to the buckling failure that produced extensive cracking. In general, the buckling capacity was only slightly increased when external loads were applied following post-tensioning. The critical buckling load was recorded as 49.5 kips in the external loading to failure. As discussed in Chapter 5, combined load tests for the 0.5-inch strand configuration were stopped before 50 kips and before 60 kips for the configuration with 0.6-inch strands. While the 0.6-inch strands clearly impart additional stiffness to the system, the overall effect on buckling capacity is small.

These observations again emphasize the importance of strand engagement on the buckling capacity of slender members. As might be expected, for members with little to no strand engagement (as in SP2), the application of PT load appears similar to the application of external load. As such, the buckling capacity appears to be the sum total of the PT and external loads, limiting the total external load that can be applied. In contrast, for members with significant strand engagement (SP1), buckling is unlikely to occur under PT loads. As such, the amount of additional external load that can be applied is much closer to the buckling capacity of the member in the absence of post-tensioning. Lin and Burns (1981) suggest that for fully-grouted tendons, the buckling capacity of the member under external loads is unaffected by the internal prestressing force. While the data is limited, the results of this study seem to support that theory. The observed strand engagement actions appear to be somewhat analogous to bonded post-tensioning, in that the buckling capacity is less affected by the level of initial PT loads.

6.3.1.2 Duct Wobble Effects

Strand engagement has been defined throughout this thesis as the interaction of the tendon and the duct wall, facilitated by the lateral displacement of the axially-loaded specimen. Strand engagement, however, can also result from initial sweep or wobble in the ducts. This was thought to be the case in SP1, where construction errors resulted in the vertical translation of the ducts during casting. As such, the strands were likely engaged from the outset of the test. As noted in Chapter 5, all PT tests in SP1 were

stopped due to the safe working load of the strands being reached; buckling was never a real concern under PT loads.

This is an observation of significant importance for the design of slender concrete elements with unbonded post-tensioning. If intentional variation in the duct profile were to be specified in design, strand engagement during post-tensioning could be ensured. This would significantly reduce the risk of instabilities during field PT operations. This technique has been used to some extent in the design of the arches; some intentional undulation in each duct profile has been specified along the length of the arch. The results of the experimental program have demonstrated that this precaution will be highly beneficial to the stability of the slender arch members during construction and placement.

6.3.2 Unrestrained Buckling

If, as in the case of the specimens used in this study, the area of the duct is large relative to the area of the tendon, buckling under post-tensioning can be a real concern. This was suggested by Benaim (2008), and has been demonstrated in the experimental program described here. While buckling in SP1 was never a concern due to strand engagement effects, each concentric PT test in SP2 was stopped for buckling concerns. Strand engagement effects have been definitively shown to significant aid in stability. However, if there is an excessive free distance through which the strand must move prior to engaging the duct wall, minimal strand engagement will occur prior to buckling. This again illustrates that unbonded post-tensioning is, in the absence of strand engagement, highly analogous to pure external loading.

In the case of this experimental program, it was noted that stiffening after softening was never noted in concentric PT tests on SP2 (as it was for several tests on SP1). Typical load versus deflection plots for concentric PT tests on each specimen are compared in Figure 6-10.

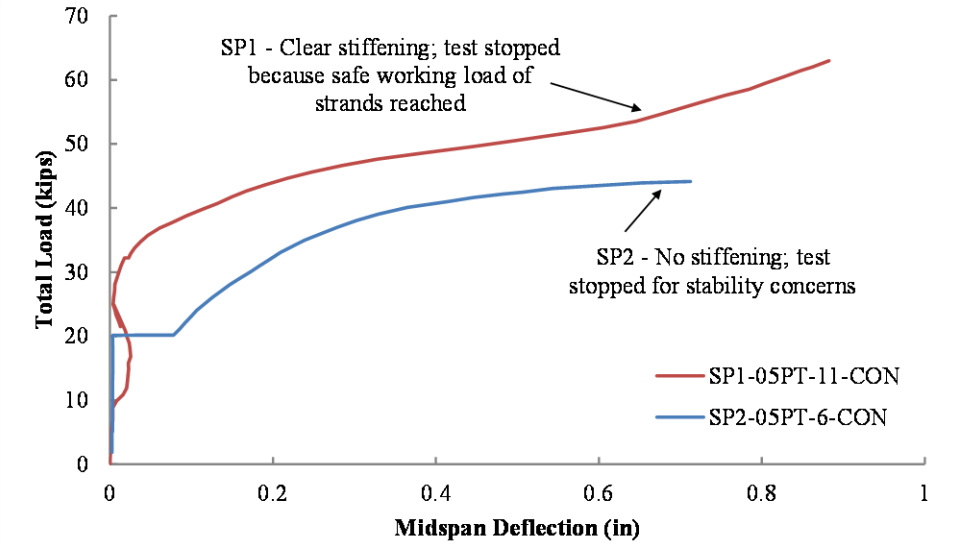

Figure 6-10: Comparison of Typical Strand Engagement Effects in SP1 and SP2

In general, the SP1 tests were stopped because the safe working load of the strands was reached. In contrast, concentric PT tests on SP2 were typically stopped because the risk of buckling was high. This again can be explained by the presence of the construction errors in SP1, in which the ducts floated upwards during casting. In SP1, the early strand engagement was not enough to prevent softening under concentric loads. This could be due either to the lack of stiffness in the strands under low loads or to the low total length of contact between the strand and duct. However, by the time buckling became a real risk, the strands were fully tensioned and the specimen had deflected enough to engage more length of the strand. As such, significant stiffness was imparted by the strands, and buckling under PT loads was not a concern. In SP2, however, large deflections were required to initiate strand engagement, meaning that the risk of buckling was very high prior to contact. As such, no additional stiffness was imparted.

It is likely that, had the specimens been allowed to buckle completely, the strands would have arrested the lateral movement. However, it is difficult to assess the amount of damage that might have occurred prior to full lateral arrest. Obviously, the induced curvature may not be acceptable in a practical application. In the interest of preserving

the specimens, the tests were not allowed to progress to this point, but future work should be conducted on the effects of sudden strand engagement.

6.4 SUMMARY

Analysis and conclusions on the results of the experimental program were provided in this chapter. The primary objectives of the study were a better understanding of gage performance and an investigation of the stability of slender post-tensioned members. Extensive discussion on the data in support of each of these objectives was provided in Chapter 5, and continues with related conclusions in this chapter.

The observed capabilities and limitations of the vibrating wire gages were presented at length. The gages were found to be generally accurate and precise both in measuring structural parameters and reporting trends in behavior. Some apparent errors were identified, but these were attributed to testing inconsistencies rather than to gage error. The gage data was also found to be highly consistent and durable, an important feature for the field monitoring operation.

Conclusions were also made on the observed stability trends for the test specimens. The effects of strand engagement were discussed at length. Strand engagement was clearly shown to increase the buckling capacity of the members. The extent of strand engagement was demonstrated to have a significant effect on the amount of additional stiffness provided. Similarly, differences in the role of strand engagement were shown for PT and external load configurations. The risk of buckling prior to strand engagement in post-tensioned elements was also discussed.

A final summary of the findings of this study, along with a schedule of future work, is presented in Chapter 7. Additional test data is included in Appendix A.

CHAPTER 7
Summary and Schedule

7.1 PROJECT SUMMARY

The work described in this thesis was conducted in support of the construction and instrumentation of a signature network arch bridge for the city of Fort Worth, TX. The twelve precast, post-tensioned arches will be cast on their sides and then rotated to the vertical orientation prior to transportation and placement. The development of critical stresses and member instability are key concerns in the arches. The fabrication and placement stages represent critical intervals in the life of the arches. As such, a research team from the University of Texas at Austin has been tasked with the instrumentation of the arches for structural monitoring during the construction operations. Vibrating wire gages (VWGs) will be installed at critical locations throughout the arches and monitored on-site using a data acquisition system.

The experimental program described in this thesis aimed to serve two primary motivations. The first was the establishment of a fundamental understanding of and confidence in the capabilities of the VWGs for field instrumentation. This confidence will greatly enhance the ability of the research team to support the construction process. The second motivation for the study was the investigation of stability behavior in slender members with unbonded post-tensioning (PT). All testing was completed at the Ferguson Structural Engineering Laboratory (FSEL) at the University of Texas at Austin.

Slender post-tensioned specimens were designed and constructed for the gage resolution and stability studies. The specimens, of rectangular cross-section with a pair of PT ducts, were loaded through PT loads, external loads, or a combination of the two. A total of three specimens were constructed; the tests results of two of the three are presented in this thesis. More than sixty individual load tests were conducted on the two specimens, representing each of the three load types. In the test setup, the specimens were supported at each end and at midspan. In most of the tests, the midspan supports were

lowered during the test once the risk of cracking in the specimen had been eliminated through PT operations.

Four VWGs were installed at midspan in each specimen, with an additional two VWGs at one of the quarter points. At midspan and the quarter point, a pair of gages was placed symmetrically about the vertical neutral axis of the section. An additional pair of gages was placed symmetrically about the horizontal neutral axis at midspan.

The raw strain data from the VWGs was used to infer stresses, axial load, and curvature at critical sections. (Horizontal curvature was monitored at both the midspan and quarter point sections; vertical curvature was also monitored at midspan.) In general, the strain and curvature data was extremely useful in identifying trends in structural behavior. The data also provide a reasonably accurate measure of axial load. Stress values inferred from the gages were highly variable. For those gages located at mid-depth of the section, the stress estimates were generally consistent with the theoretical values. However, the gages at the top and bottom of the section were found to be highly inconsistent with the calculated stresses. These errors were thought to be due to simplifying assumptions in calculation and not to gage inconsistencies. Many of the parameters that affected these errors are related to scale factors and should be significantly lessened on the larger sections of the arch.

In general, the VWGs were found to be both accurate and precise in measuring structural parameters and reporting trends in behavior, even at low loads. Some apparent errors were identified, but these were attributed to testing inconsistencies rather than to gage error. The instrumentation was also demonstrated to be highly reliable and durable, an important feature for the field monitoring operation.

A key component of the stability study was the identification of buckling or the onset of structural instability. An impending buckling event was predicted through the qualitative monitoring of the changes in stiffness and curvature, the estimation of the deflected shape, and the quantitative prediction of the critical buckling load using the Southwell plotting technique. The data collected from the VWGs was found to be highly consistent with the observed structural behavior.

The contact of the tensioned strand with the duct wall was defined as *strand engagement*. Strand engagement was typically initiated as the lateral deflection of the member increased under axial load. The effects of strand engagement were found to be highly significant in the stability behavior of slender members. Strand engagement was clearly shown to increase the buckling capacity of the members through stiffening action. The extent of strand engagement was demonstrated to have a substantial effect on the amount of additional stiffness provided. Similarly, differences in the role of strand engagement were shown for PT and external load configurations. A risk of buckling prior to strand engagement in post-tensioned elements was also demonstrated to exist.

Both the gage resolution study and the stability tests will significantly enhance the ability of the research team to support the arch construction operations. The gage study yielded an enhanced understanding of the gage capabilities. Similarly, the stability studies served to identify the behavior trends that indicate the onset of instability. Knowledge of the data reported by the gages as a member progresses toward buckling is critical for stability monitoring in the field. Based on the findings of the experimental program, the research team is confident that the gages will provide an effective means of monitoring the behavior of the arches. In addition, it is believed that the precautionary measures taken in design of the arches (e.g., intentional duct wobble) and in the fabrication, lifting, and rotation operations will aid in the minimization of instability of the arch members.

7.2 RECOMMENDATIONS AND FUTURE WORK

The results of this study have served to both enhance the understanding of the capacity of the instrumentation and to contribute to the knowledge of the behavior of slender post-tensioned members. While much has been learned, the experimental program has introduced a number of topics in which further study could be of significant value.

As previously noted, this thesis contains test results for two of the three constructed specimens. The third specimen included a pair of fabricated cracks placed

equidistant in either direction from midspan on opposite sides of the member. The same axial loading schemes will be applied to the third specimen. These tests will be valuable in investigating the influence of localized cracking on the global stability behavior of a slender member under post-tensioning.

In this testing program, the specimens were not allowed to fully buckle in any load tests involving post-tensioning. Rather, each specimen was failed under pure external load to establish a conventional buckling capacity. The effects of strand engagement in a buckling failure event could be further investigated. It is thought that, even if the strands are not engaged at the time of a sudden buckling event, the tensioned tendons could arrest the lateral deflection, limiting the damage to the specimen. Tests in which a post-tensioned specimen is buckled, either under additional PT or external loads, would be very useful in further investigated the effects of sudden strand engagement.

The specimens used in this program were limited by geometric constraints to a pair of concentrically-placed ducts. It would be of significant value to investigate similar stability behavior in specimens with different strand configurations. The stiffening effects noted in this study were thought to be due to the resistance of the tensioned strand to lateral displacement at midspan. However, it is possible that the buckling restraint could be provided by the necessary elongation of the strand from the flexural deformations associated with buckling. In theory, the energy required to lengthen a strand far surpasses that required for lateral deflection of the specimen. As such, buckling of the member is inhibited. If larger specimens are constructed, the duct configuration can be varied. Ducts with an area only slightly larger than the tendons could be placed such that they do not lie on the neutral axis of the specimen. Additionally, the duct profile could be varied over the length of the specimen. This will allow the investigation of the specific mechanisms involved in stiffening provided by strand engagement.

The test setup used in this program did not have the capacity to identify the extent of strand engagement during testing. Rather, qualitative assessments were made based on the knowledge of specimen geometry and construction process. If the total length of engaged strand could be monitored, efforts could be made to quantify the effects of

strand engagement on buckling capacity. In future specimens, a "window" could be incorporated at select locations, such as around the midspan region. This window could provide an indication of the strand location relative to the duct wall and would be useful in further study of strand engagement effects.

7.3 CONCLUSION OF RESEARCH PROJECT

The arch instrumentation operations are expected to begin in June 2012. At that point, a team from The University of Texas at Austin will instrument the first two arches with forty VWGs each. The arches will be cast shortly thereafter, followed by post-tensioning operations five days later. The contractor has developed two sets of arch formwork to expedite the construction. As the freshly placed concrete on one arch is curing, work on cage assembly on the next arch can begin. After each arch has been completed and is stressed, it will be placed in storage. The instrumentation protocol for the remaining arches will be reassessed, as the research team will be better able to identify the critical sections in the arches. The number of VWGs embedded in each arch is expected to progressively decrease based upon experience from the preceding arches.

Arch construction will continue throughout the summer and fall of 2012. The research team will be on-site for all instrumentation prior to casting and for monitoring during the post-tensioning and rotation phases for every arch. In addition, on-site monitoring will continue through 2013 as the arches are transported to the bridge site and erected, and as the floor beams and deck are added.

The bridge is scheduled for completion in late 2013. Prior to the bridge opening to traffic, the instrumentation will be placed in secure locations on the structure. Once the bridge is in service, data from the VWGs can be remotely acquired, should long-term performance monitoring be desired.

APPENDIX A

Test Data

A.1 INTRODUCTION

In the preceding chapters, data selected as representative of test results was presented. A more comprehensive overview of the data from the experimental program is provided in this appendix. Presented here for every load test are plots of total load versus lateral displacement, total load versus horizontal/lateral curvature, and a comparison of the axial load measured from the load cells to that calculated from the vibrating wire gages. A selection of Southwell plots are also provided where applicable (primarily for tests with concentric loading with measureable lateral deflection). While many other parameters, including strain and stress, were monitored throughout testing, the graphs included here were deemed most indicative of the structural behavior monitored throughout the study.

The nomenclature used for the tests is shown in Figure A-1 and Figure A-2. This nomenclature was introduced in the previous chapters, but is repeated here for the reader's reference.

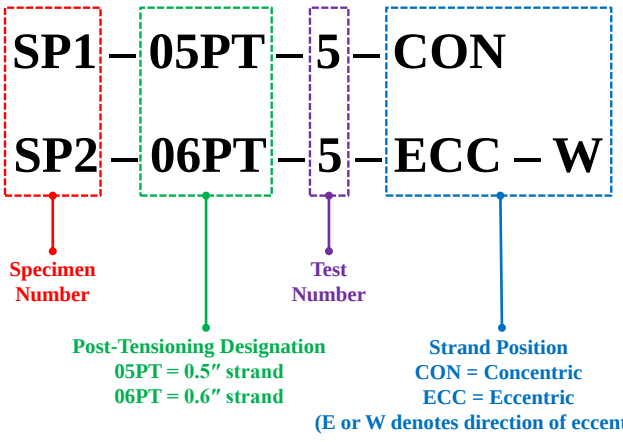

Figure A-1: Standard Test Nomenclature: Post-Tensioning

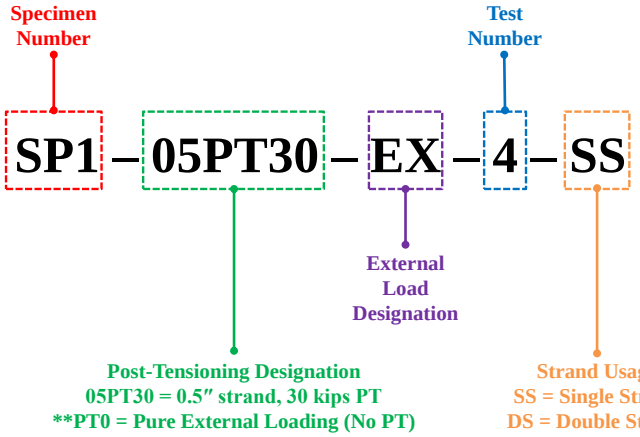

Figure A-2: Standard Test Nomenclature: External and Combined Loading

Table A-1 provides a summary of all load tests performed on the two specimens. Selected data from every test is provided in this appendix.

Table A-1: Load Test Summary

Number of Tests Performed			
Loading Scheme	**Specimen 1**	**Specimen 2**	
Post-tensioning	21	22	**PRE-FAILURE**
External Only	2	1	
Combined Loading	0	12	
Post-tensioning	1	0	**POST-FAILURE**
External Only	2	0	
Combined Loading	1	0	
Total	**27**	**35**	

It is important to note that this appendix provides a comprehensive overview of the test data in plot format for the reader's reference. There are many plots of data in this appendix, but discussion of these plots is very limited. An in-depth explanation of the trends and behavior expressed in the plots is provided in the previous chapters. Similarly,

the reader should refer to the body of this thesis for a discussion of the experimental procedures and the influence of these procedures on the data shown in the plots.

A.2 LOAD VS. LATERAL DISPLACEMENT DATA

This portion of the appendix provides plots of total axial load versus lateral displacement measurements for all load tests. As discussed in the previous chapters, the lateral deflection was measured by linear potentiometers.

A.2.1 Specimen 1 (SP1)

This subsection includes load versus lateral deflection plots for a total of 27 load tests on the first specimen (SP1). Notes on individual tests are included in the figure captions where applicable.

A.2.1.1 SP1 Post-tensioned Tests

This subsection includes load versus lateral deflection plots for all PT load tests on SP1. There were a total of 21 pre-failure tests and one post-failure test performed.

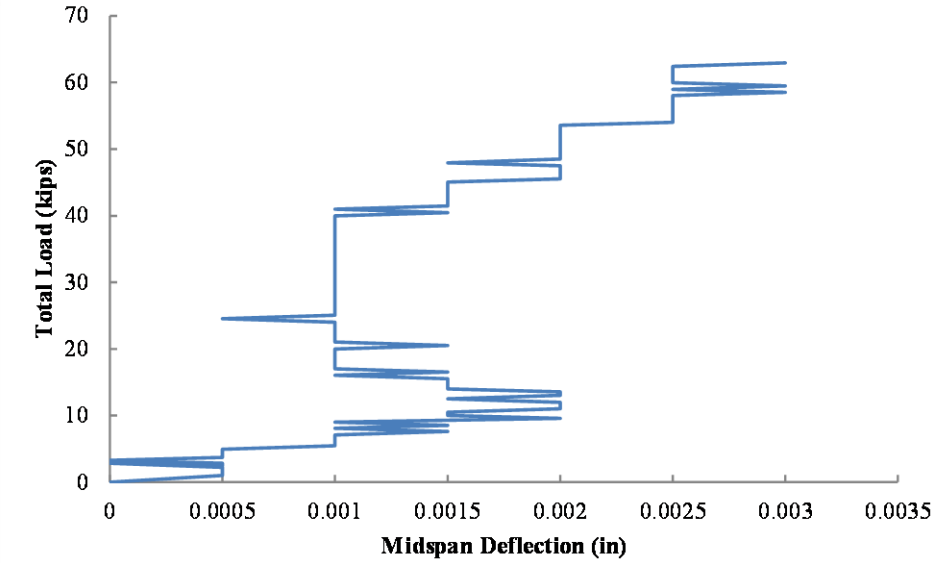

Figure A-3: Load vs. Lateral Displacement for SP1-05PT-1-CON (Midspan supports were not lowered; friction inhibited significant lateral displacement.)

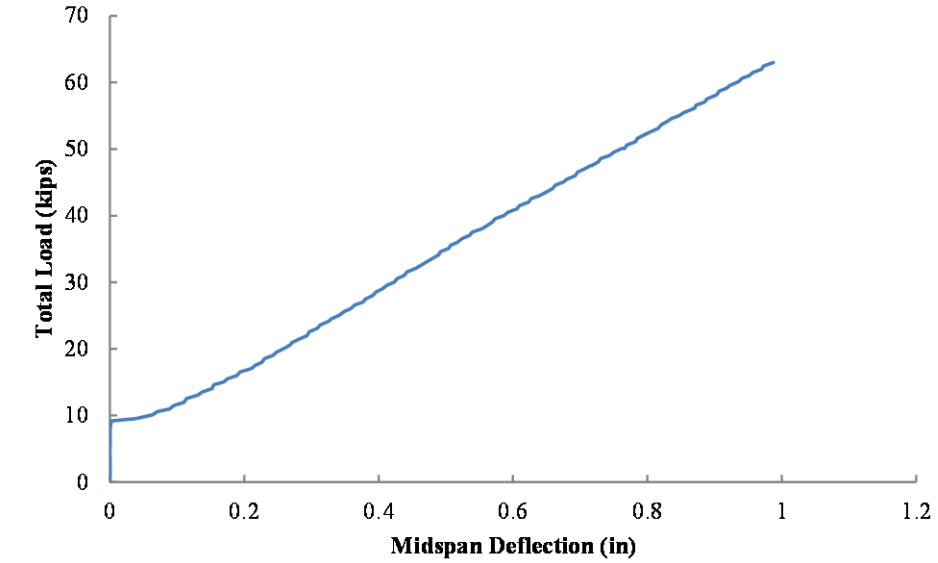

Figure A-4: Load vs. Lateral Displacement for SP1-05PT-2-ECC-E

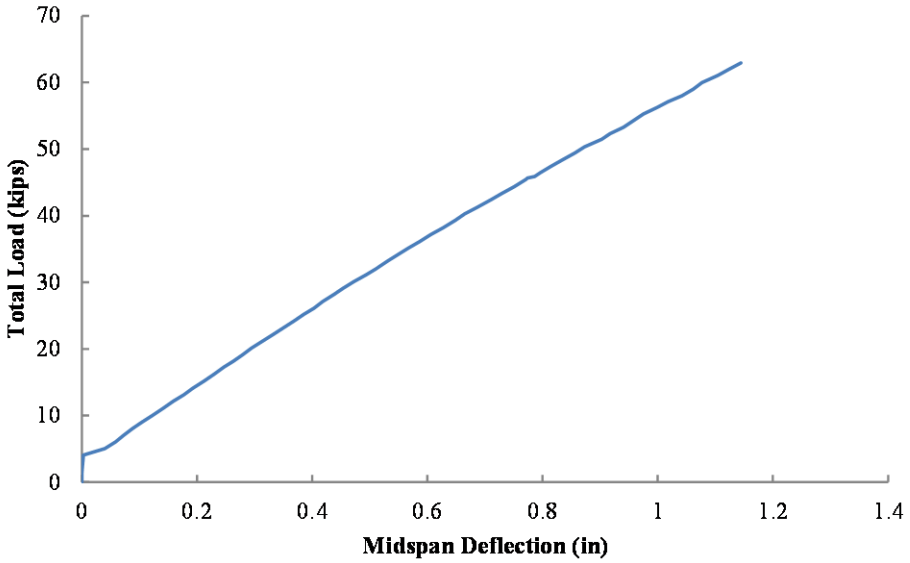

Figure A-5: Load vs. Lateral Displacement for SP1-05PT-3-ECC-W

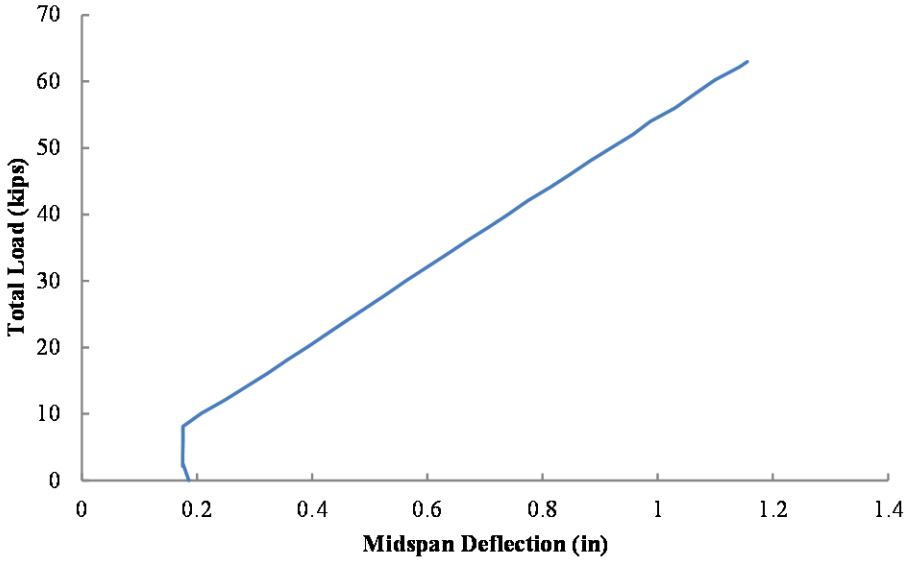

Figure A-6: Load vs. Lateral Displacement for SP1-05PT-4-ECC-W

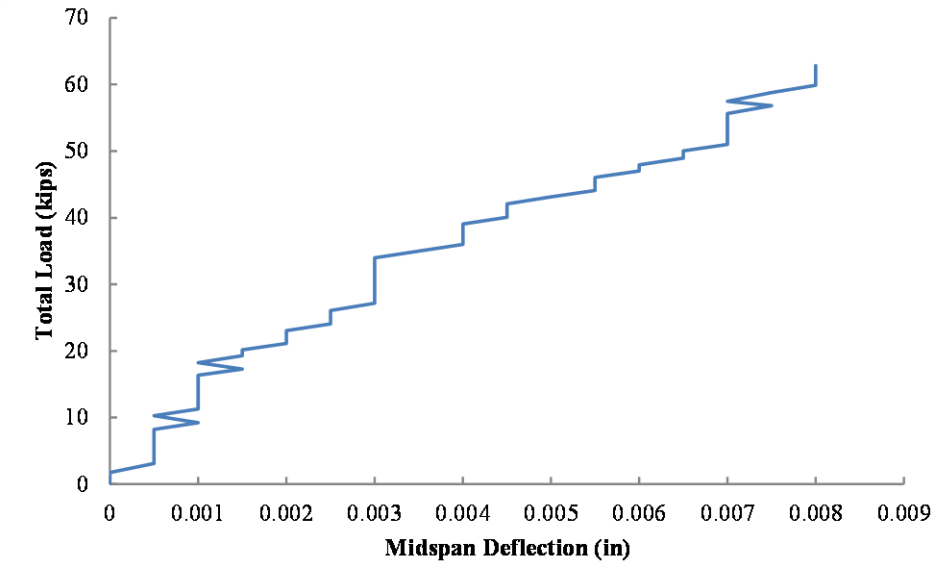

Figure A-7: Load vs. Lateral Displacement for SP1-05PT-5-CON (Midspan supports were not lowered; friction inhibited significant lateral displacement.)

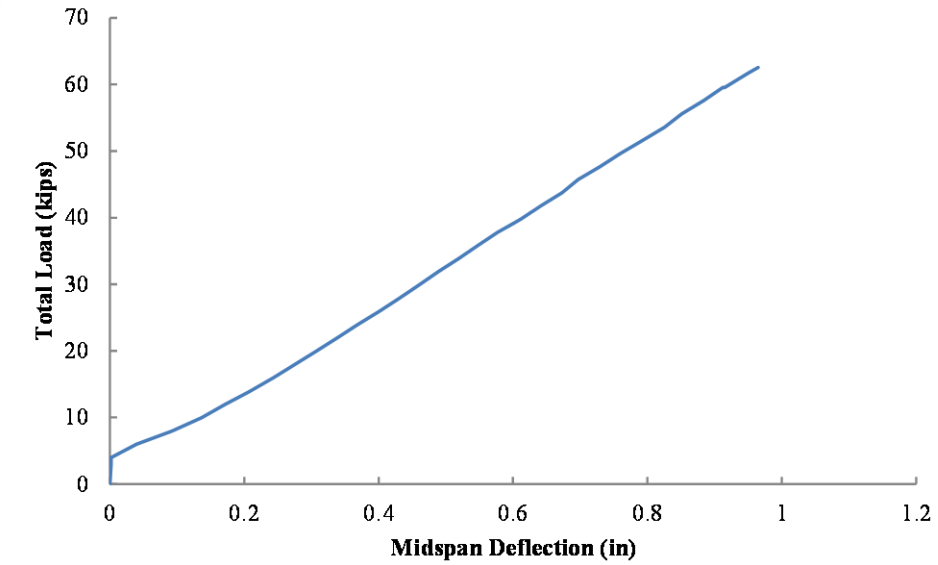

Figure A-8: Load vs. Lateral Displacement for SP1-05PT-6-ECC-E

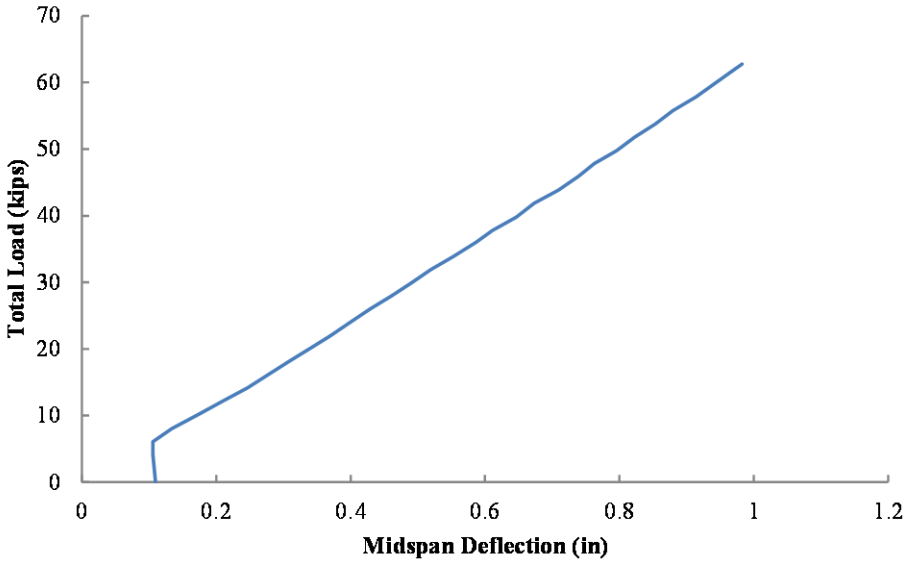

Figure A-9: Load vs. Lateral Displacement for SP1-05PT-7-ECC-E

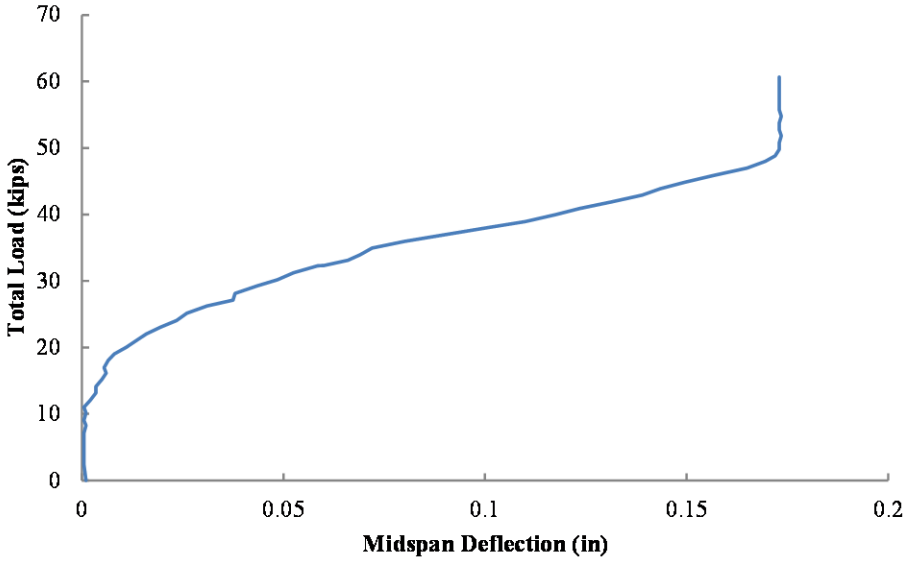

Figure A-10: Load vs. Lateral Displacement for SP1-05PT-8-CON (Specimen cambered off supports, but supports not lowered. When top strand loaded, specimen sagged, reintroducing friction to the system and limiting additional deflection.)

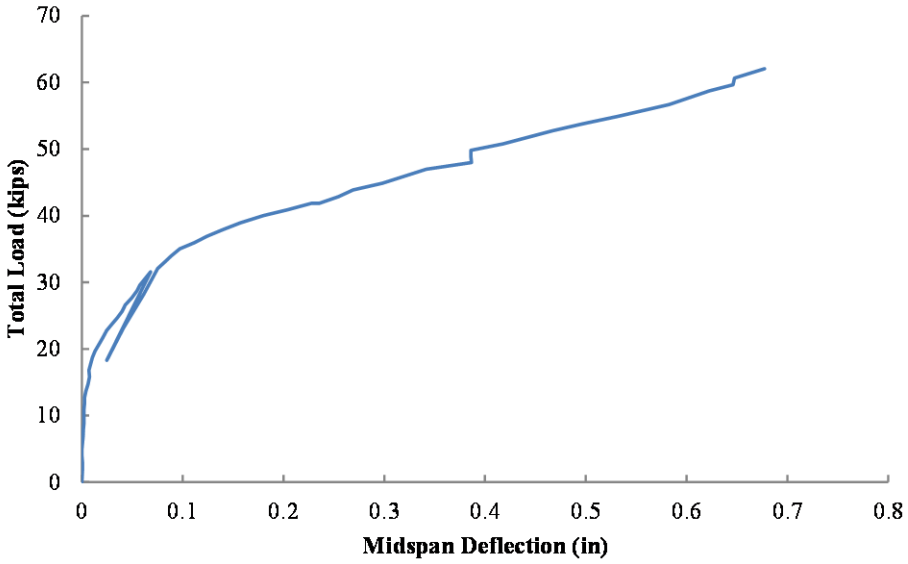

Figure A-11: Load vs. Lateral Displacement for SP1-05PT-9-CON

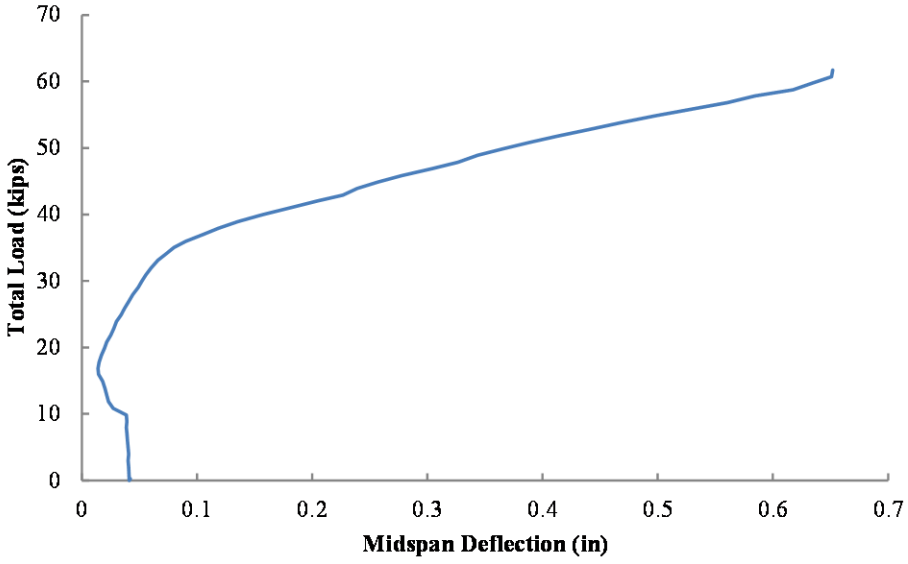

Figure A-12: Load vs. Lateral Displacement for SP1-05PT-10-CON

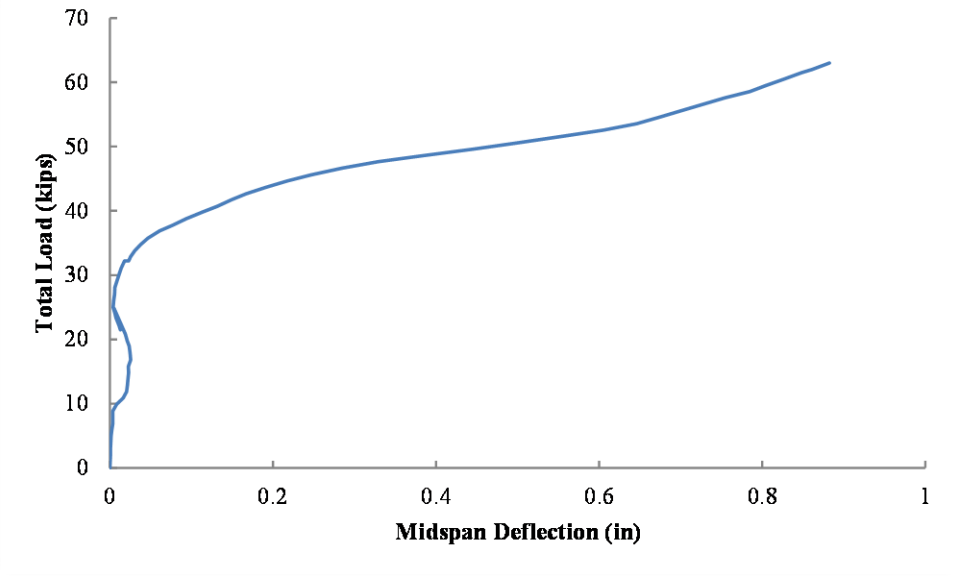

Figure A-13: Load vs. Lateral Displacement for SP1-05PT-11-CON

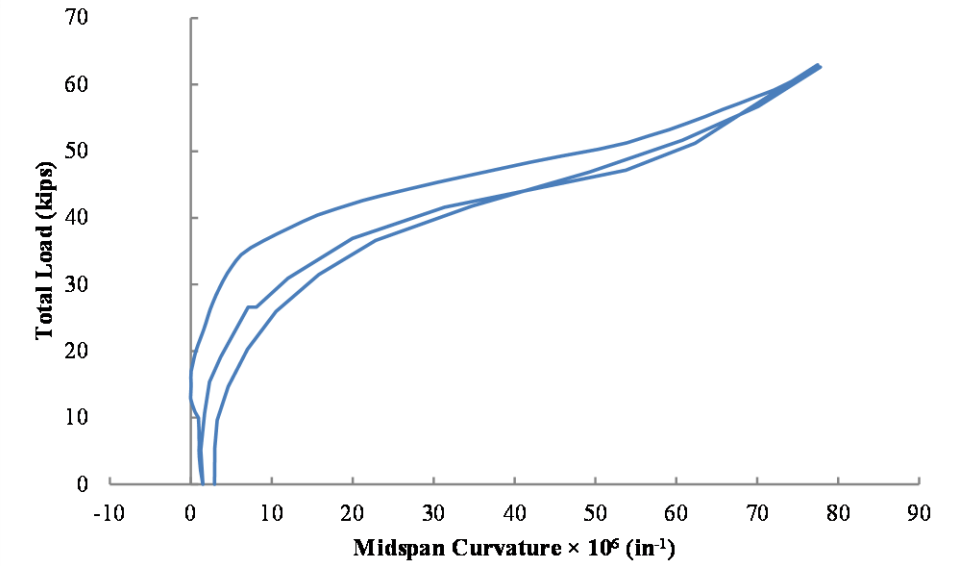

Figure A-14: Load vs. Lateral Displacement for SP1-05PT-12-CON (Two full loading and unloading cycles shown.)

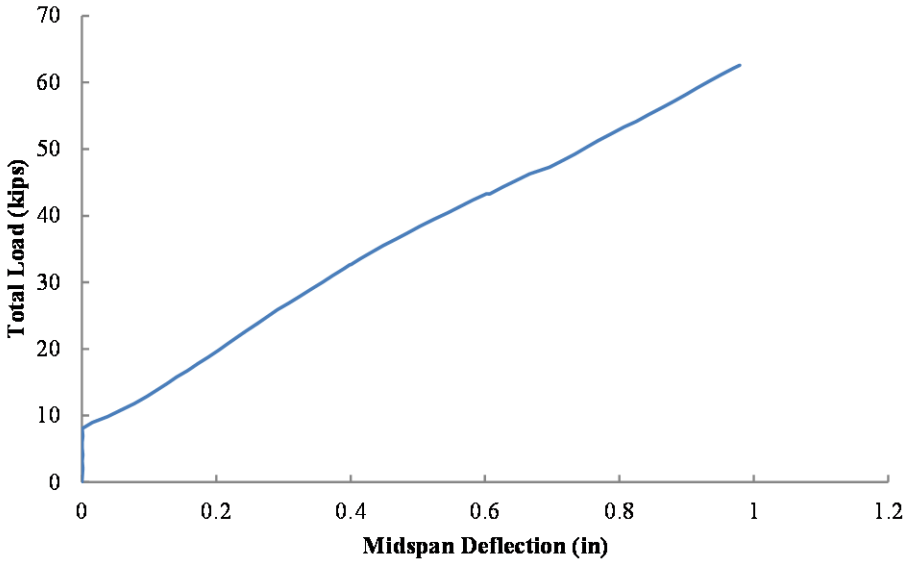

Figure A-15: Load vs. Lateral Displacement for SP1-05PT-13-ECC-E

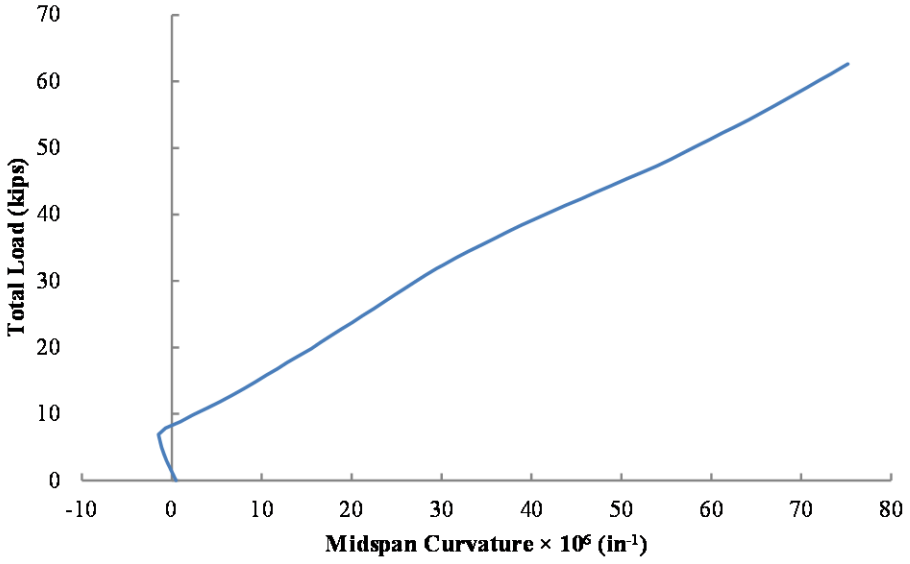

Figure A-16: Load vs. Lateral Displacement for SP1-05PT-14-ECC-E

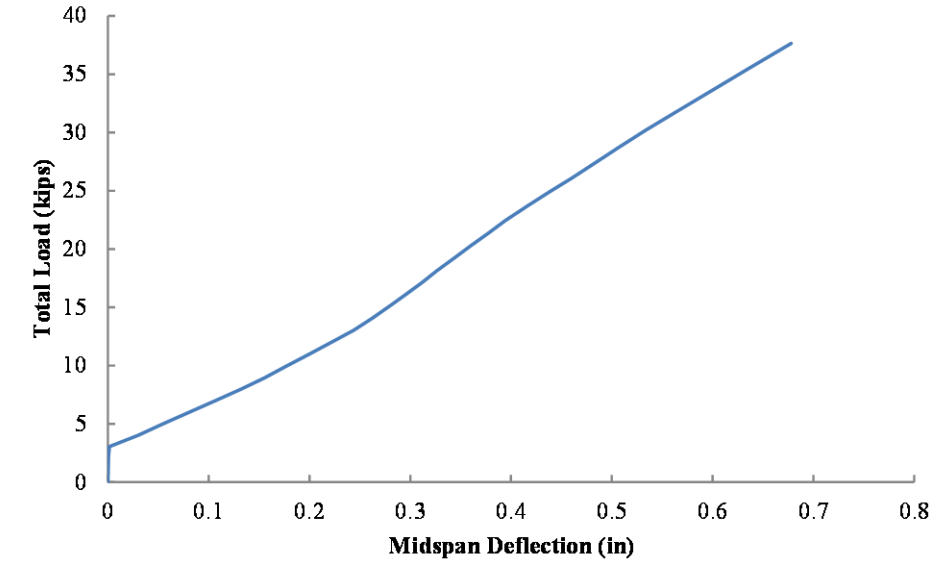

Figure A-17: Load vs. Lateral Displacement for SP1-05PT-15-ECC-W

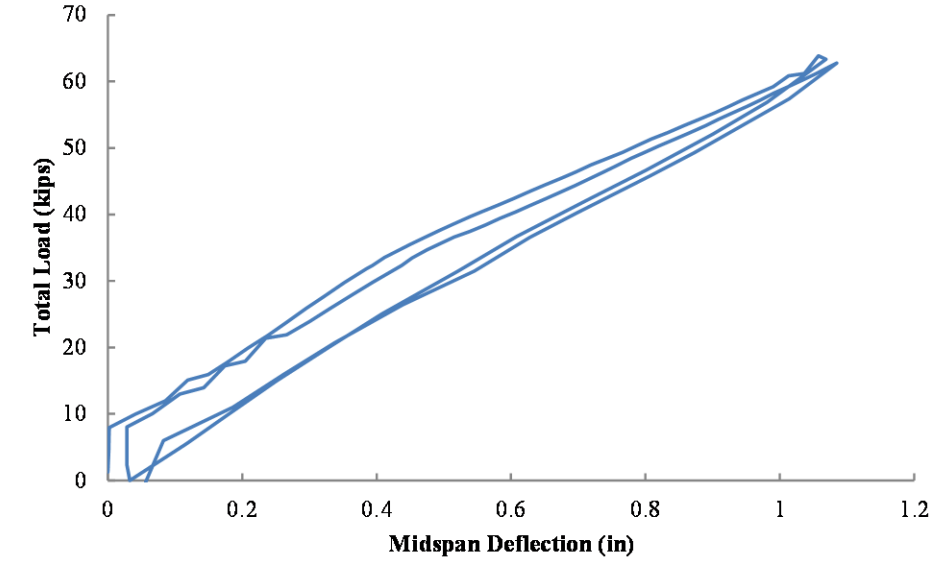

Figure A-18: Load vs. Lateral Displacement for SP1-05PT-16-ECC-W (Two full loading and unloading cycles shown.)

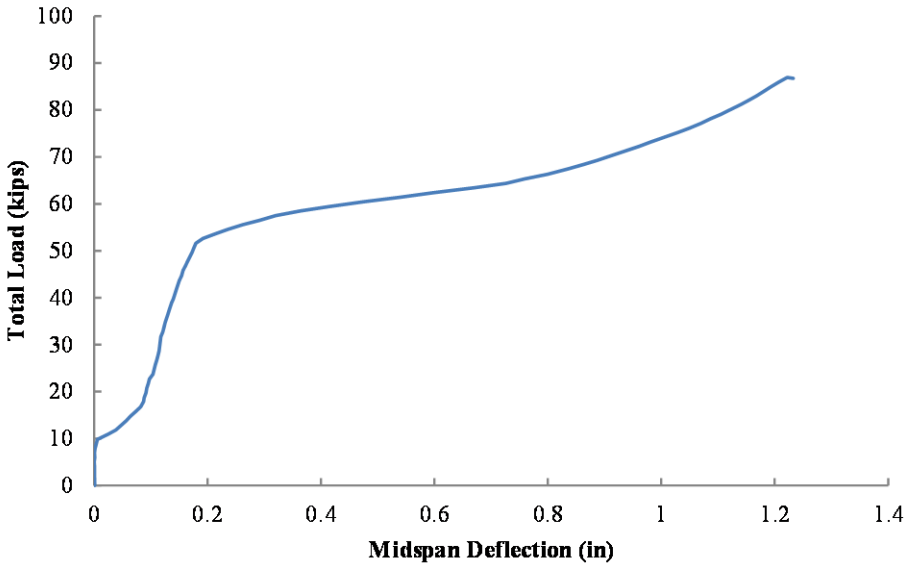

Figure A-19: Load vs. Lateral Displacement for SP1-06PT-1-CON

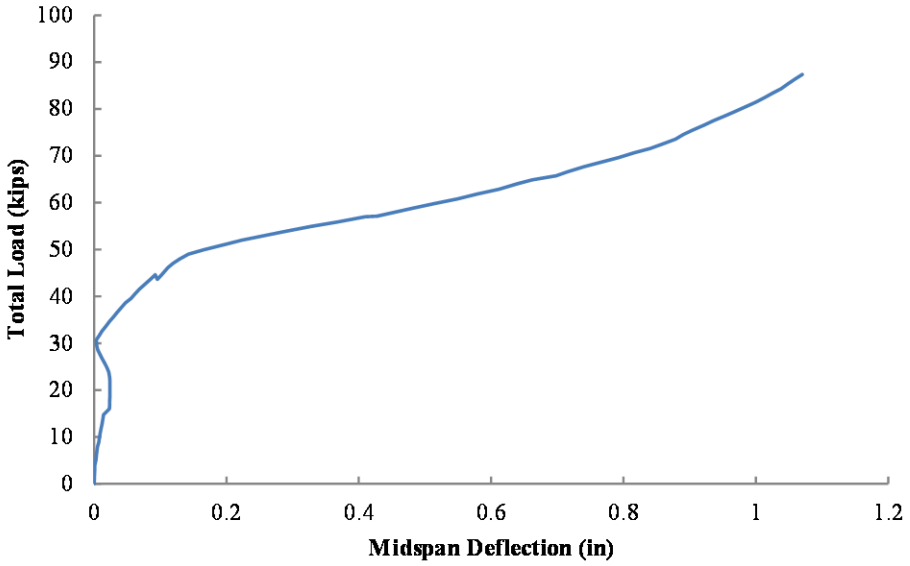

Figure A-20: Load vs. Lateral Displacement for SP1-06PT-2-CON

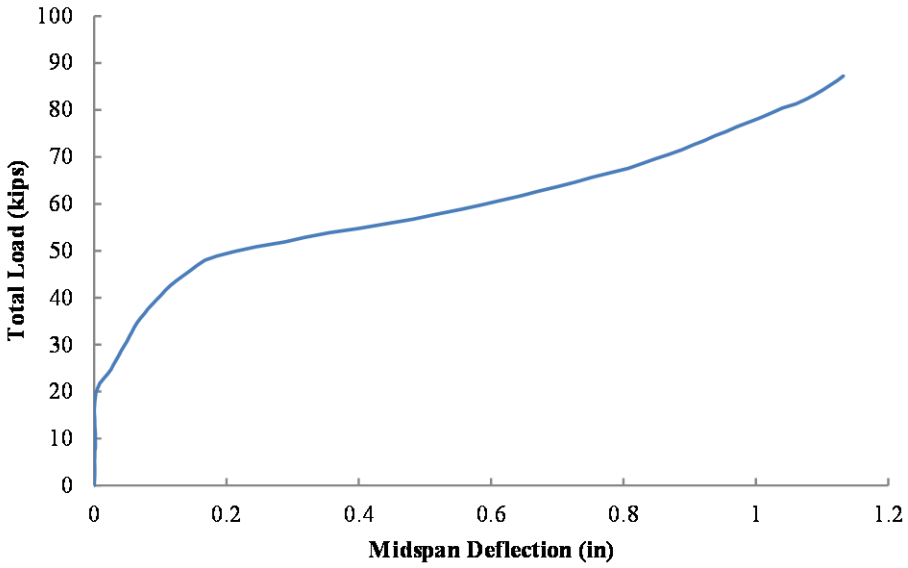

Figure A-21: Load vs. Lateral Displacement for SP1-06PT-3-CON

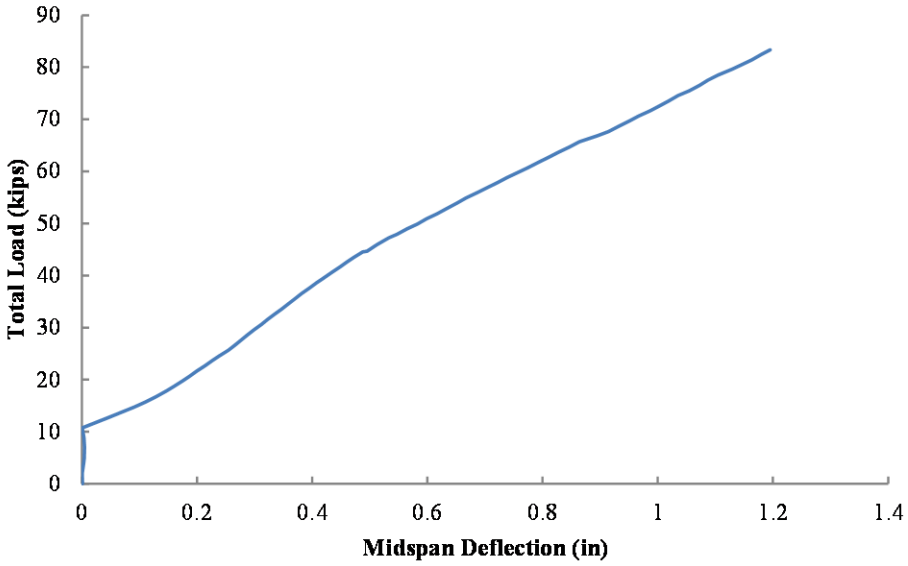

Figure A-22: Load vs. Lateral Displacement for SP1-06PT-4-ECC-E

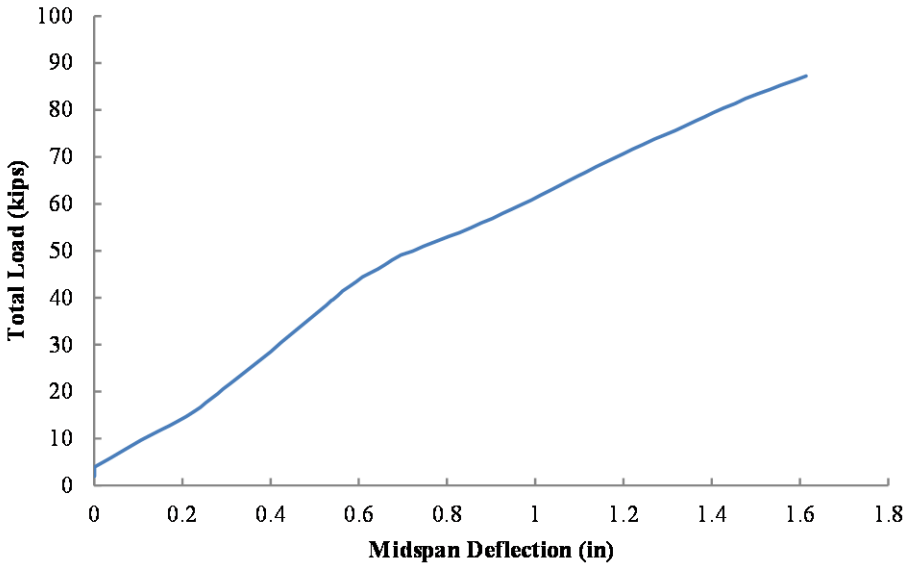

Figure A-23: Load vs. Lateral Displacement for SP1-06PT-5-ECC-W

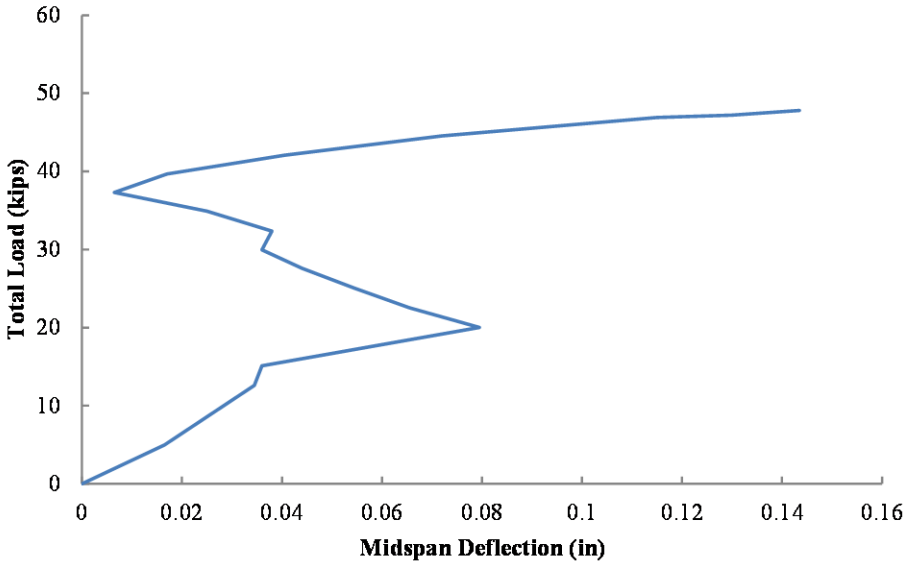

Figure A-24: Load vs. Lateral Displacement for SP1-06PT-6-CON

A.2.1.2 SP1 Combined Load Tests

The only combined load test in SP1 was performed after the specimen was cracked extensively due to a buckling failure.

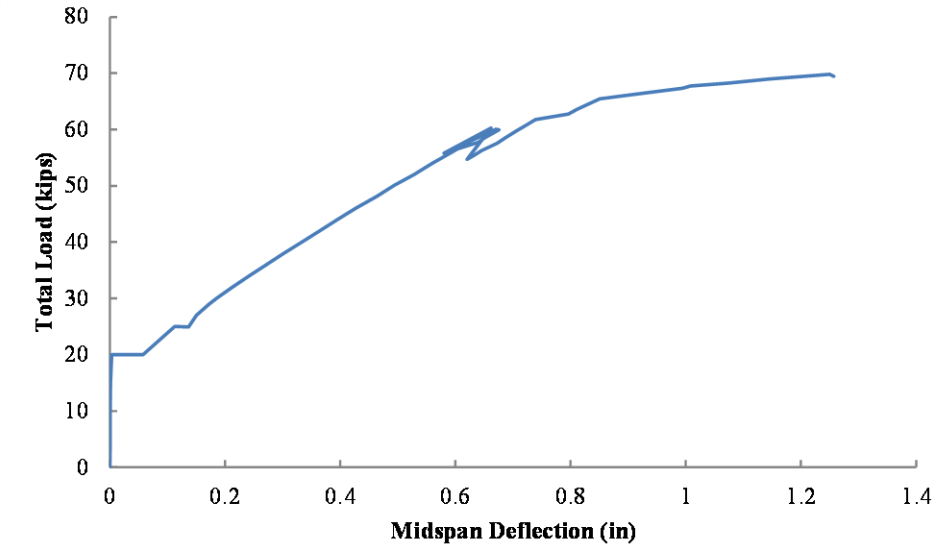

Figure A-25: Load vs. Lateral Displacement for SP1-06PT60-EX-1

A.2.1.3 SP1 External Load Tests

This sub-section includes the load versus lateral deflection plots constructed from the external load tests on SP1. There were a total of four external load tests performed.

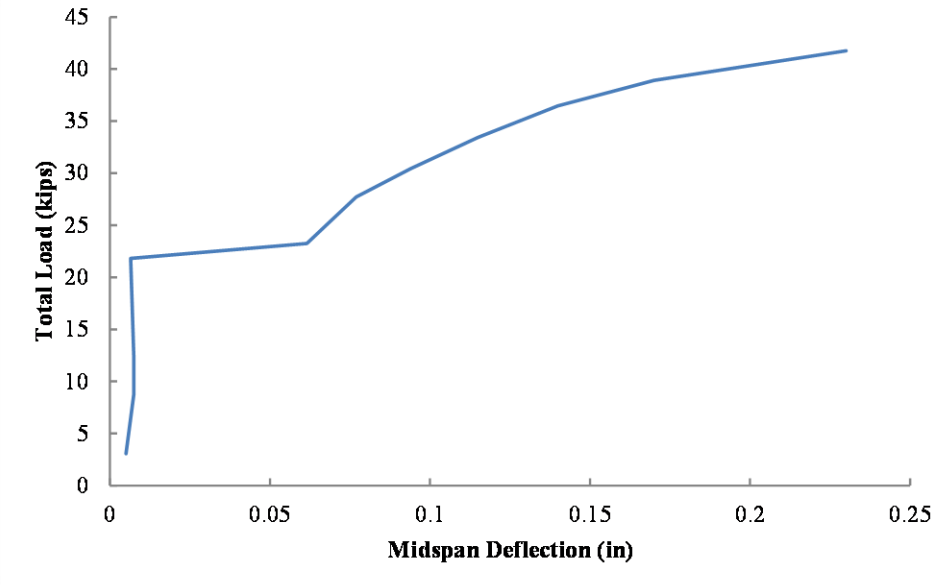

Figure A-26: Load vs. Lateral Displacement for SP1-PT0-EX-1

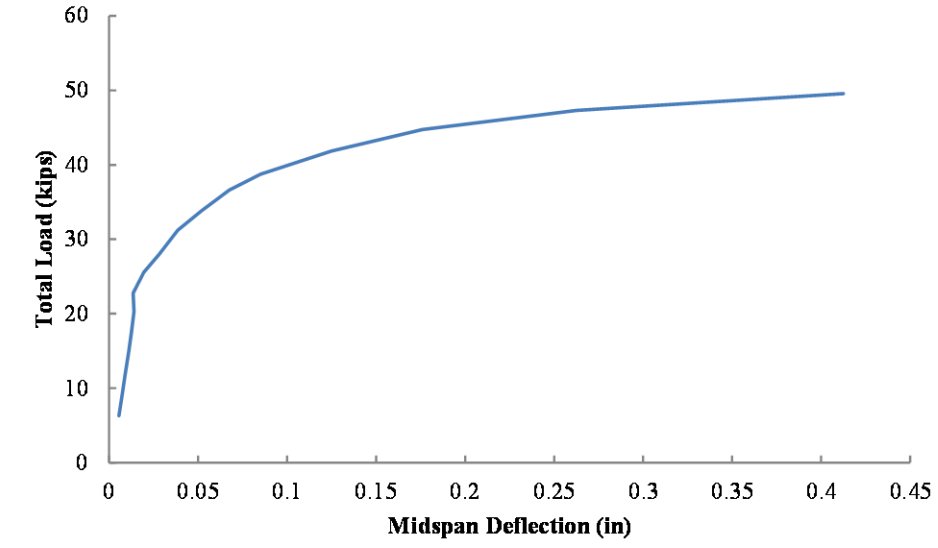

Figure A-27: Load vs. Lateral Displacement for SP1-PT0-EX-2

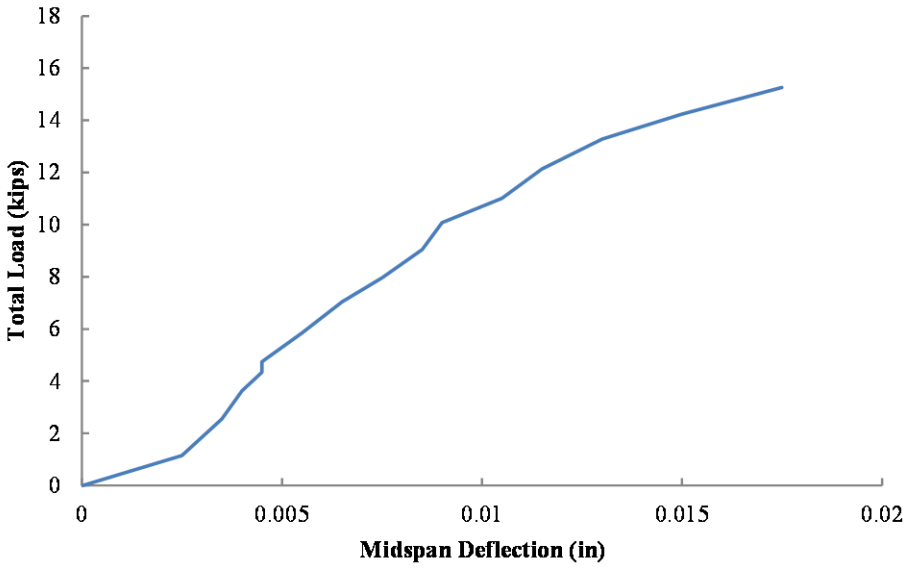

Figure A-28: Load vs. Lateral Displacement for SP1-PT0-EX-3

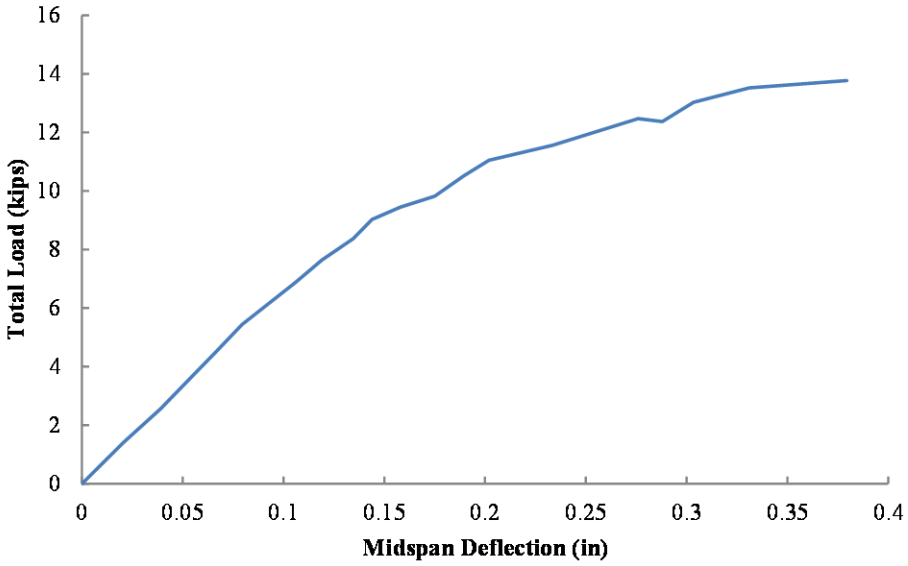

Figure A-29: Load vs. Lateral Displacement for SP1-PT0-EX-4

A.2.2 Specimen 2 (SP2)

This subsection includes load versus lateral deflection plots for each of the 35 load tests on the second specimen (SP2). Notes on individual tests are included in the figure captions where applicable.

A.2.2.1 SP2 Post-tensioned Tests

This subsection includes load versus lateral deflection plots for all PT load tests on SP2. There were a total of 22 pre-failure tests performed. No post-failure tests were performed.

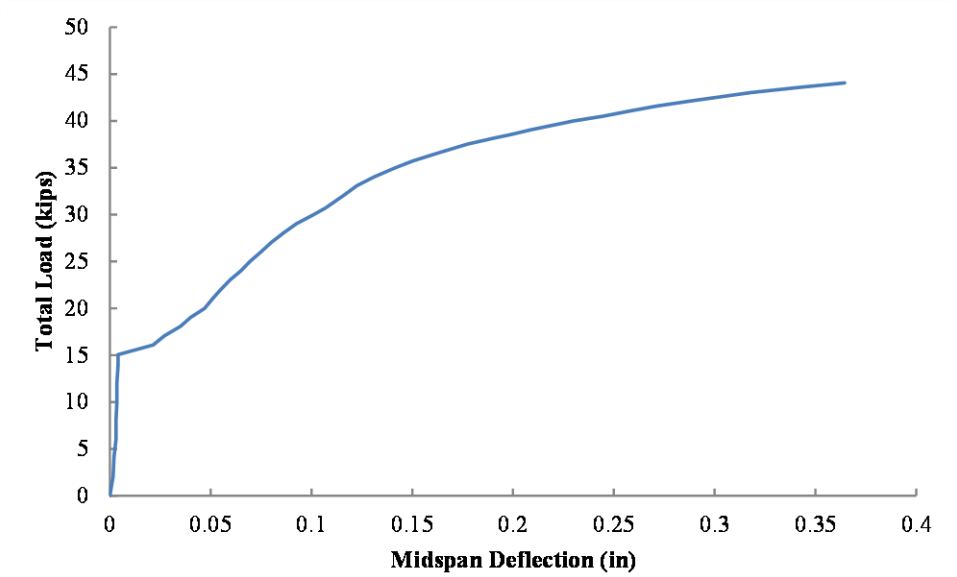

Figure A-30: Load vs. Lateral Displacement for SP2-05PT-1-CON

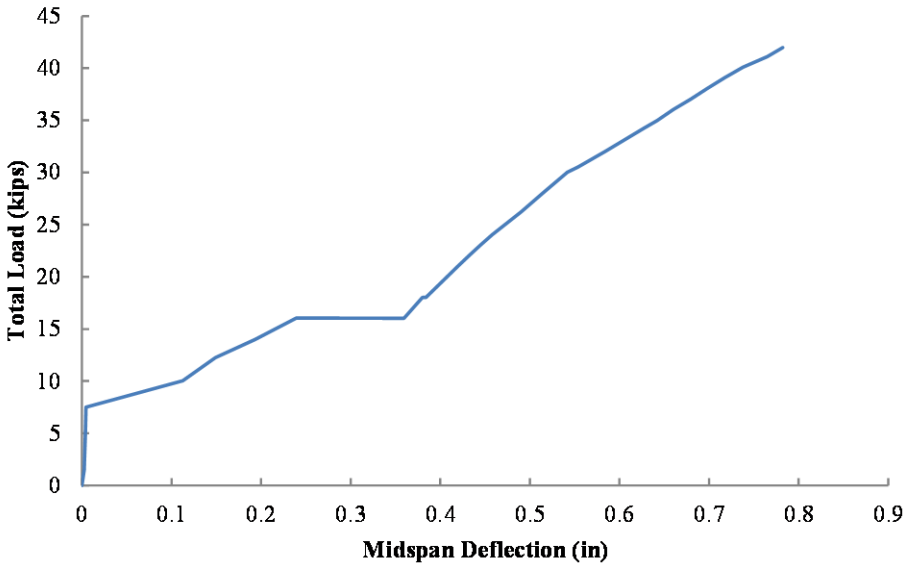

Figure A-31: Load vs. Lateral Displacement for SP2-05PT-2-ECC-W

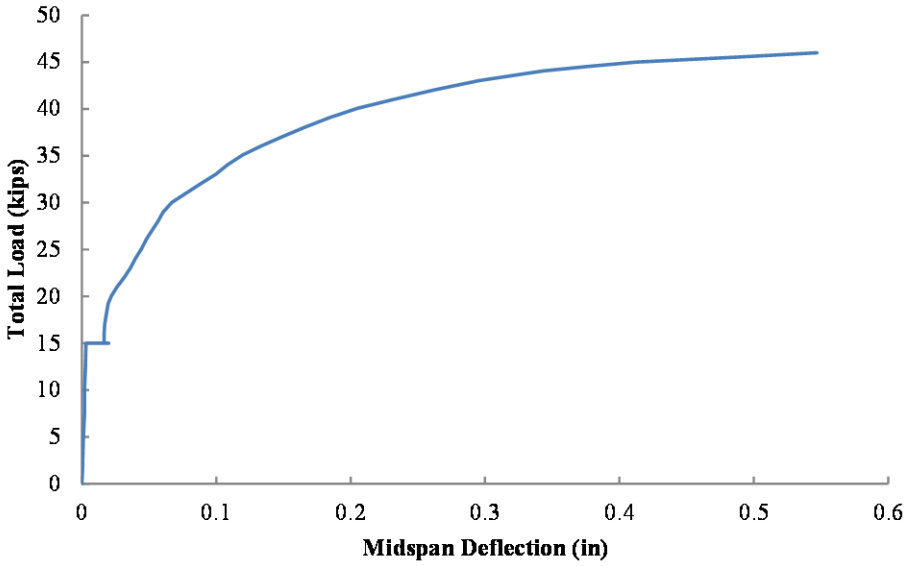

Figure A-32: Load vs. Lateral Displacement for SP2-05PT-3-CON

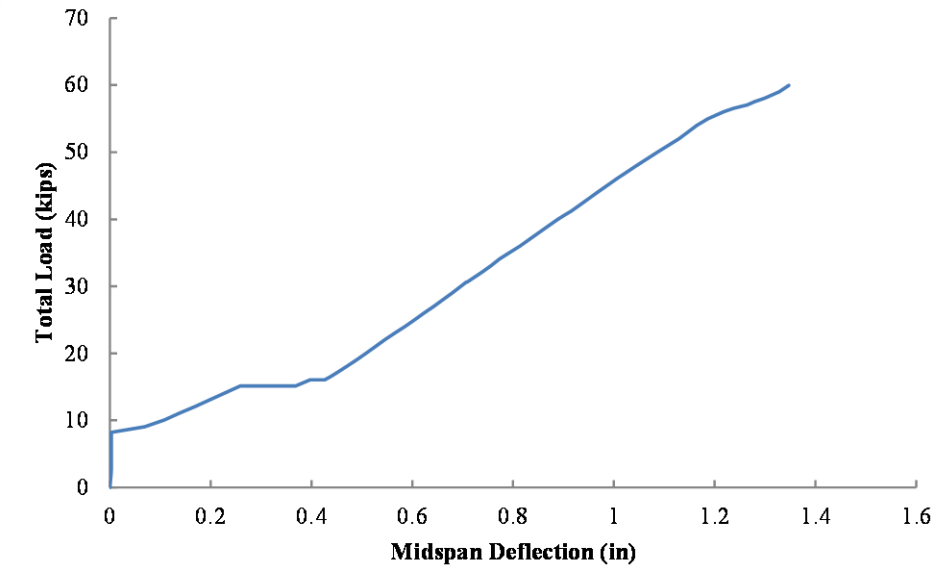

Figure A-33: Load vs. Lateral Displacement for SP2-05PT-4-ECC-E

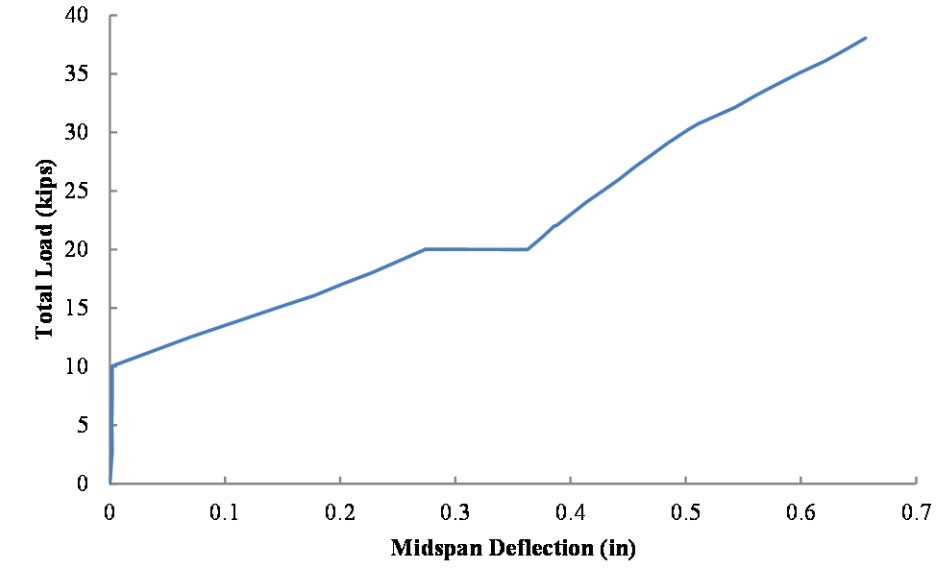

Figure A-34: Load vs. Lateral Displacement for SP2-05PT-5-ECC-W

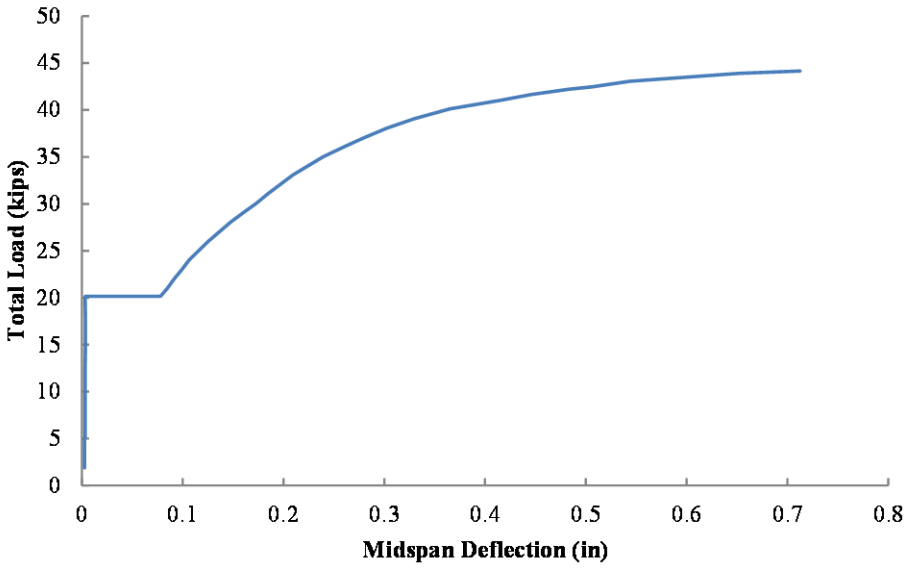

Figure A-35: Load vs. Lateral Displacement for SP2-05PT-6-CON

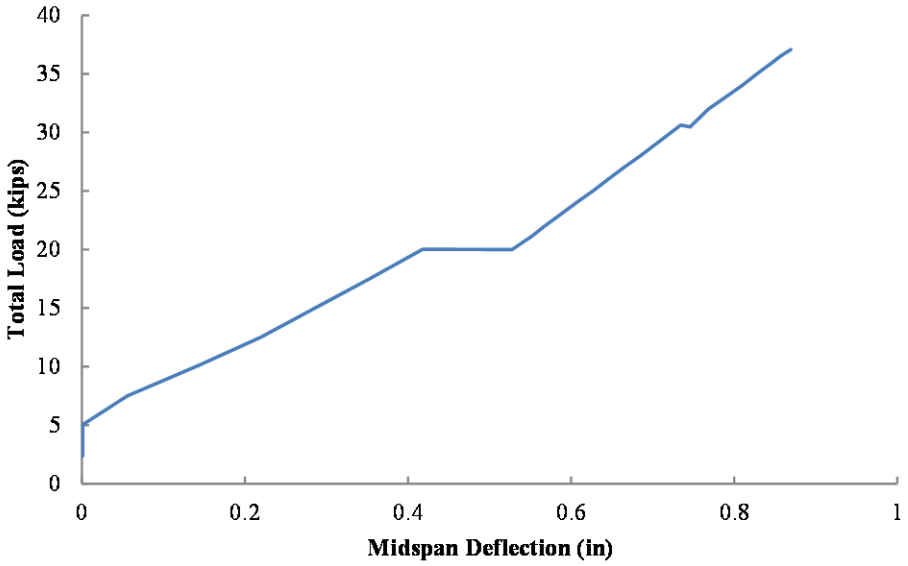

Figure A-36: Load vs. Lateral Displacement for SP2-05PT-7-ECC-E

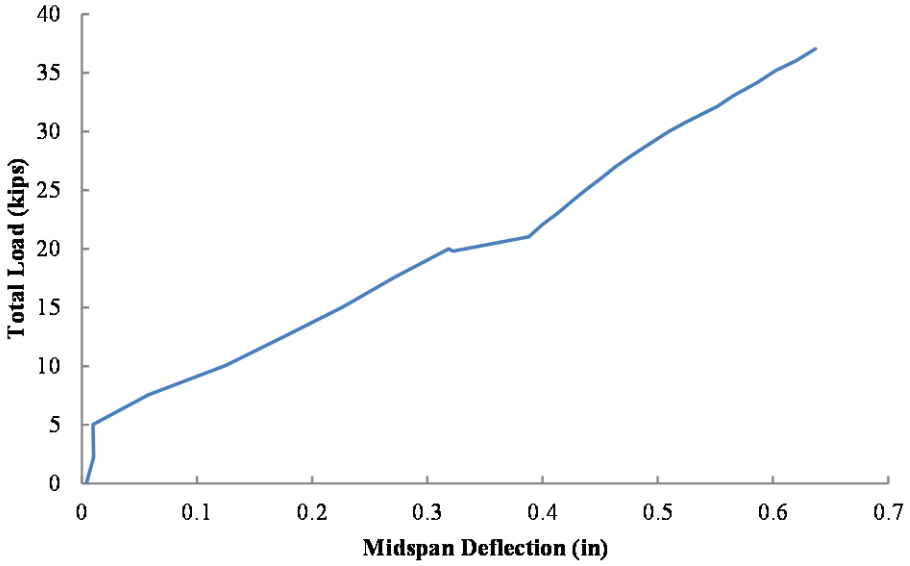

Figure A-37: Load vs. Lateral Displacement for SP2-05PT-8-ECC-W

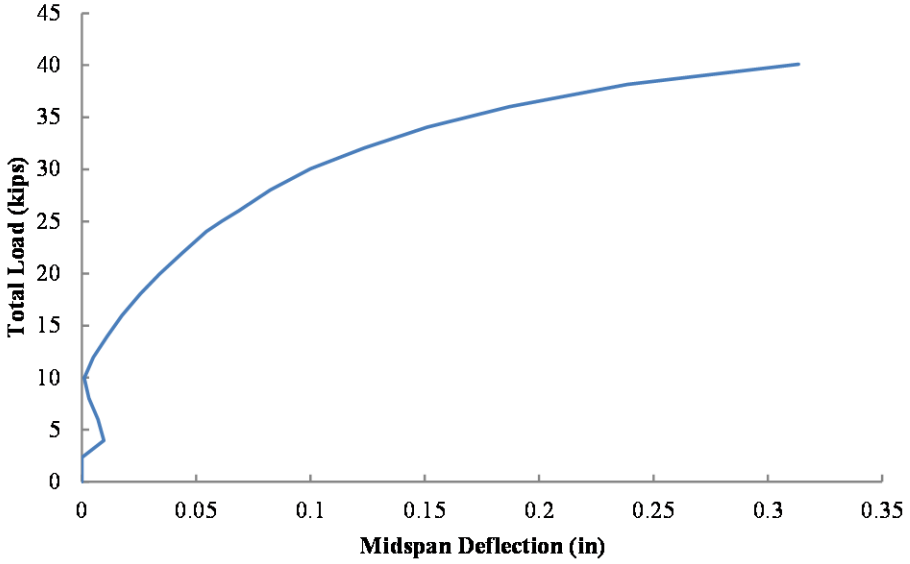

Figure A-38: Load vs. Lateral Displacement for SP2-06PT-1-CON

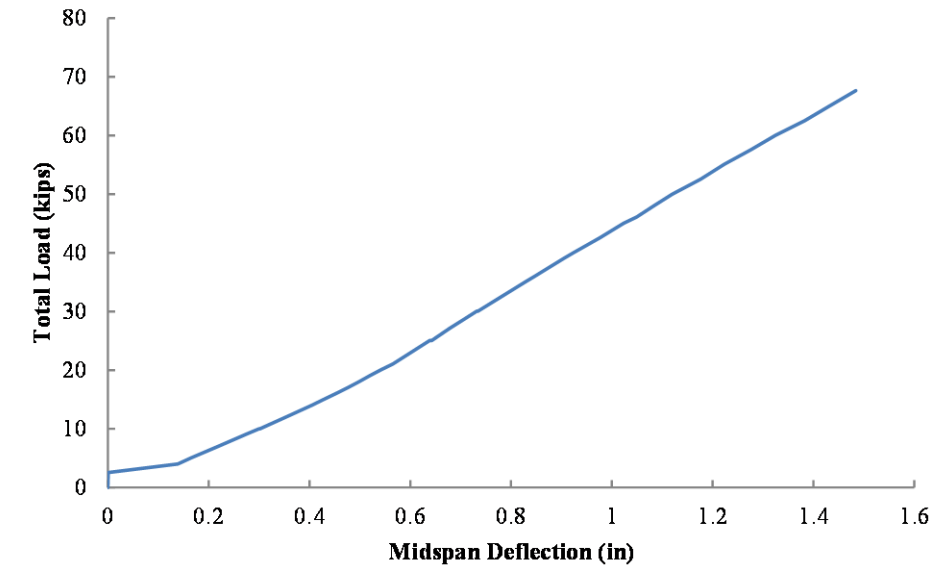

Figure A-39: Load vs. Lateral Displacement for SP2-06PT-2-ECC-E

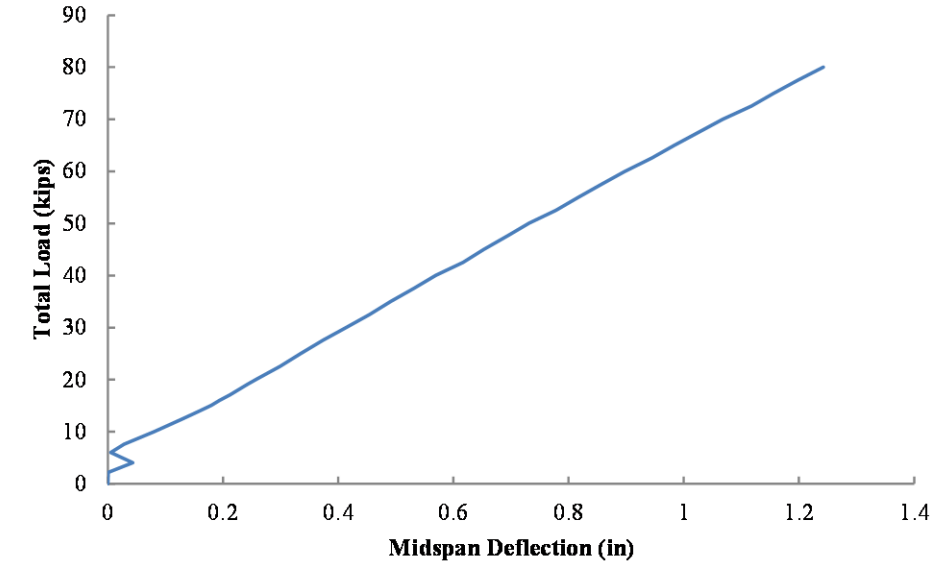

Figure A-40: Load vs. Lateral Displacement for SP2-06PT-3-ECC-W

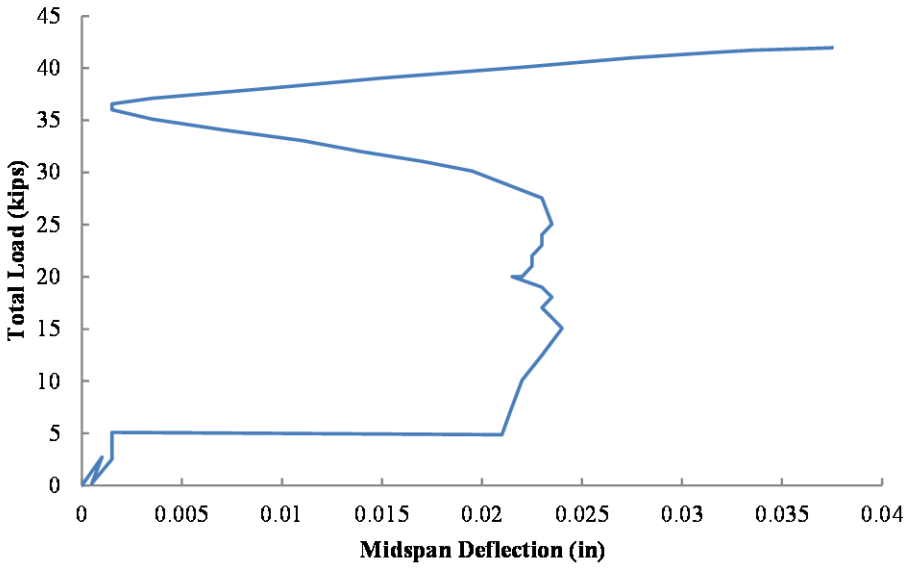

Figure A-41: Load vs. Lateral Displacement for SP2-06PT-4-CON

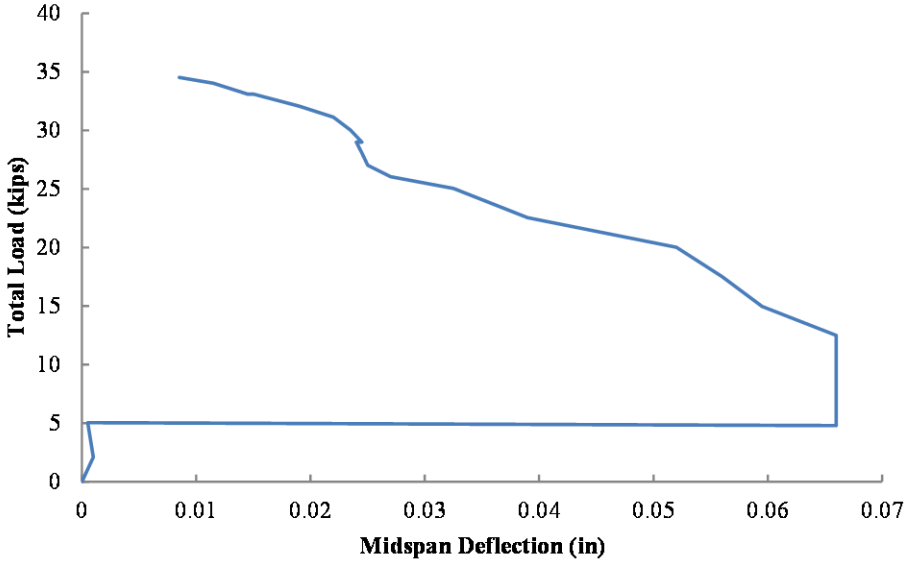

Figure A-42: Load vs. Lateral Displacement for SP2-06PT-5-CON

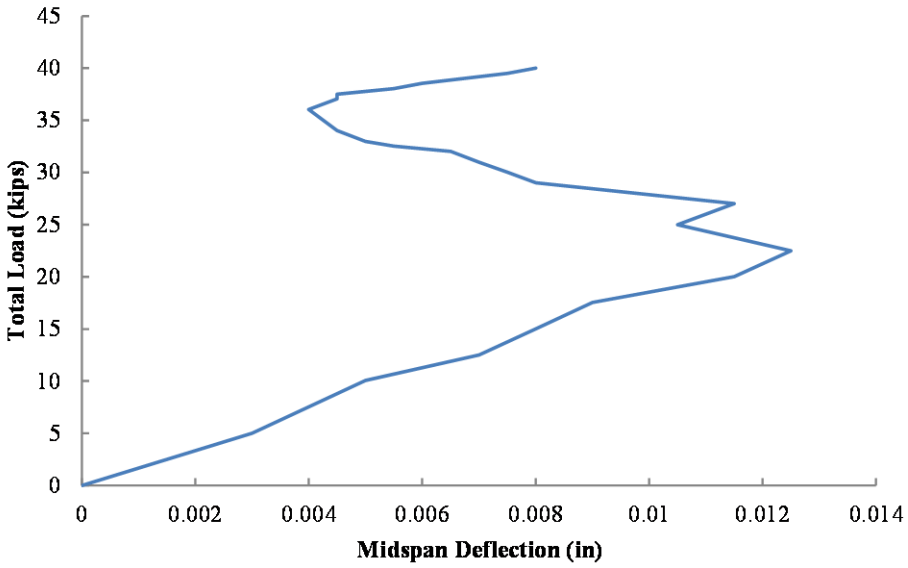

Figure A-43: Load vs. Lateral Displacement for SP2-06PT-6-CON

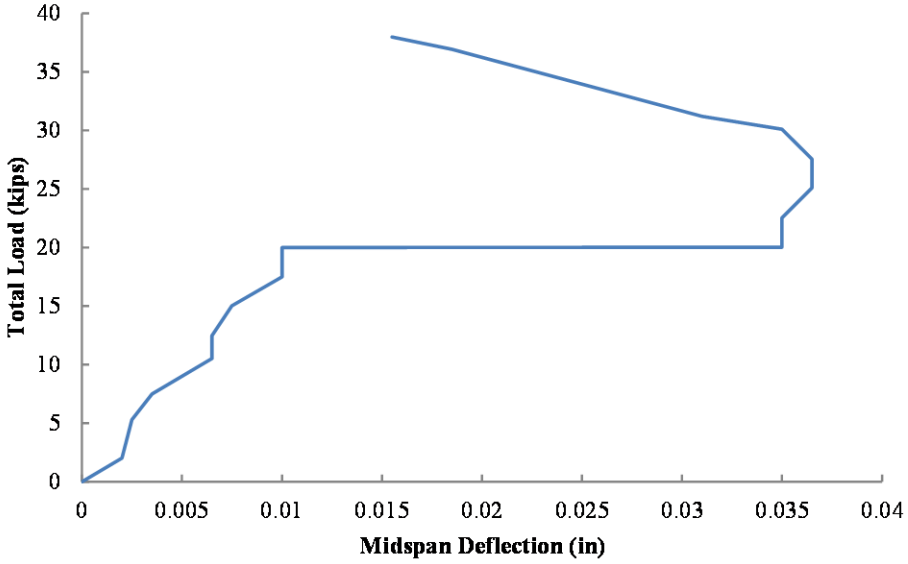

Figure A-44: Load vs. Lateral Displacement for SP2-06PT-7-CON

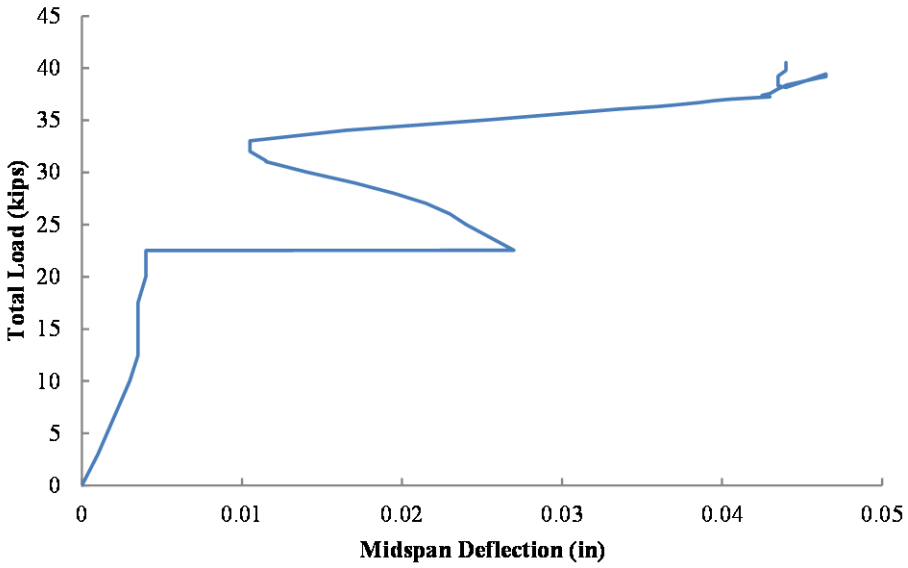

Figure A-45: Load vs. Lateral Displacement for SP2-06PT-8-CON

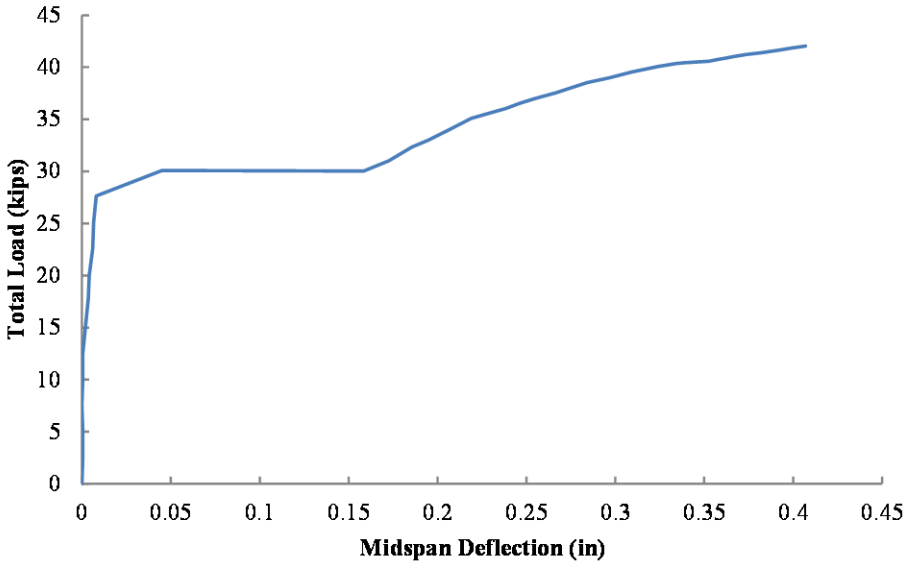

Figure A-46: Load vs. Lateral Displacement for SP2-06PT-9-CON

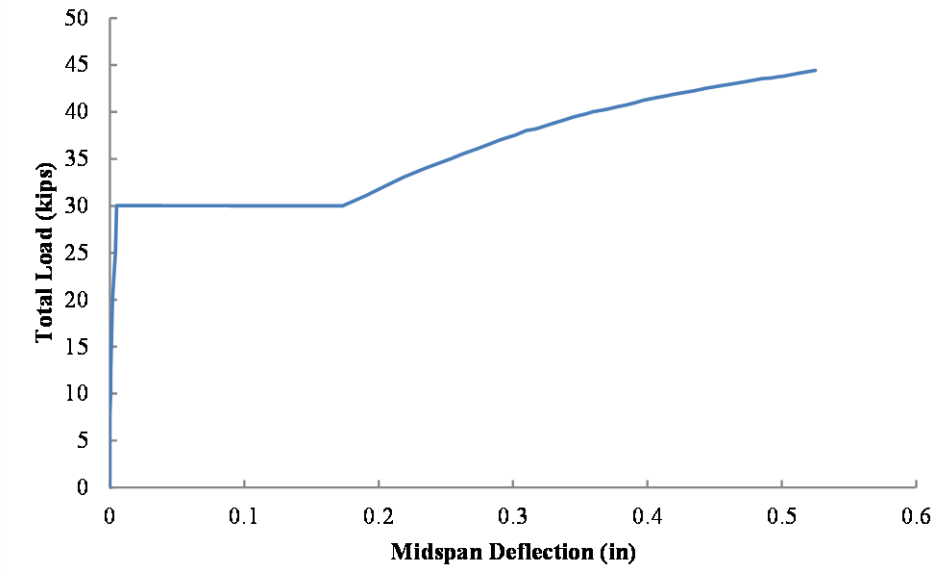

Figure A-47: Load vs. Lateral Displacement for SP2-06PT-10-CON

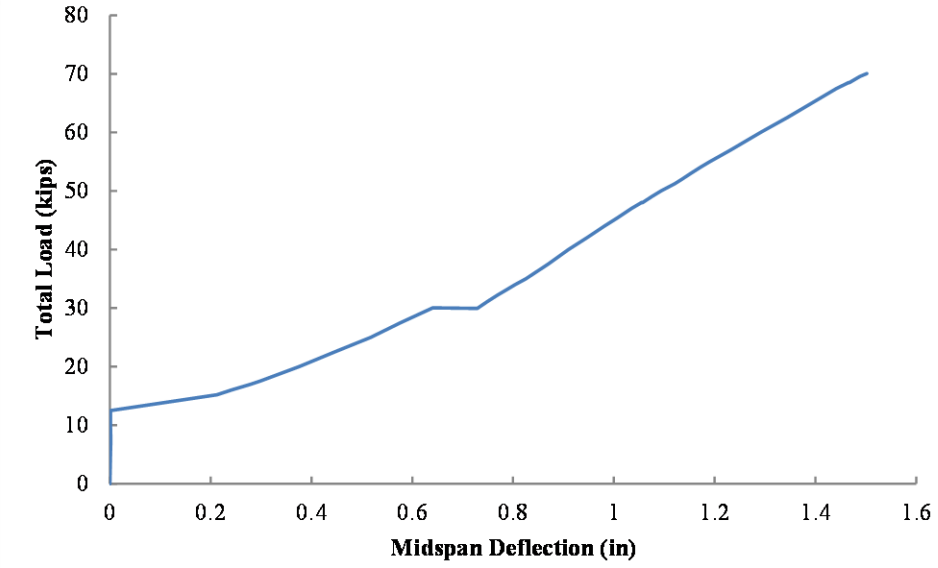

Figure A-48: Load vs. Lateral Displacement for SP2-06PT-11-ECC-E

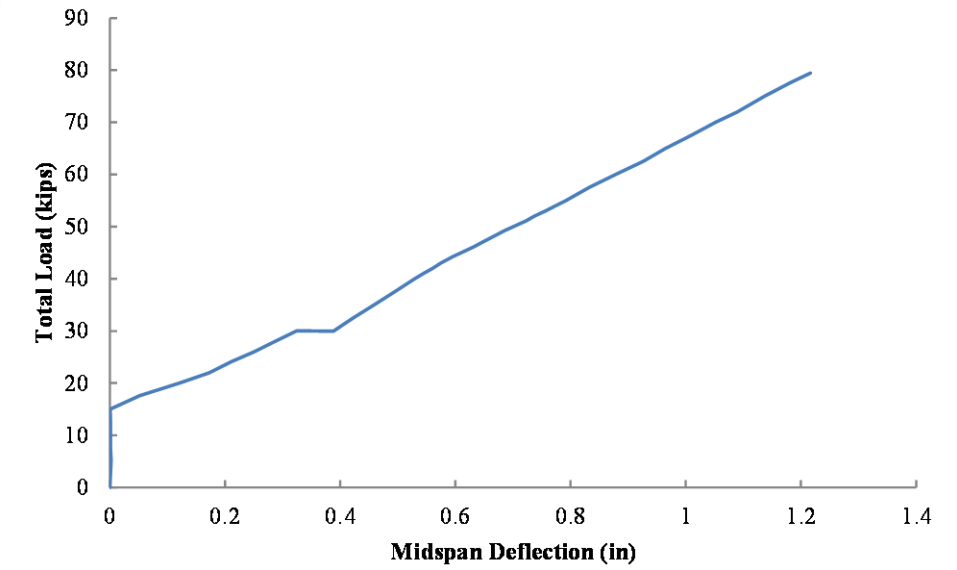

Figure A-49: Load vs. Lateral Displacement for SP2-06PT-12-ECC-W

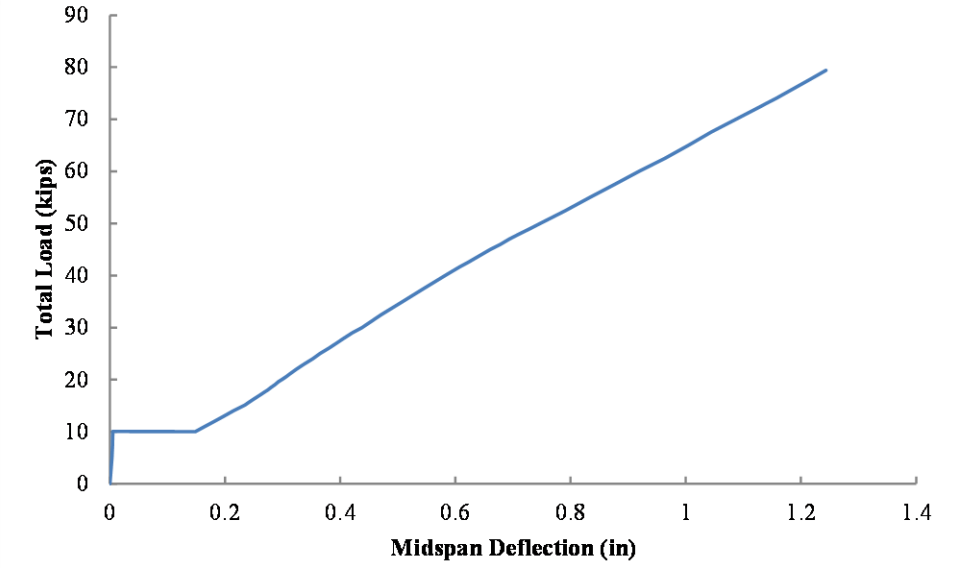

Figure A-50: Load vs. Lateral Displacement for SP2-06PT-13-ECC-W

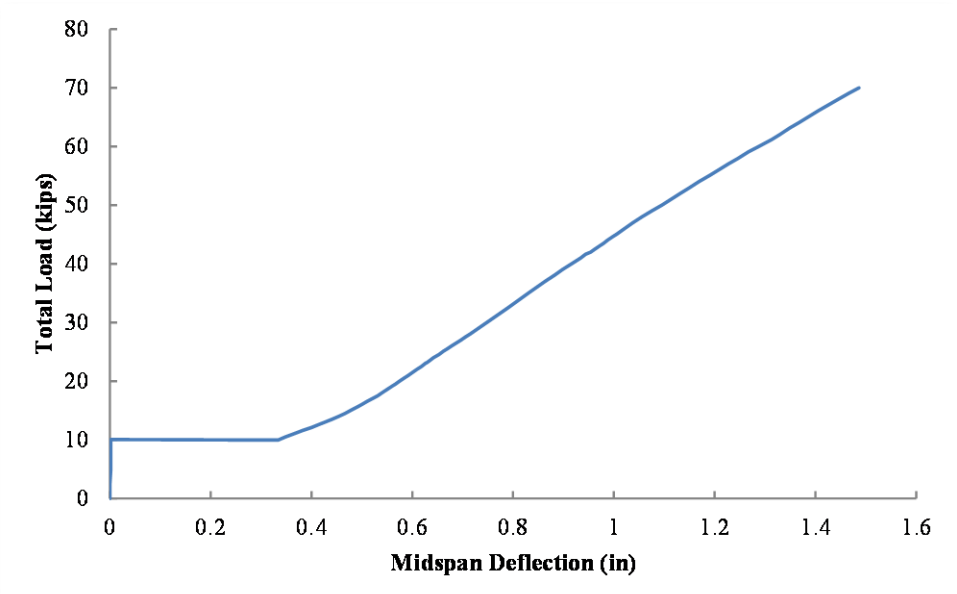

Figure A-51: Load vs. Lateral Displacement for SP2-06PT-14-ECC-E

A.2.2.2 SP2 Combined Load Tests

This subsection includes load versus lateral deflection plots for each of the combined load tests on SP2. There were a total of twelve combined load tests performed.

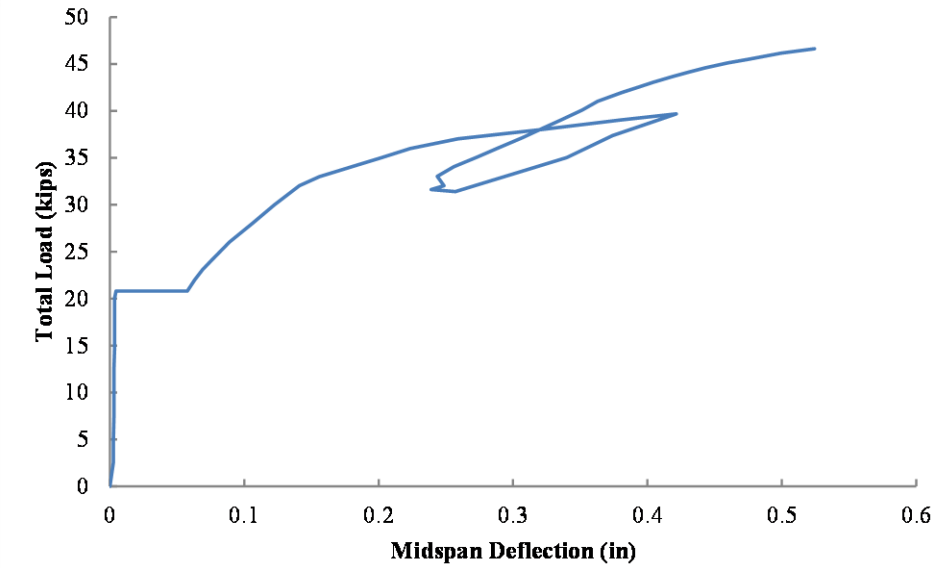

Figure A-52: Load vs. Lateral Displacement for SP2-05PT30-EX-1-DS

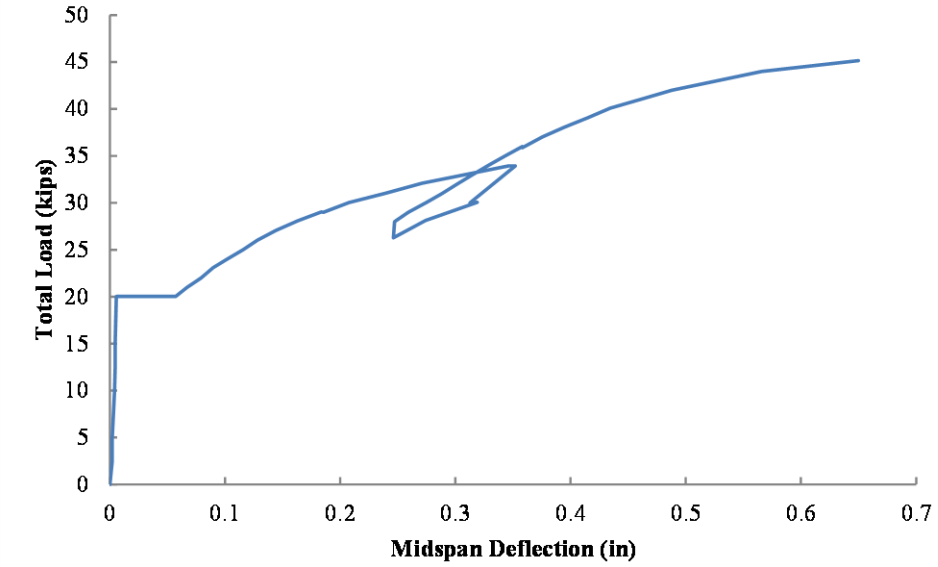

Figure A-53: Load vs. Lateral Displacement for SP2-05PT25-EX-2-DS

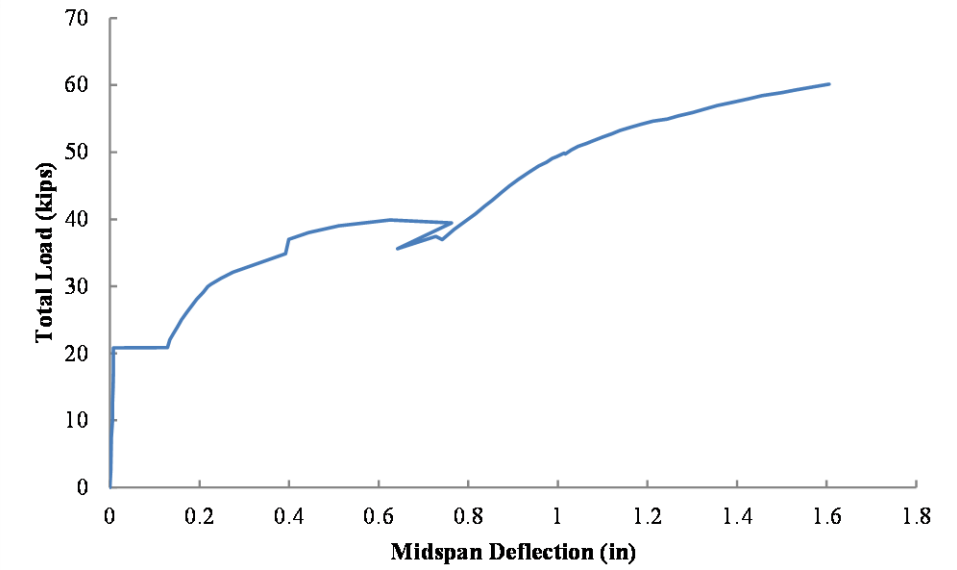

Figure A-54: Load vs. Lateral Displacement for SP2-05PT35-EX-3-DS

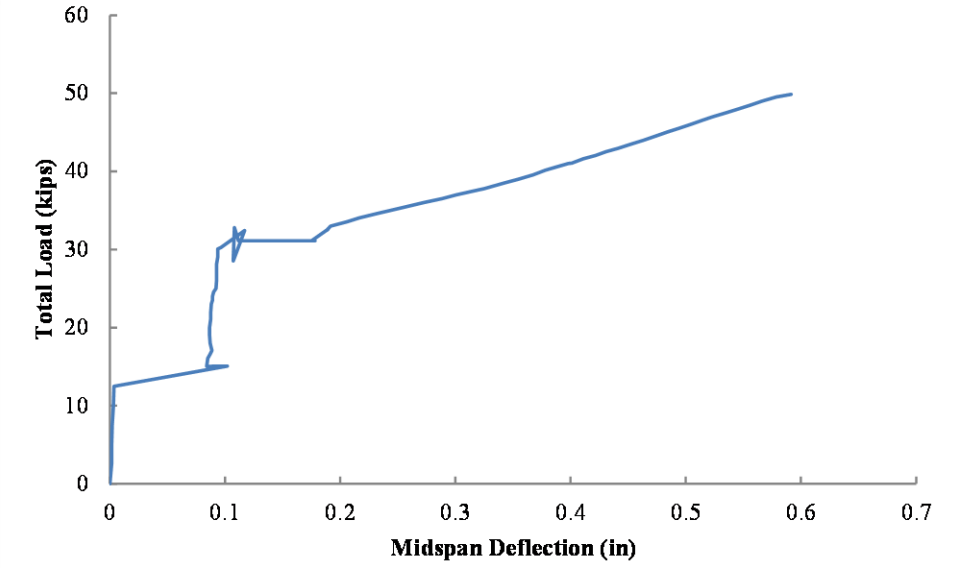

Figure A-55: Load vs. Lateral Displacement for SP2-06PT30-EX-1-DS

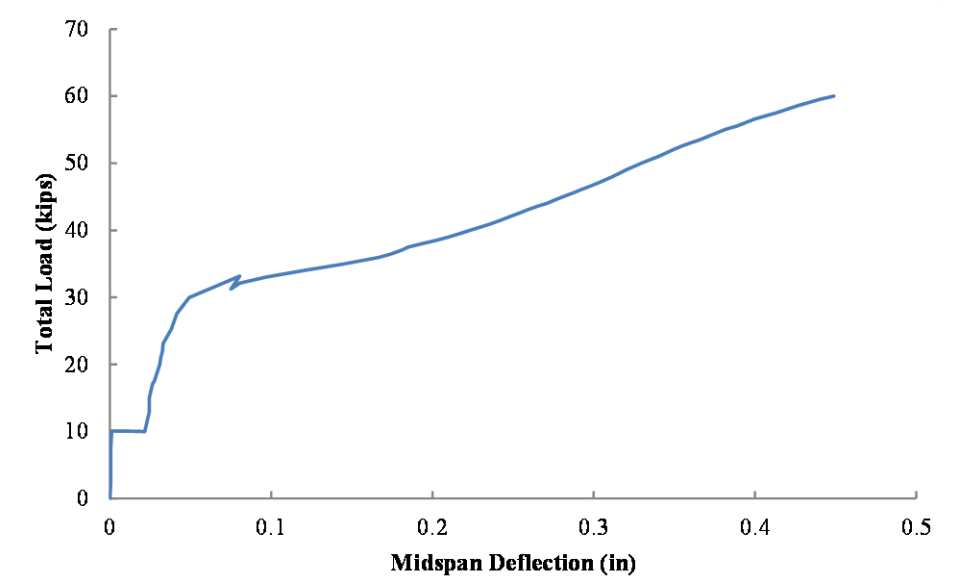

Figure A-56: Load vs. Lateral Displacement for SP2-06PT30-EX-2-DS

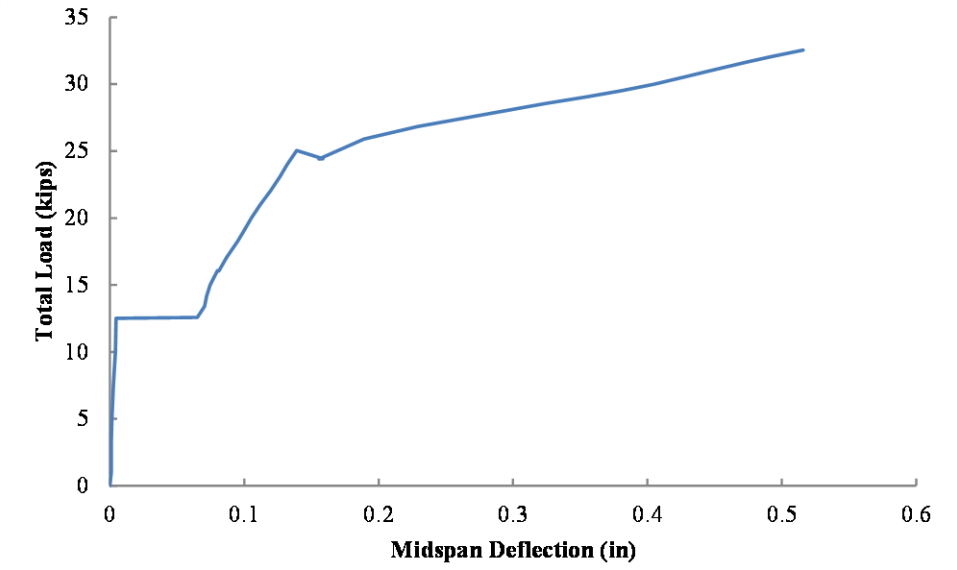

Figure A-57: Load vs. Lateral Displacement for SP2-06PT25-EX-3-DS

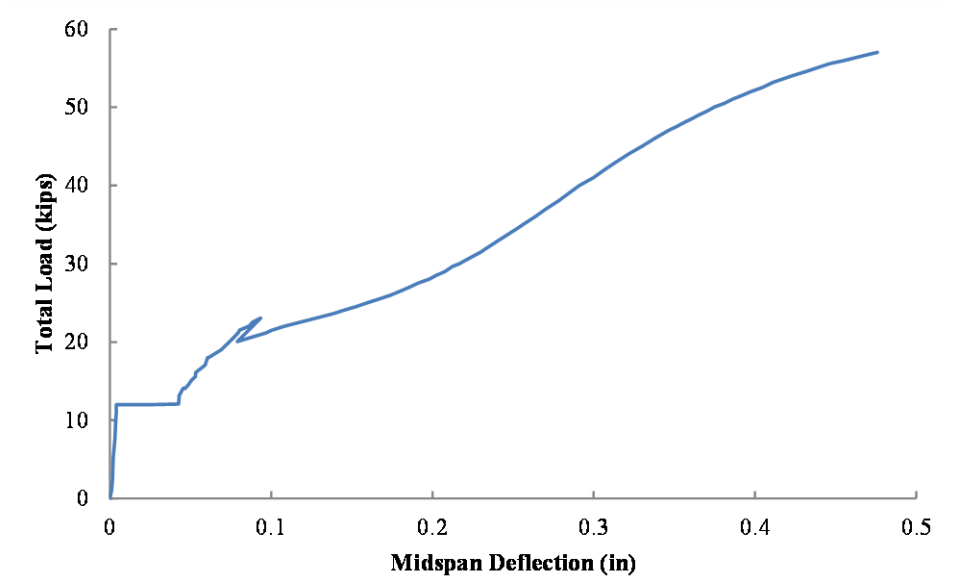

Figure A-58: Load vs. Lateral Displacement for SP2-06PT20-EX-4-DS

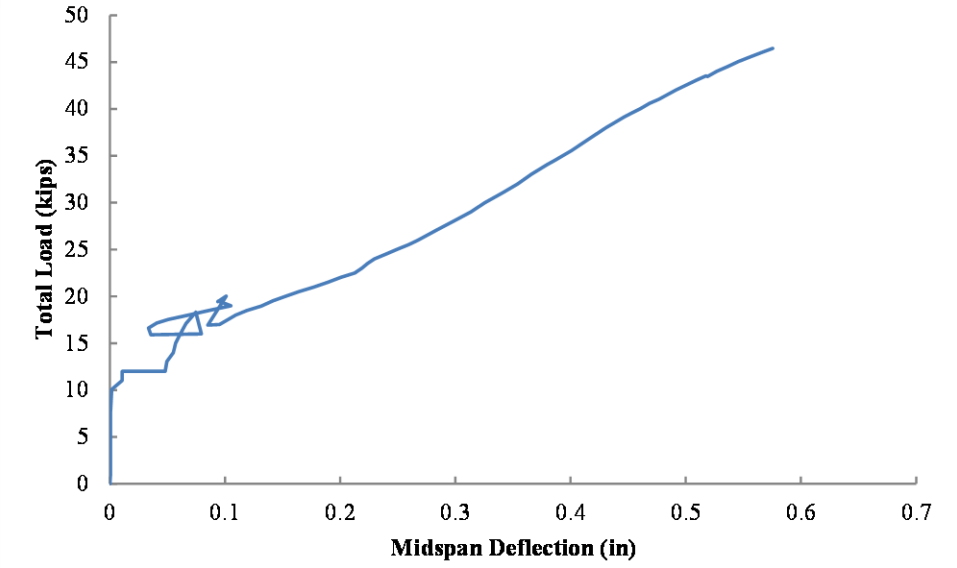

Figure A-59: Load vs. Lateral Displacement for SP2-06PT15-EX-5-DS

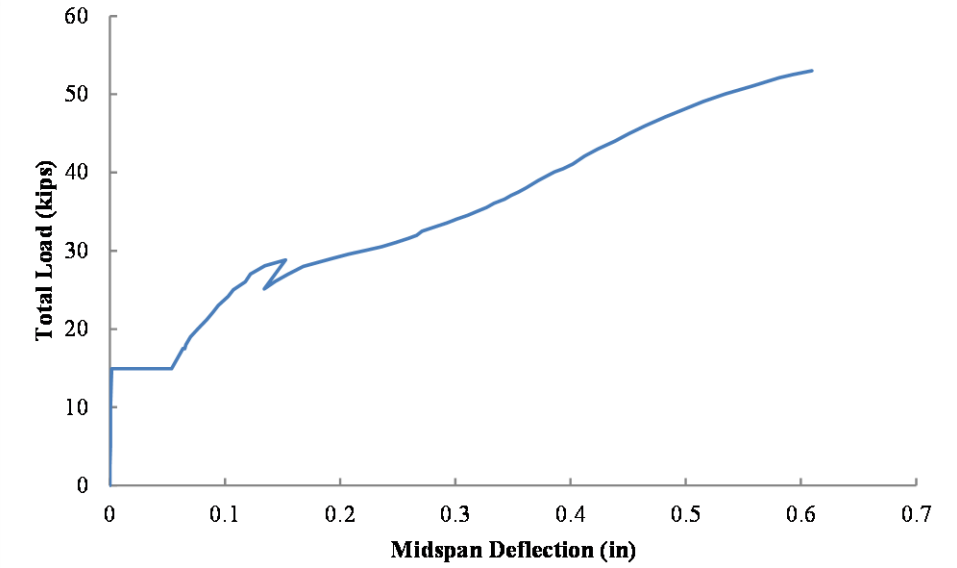

Figure A-60: Load vs. Lateral Displacement for SP2-06PT25-EX-6-DS

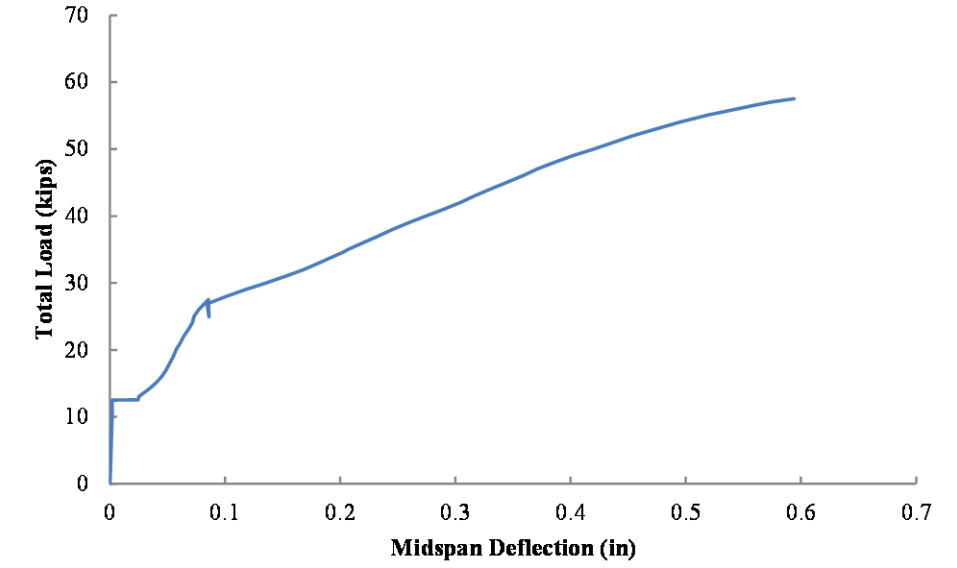

Figure A-61: Load vs. Lateral Displacement for SP2-06PT25-EX-7-SS

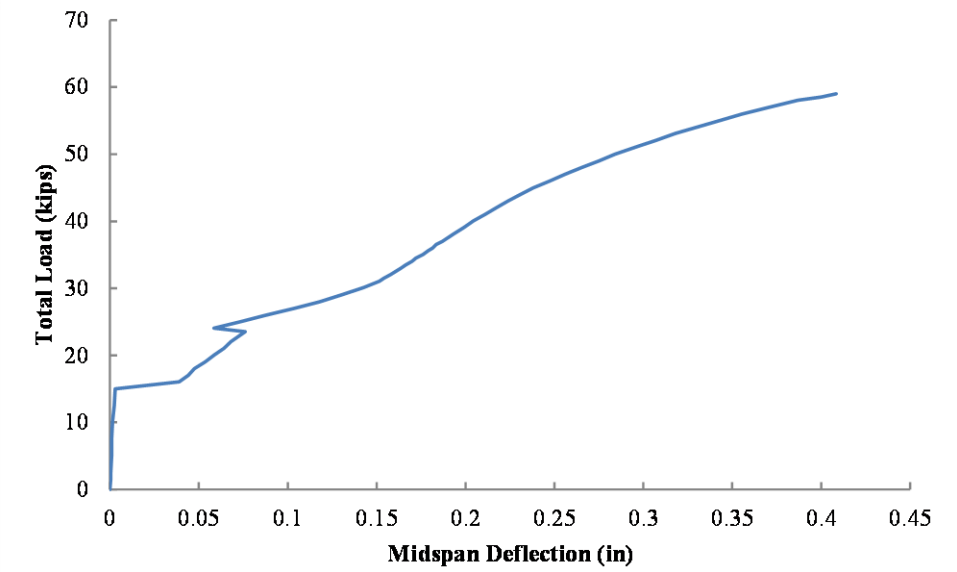

Figure A-62: Load vs. Lateral Displacement for SP2-06PT20-EX-8-SS

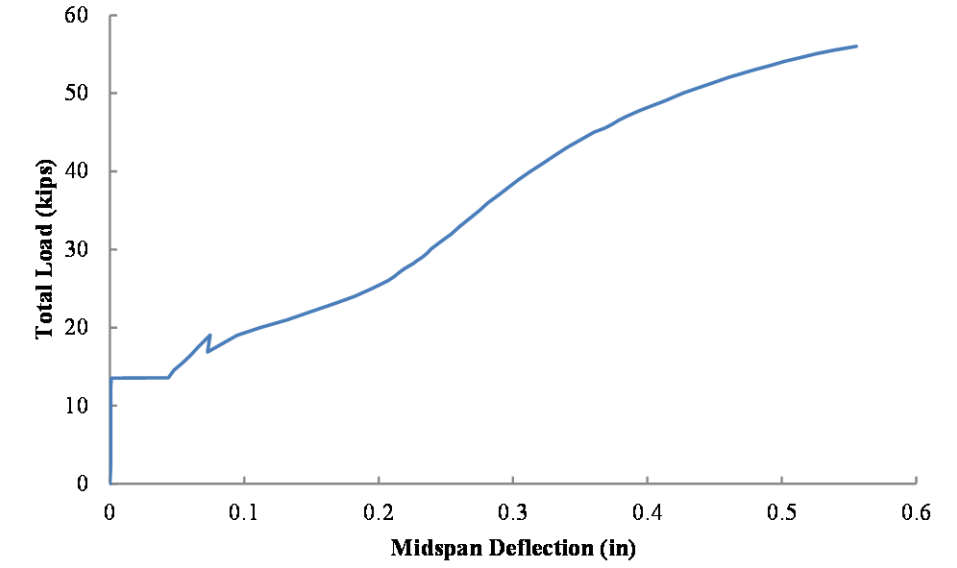

Figure A-63: Load vs. Lateral Displacement for SP2-06PT15-EX-9-SS

A.2.2.3 SP2 External Load Tests

This subsection includes the load versus lateral deflection plot from the single external load test on SP2. The test ended in a full buckling failure which resulted in extensive cracking in the member.

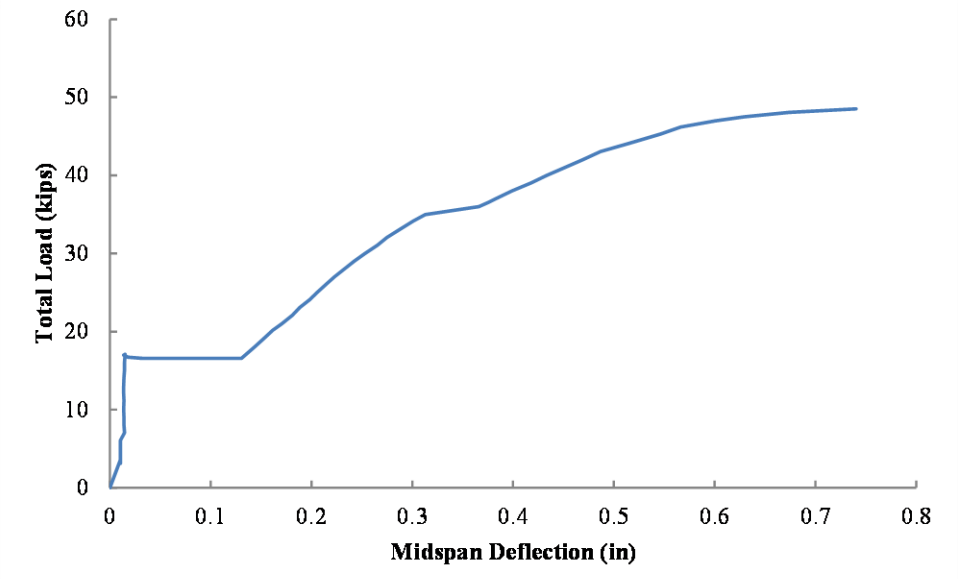

Figure A-64: Load vs. Lateral Displacement for SP2-PT0-EX-1

A.3 LOAD VS. LATERAL CURVATURE DATA

This portion of the appendix provides plots of total axial load versus lateral curvature measurements for all load tests. As discussed in the previous chapters, the lateral curvature was found as the ratio of the strain differential between a pair of mid-depth gages to the distance between the gages. Curves are provided for both the midspan and quarter point gages.

A.3.1 Specimen 1 (SP1)

This subsection includes load versus lateral curvature plots for a total of 27 load tests on the first specimen (SP1). Notes on individual tests are included in the figure captions where applicable.

A.3.1.1 SP1 Post-tensioned Tests

This subsection includes load versus lateral curvature plots for all PT load tests conducted on SP1. There were a total of 21 pre-failure tests and one post-failure test performed.

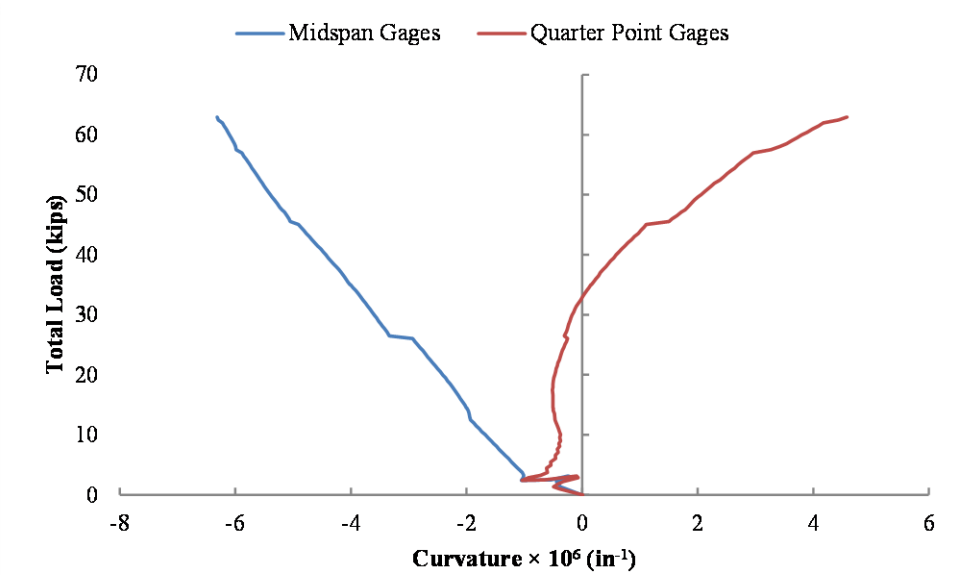

Figure A-65: Load vs. Lateral Curvature for SP1-05PT-1-CON (Midspan supports were not lowered; friction inhibited significant lateral displacement.)

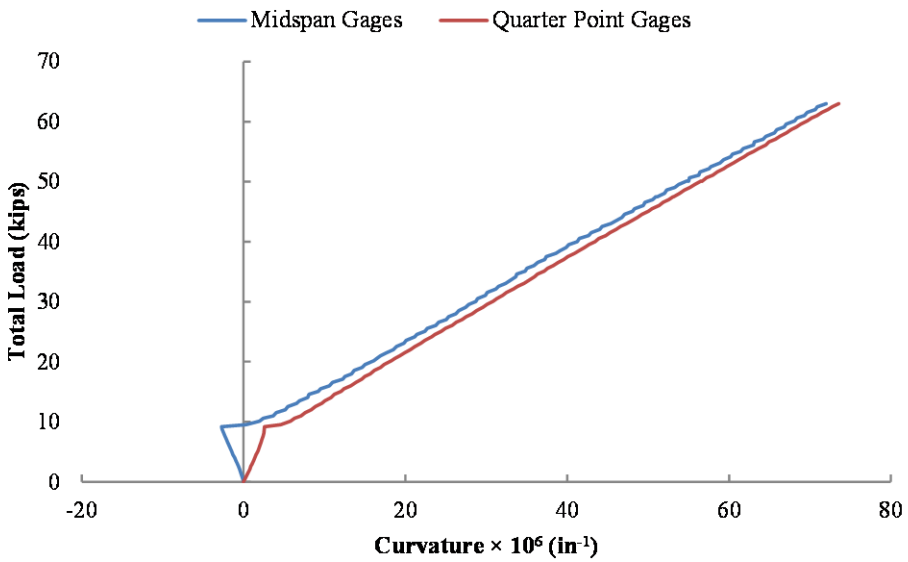

Figure A-66: Load vs. Lateral Curvature for SP1-05PT-2-ECC-E

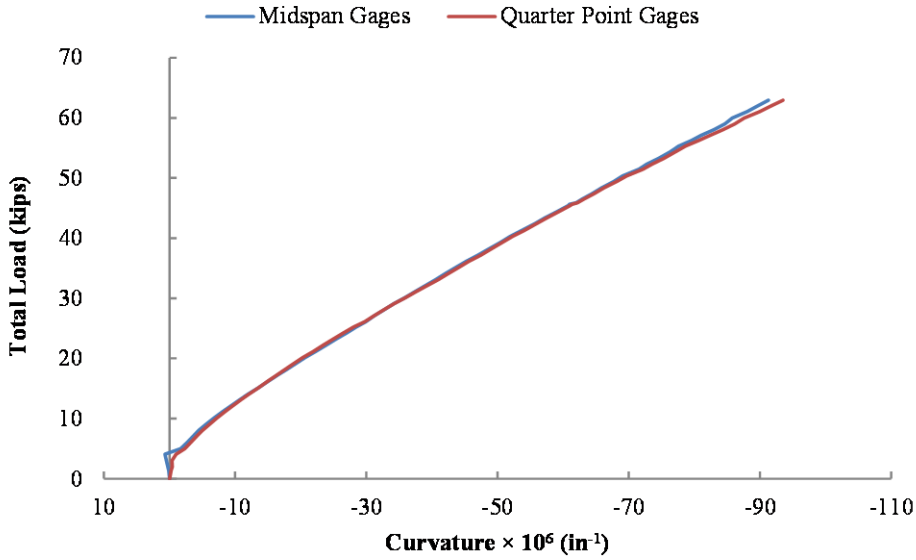

Figure A-67: Load vs. Lateral Curvature for SP1-05PT-3-ECC-W

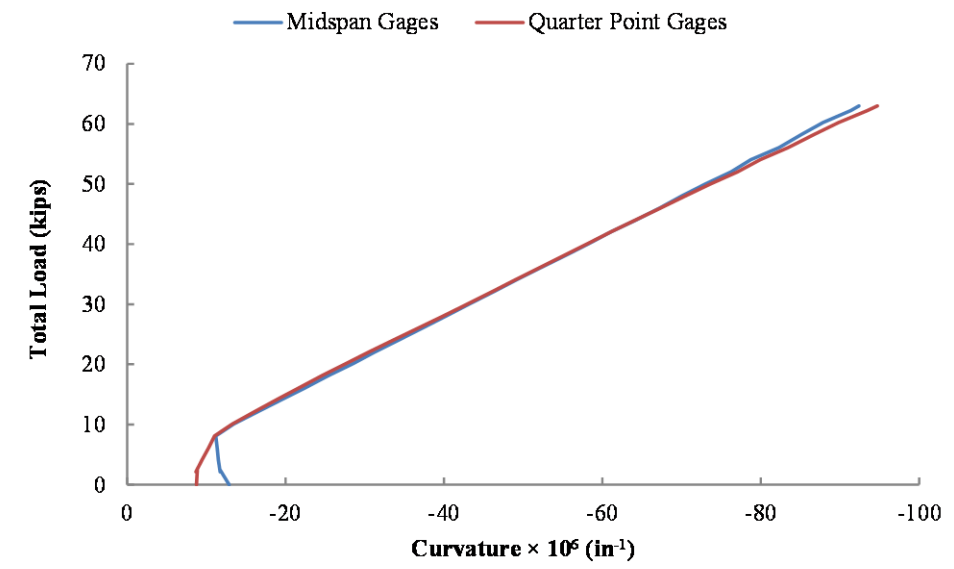

Figure A-68: Load vs. Lateral Curvature for SP1-05PT-4-ECC-W

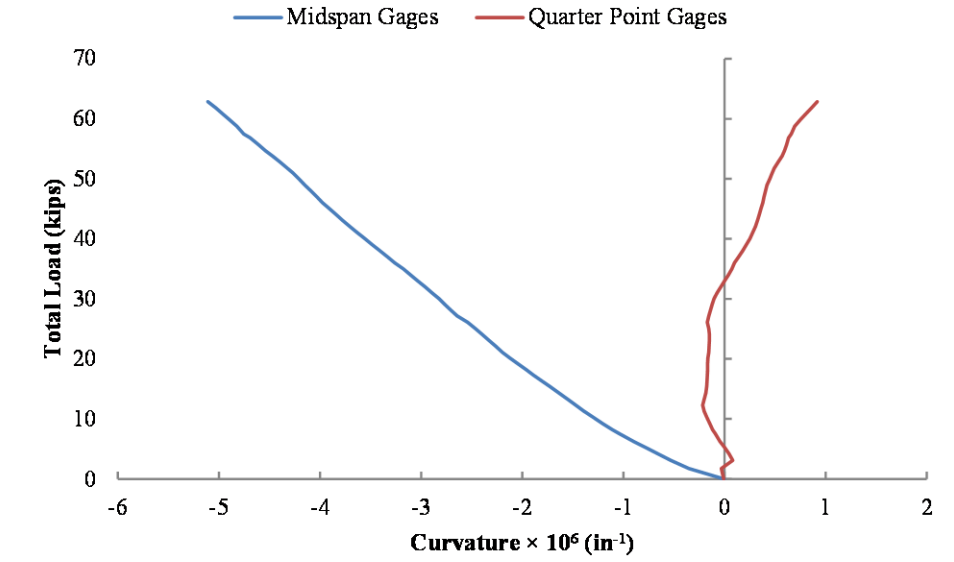

Figure A-69: Load vs. Lateral Curvature for SP1-05PT-5-CON (Midspan supports were not lowered; friction inhibited significant lateral displacement.)

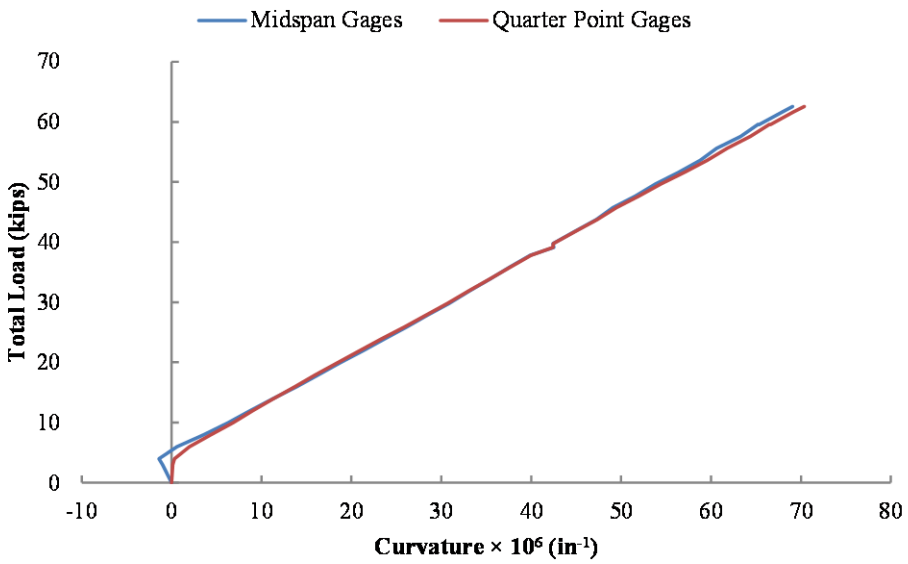

Figure A-70: Load vs. Lateral Curvature for SP1-05PT-6-ECC-E

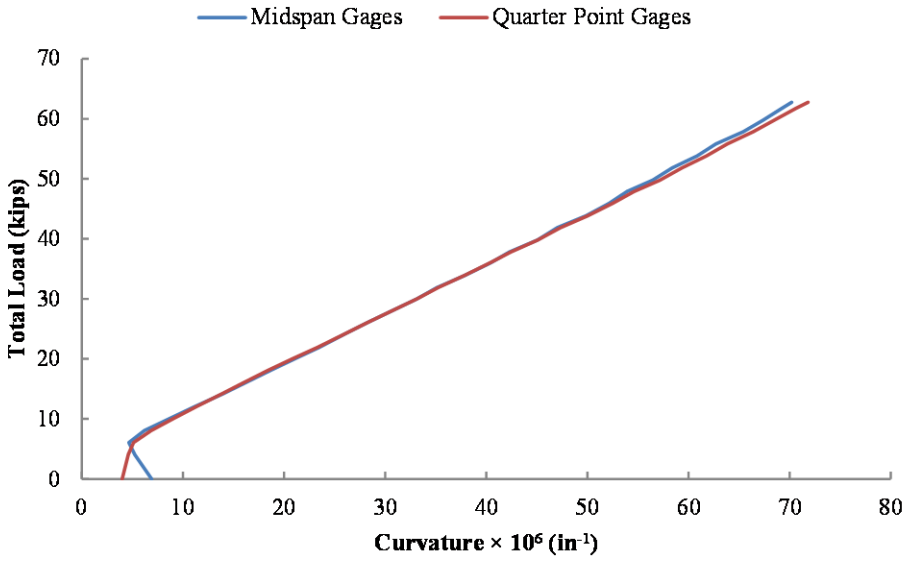

Figure A-71: Load vs. Lateral Curvature for SP1-05PT-7-ECC-E

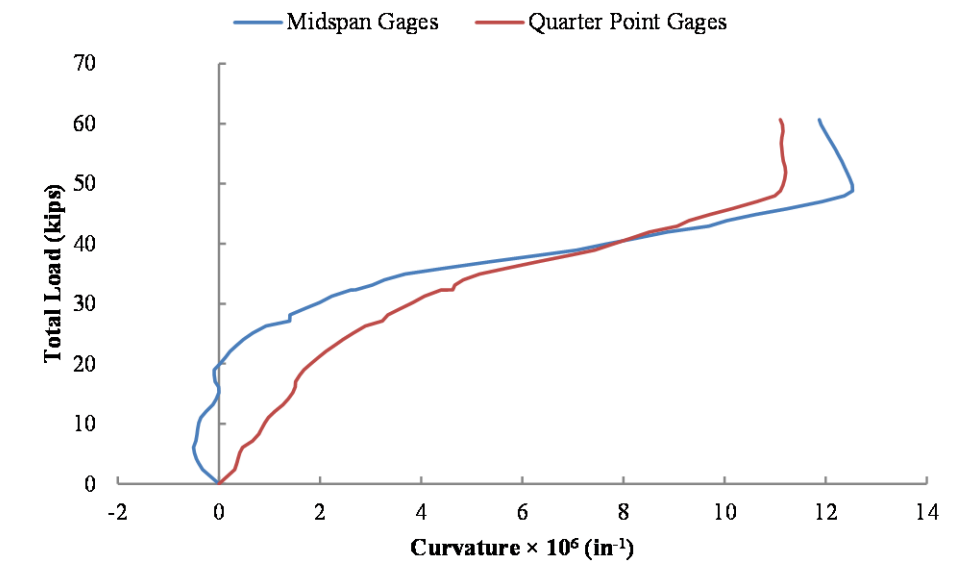

Figure A-72: Load vs. Lateral Curvature for SP1-05PT-8-CON (Specimen cambered off supports, but supports not lowered. When top strand loaded, specimen sagged, reintroducing friction to the system and limiting additional deflection.)

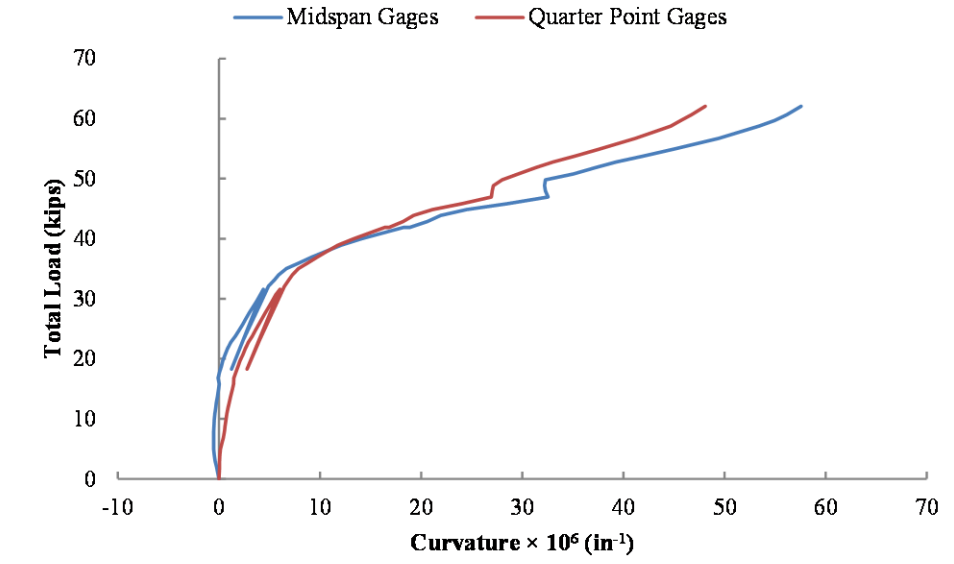

Figure A-73: Load vs. Lateral Curvature for SP1-05PT-9-CON

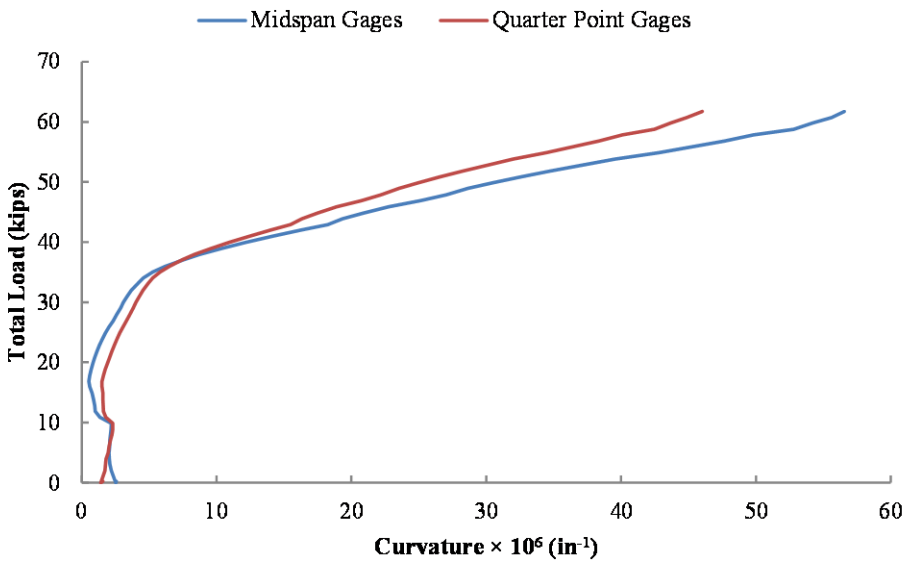

Figure A-74: Load vs. Lateral Curvature for SP1-05PT-10-CON

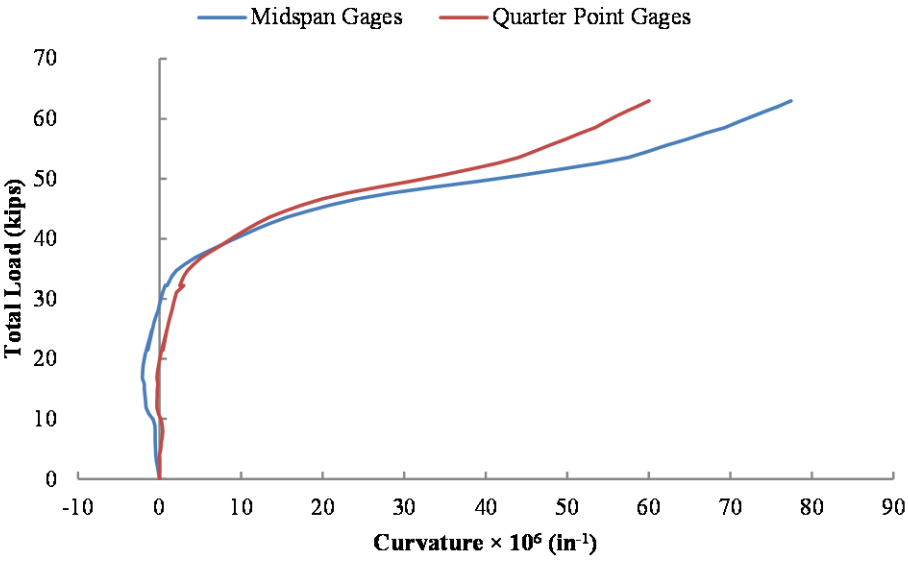

Figure A-75: Load vs. Lateral Curvature for SP1-05PT-11-CON

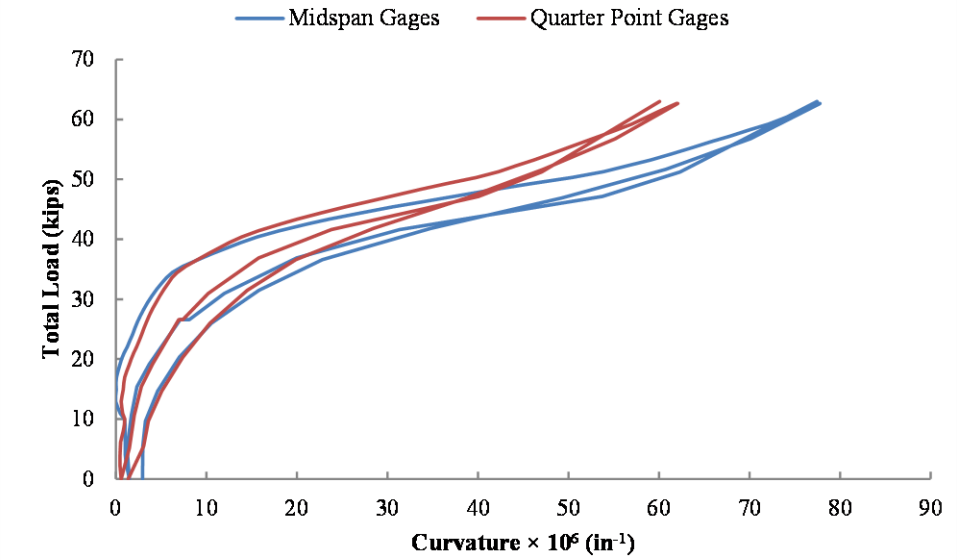

Figure A-76: Load vs. Lateral Curvature for SP1-05PT-12-CON (Two full loading and unloading cycles shown.)

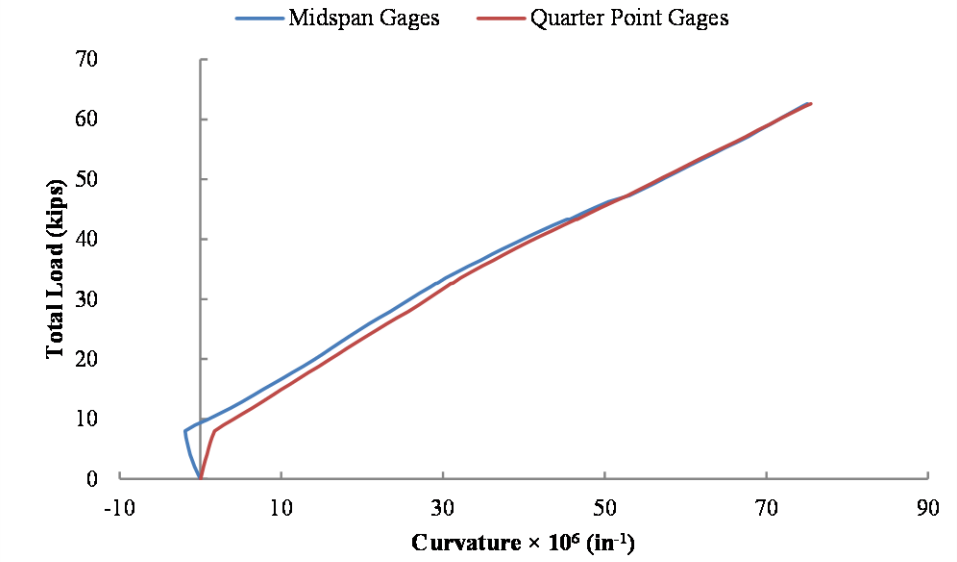

Figure A-77: Load vs. Lateral Curvature for SP1-05PT-13-ECC-E

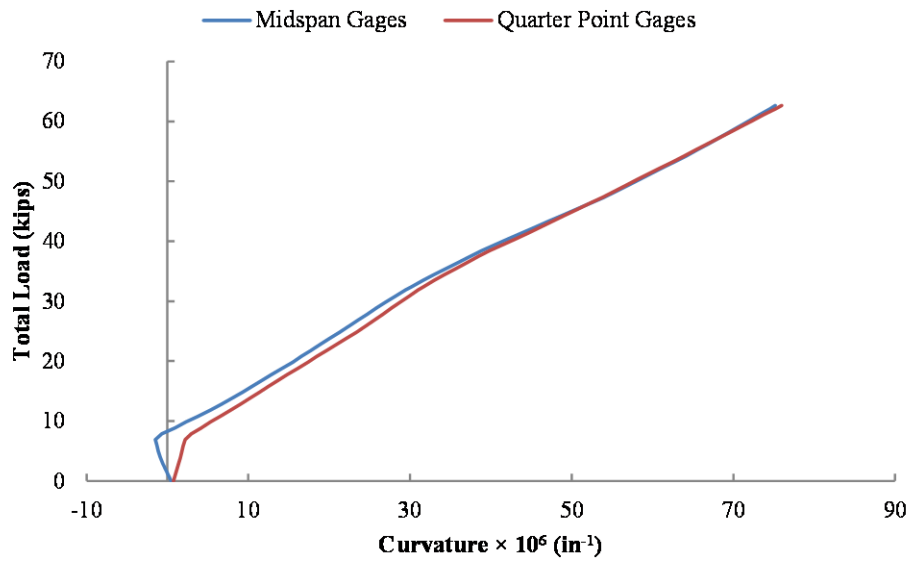

Figure A-78: Load vs. Lateral Curvature for SP1-05PT-14-ECC-E

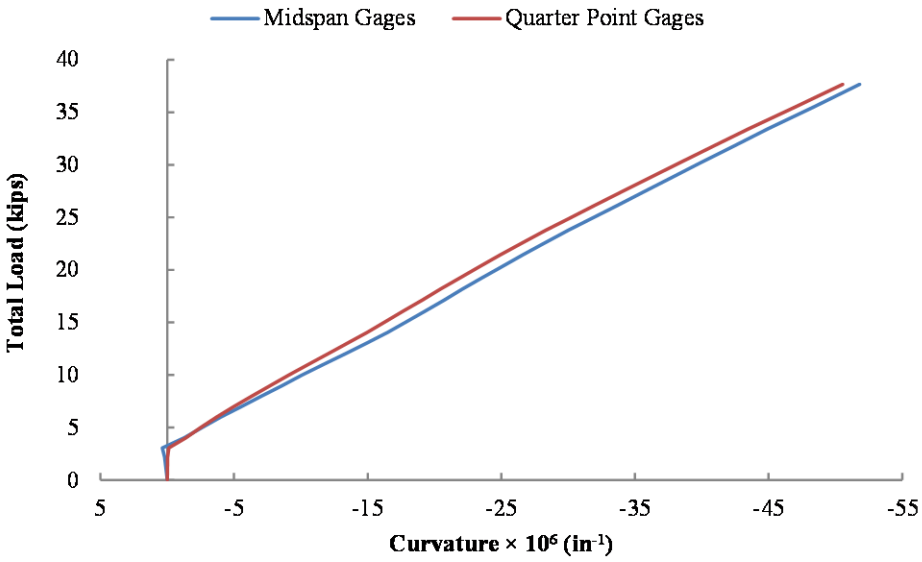

Figure A-79: Load vs. Lateral Curvature for SP1-05PT-15-ECC-W

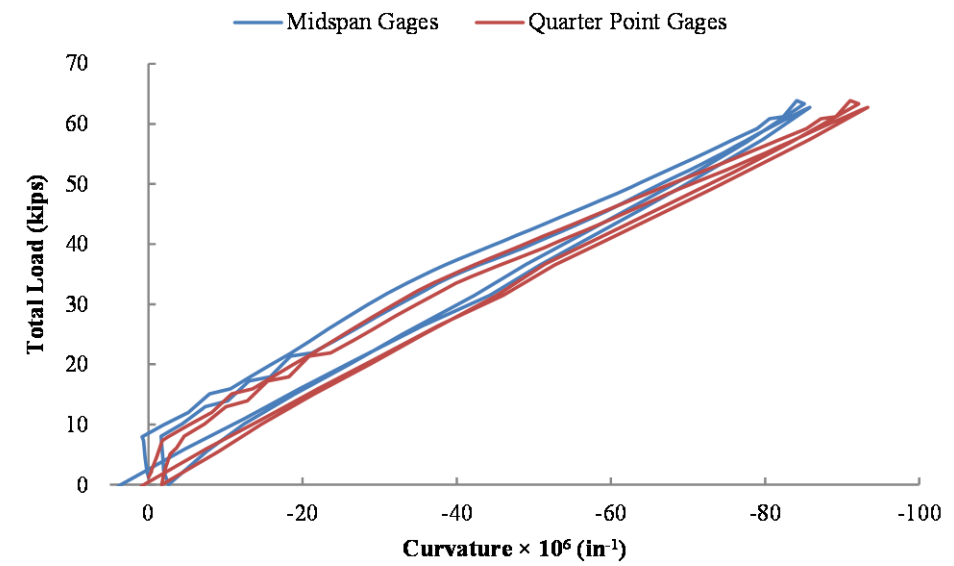

Figure A-80: Load vs. Lateral Curvature for SP1-05PT-16-ECC-W (Two full loading and unloading cycles shown.)

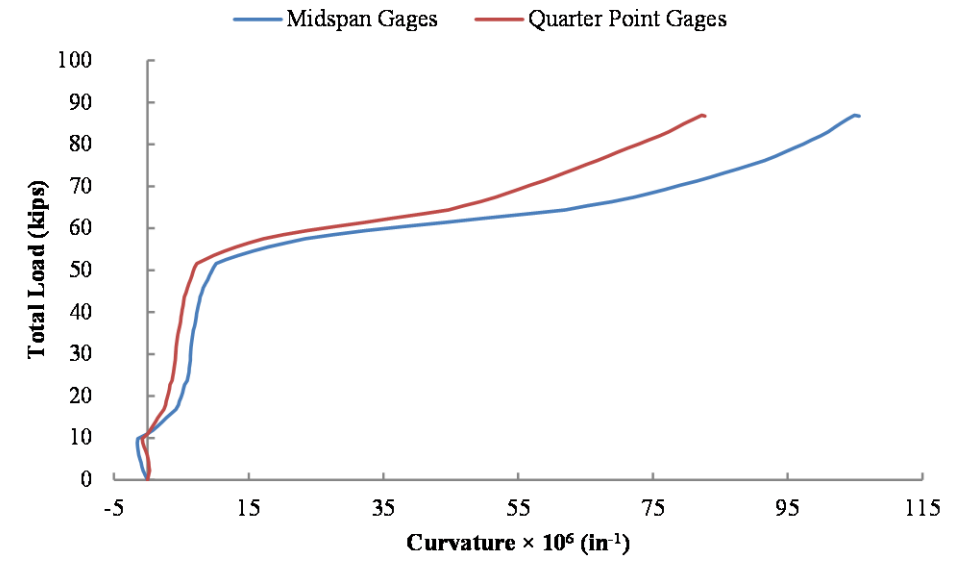

Figure A-81: Load vs. Lateral Curvature for SP1-06PT-1-CON

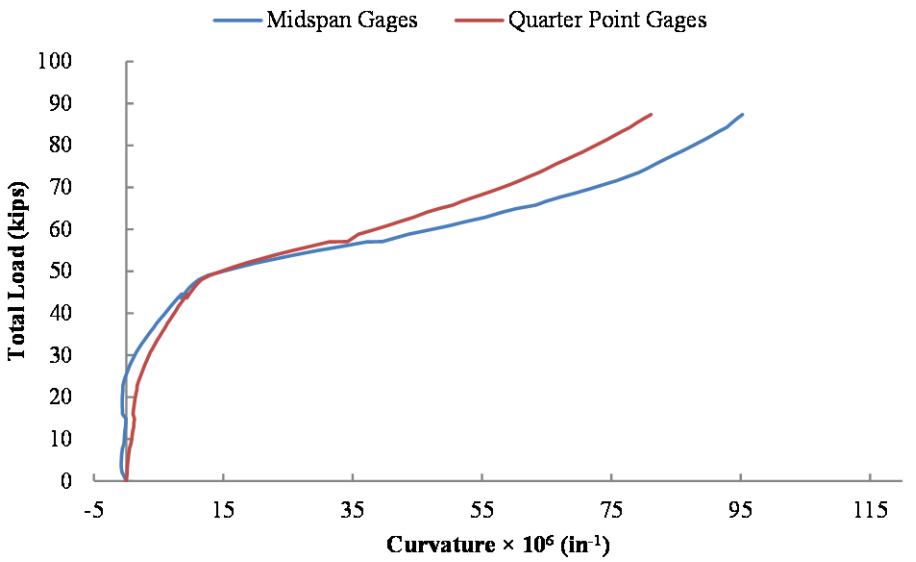

Figure A-82: Load vs. Lateral Curvature for SP1-06PT-2-CON

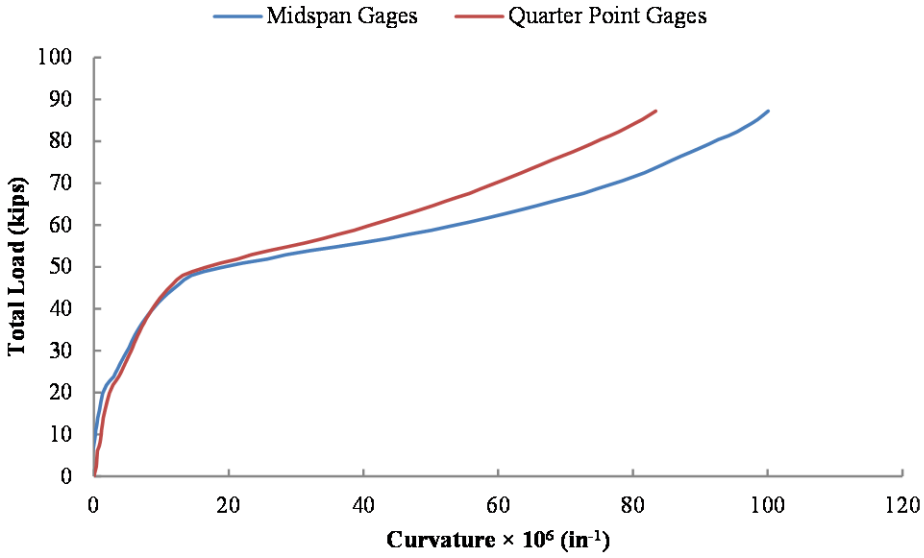

Figure A-83: Load vs. Lateral Curvature for SP1-06PT-3-CON

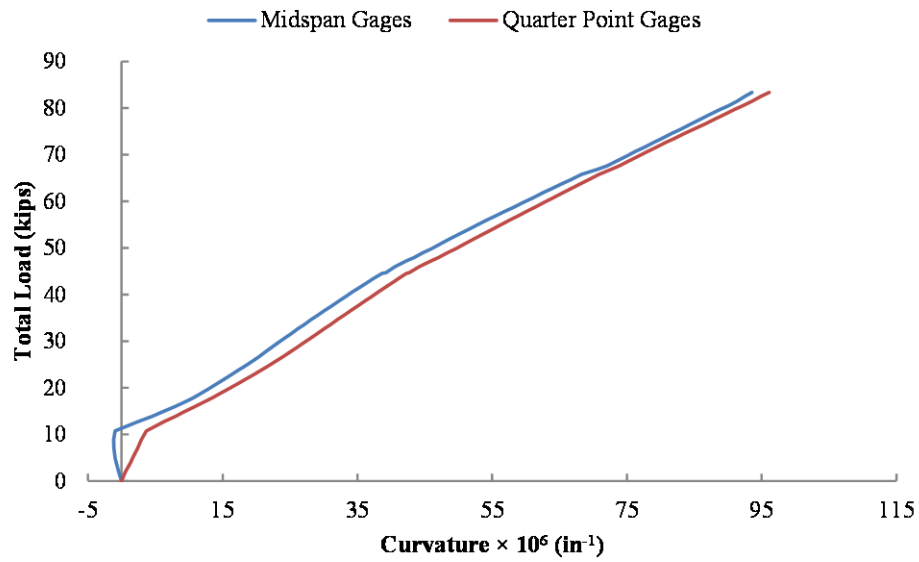

Figure A-84: Load vs. Lateral Curvature for SP1-06PT-4-ECC-E

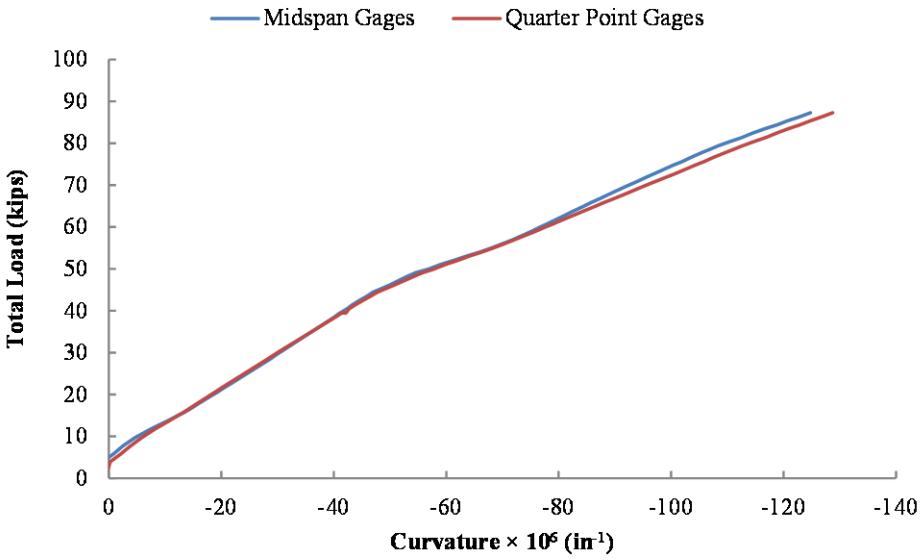

Figure A-85: Load vs. Lateral Curvature for SP1-06PT-5-ECC-W

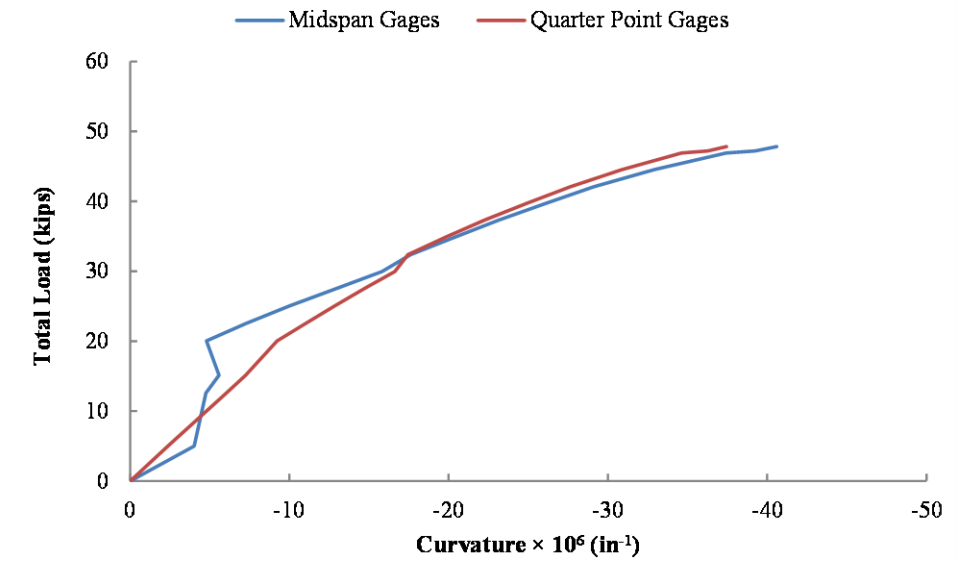

Figure A-86: Load vs. Lateral Curvature for SP1-06PT-6-CON

A.3.1.2 SP1 Combined Load Tests

The only combined load test in SP1 was performed after the specimen was cracked extensively due to a buckling failure.

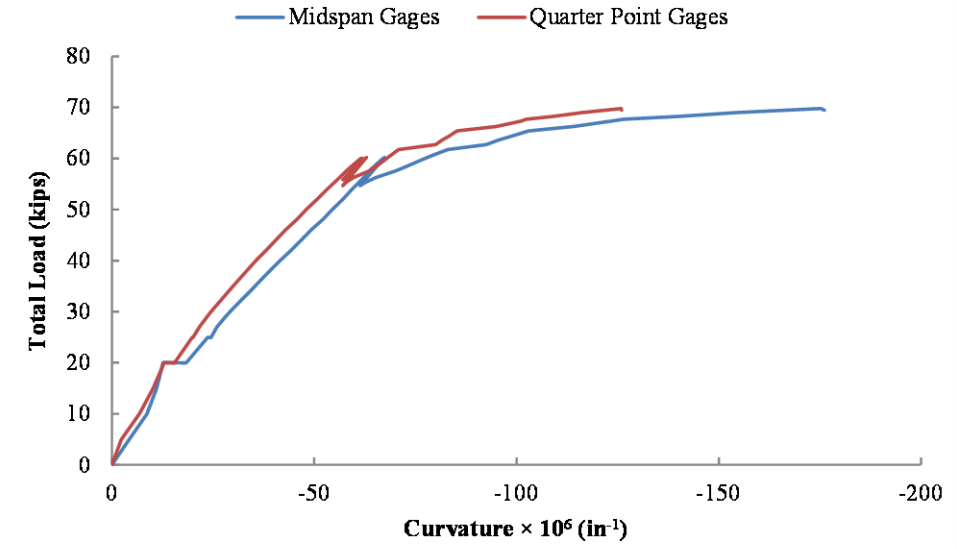

Figure A-87: Load vs. Lateral Curvature for SP1-06PT60-EX-1

A.3.1.3 SP1 External Load Tests

This sub-section includes the load versus lateral curvature plots constructed from the external load tests on SP1. There were a total of four external load tests performed.

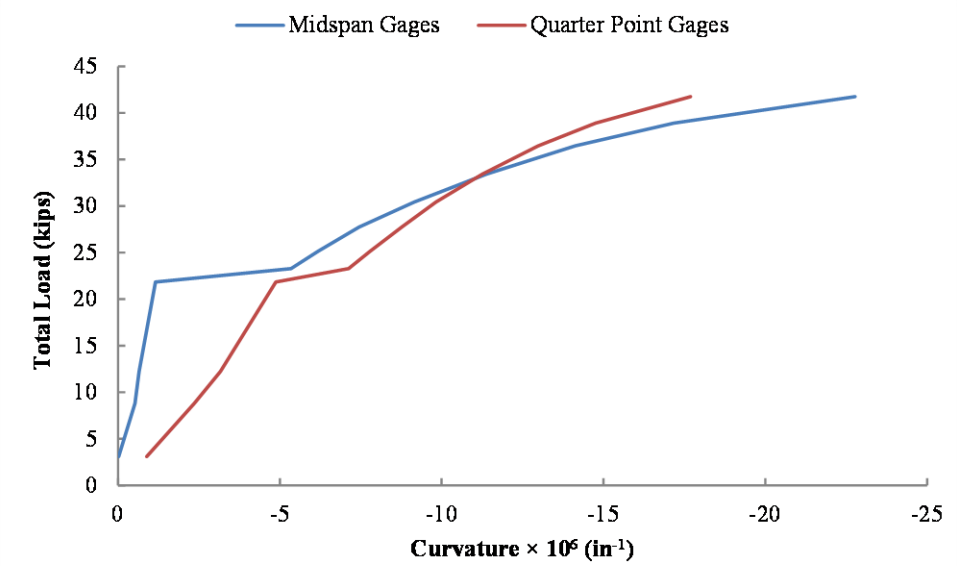

Figure A-88: Load vs. Lateral Curvature for SP1-PT0-EX-1

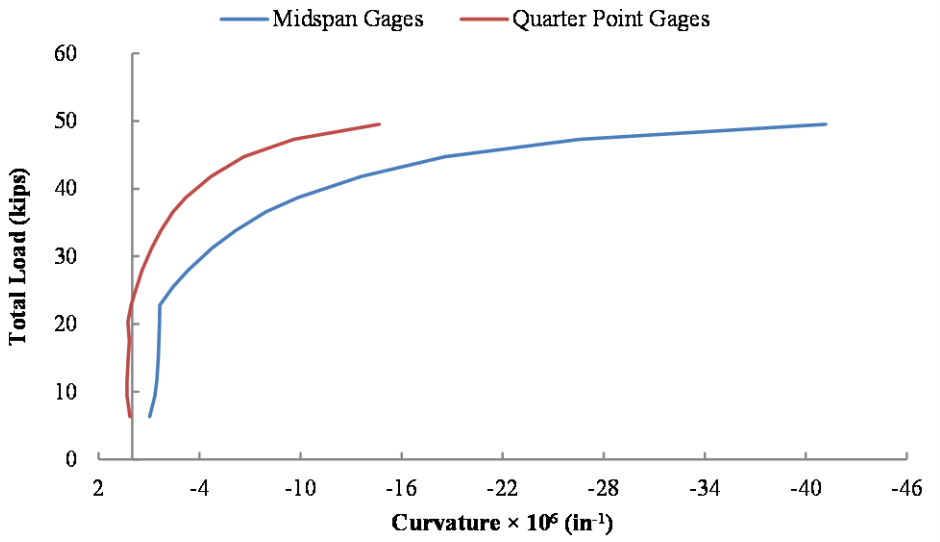

Figure A-89: Load vs. Lateral Curvature for SP1-PT0-EX-2

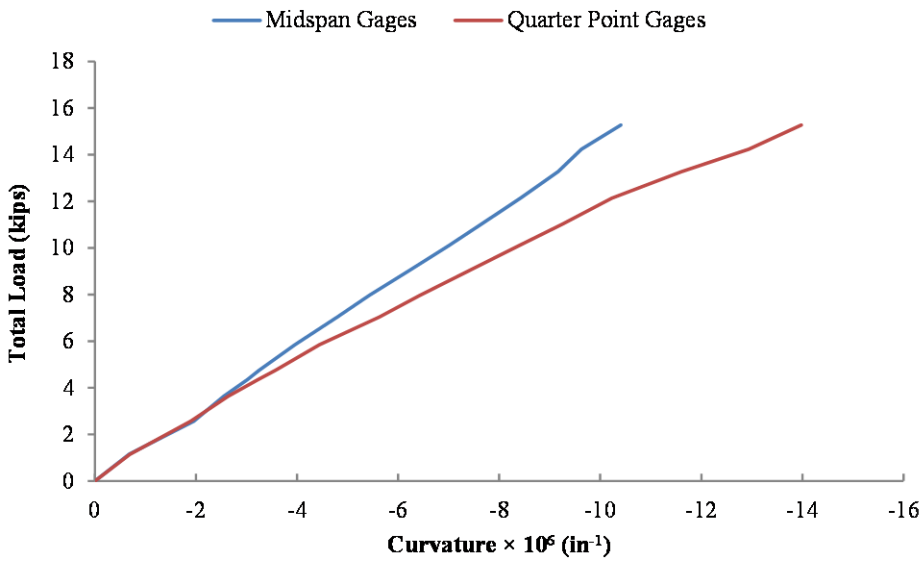

Figure A-90: Load vs. Lateral Curvature for SP1-PT0-EX-3

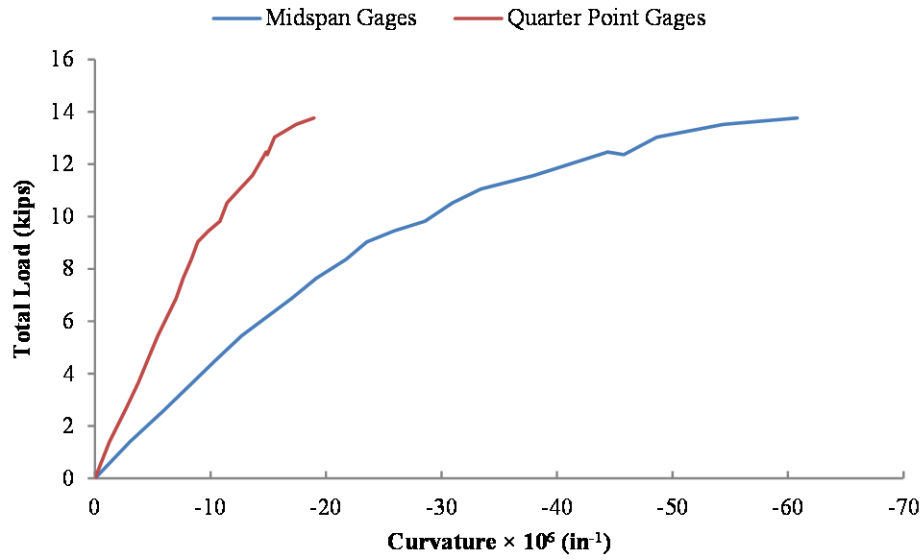

Figure A-91: Load vs. Lateral Curvature for SP1-PT0-EX-4

A.3.2 Specimen 2 (SP2)

This subsection includes load versus lateral curvature plots for each of the 35 load tests on the second specimen (SP2). Notes on individual tests are included in the figure captions where applicable.

A.3.2.1 SP2 Post-tensioned Tests

This subsection includes load versus lateral curvature plots for all PT load tests on SP2. There were a total of 22 pre-failure tests performed. No post-failure tests were performed.

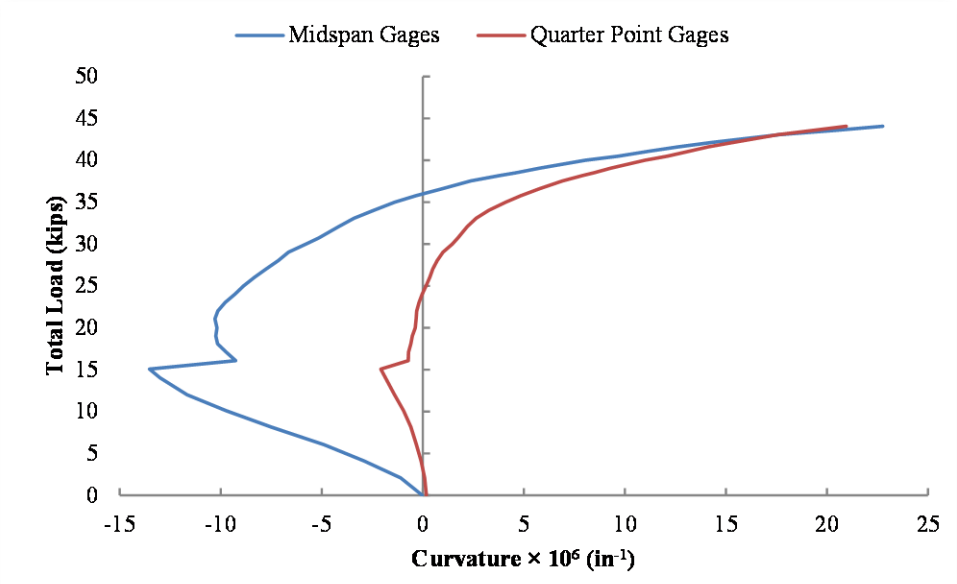

Figure A-92: Load vs. Lateral Curvature for SP2-05PT-1-CON

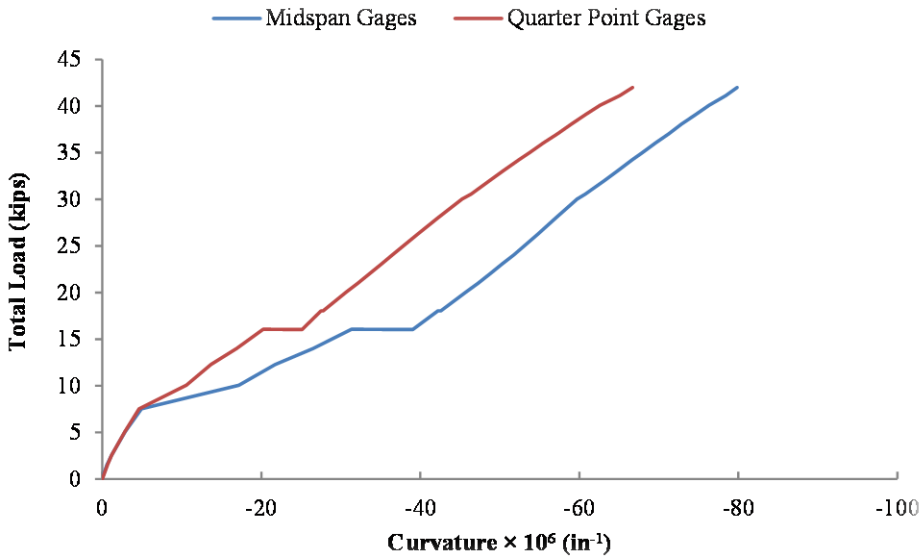

Figure A-93: Load vs. Lateral Curvature for SP2-05PT-2-ECC-W

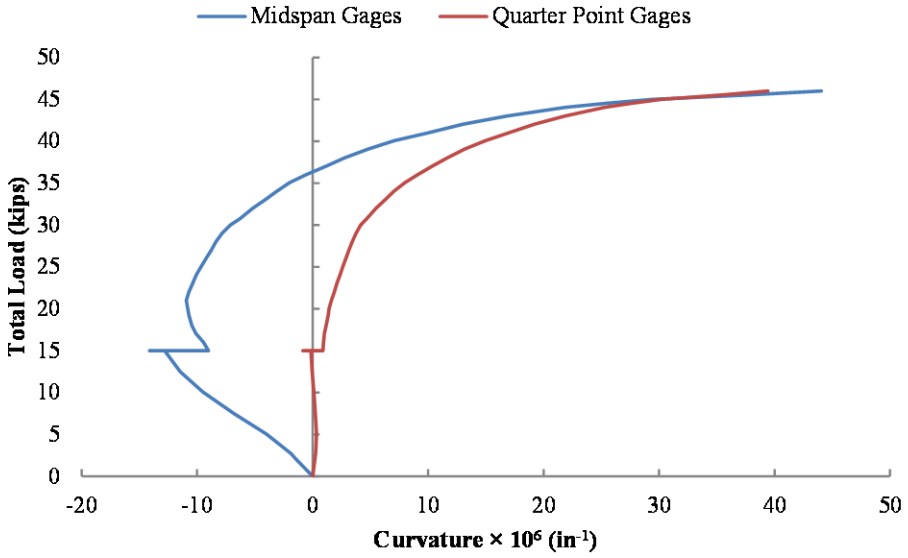

Figure A-94: Load vs. Lateral Curvature for SP2-05PT-3-CON

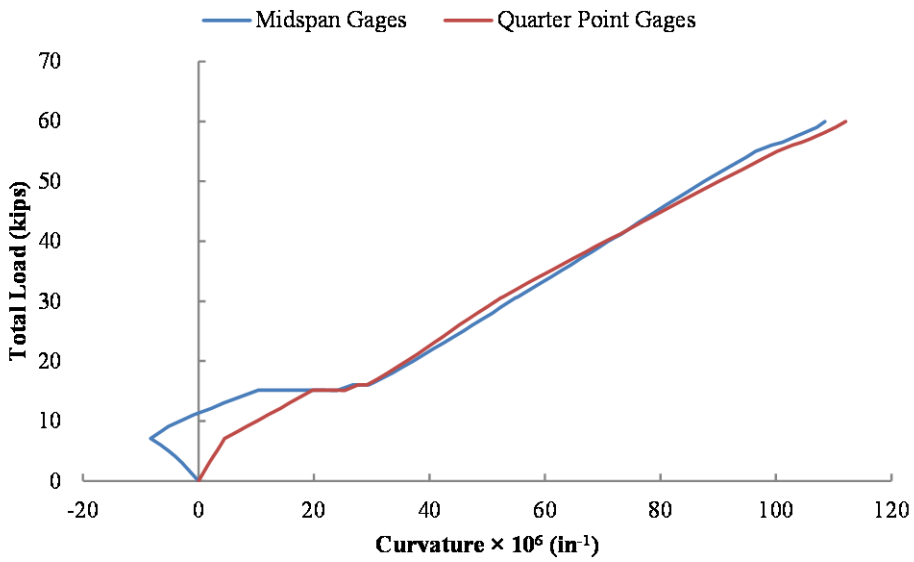

Figure A-95: Load vs. Lateral Curvature for SP2-05PT-4-ECC-E

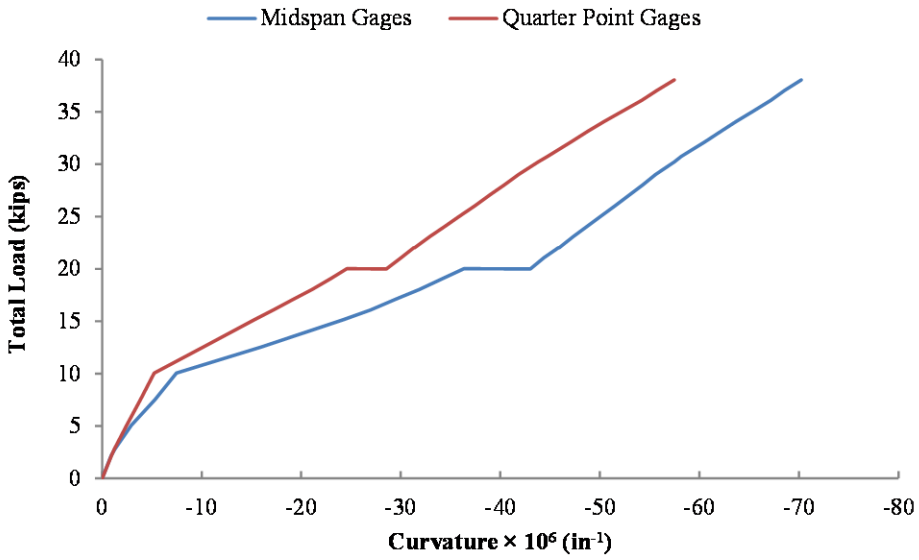

Figure A-96: Load vs. Lateral Curvature for SP2-05PT-5-ECC-W

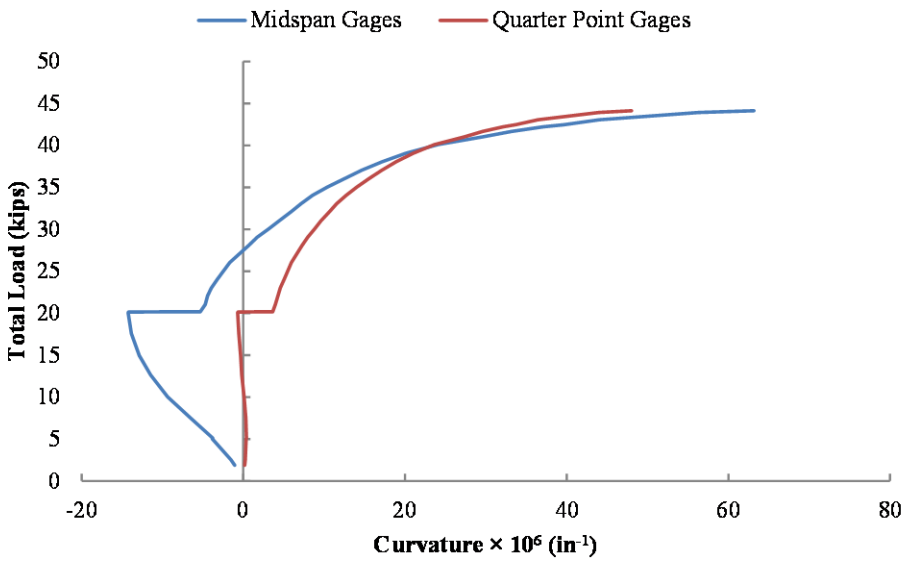

Figure A-97: Load vs. Lateral Curvature for SP2-05PT-6-CON

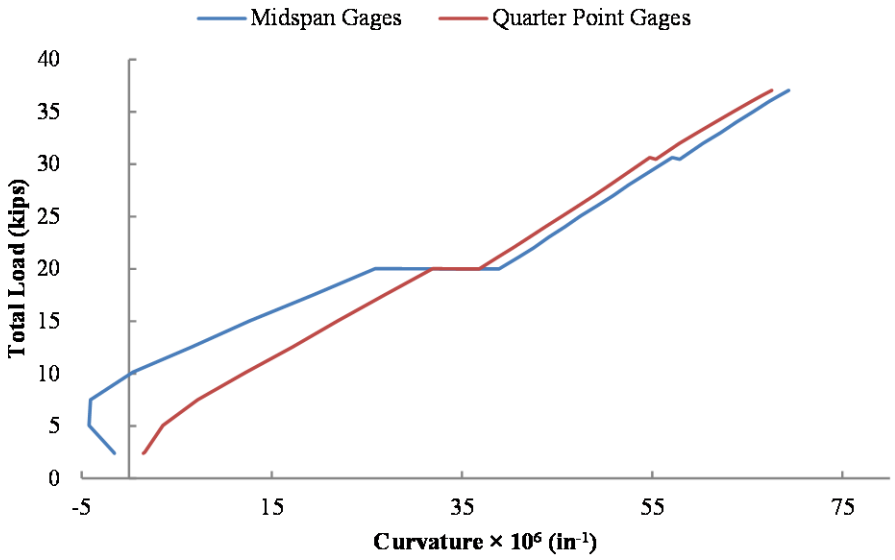

Figure A-98: Load vs. Lateral Curvature for SP2-05PT-7-ECC-E

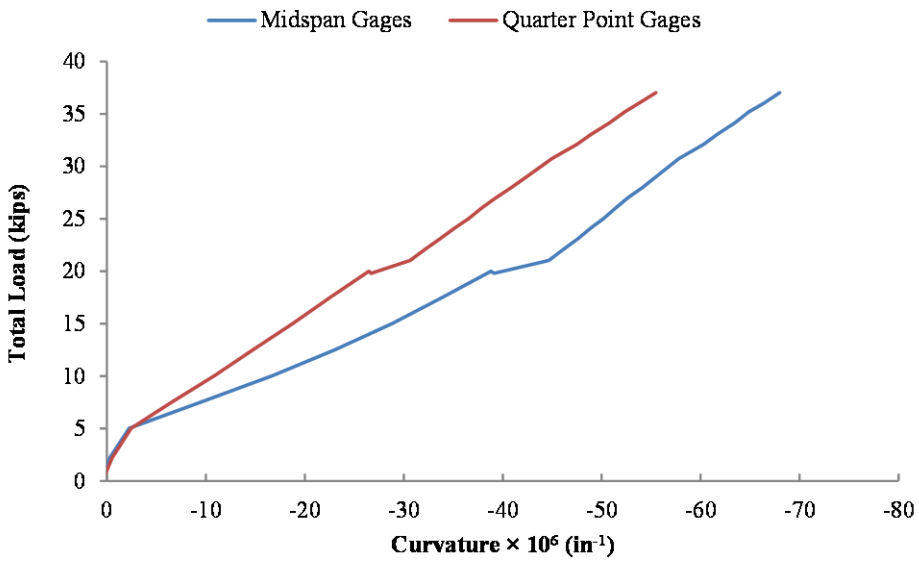

Figure A-99: Load vs. Lateral Curvature for SP2-05PT-8-ECC-W

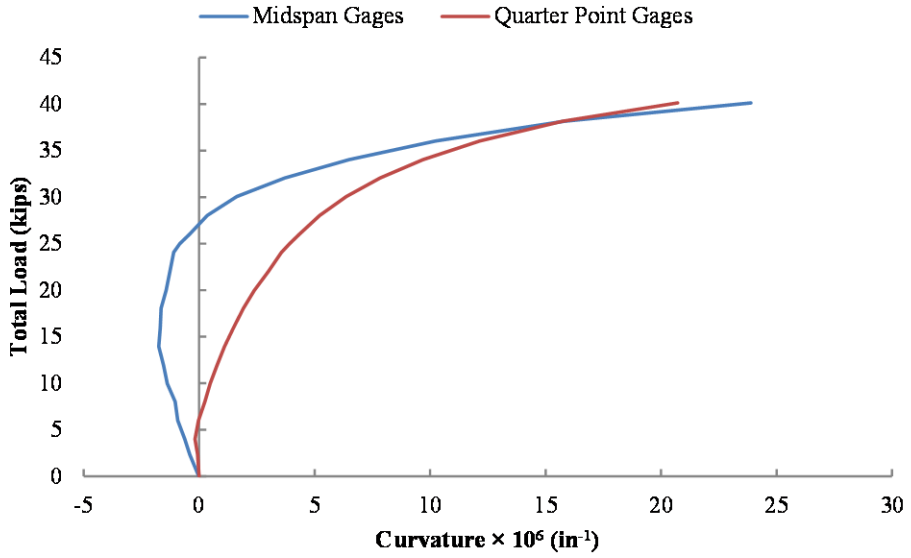

Figure A-100: Load vs. Lateral Curvature for SP2-06PT-1-CON

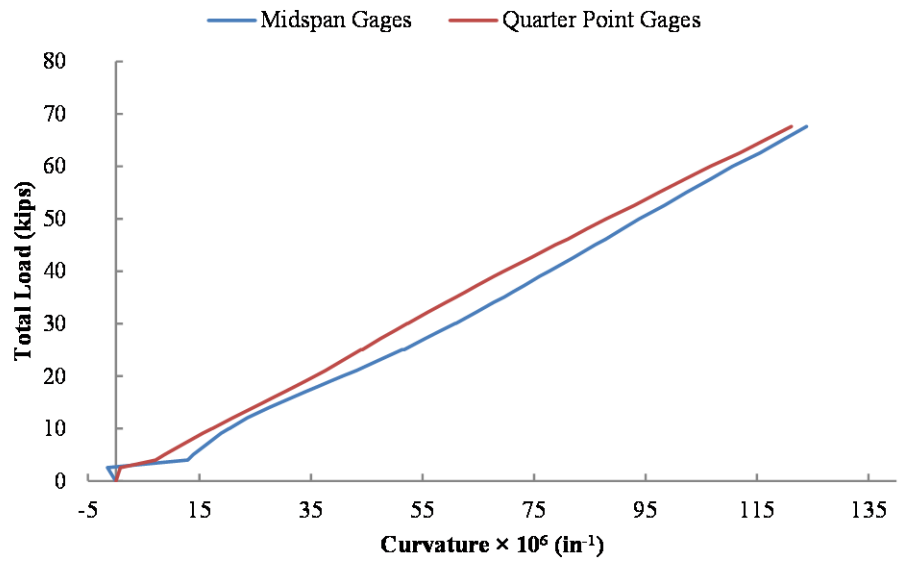

Figure A-101: Load vs. Lateral Curvature for SP2-06PT-2-ECC-E

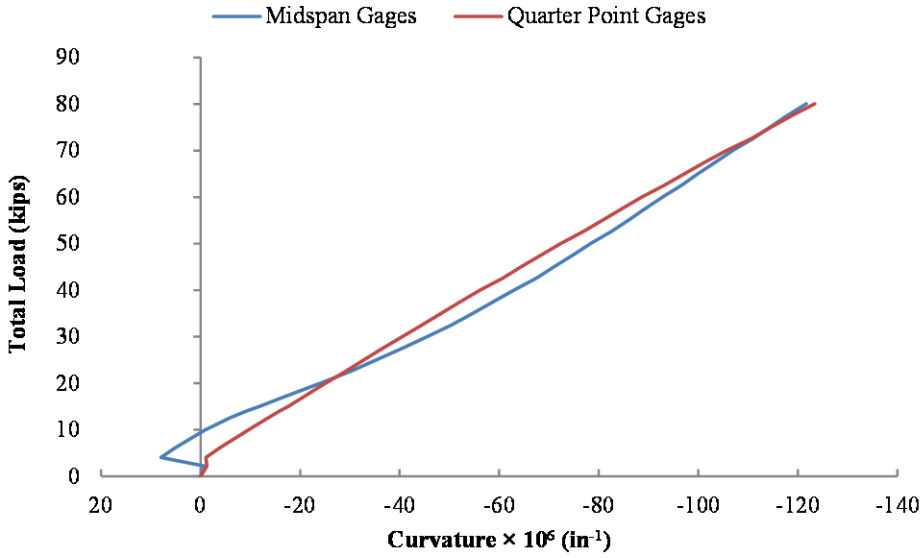

Figure A-102: Load vs. Lateral Curvature for SP2-06PT-3-ECC-W

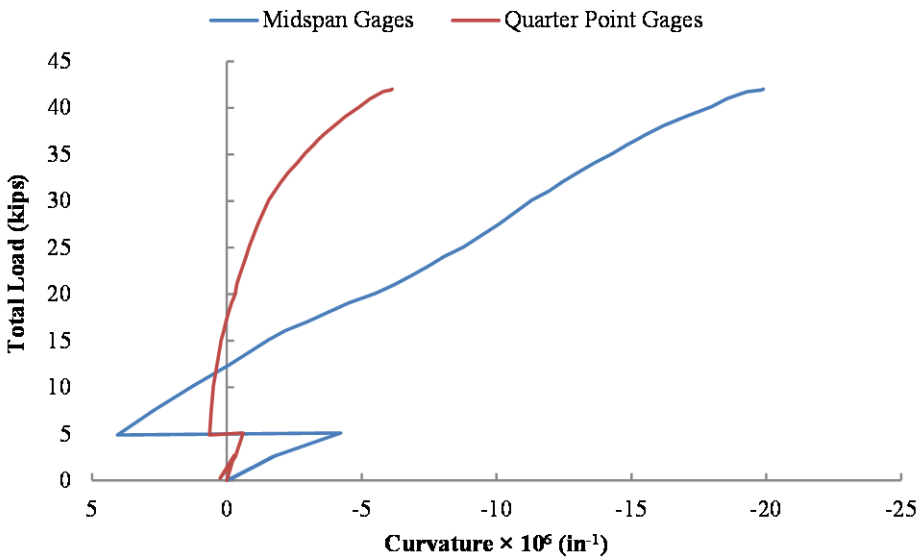

Figure A-103: Load vs. Lateral Curvature for SP2-06PT-4-CON

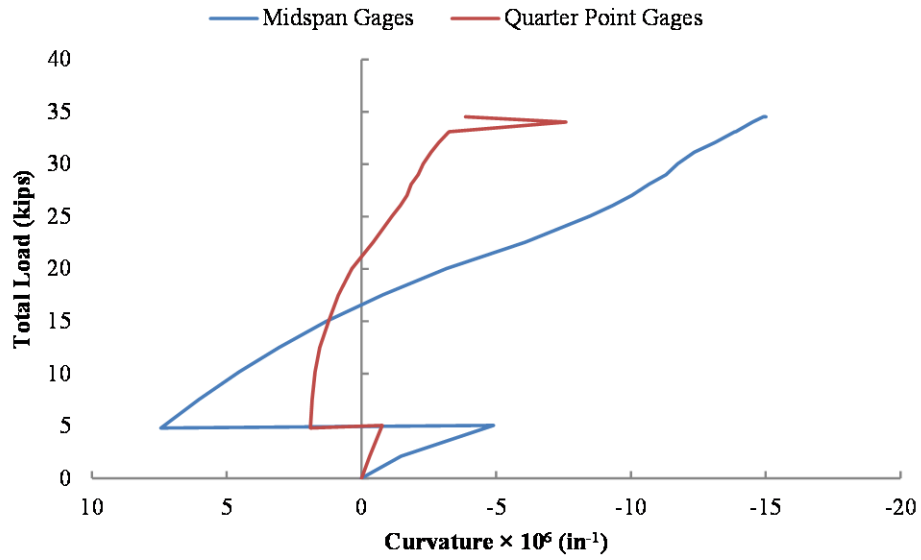

Figure A-104: Load vs. Lateral Curvature for SP2-06PT-5-CON

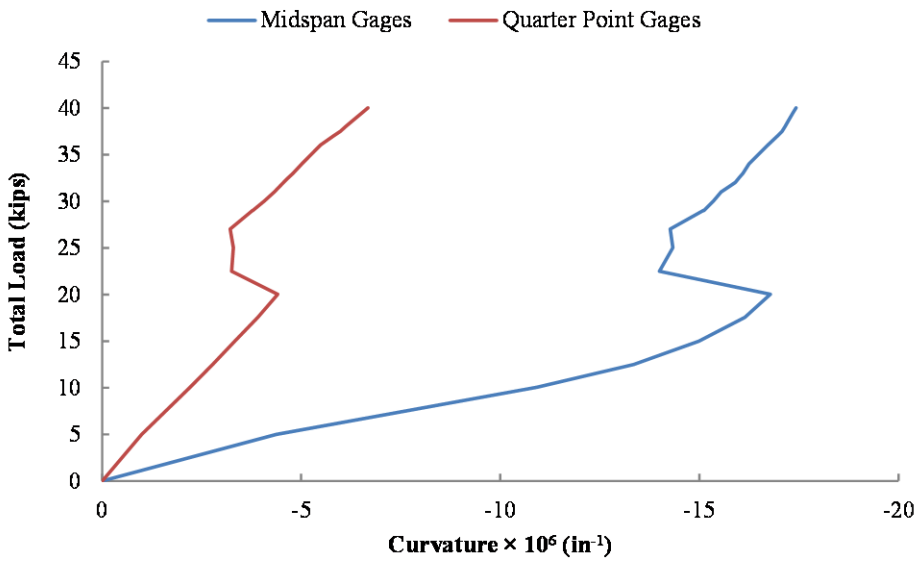

Figure A-105: Load vs. Lateral Curvature for SP2-06PT-6-CON

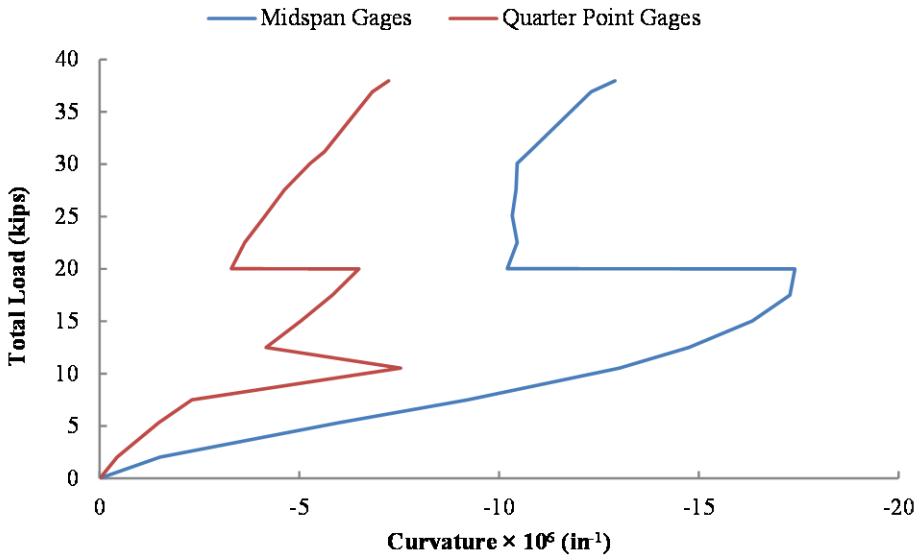

Figure A-106: Load vs. Lateral Curvature for SP2-06PT-7-CON

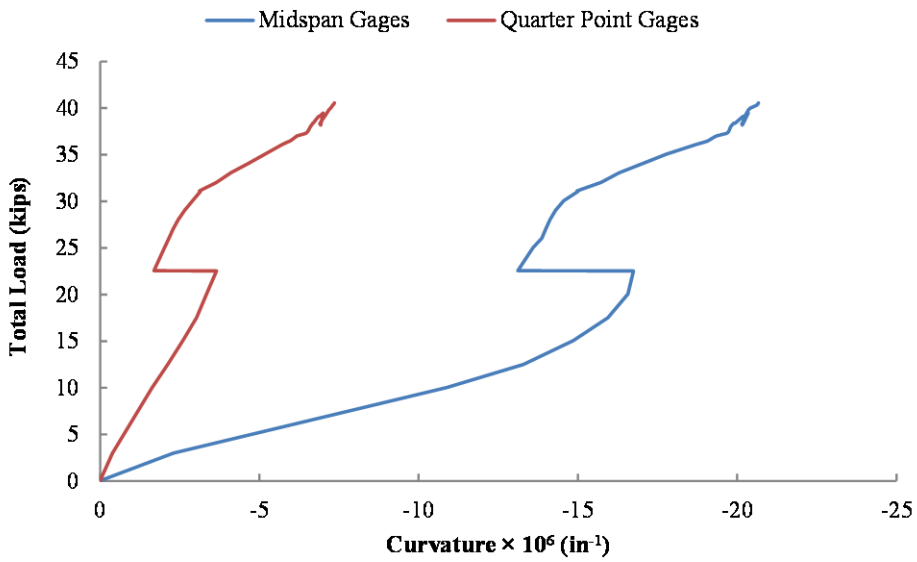

Figure A-107: Load vs. Lateral Curvature for SP2-06PT-8-CON

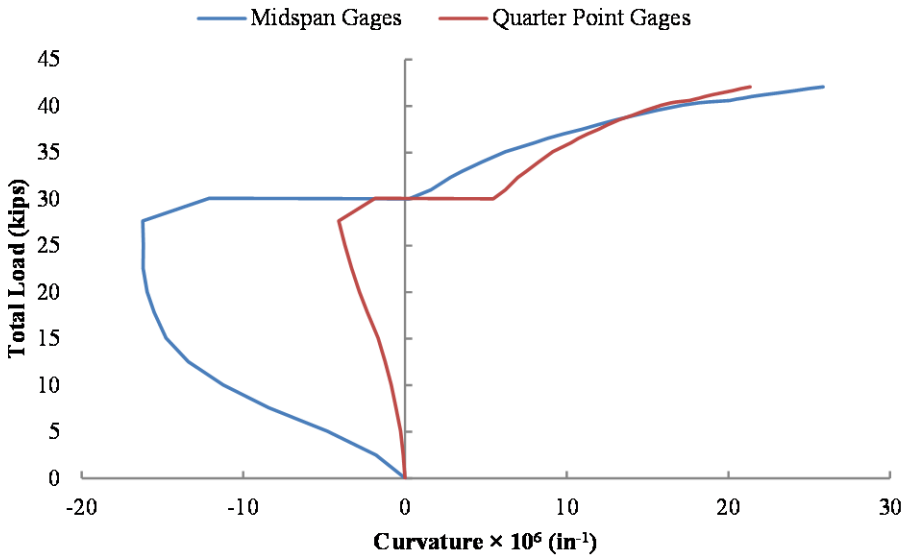

Figure A-108: Load vs. Lateral Curvature for SP2-06PT-9-CON

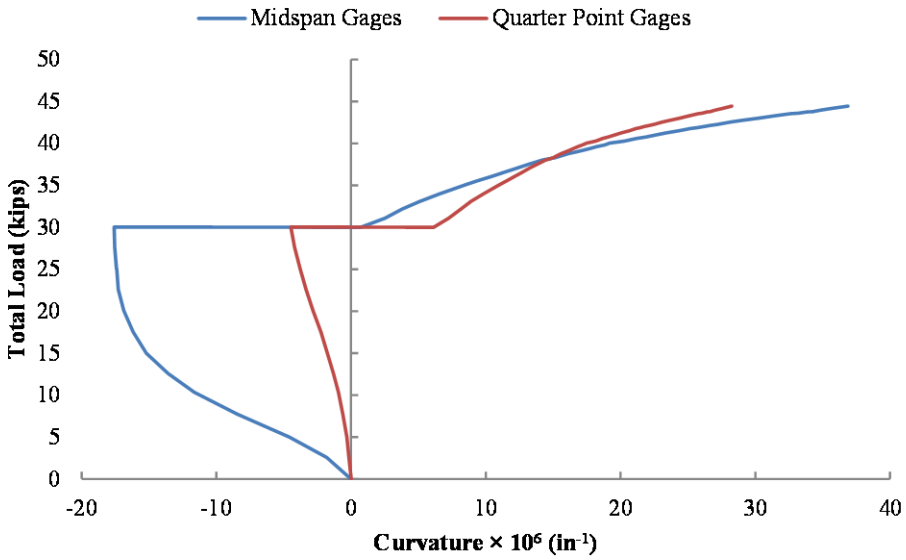

Figure A-109: Load vs. Lateral Curvature for SP2-06PT-10-CON

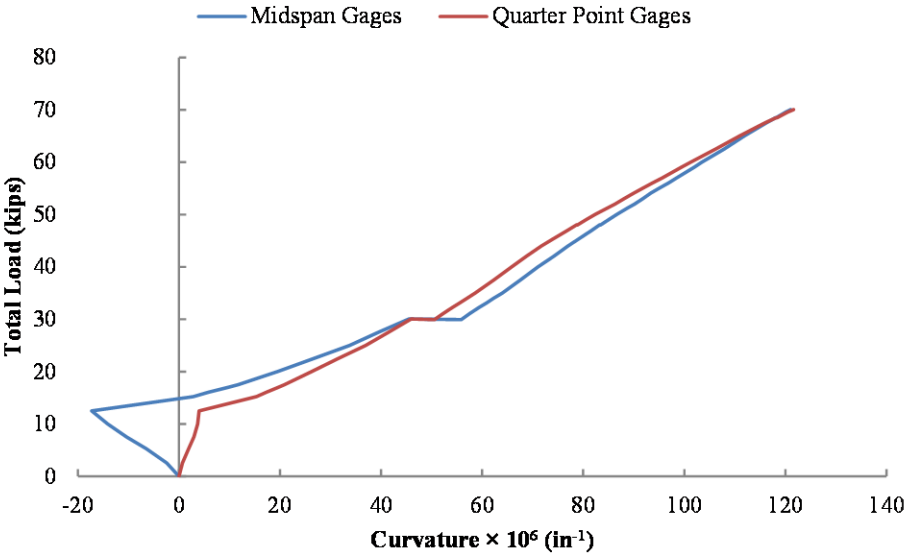

Figure A-110: Load vs. Lateral Curvature for SP2-06PT-11-ECC-E

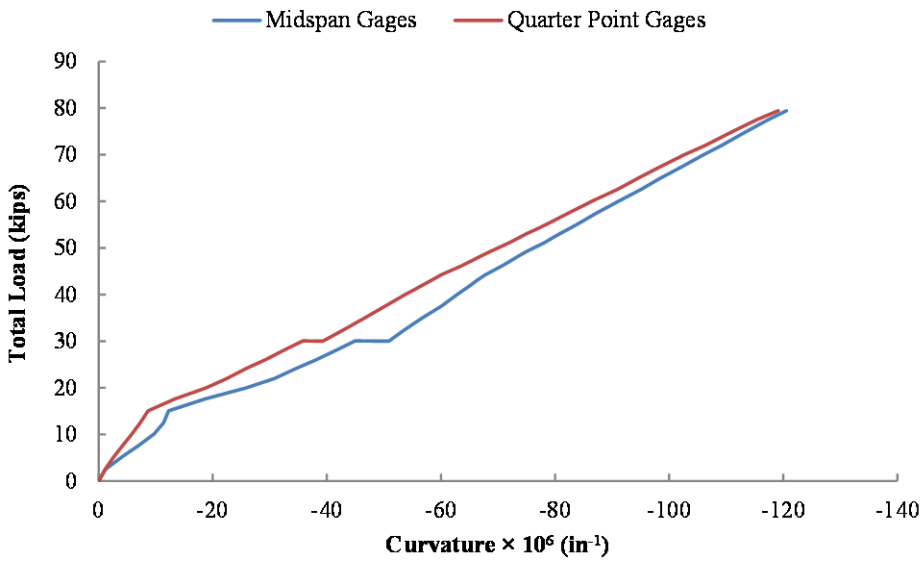

Figure A-111: Load vs. Lateral Curvature for SP2-06PT-12-ECC-W

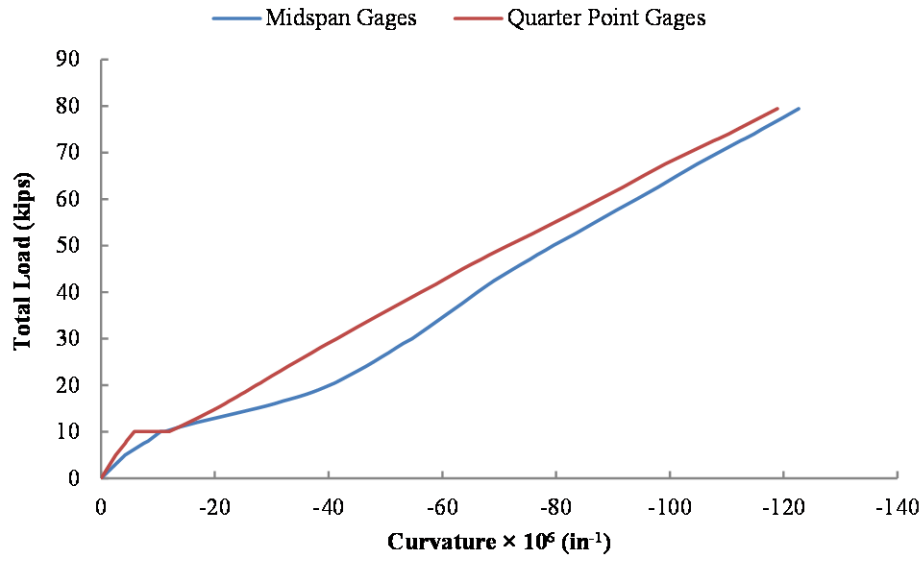

Figure A-112: Load vs. Lateral Curvature for SP2-06PT-13-ECC-W

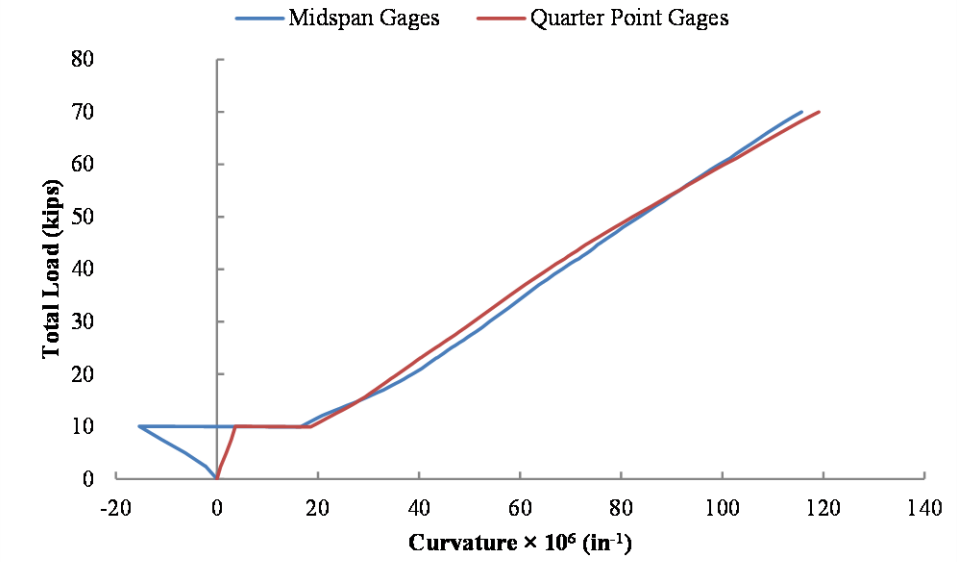

Figure A-113: Load vs. Lateral Curvature for SP2-06PT-14-ECC-E

A.3.2.2 SP2 Combined Load Tests

This subsection includes load versus lateral curvature plots for each of the combined load tests on SP2. There were a total of twelve combined load tests performed.

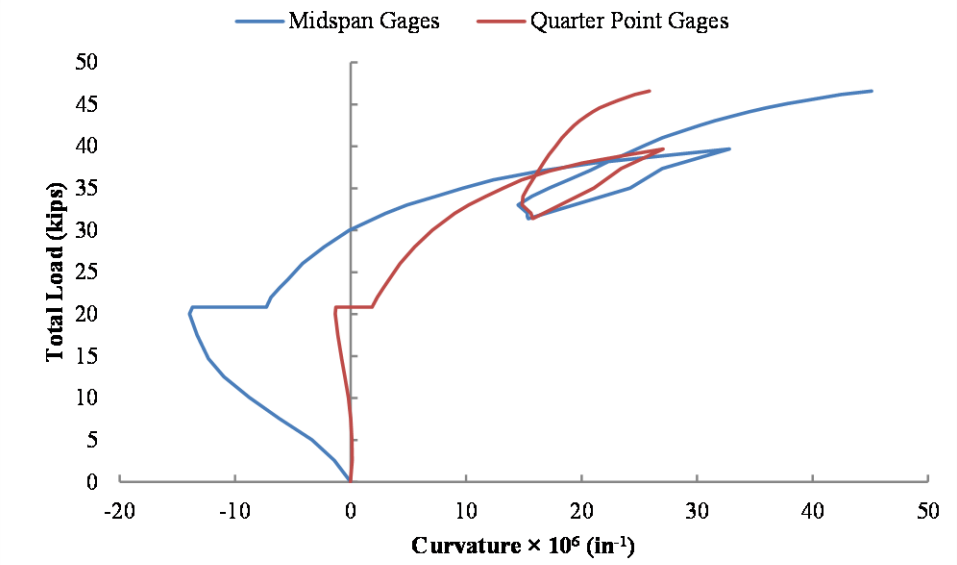

Figure A-114: Load vs. Lateral Curvature for SP2-05PT30-EX-1-DS

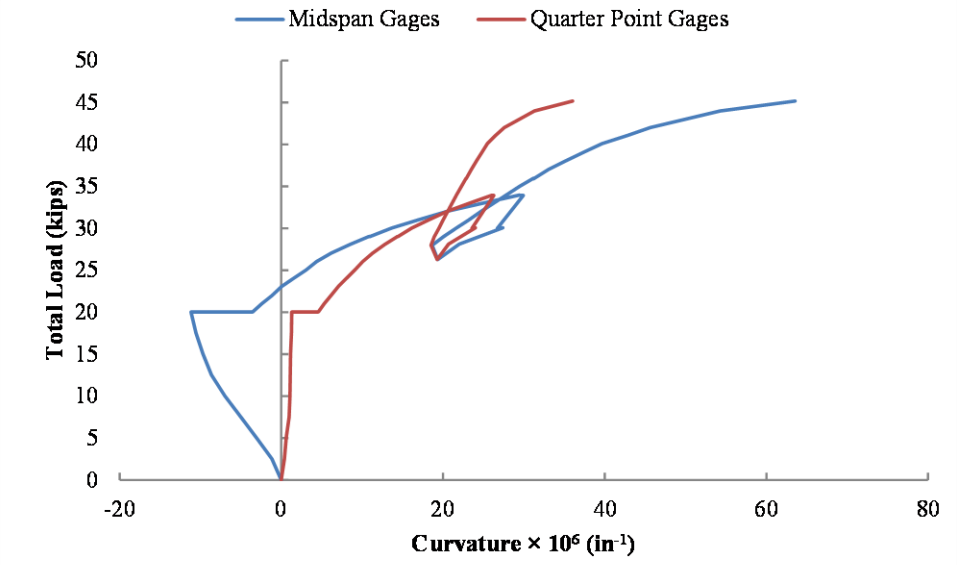

Figure A-115: Load vs. Lateral Curvature for SP2-05PT25-EX-2-DS

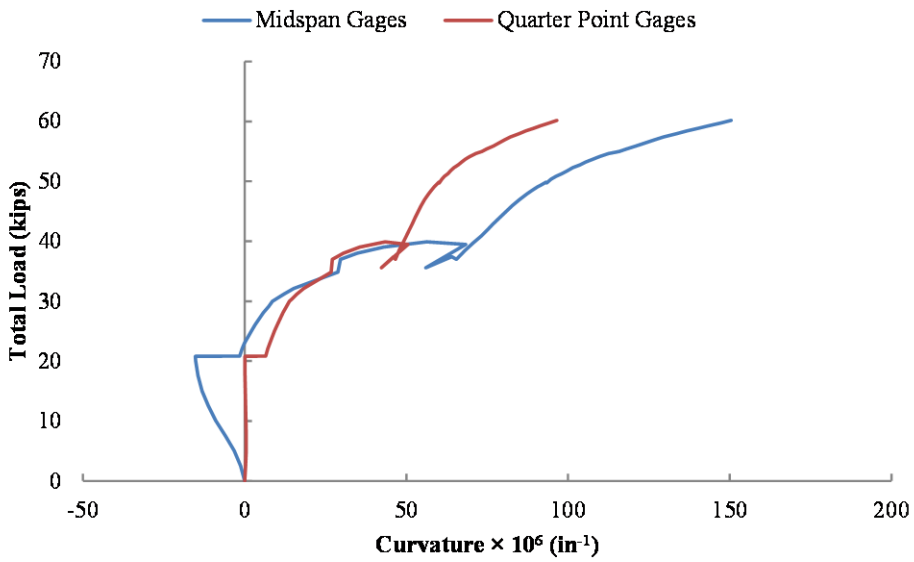

Figure A-116: Load vs. Lateral Curvature for SP2-05PT35-EX-3-DS

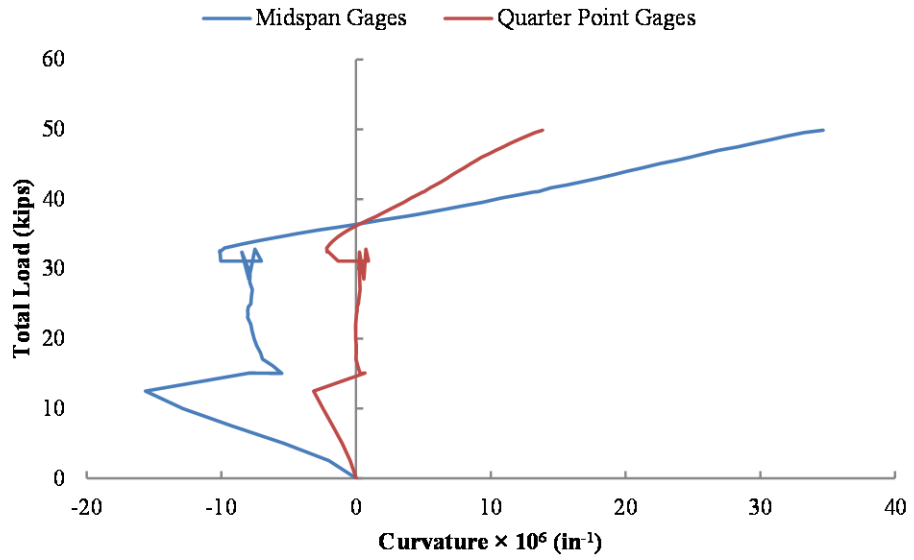

Figure A-117: Load vs. Lateral Curvature for SP2-06PT30-EX-1-DS

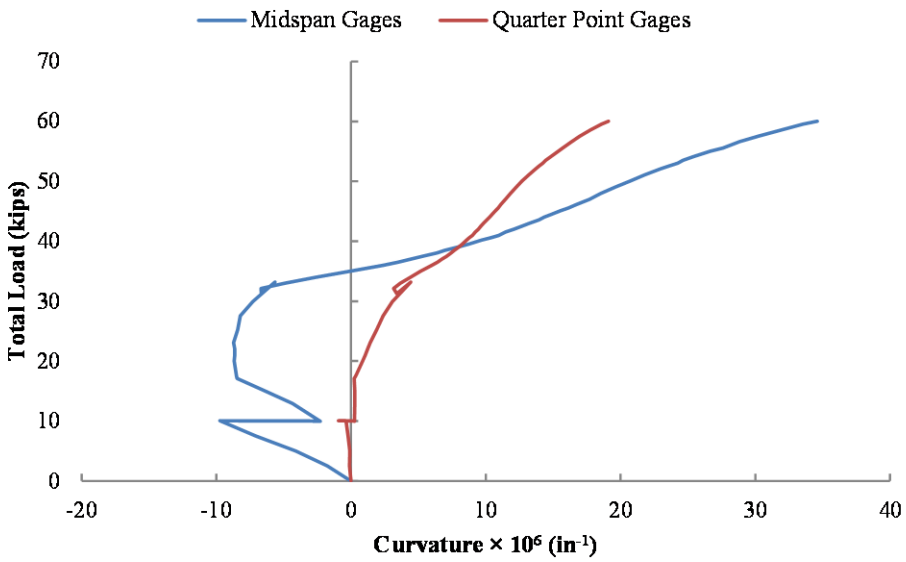

Figure A-118: Load vs. Lateral Curvature for SP2-06PT30-EX-2-DS

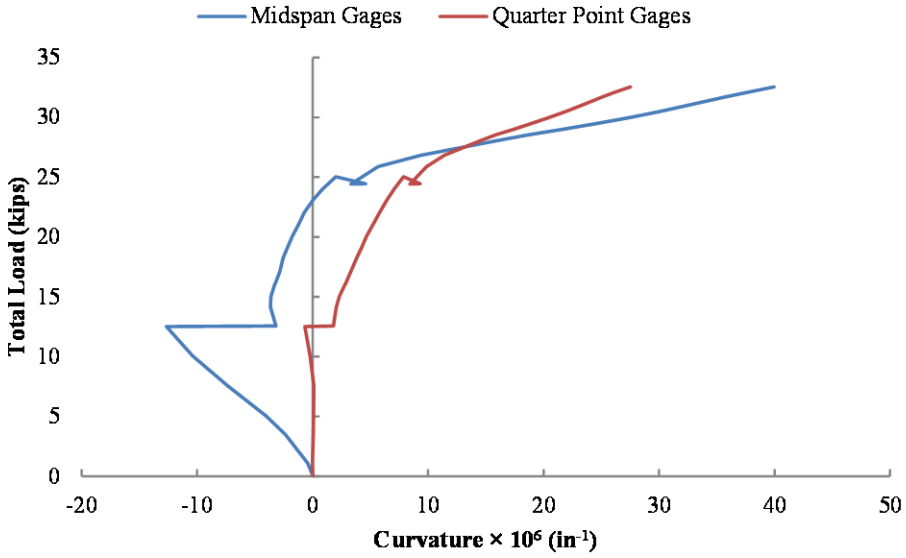

Figure A-119: Load vs. Lateral Curvature for SP2-06PT25-EX-3-DS

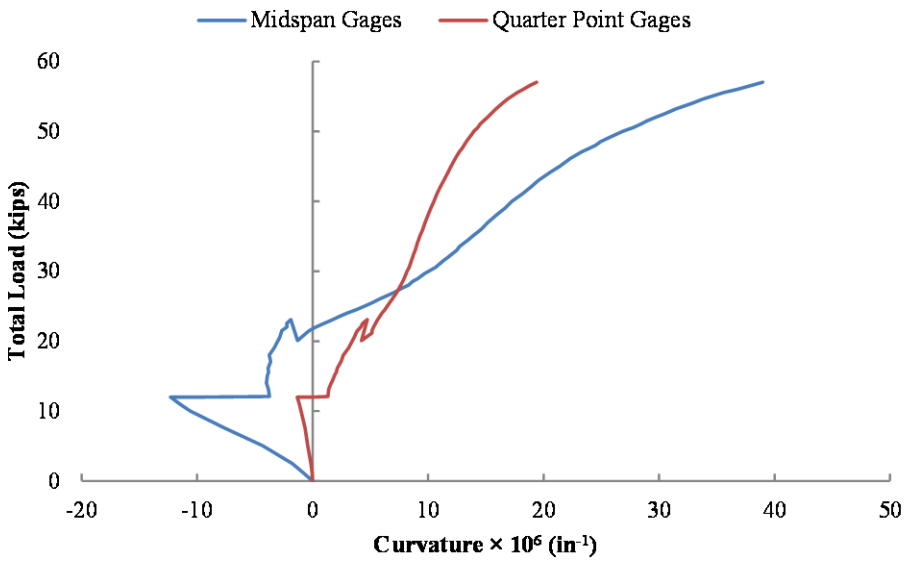

Figure A-120: Load vs. Lateral Curvature for SP2-06PT20-EX-4-DS

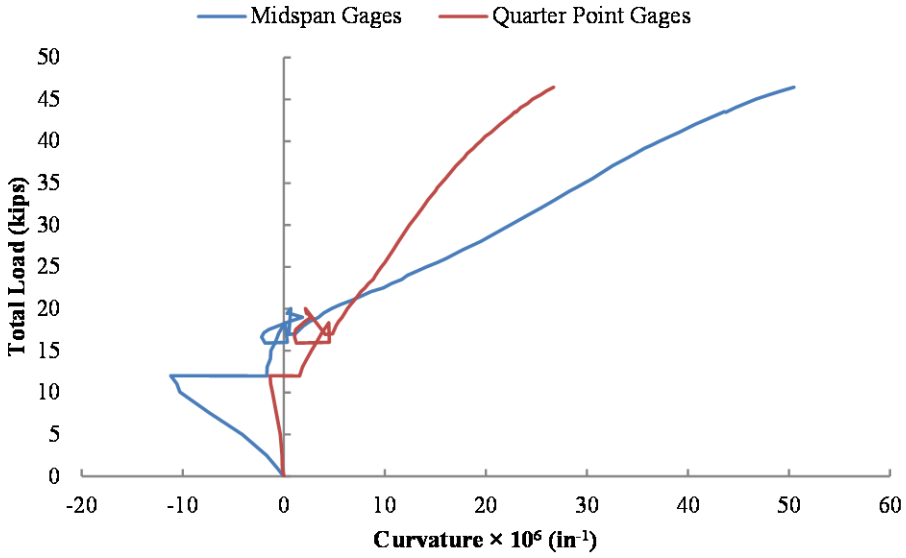

Figure A-121: Load vs. Lateral Curvature for SP2-06PT15-EX-5-DS

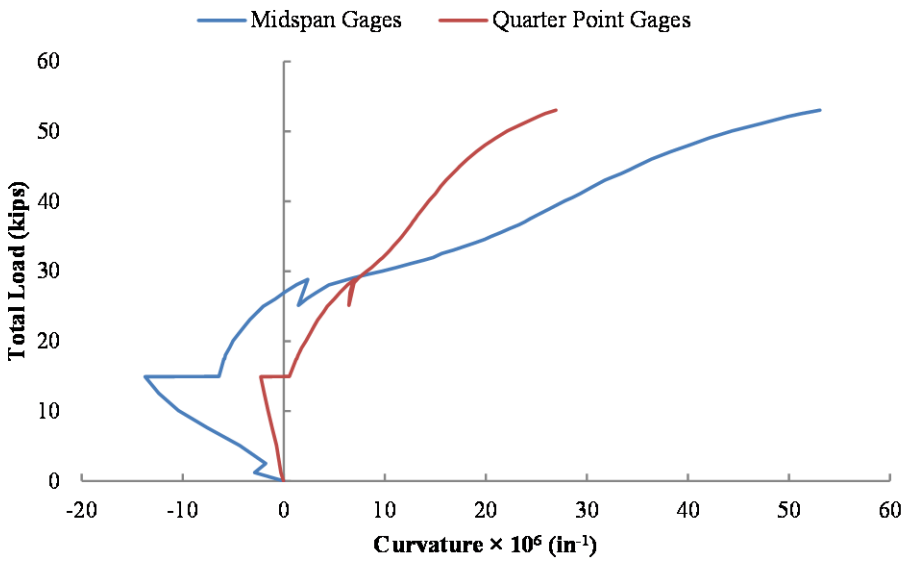

Figure A-122: Load vs. Lateral Curvature for SP2-06PT25-EX-6-DS

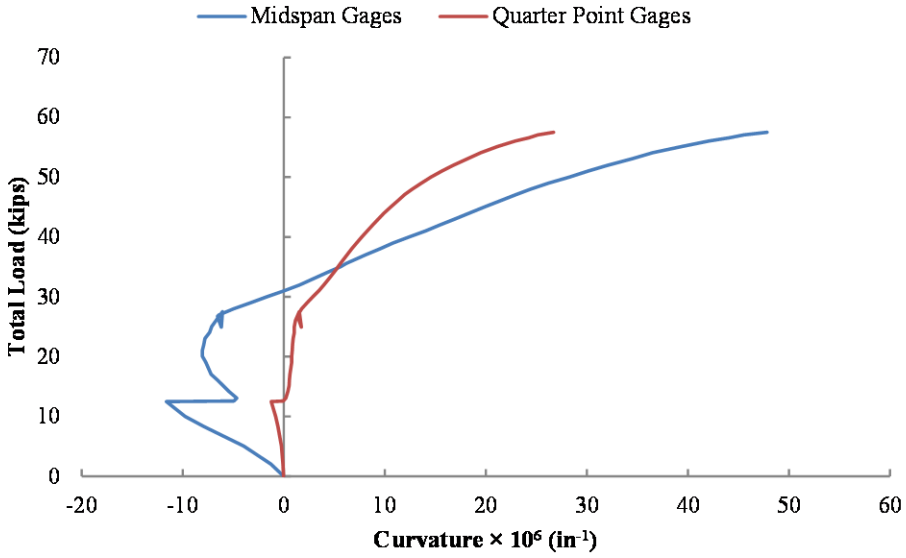

Figure A-123: Load vs. Lateral Curvature for SP2-06PT25-EX-7-SS

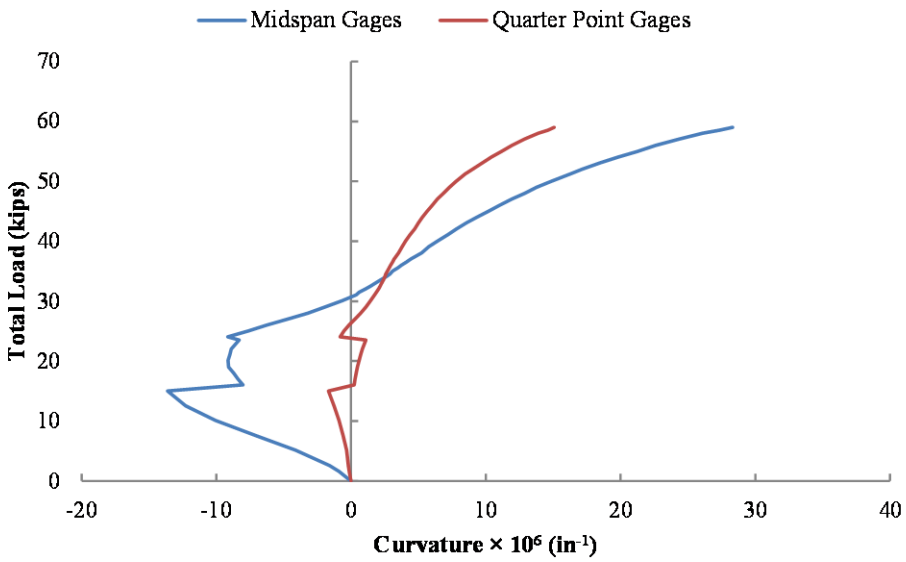

Figure A-124: Load vs. Lateral Curvature for SP2-06PT20-EX-8-SS

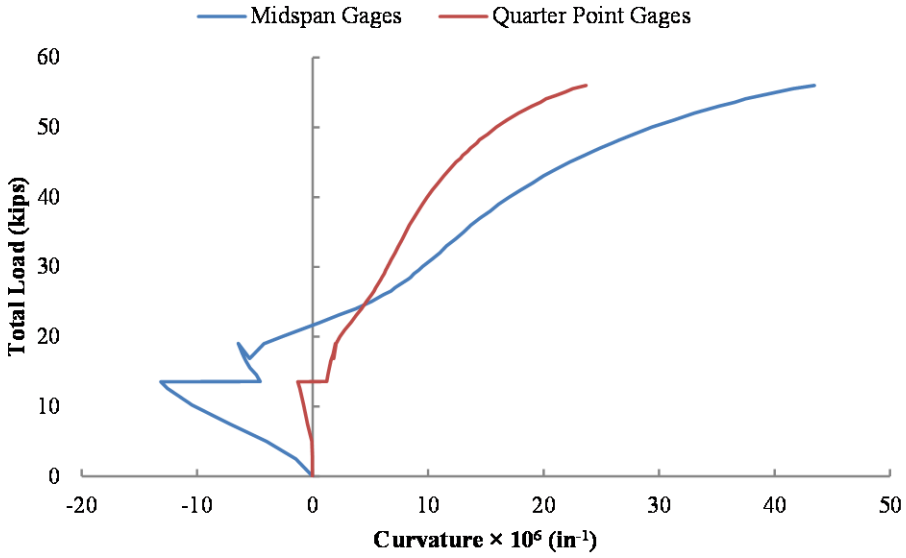

Figure A-125: Load vs. Lateral Curvature for SP2-06PT15-EX-9-SS

A.3.2.3 SP2 External Load Tests

This subsection includes the load versus lateral curvature plot from the single external load test on SP2. The test ended in a full buckling failure which resulted in extensive cracking in the member.

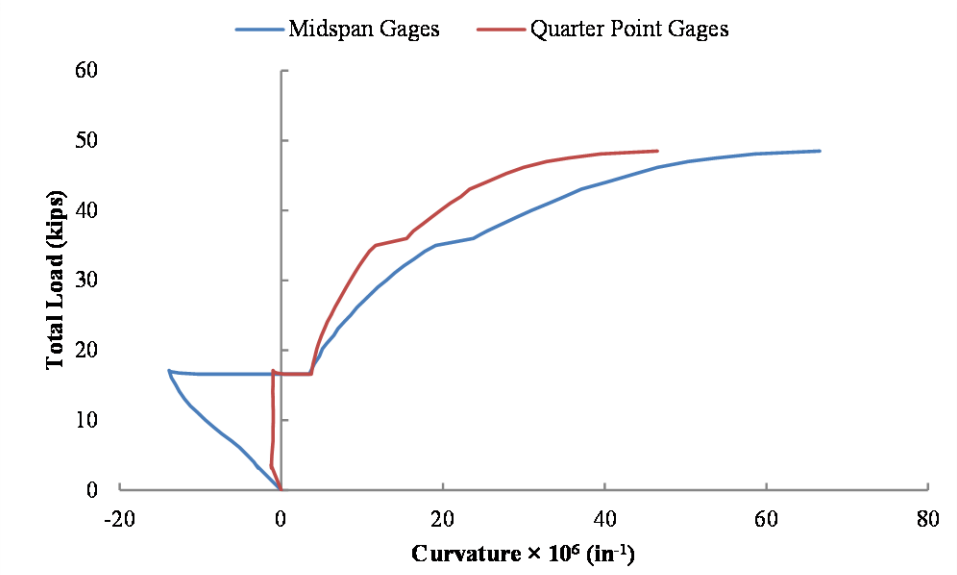

Figure A-126: Load vs. Lateral Curvature for SP2-PT0-EX-1

A.4 AXIAL LOAD ESTIMATES

This portion of the appendix provides a comparison of axial load measurements for all load tests. As discussed in the previous chapters, the axial load was calculated from the strain values reported by the vibrating wire gages (VWGs) and was measured by the load cells. Each plot includes the ratio of the calculated axial load to the load measured by the load cells. Estimates are provided for both the midspan and quarter point gages.

A.4.1 Specimen 1 (SP1)

This subsection includes axial load estimates for a total of 27 load tests on the first specimen (SP1). Notes on individual tests are included in the figure captions where applicable.

A.4.1.1 SP1 Post-tensioned Tests

This subsection includes axial load estimates for all PT load tests on SP1. There were a total of 21 pre-failure tests and one post-failure test performed.

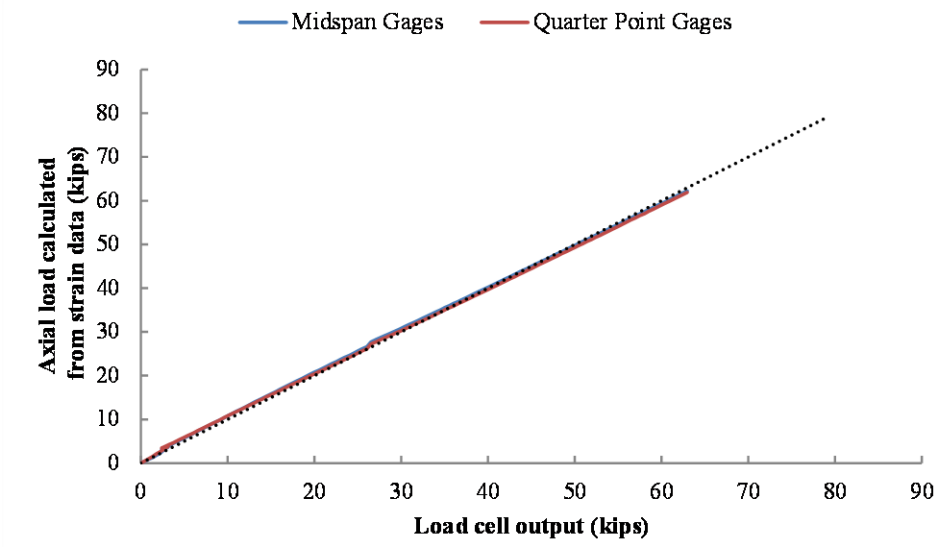

Figure A-127: Axial Load Comparison for SP1-05PT-1-CON

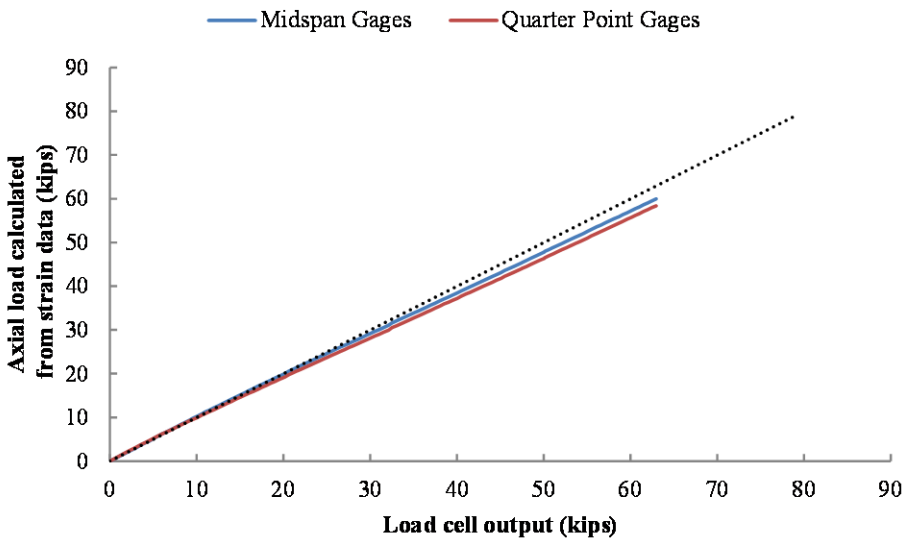

Figure A-128: Axial Load Comparison for SP1-05PT-2-ECC-E

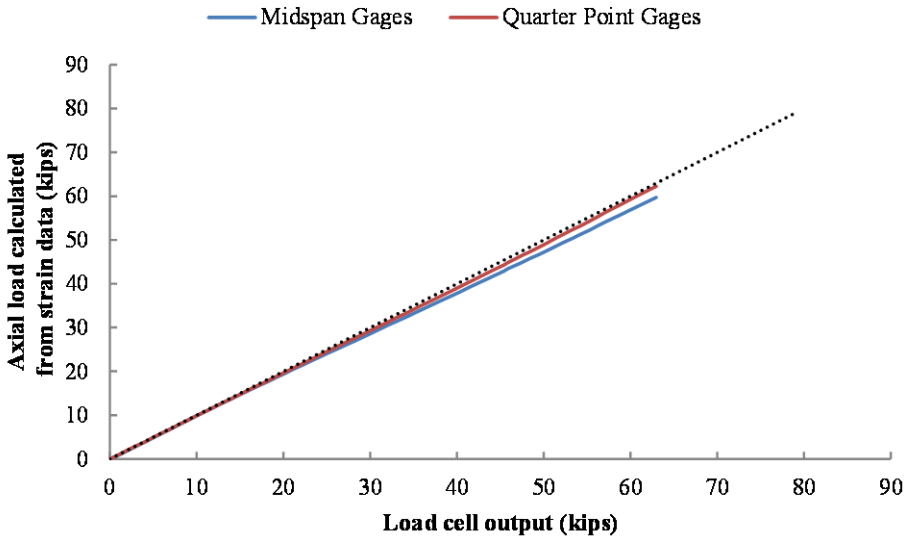

Figure A-129: Axial Load Comparison for SP1-05PT-3-ECC-W

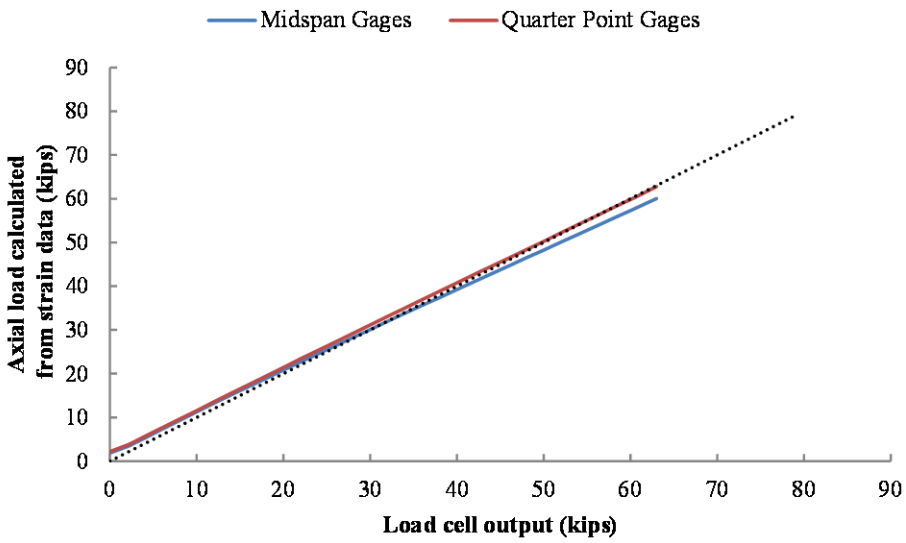

Figure A-130: Axial Load Comparison for SP1-05PT-4-ECC-W

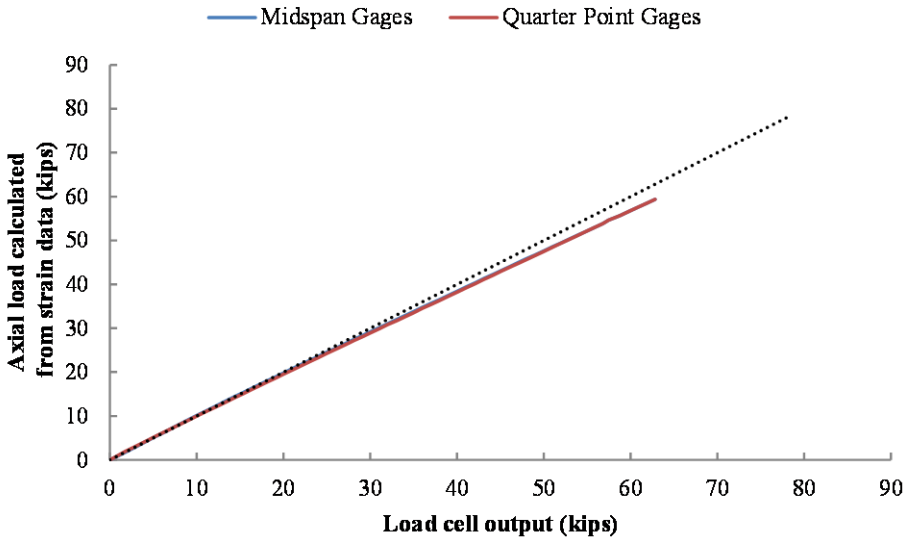

Figure A-131: Axial Load Comparison for SP1-05PT-5-CON

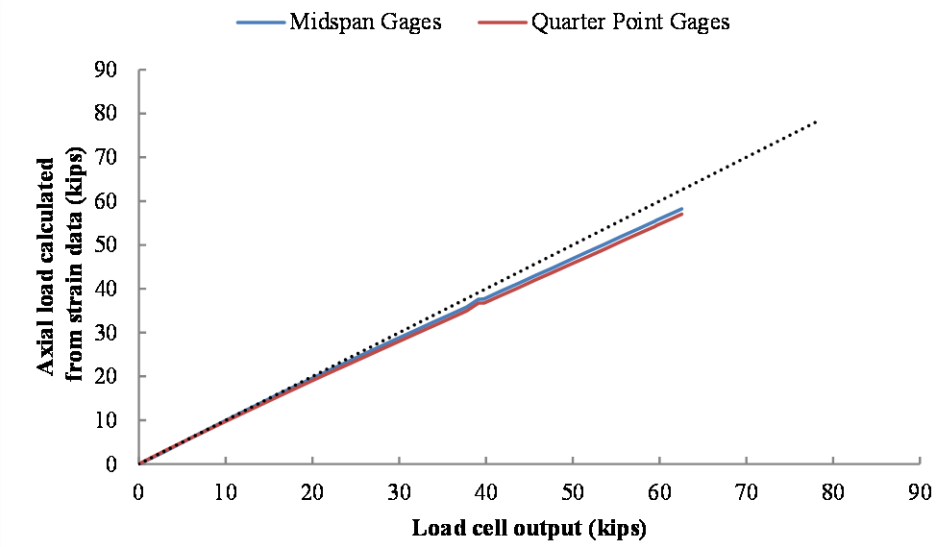

Figure A-132: Axial Load Comparison for SP1-05PT-6-ECC-E

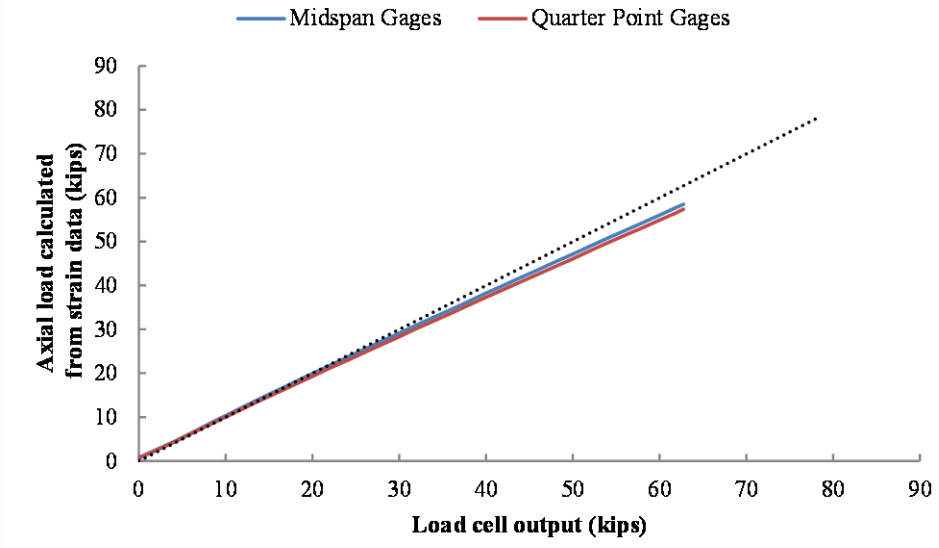

Figure A-133: Axial Load Comparison for SP1-05PT-7-ECC-E

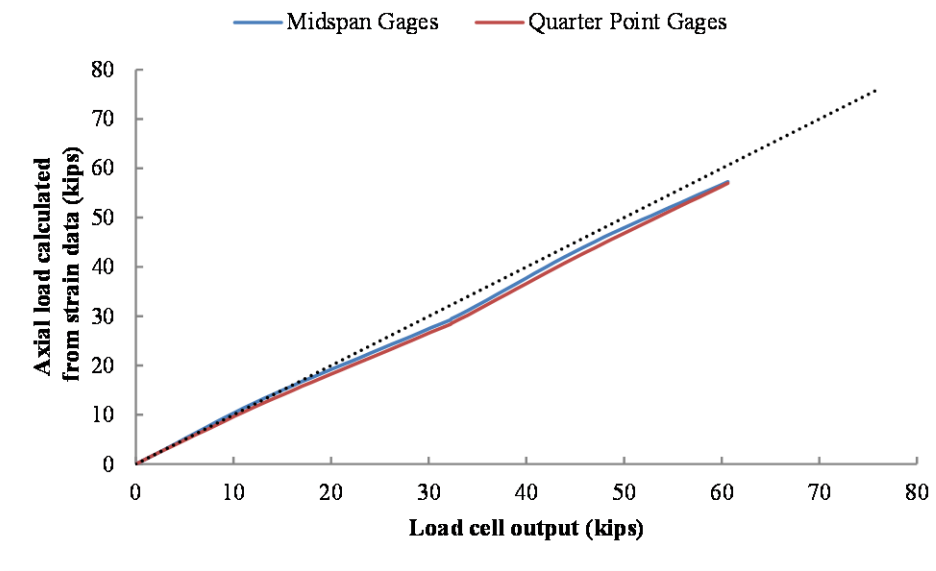

Figure A-134: Axial Load Comparison for SP1-05PT-8-CON

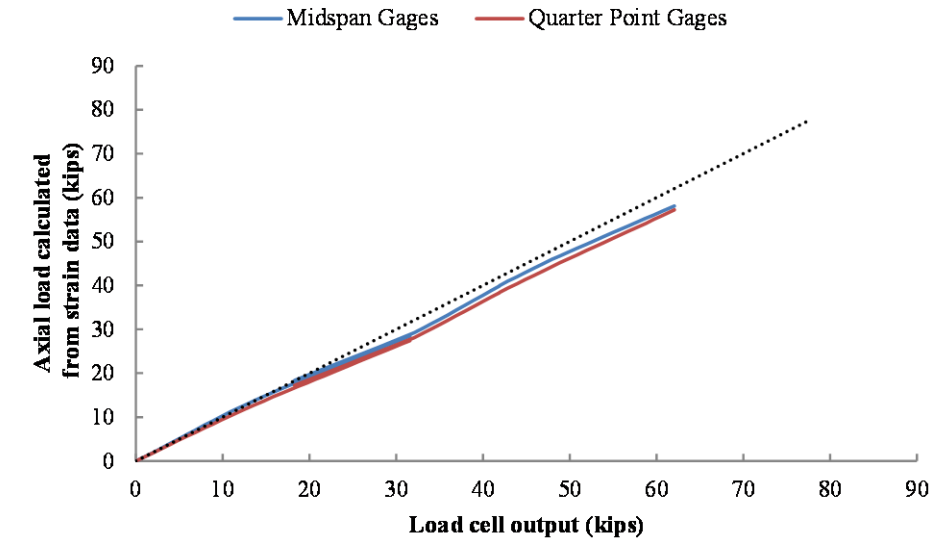

Figure A-135: Axial Load Comparison for SP1-05PT-9-CON

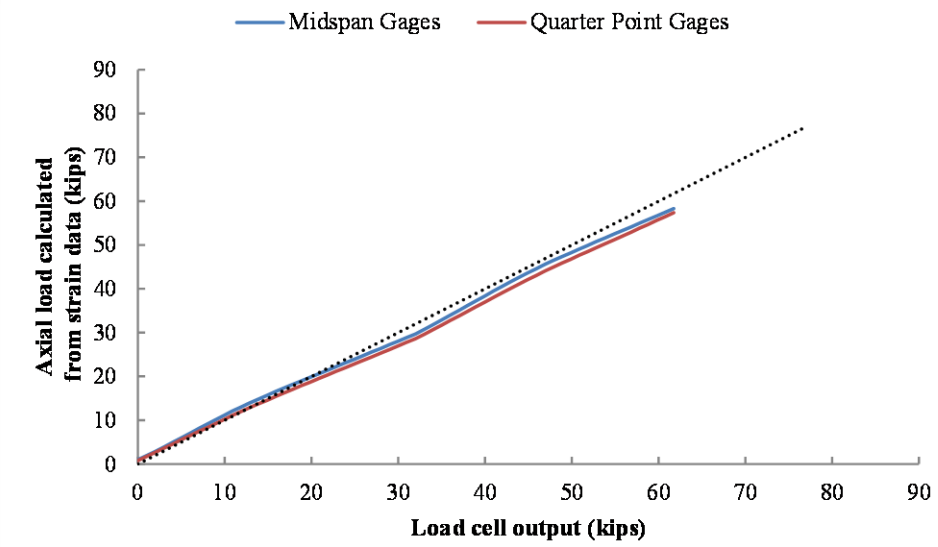

Figure A-136: Axial Load Comparison for SP1-05PT-10-CON

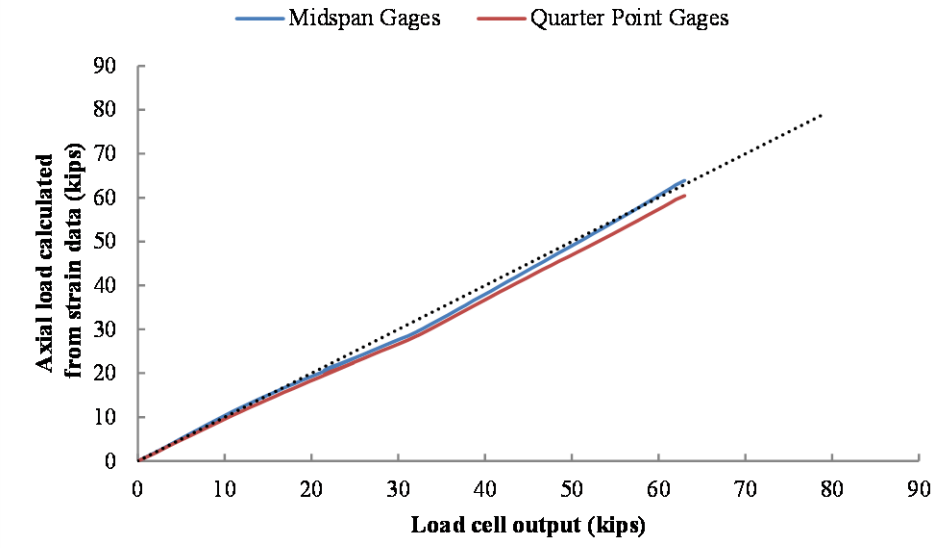

Figure A-137: Axial Load Comparison for SP1-05PT-11-CON

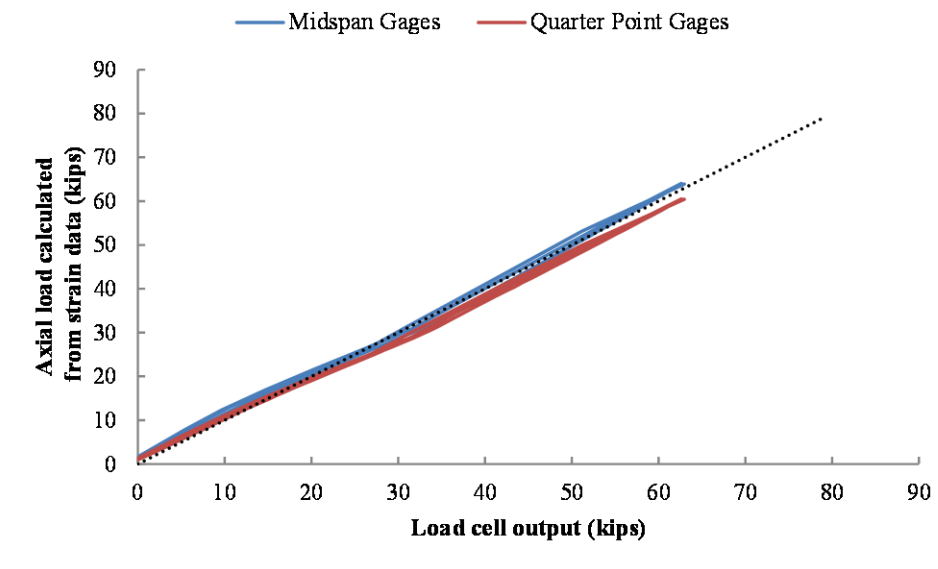

Figure A-138: Axial Load Comparison for SP1-05PT-12-CON (Two full loading and unloading cycles shown.)

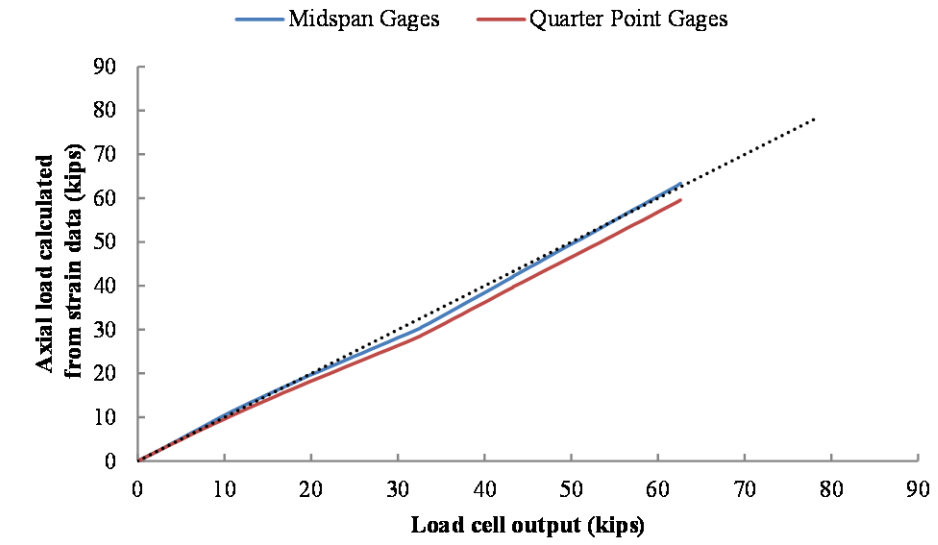

Figure A-139: Axial Load Comparison for SP1-05PT-13-ECC-E

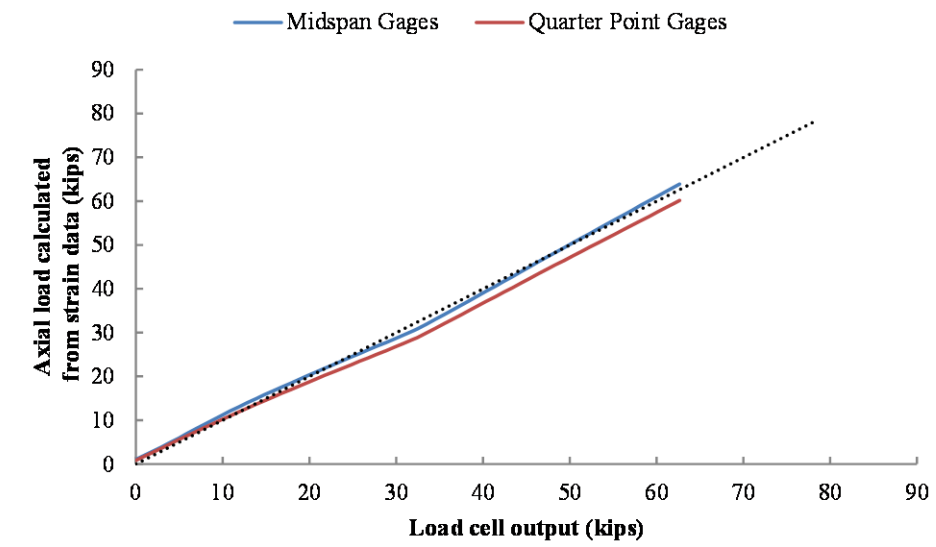

Figure A-140: Axial Load Comparison for SP1-05PT-14-ECC-E

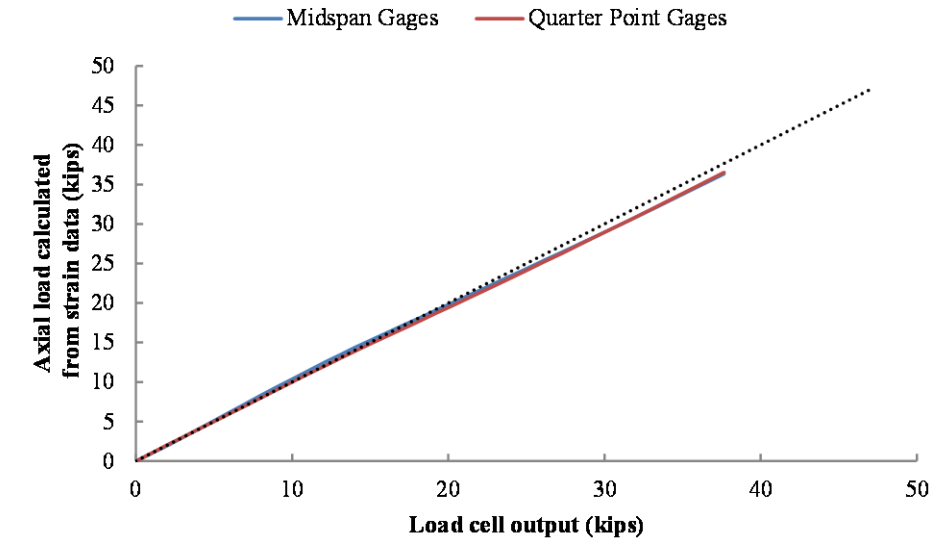

Figure A-141: Axial Load Comparison for SP1-05PT-15-ECC-W

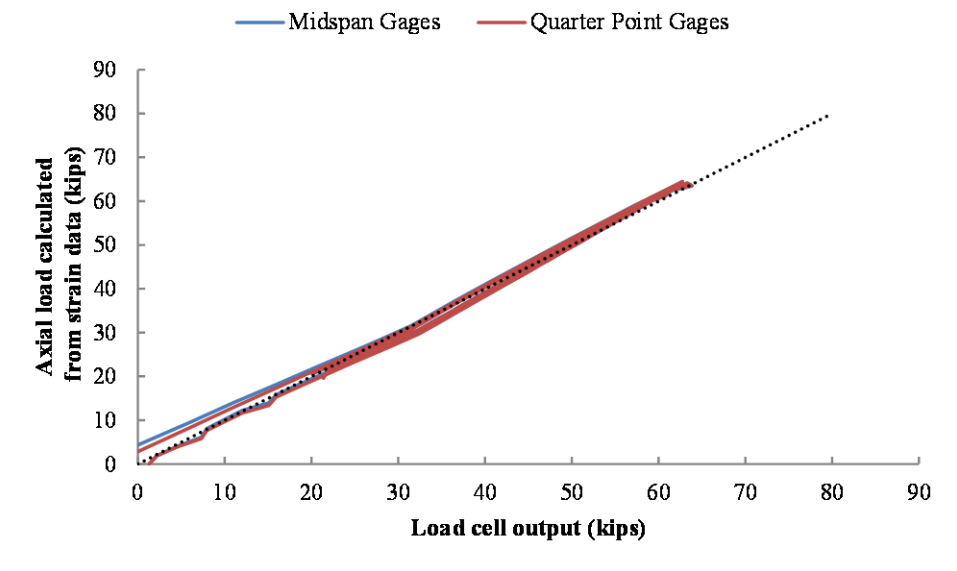

Figure A-142: Axial Load Comparison for SP1-05PT-16-ECC-W (Two full loading and unloading cycles shown.)

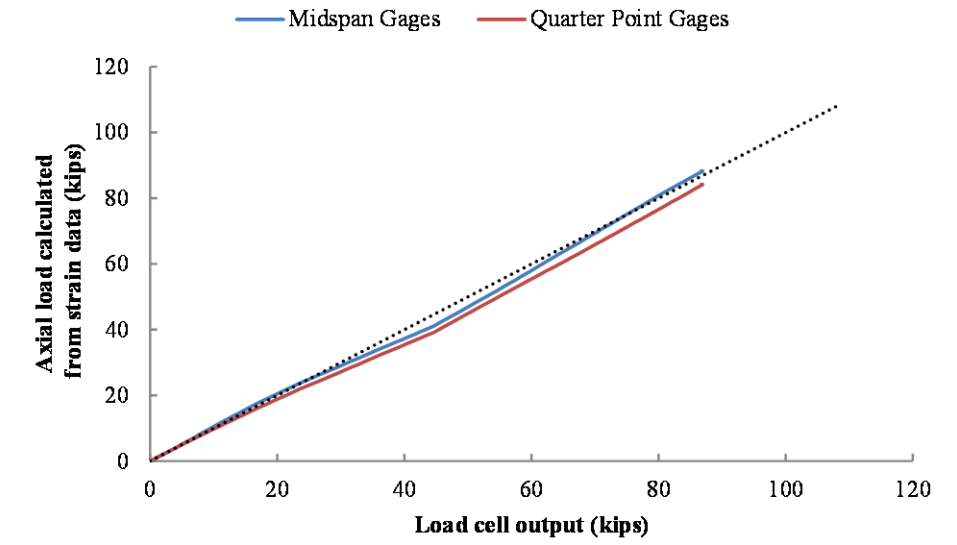

Figure A-143: Axial Load Comparison for SP1-06PT-1-CON

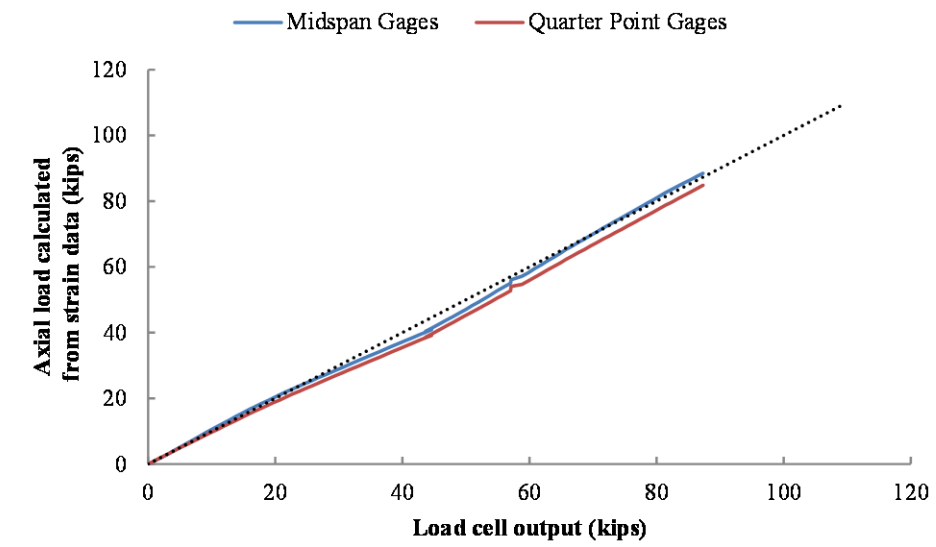

Figure A-144: Axial Load Comparison for SP1-06PT-2-CON

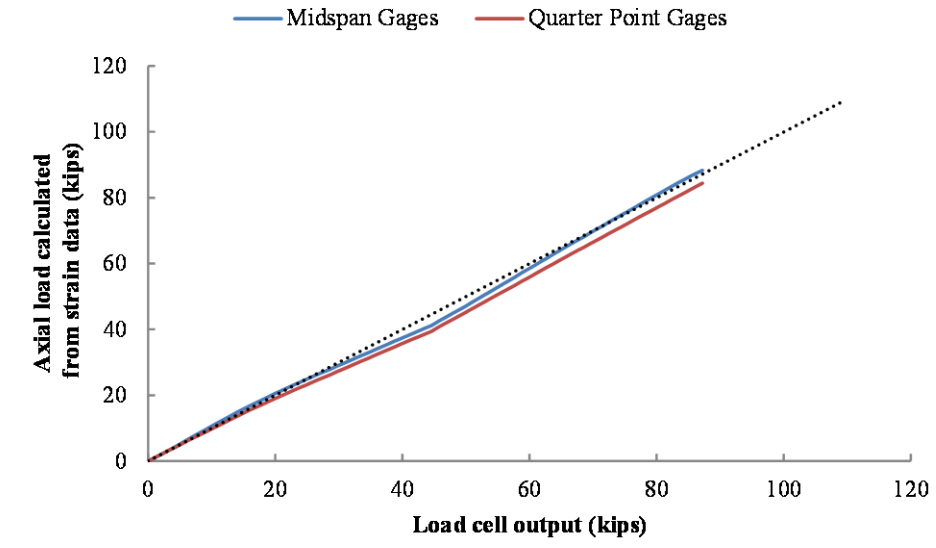

Figure A-145: Axial Load Comparison for SP1-06PT-3-CON

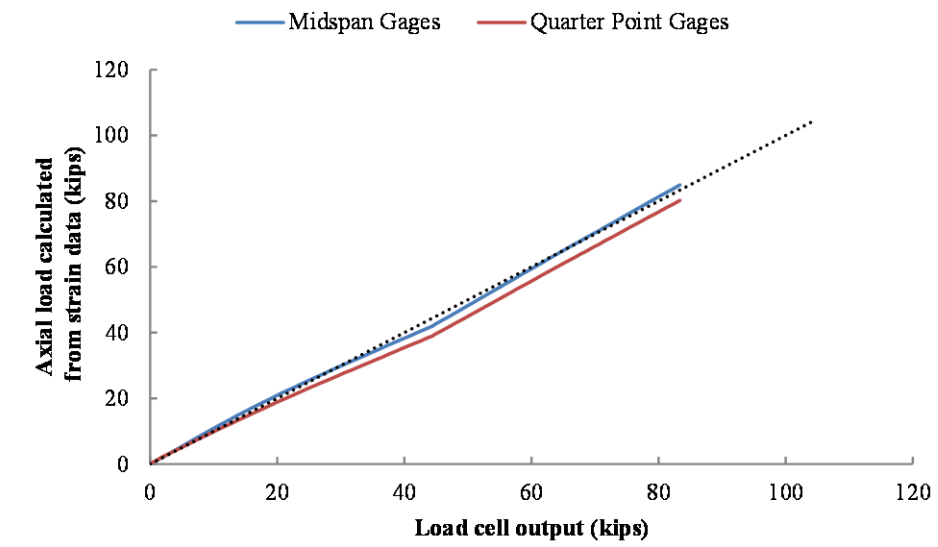

Figure A-146: Axial Load Comparison for SP1-06PT-4-ECC-E

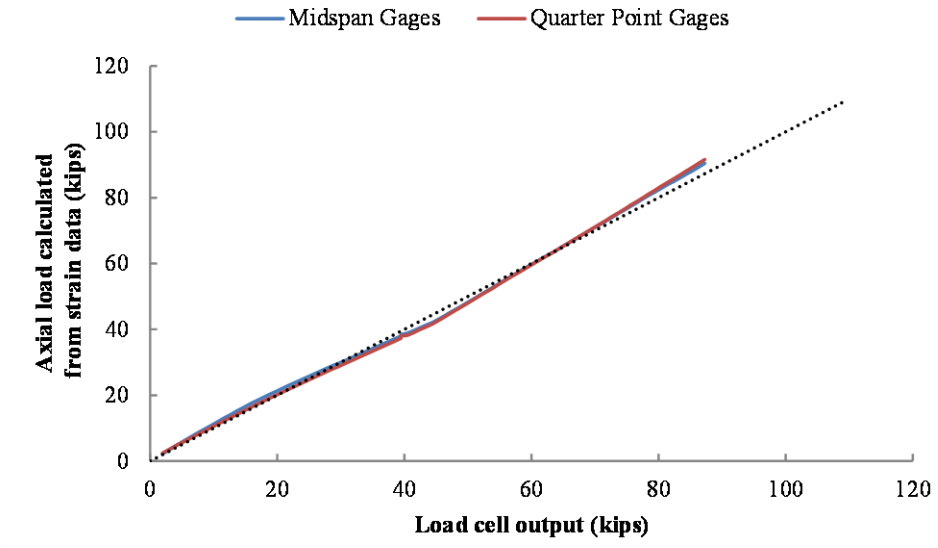

Figure A-147: Axial Load Comparison for SP1-06PT-5-ECC-W

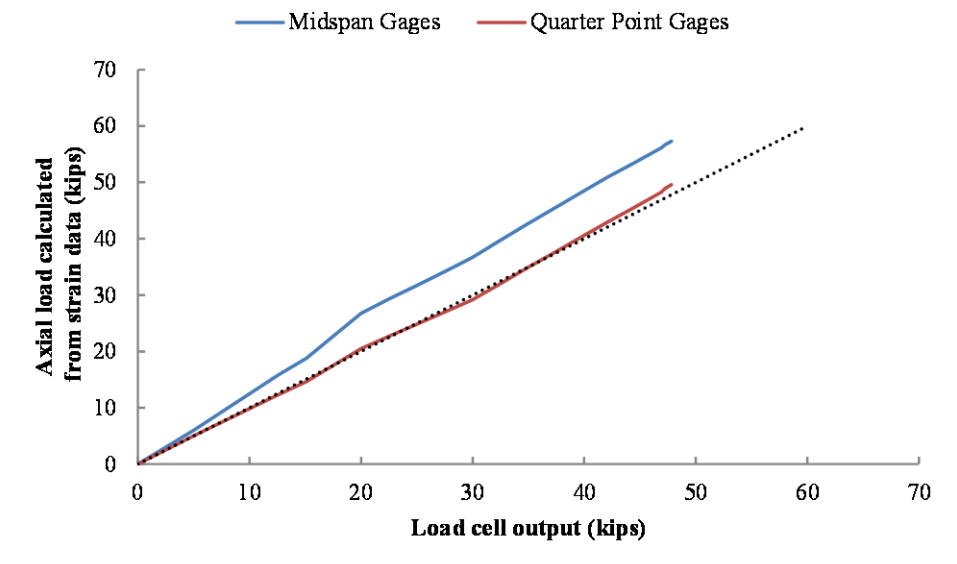

Figure A-148: Axial Load Comparison for SP1-06PT-6-CON

A.4.1.2 SP1 Combined Load Tests

The only combined load test in SP1 was performed after the specimen was cracked extensively due to a buckling failure. The assumptions made in calculating stresses in the section likely did not hold after buckling. As such, the accuracy of the axial load estimates is significantly reduced the post-failure test.

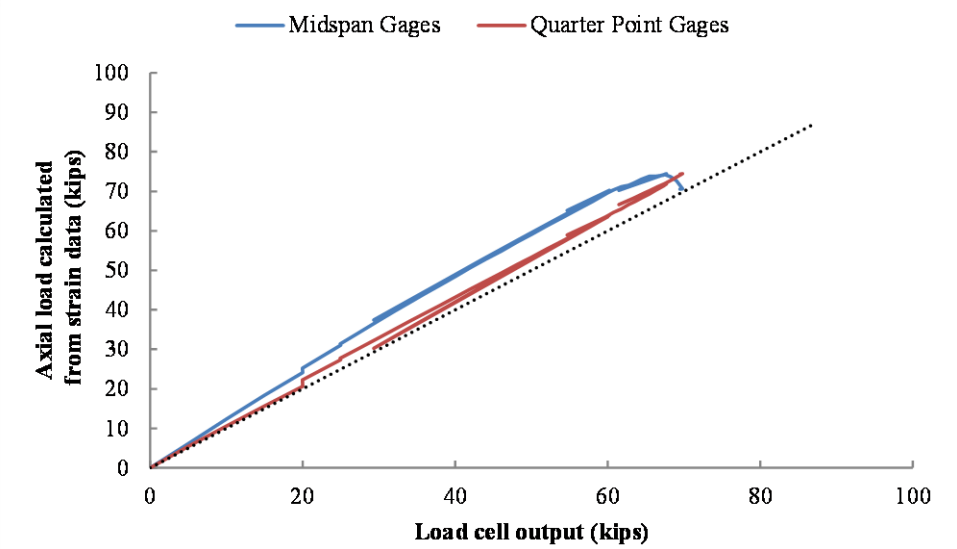

Figure A-149: Axial Load Comparison for SP1-06PT60-EX-1

A.4.1.3 SP1 External Load Tests

This section includes the axial load estimates for the external load tests on SP1. There were a total of four external load tests performed. The first two tests occurred prior to cracking, and as such, demonstrate a much higher degree of accuracy in the load estimates than do the two post-failure tests.

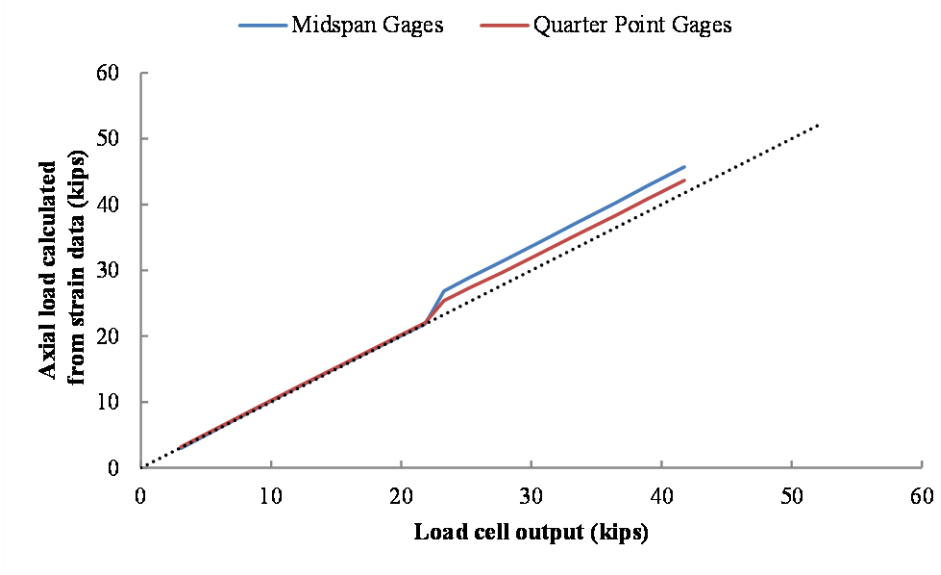

Figure A-150: Axial Load Comparison for SP1-PT0-EX-1

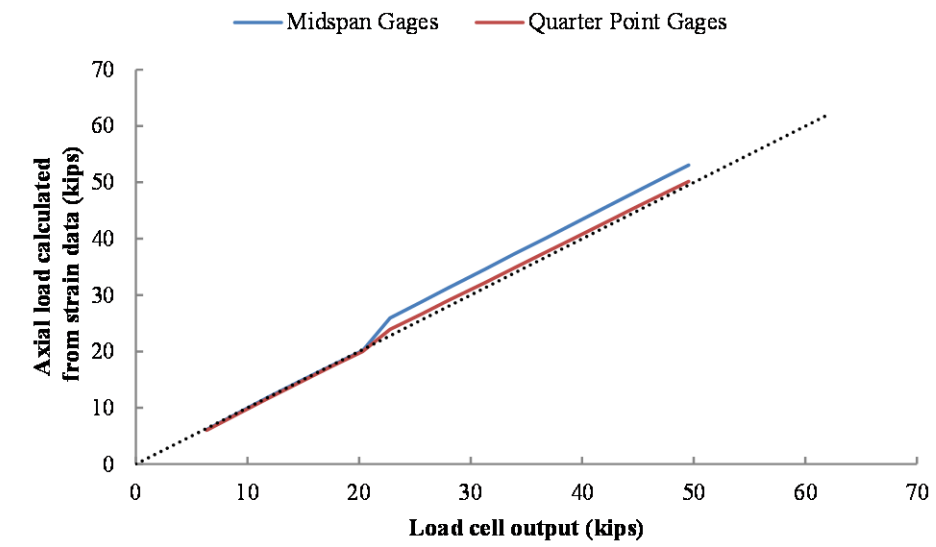

Figure A-151: Axial Load Comparison for SP1-PT0-EX-2

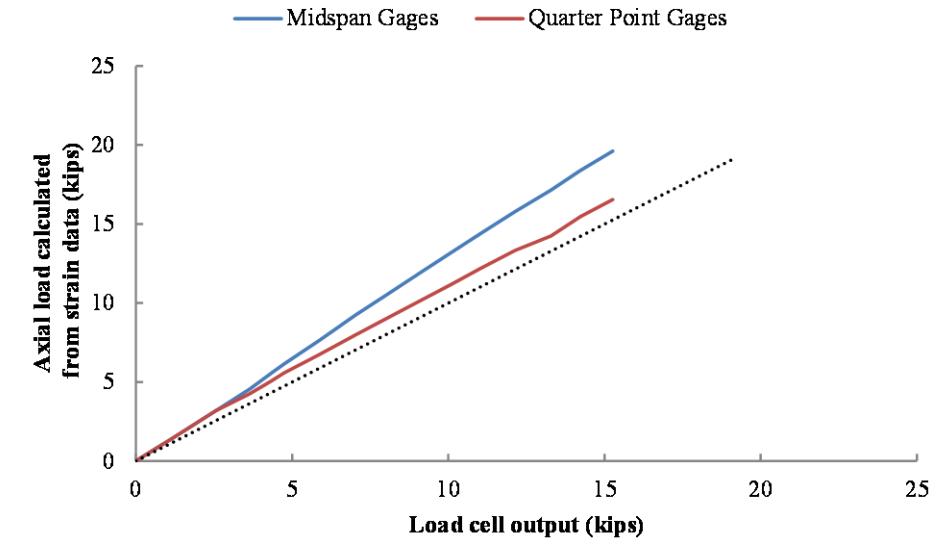

Figure A-152: Axial Load Comparison for SP1-PT0-EX-3

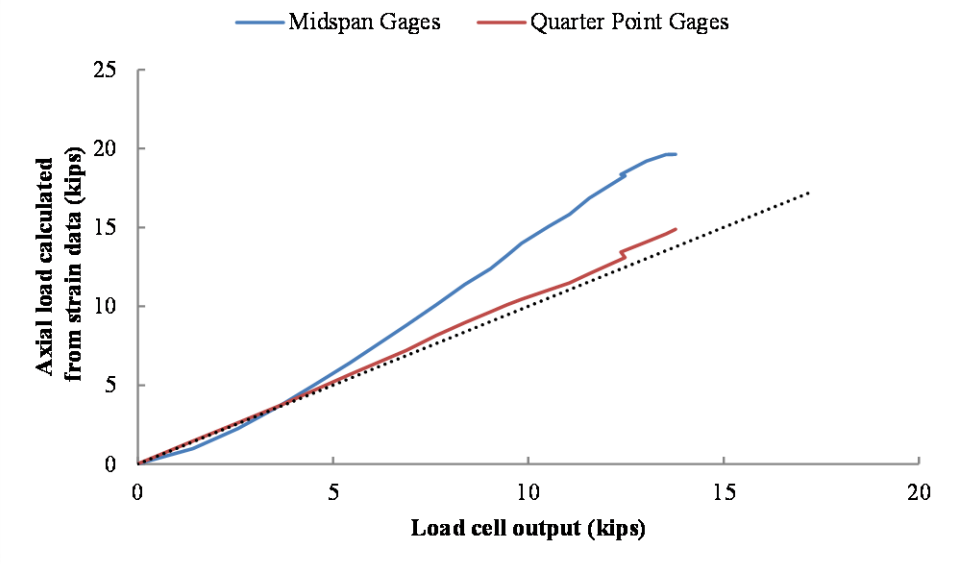

Figure A-153: Axial Load Comparison for SP1-PT0-EX-4

A.4.2 Specimen 2 (SP2)

This subsection includes axial load estimates for each of the 35 load tests on the second specimen (SP2). Notes on individual tests are included in the figure captions where applicable.

A.4.2.1 SP2 Post-tensioned Tests

This subsection includes axial load estimates for all PT load tests on SP2. There were a total of 22 pre-failure tests performed. No post-failure tests were performed.

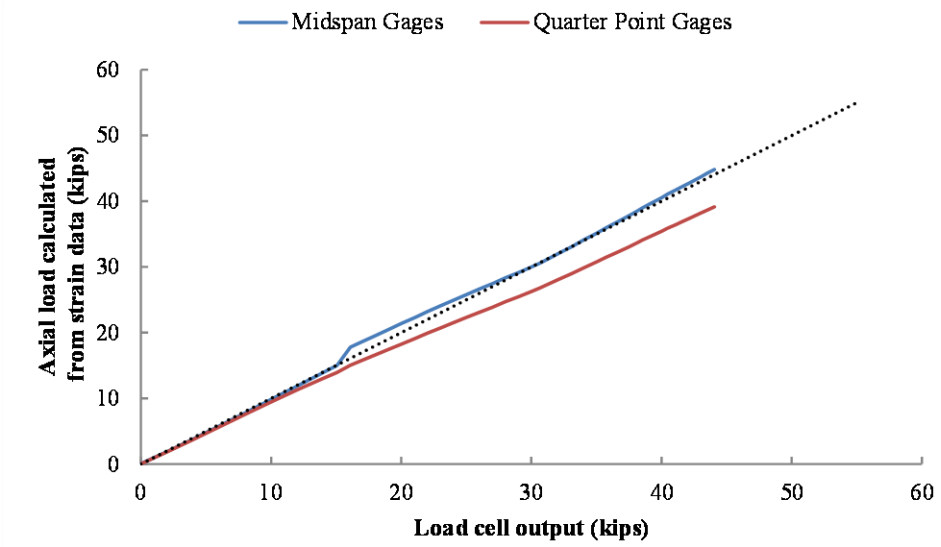

Figure A-154: Axial Load Comparison for SP2-05PT-1-CON

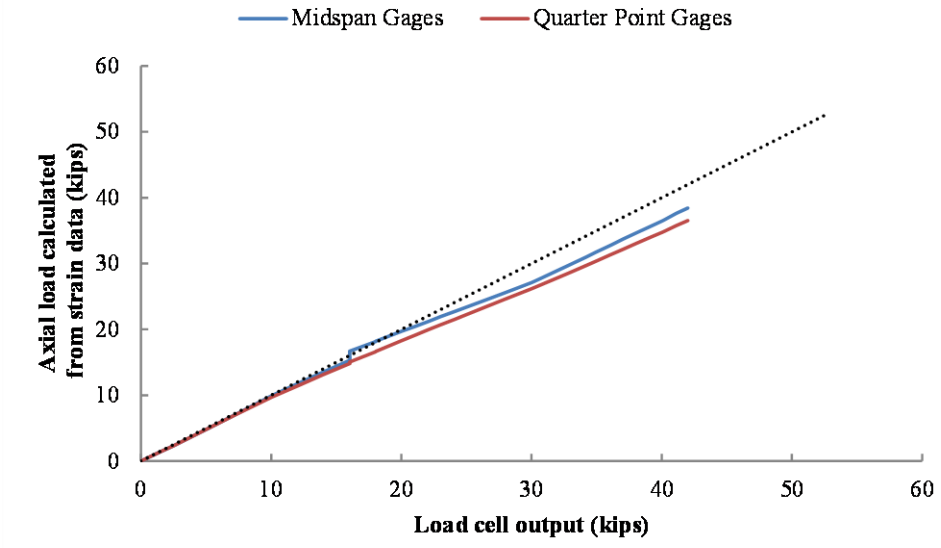

Figure A-155: Axial Load Comparison for SP2-05PT-2-ECC-W

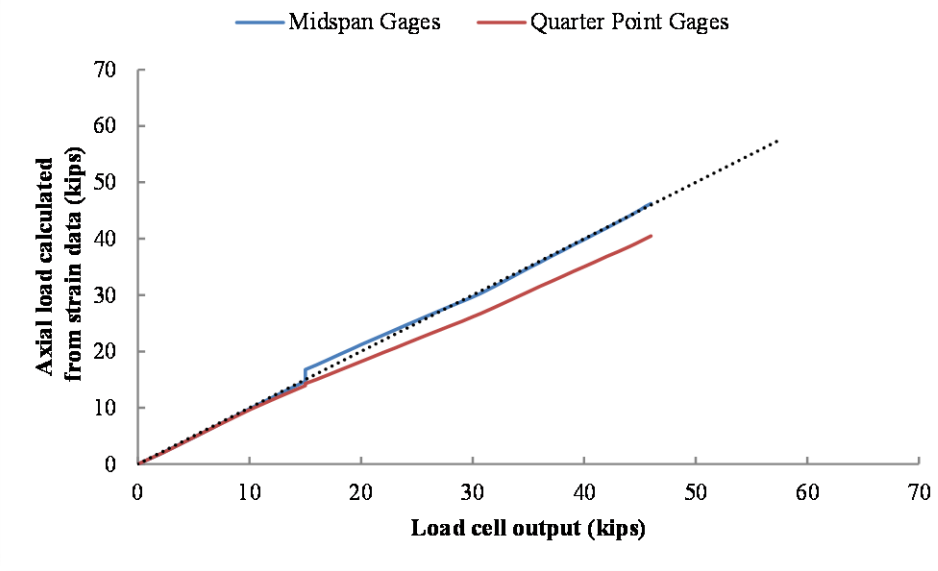

Figure A-156: Axial Load Comparison for SP2-05PT-3-CON

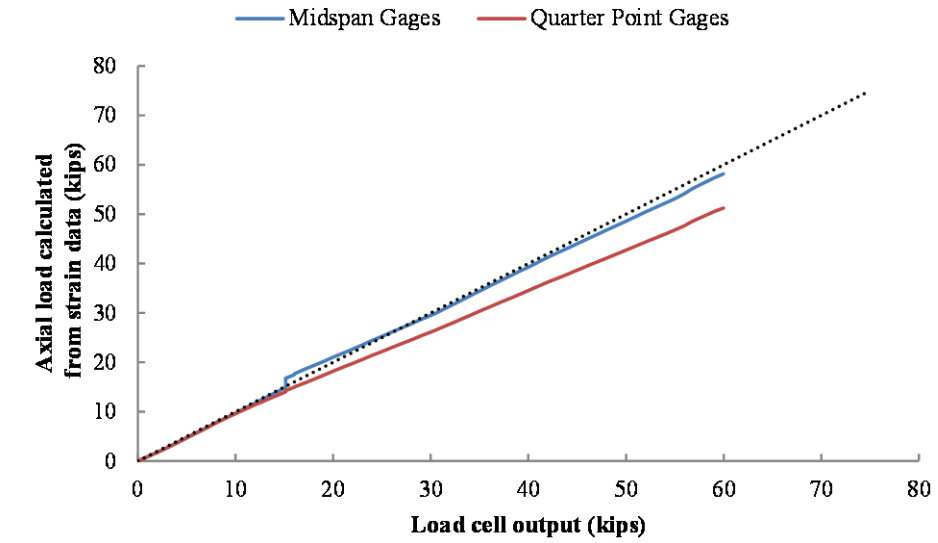

Figure A-157: Axial Load Comparison for SP2-05PT-4-ECC-E

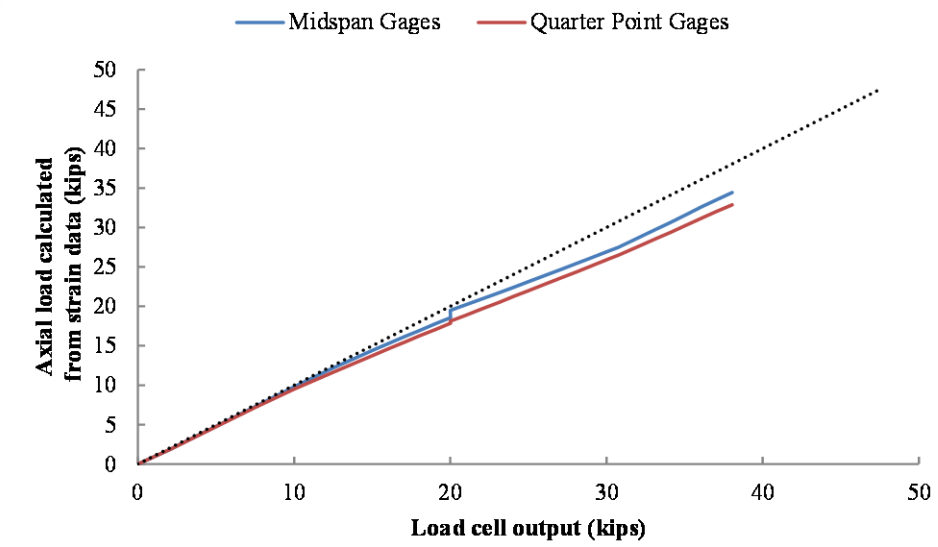

Figure A-158: Axial Load Comparison for SP2-05PT-5-ECC-W

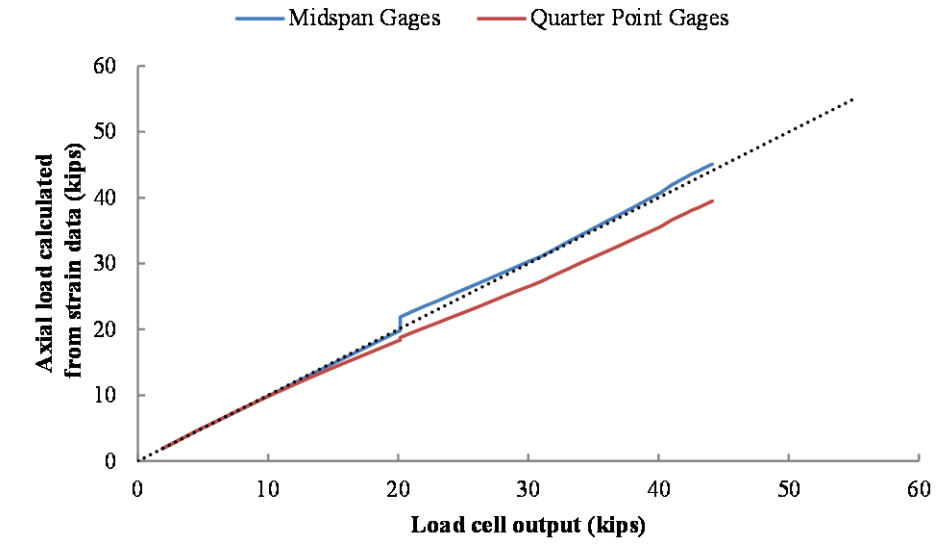

Figure A-159: Axial Load Comparison for SP2-05PT-6-CON

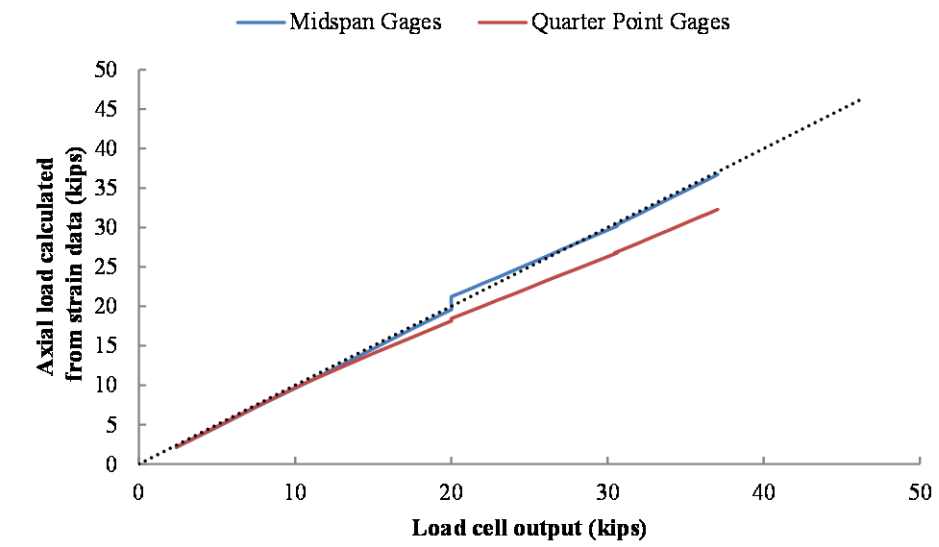

Figure A-160: Axial Load Comparison for SP2-05PT-7-ECC-E

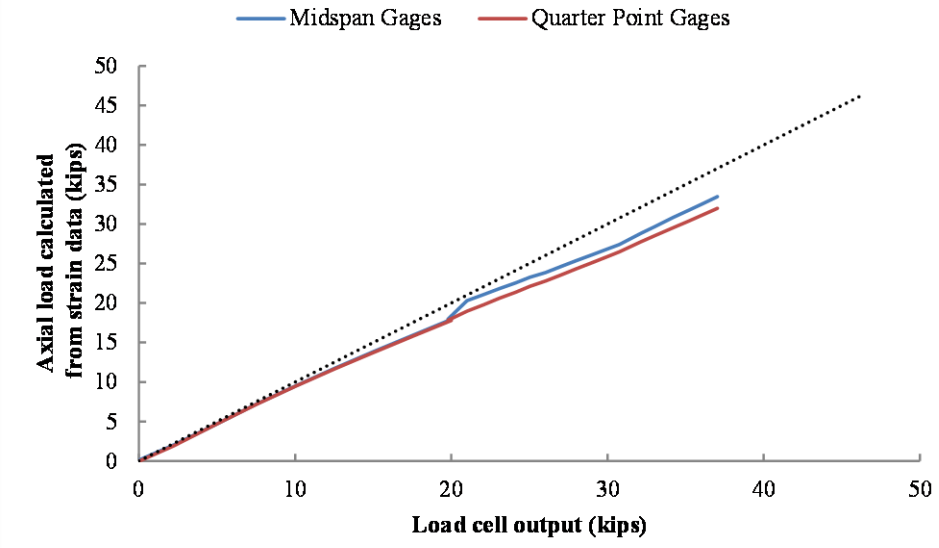

Figure A-161: Axial Load Comparison for SP2-05PT-8-ECC-W

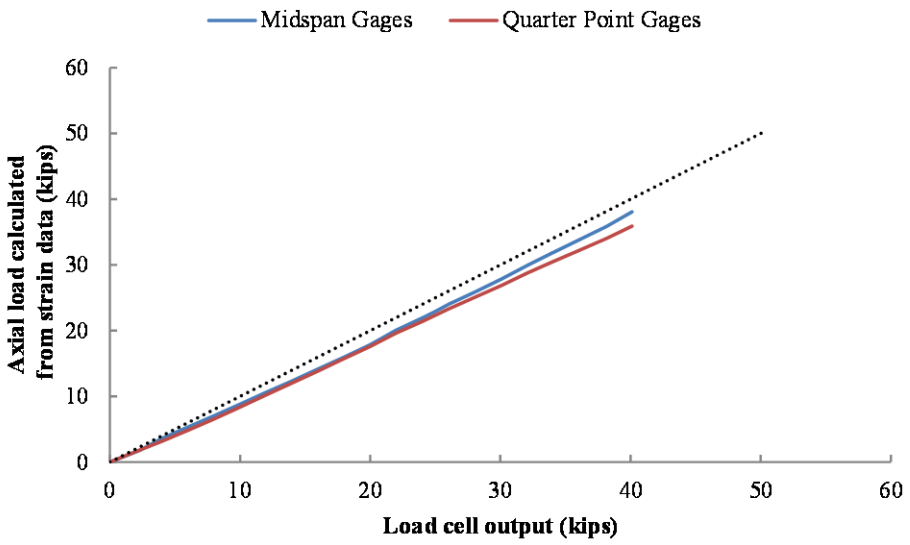

Figure A-162: Axial Load Comparison for SP2-06PT-1-CON

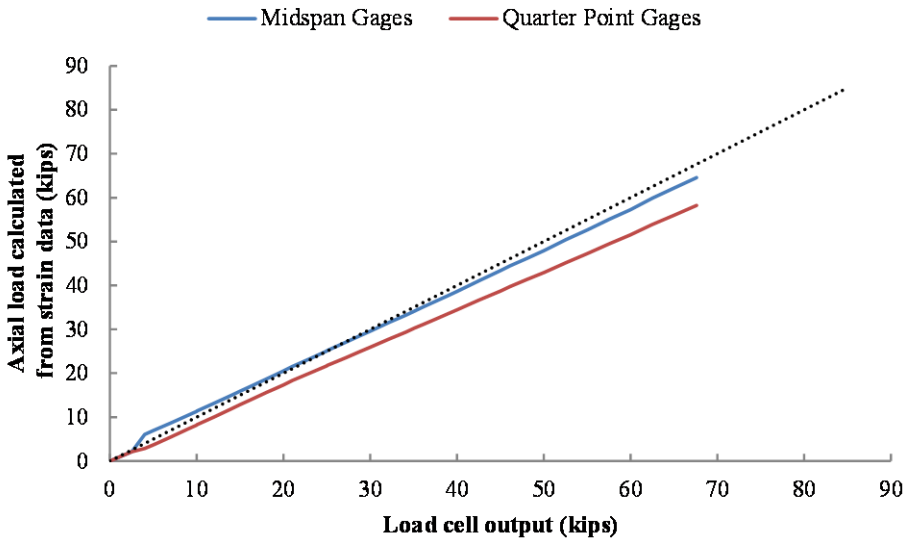

Figure A-163: Axial Load Comparison for SP2-06PT-2-ECC-E

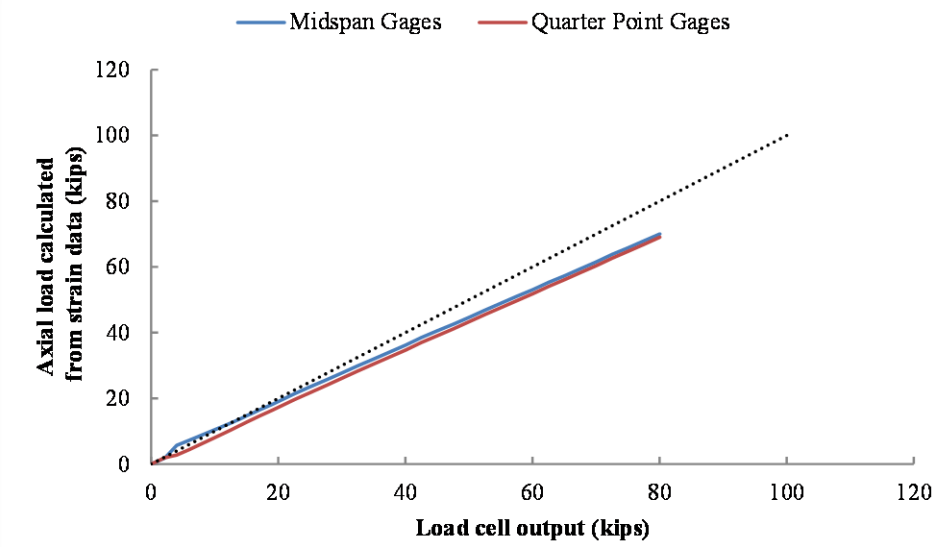

Figure A-164: Axial Load Comparison for SP2-06PT-3-ECC-W

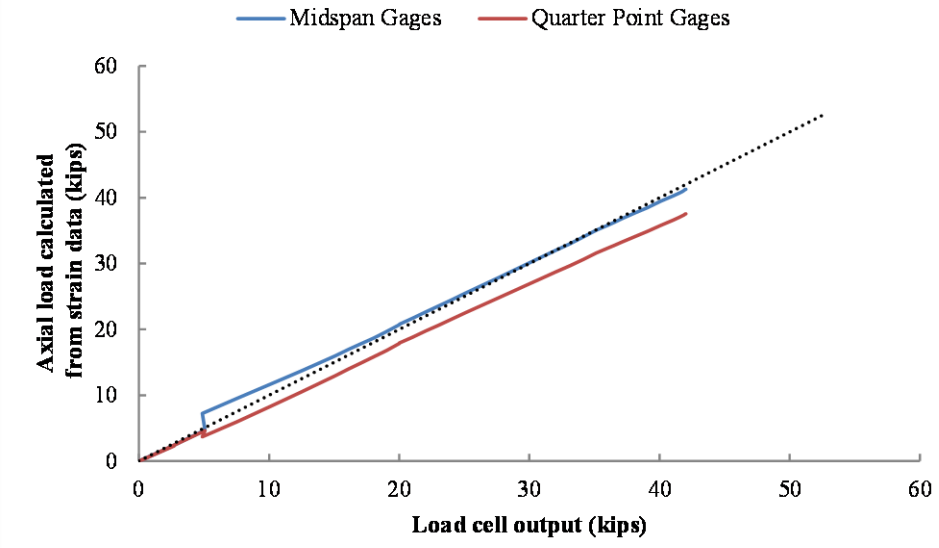

Figure A-165: Axial Load Comparison for SP2-06PT-4-CON

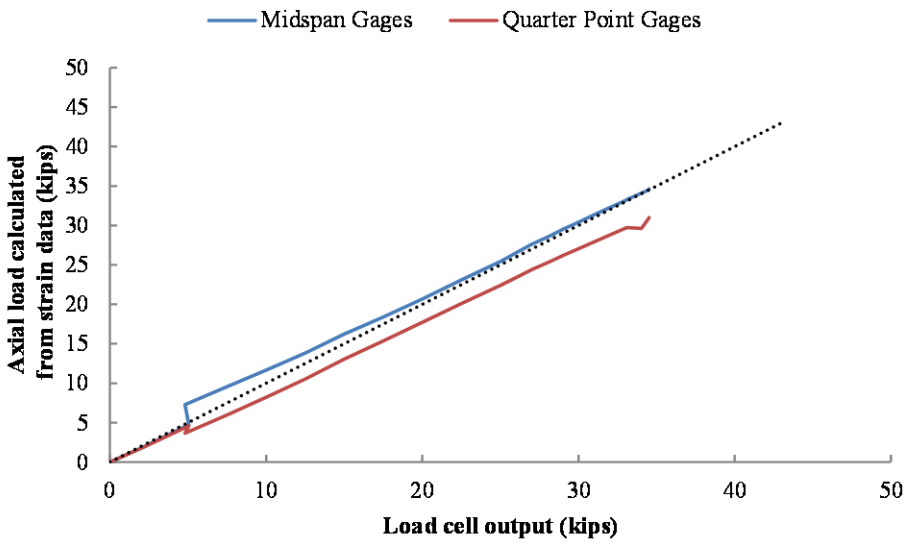

Figure A-166: Axial Load Comparison for SP2-06PT-5-CON

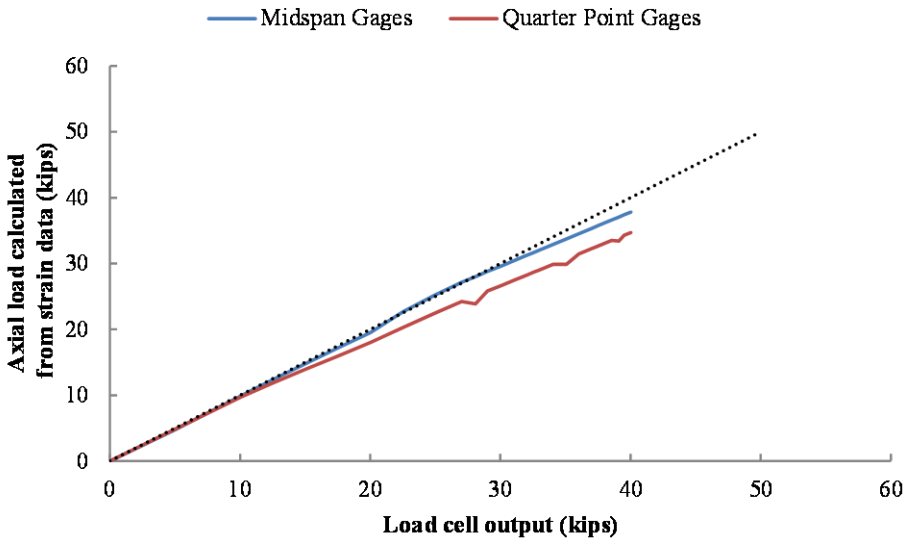

Figure A-167: Axial Load Comparison for SP2-06PT-6-CON

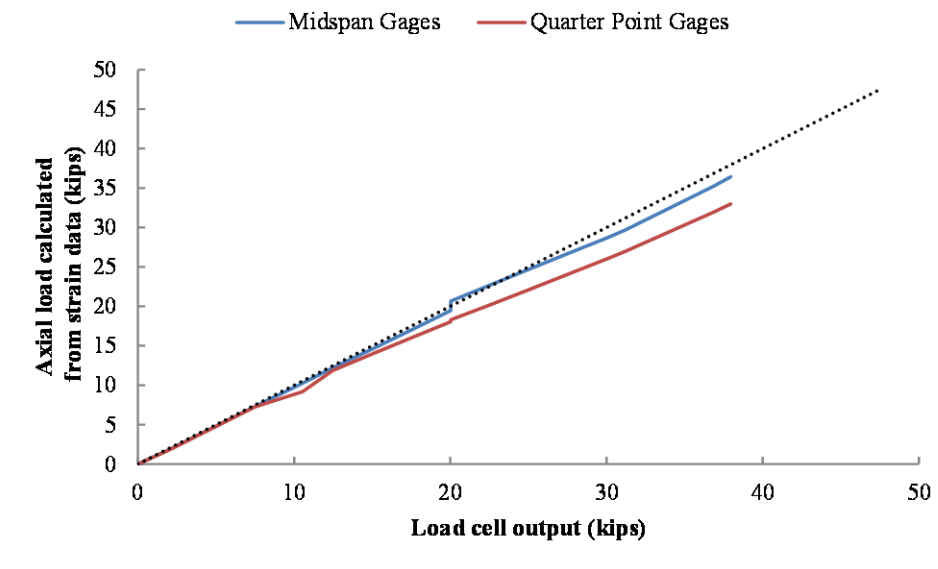

Figure A-168: Axial Load Comparison for SP2-06PT-7-CON

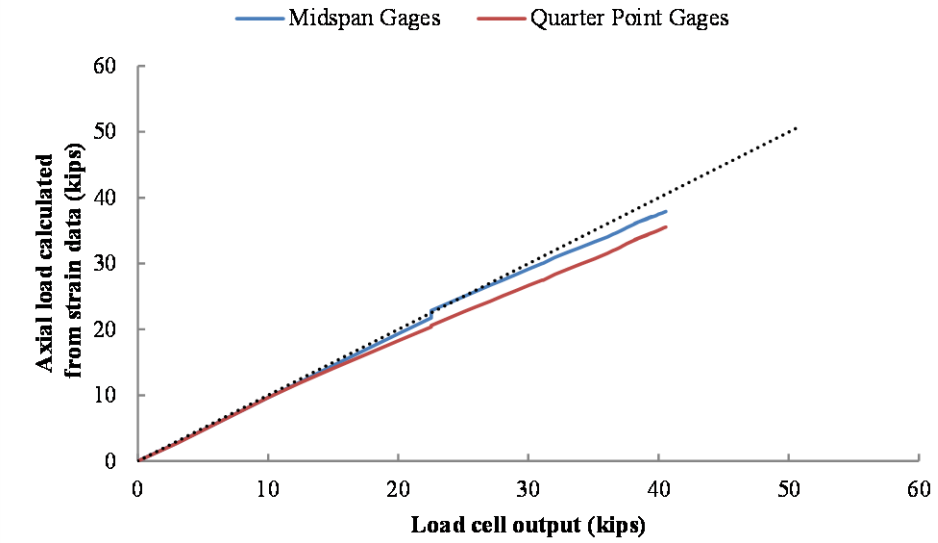

Figure A-169: Axial Load Comparison for SP2-06PT-8-CON

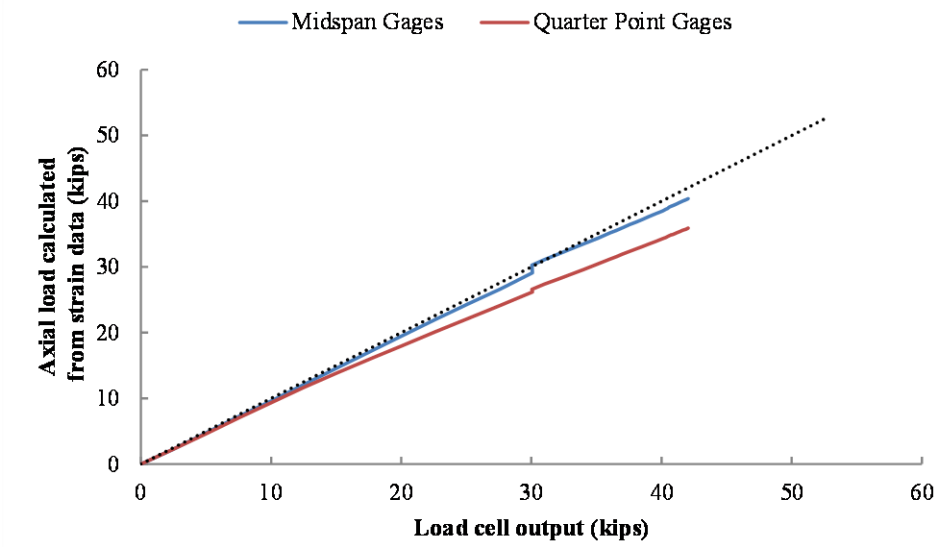

Figure A-170: Axial Load Comparison for SP2-06PT-9-CON

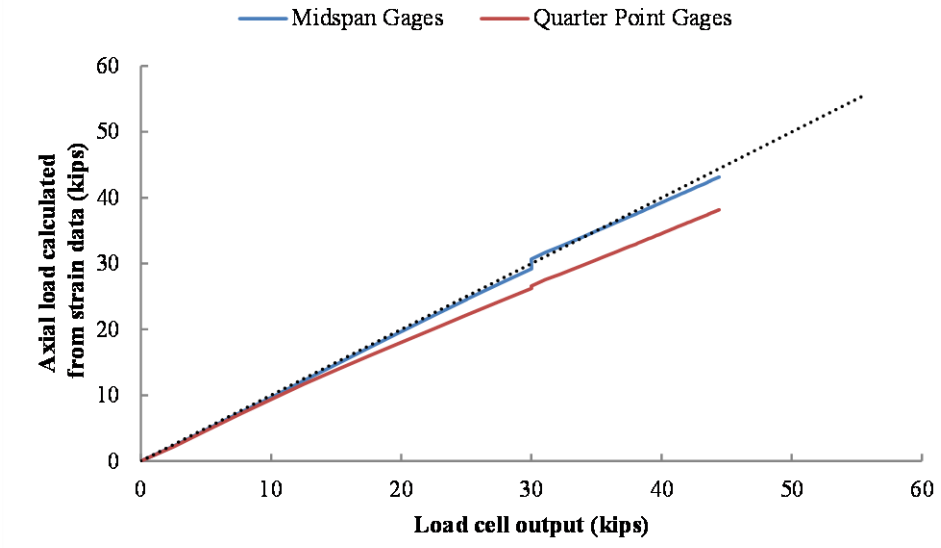

Figure A-171: Axial Load Comparison for SP2-06PT-10-CON

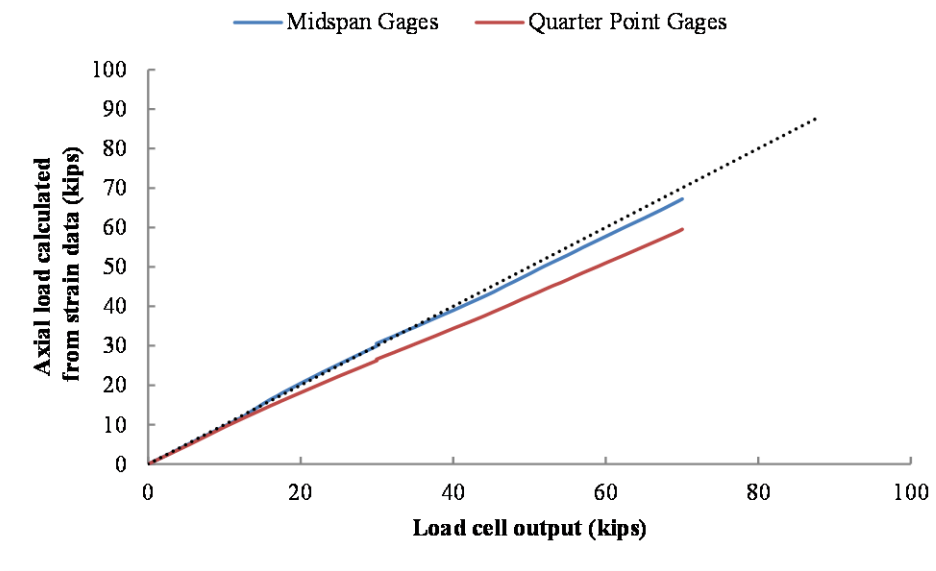

Figure A-172: Axial Load Comparison for SP2-06PT-11-ECC-E

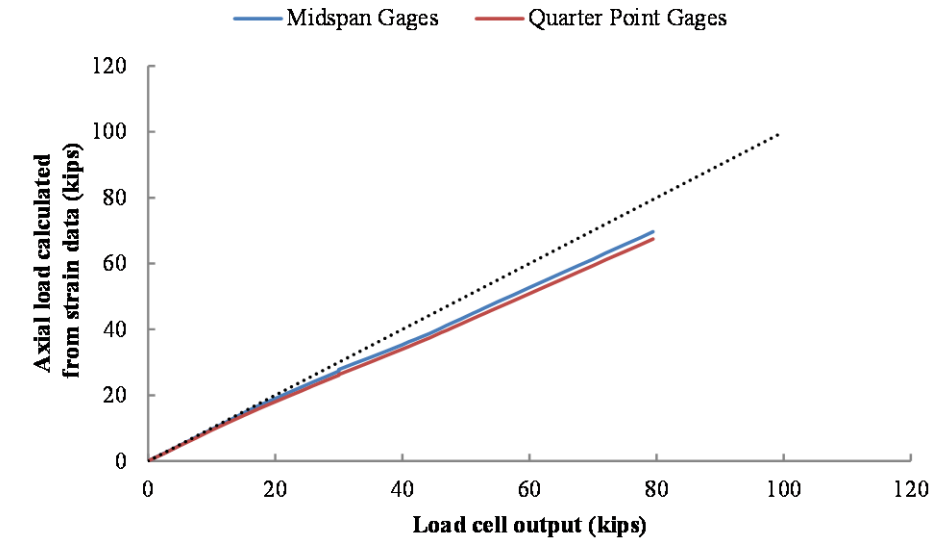

Figure A-173: Axial Load Comparison for SP2-06PT-12-ECC-W

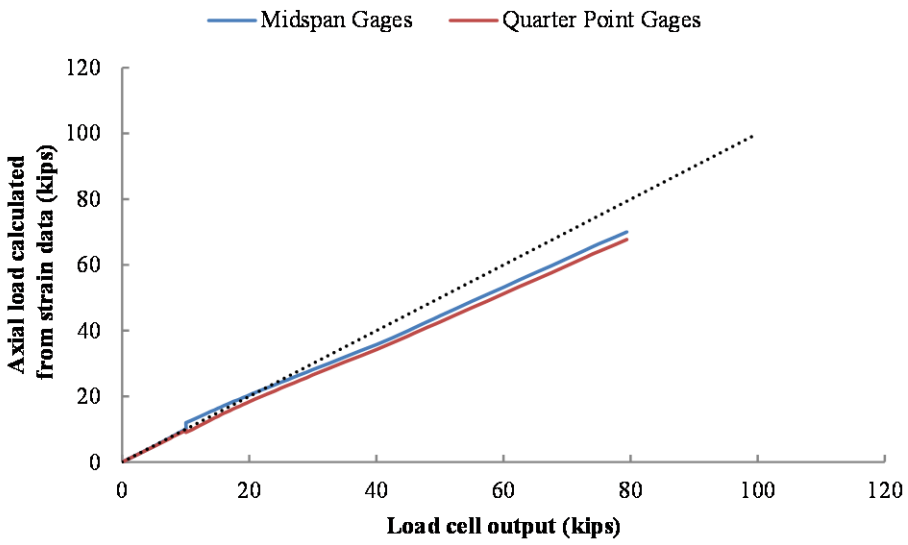

Figure A-174: Axial Load Comparison for SP2-06PT-13-ECC-W

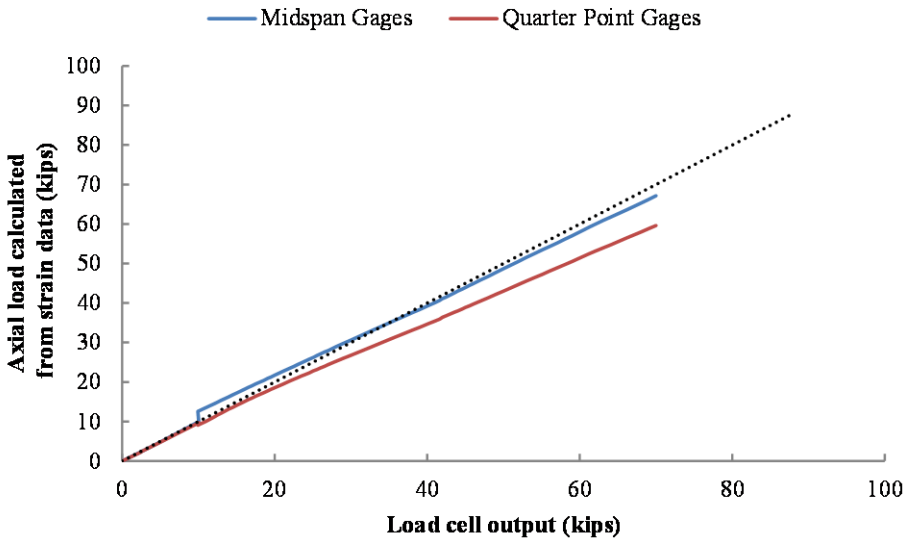

Figure A-175: Axial Load Comparison for SP2-06PT-14-ECC-E

A.4.2.2 SP2 Combined Load Tests

This subsection includes the axial load estimates for each of the combined load tests on SP2. There were a total of twelve combined load tests performed.

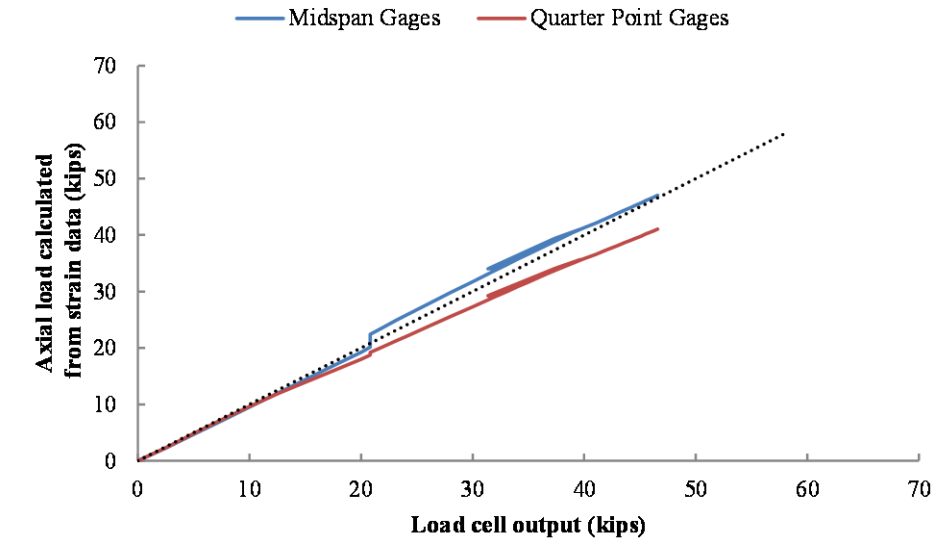

Figure A-176: Axial Load Comparison for SP2-05PT30-EX-1-DS

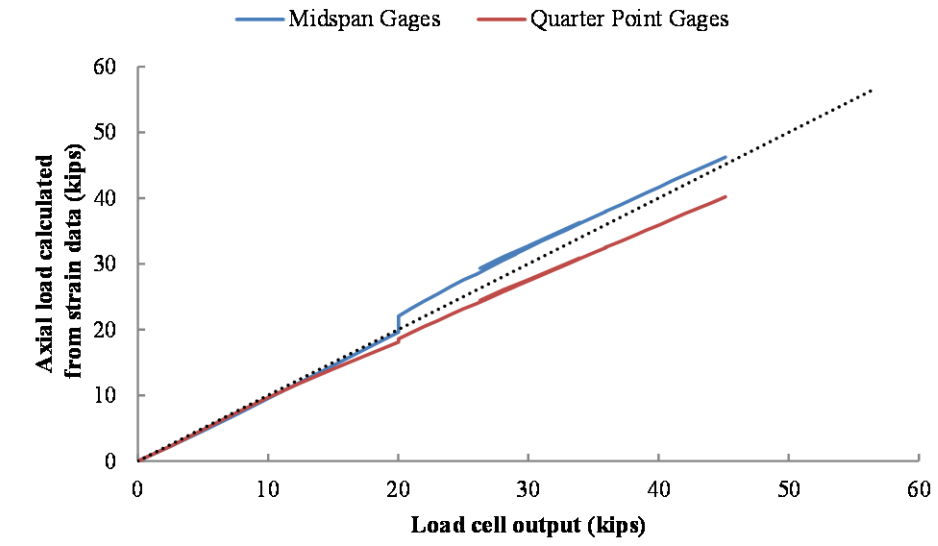

Figure A-177: Axial Load Comparison for SP2-05PT25-EX-2-DS

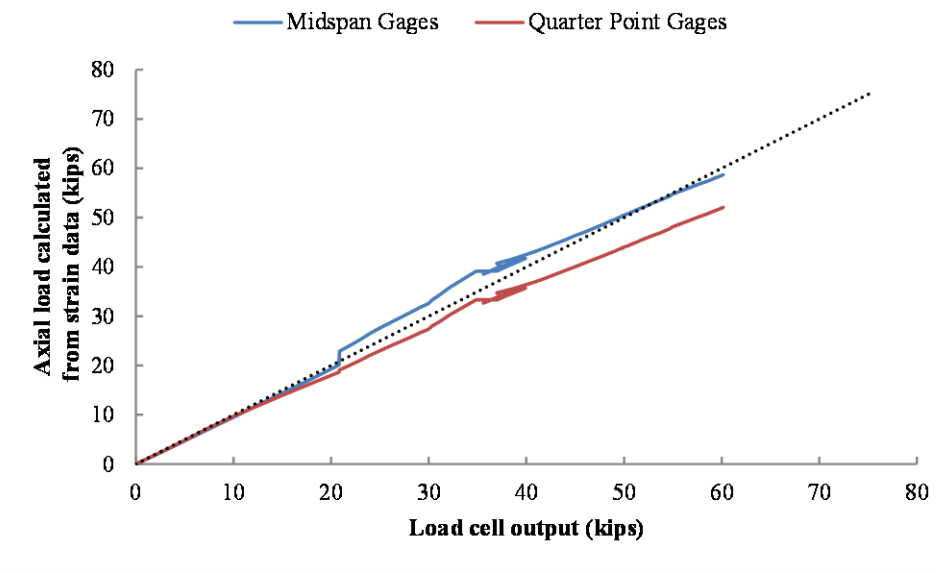

Figure A-178: Axial Load Comparison for SP2-05PT35-EX-3-DS

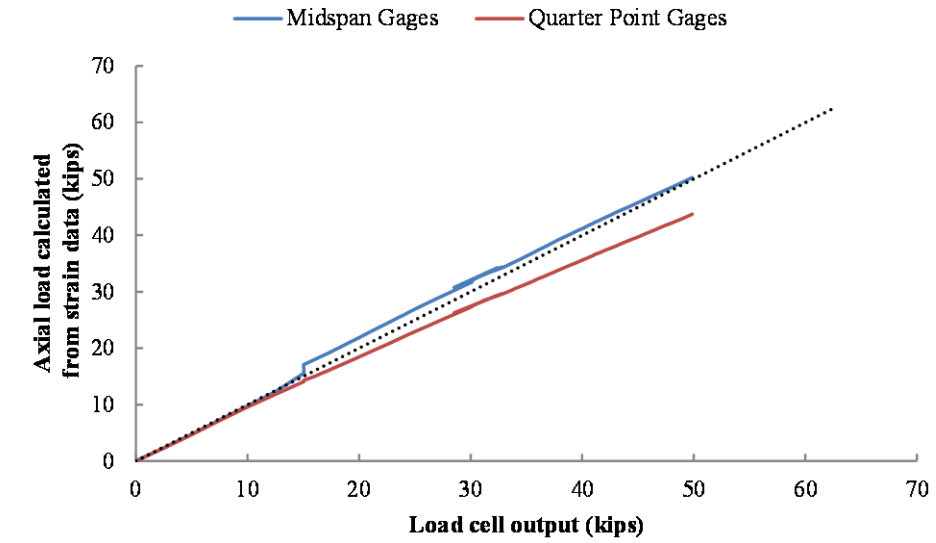

Figure A-179: Axial Load Comparison for SP2-06PT30-EX-1-DS

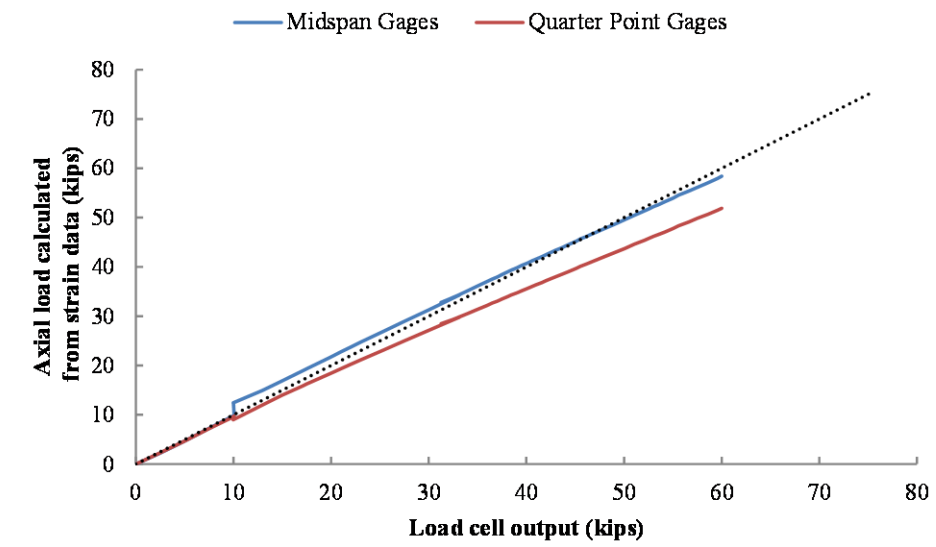

Figure A-180: Axial Load Comparison for SP2-06PT30-EX-2-DS

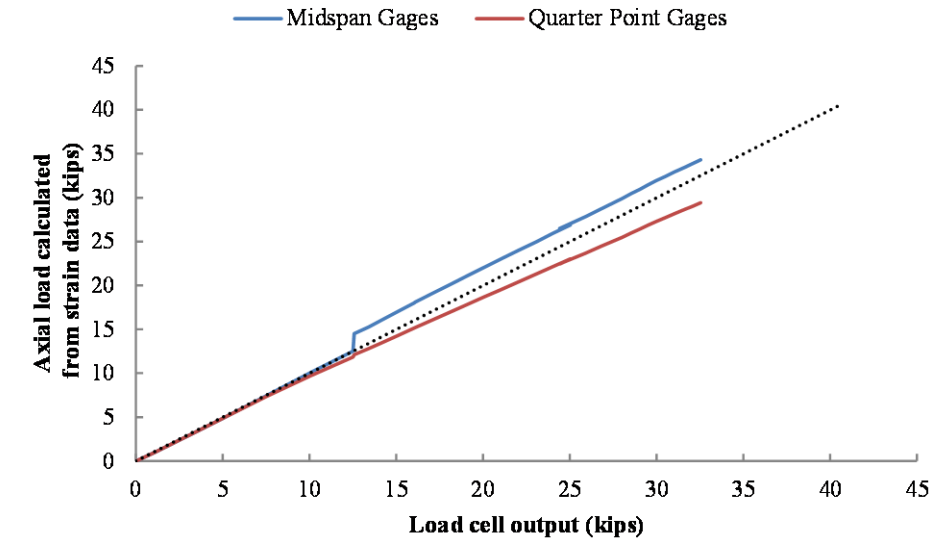

Figure A-181: Axial Load Comparison for SP2-06PT25-EX-3-DS

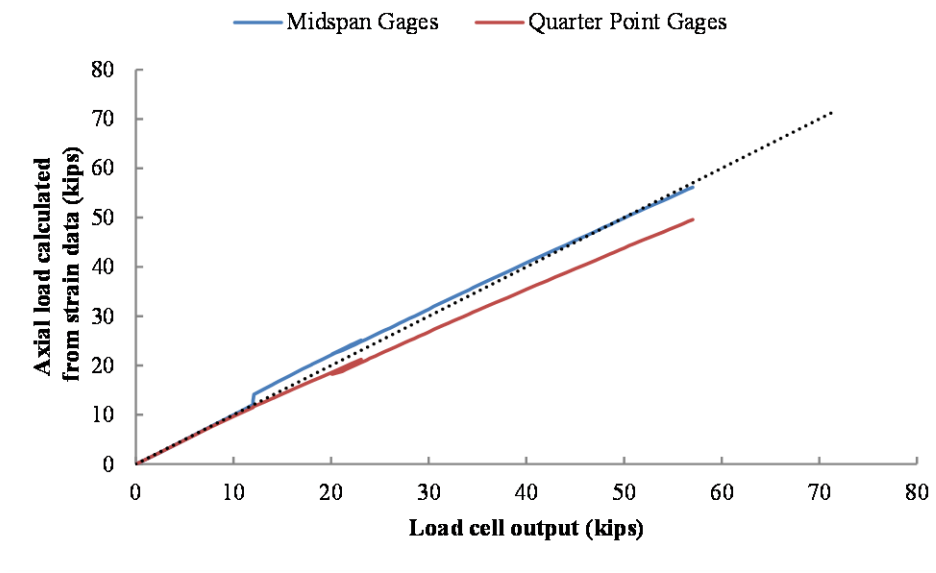

Figure A-182: Axial Load Comparison for SP2-06PT20-EX-4-DS

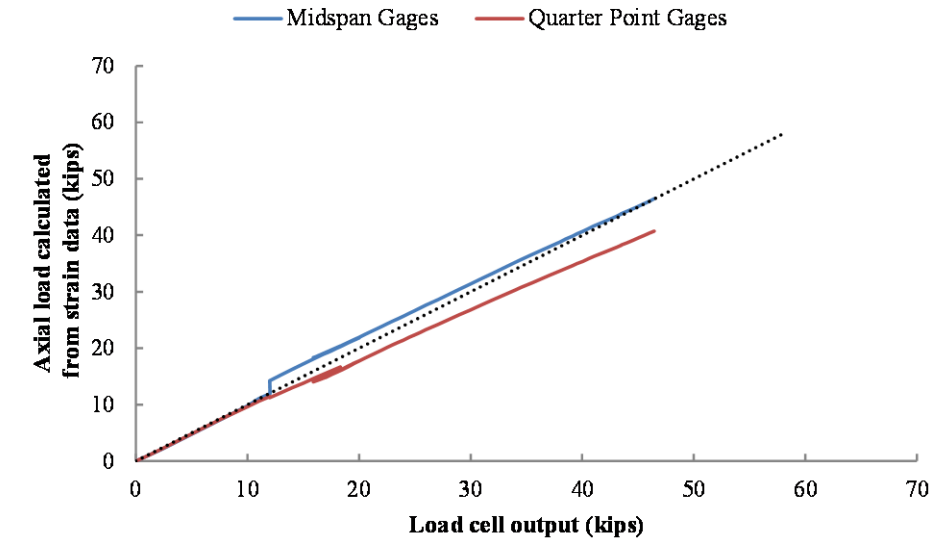

Figure A-183: Axial Load Comparison for SP2-06PT15-EX-5-DS

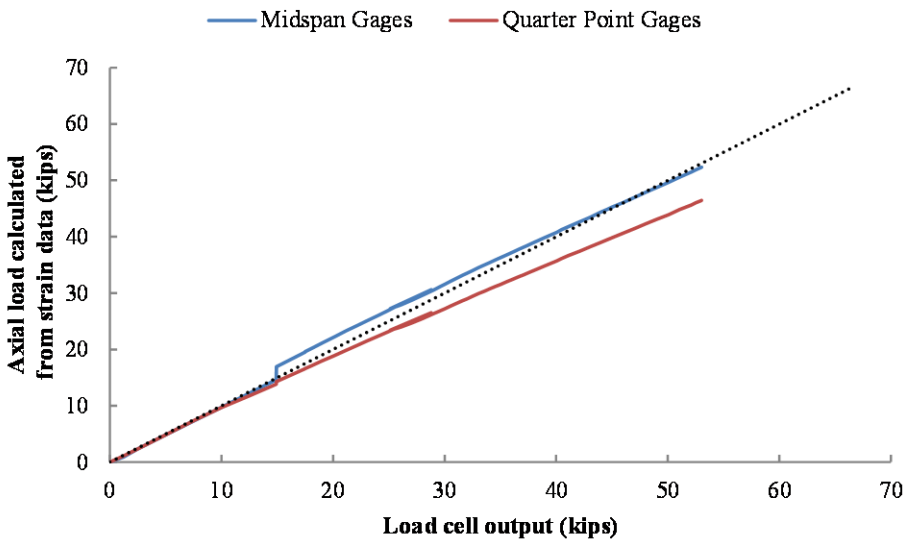

Figure A-184: Axial Load Comparison for SP2-06PT25-EX-6-DS

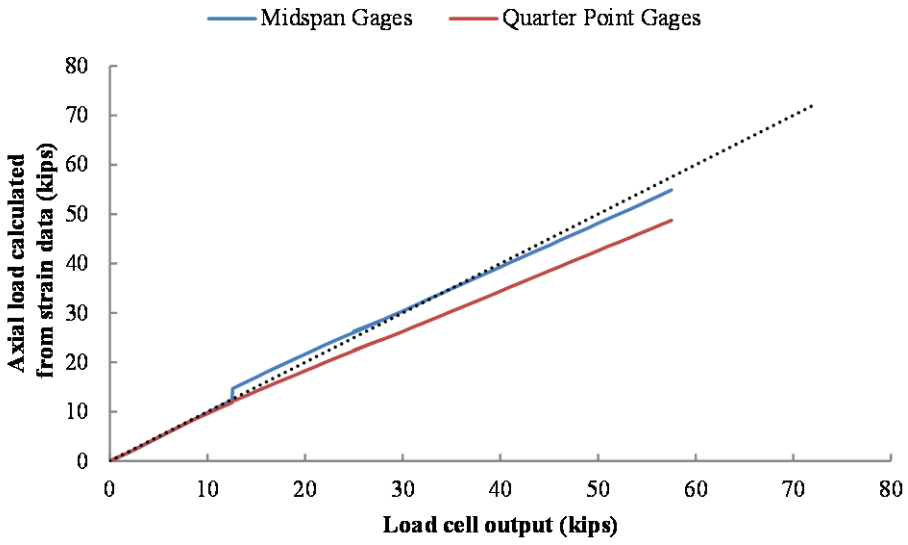

Figure A-185: Axial Load Comparison for SP2-06PT25-EX-7-SS

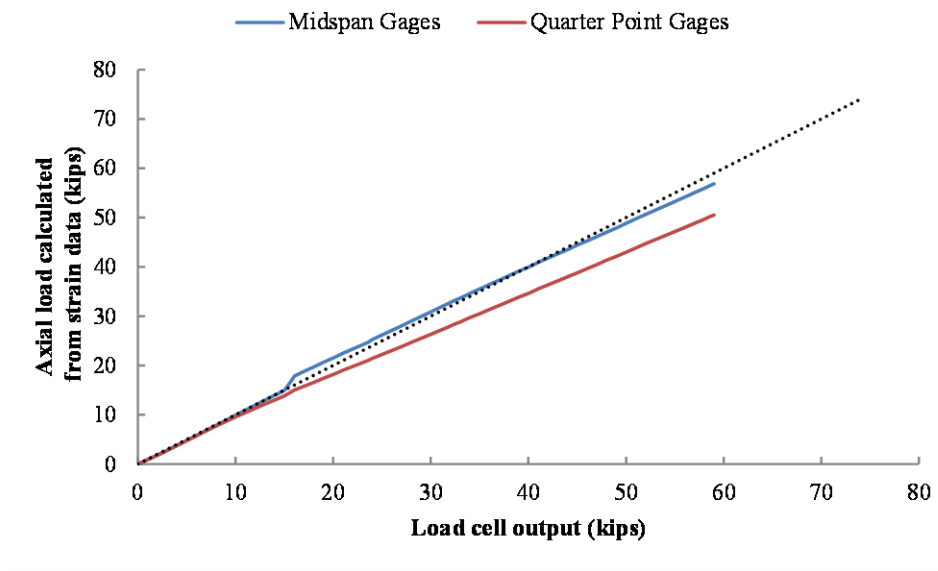

Figure A-186: Axial Load Comparison for SP2-06PT20-EX-8-SS

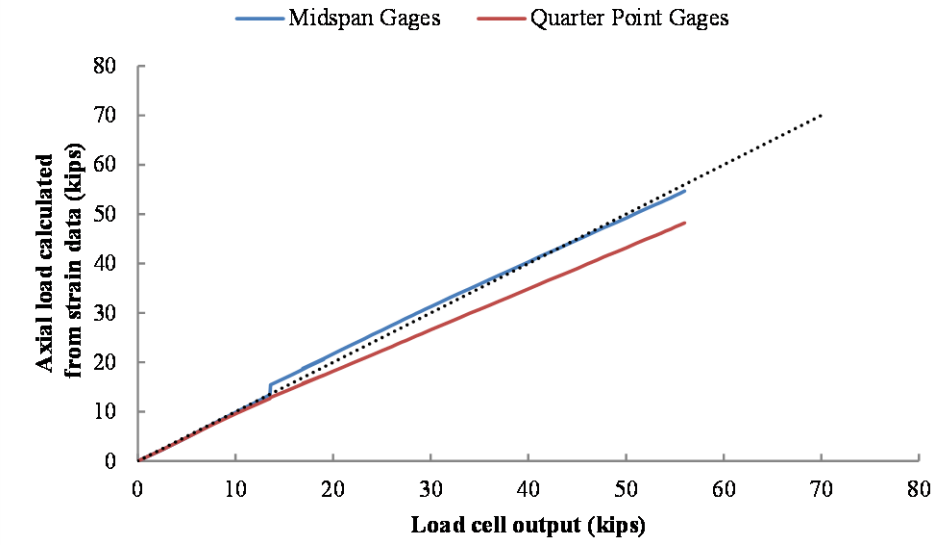

Figure A-187: Axial Load Comparison for SP2-06PT15-EX-9-SS

A.4.2.3 SP2 External Load Tests

This subsection includes the axial load estimate from the single external load test on SP2. The test ended in a full buckling failure which resulted in extensive cracking in the member.

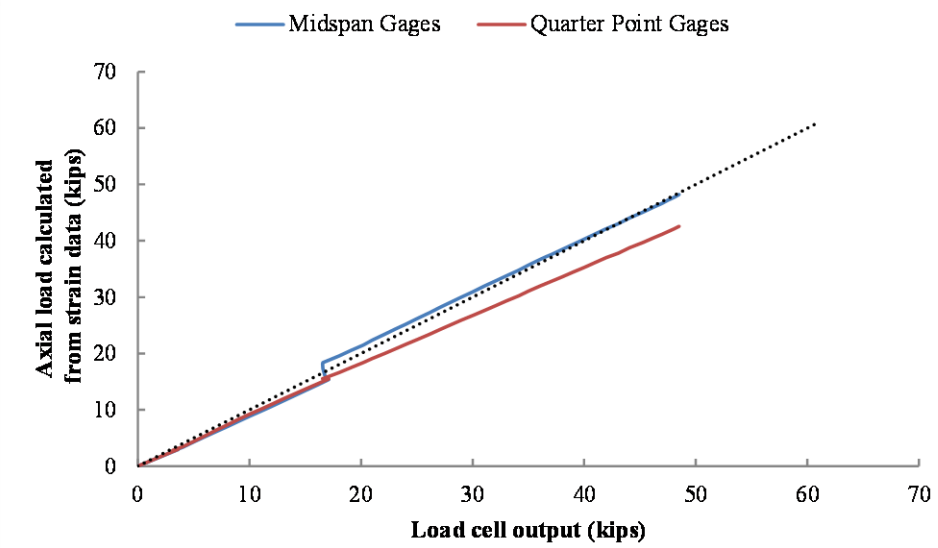

Figure A-188: Axial Load Comparison for SP2-PT0-EX-1

A.5 SOUTHWELL PLOTS

This portion of the appendix provides Southwell plots for selected tests. As discussed in the previous chapters, Southwell plots were constructed for tests with concentric loading only. (Southwell plots as they were used in this study become less meaningful with variations in the assumed magnitude and shape of initial deflections.) In addition, meaningful Southwell plots could not be constructed for some concentric tests due to a lack of lateral displacement (often caused by excessive friction or end fixity in the test setup). Each plot shown includes an estimate of the critical buckling capacity and initial imperfection as indicated by the Southwell relationship. In some cases where stiffening or softening behavior is noted, a load versus lateral curvature plot is also

included. A table summarizing the change in the predicted buckling capacity of the member as stiffening or softening occurred is also provided. As discussed in the text, these estimates should not be interpreted as the actual buckling capacity of the member, but rather as an illustration of the effects of strand engagement on the stability of the member.

A.5.1 Specimen 1 (SP1)

This subsection includes Southwell plots for a total of thirteen load tests on the first specimen (SP1). Notes on individual tests are included in the figure captions where applicable.

A.5.1.1 SP1 Post-tensioned Tests

This subsection includes the Southwell plots constructed from the PT tests on SP1. There were a total of 22 pre-failure PT load tests performed. Southwell plots were constructed for nine of the 22 tests.

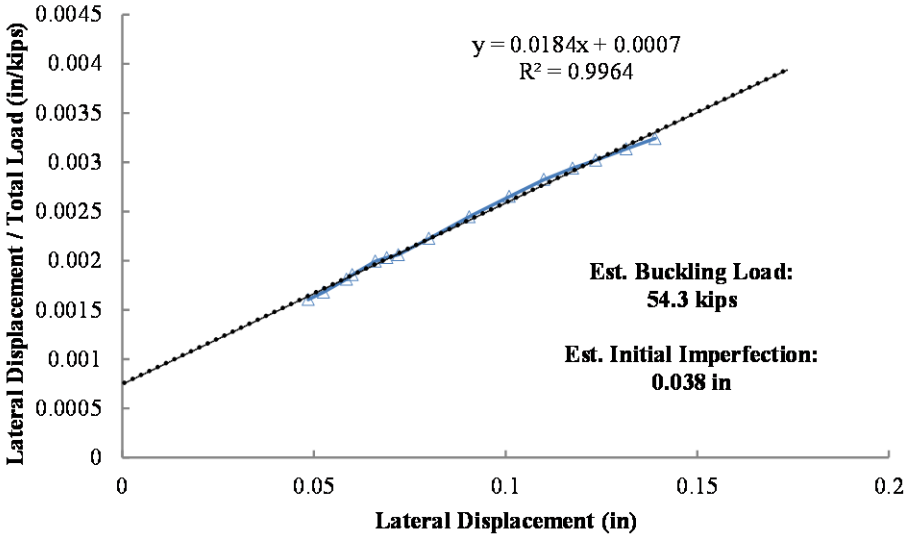

Figure A-189: Southwell Plot for SP1-05PT-8-CON

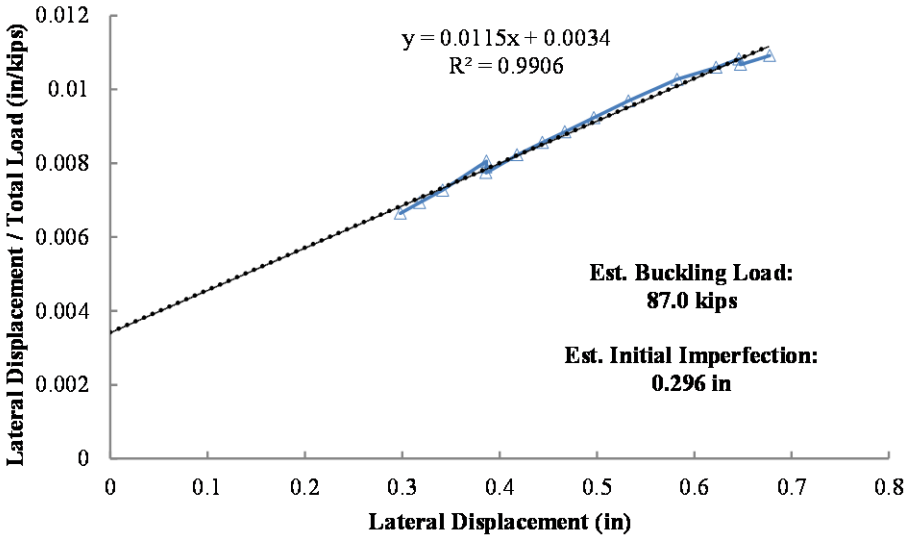

Figure A-190: Southwell Plot for SP1-05PT-9-CON

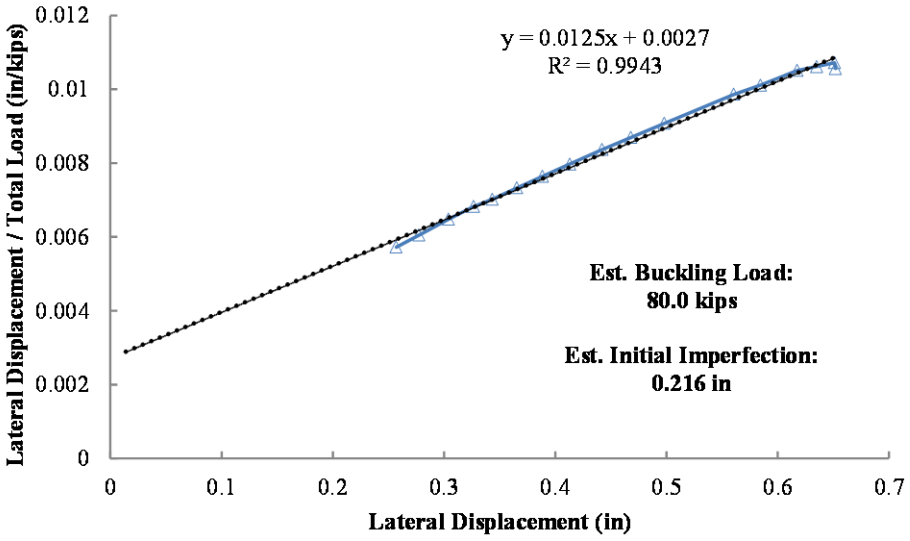

Figure A-191: Southwell Plot for SP1-05PT-10-CON

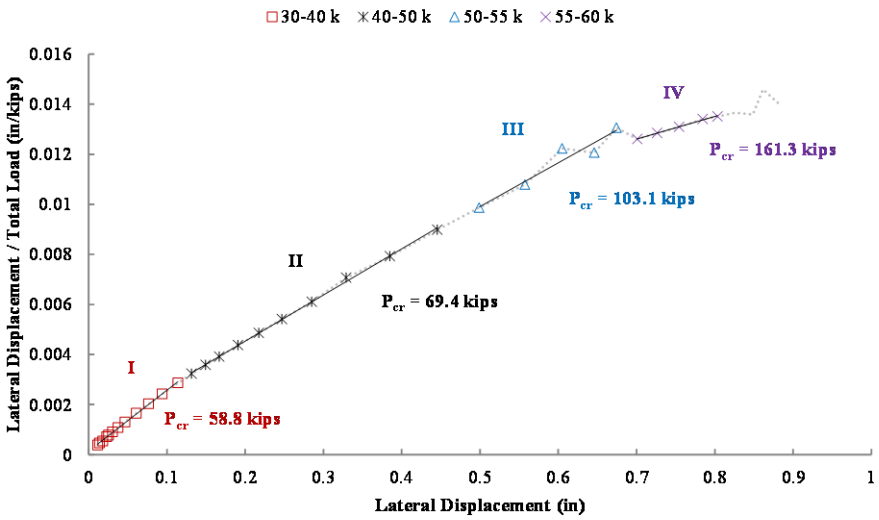

Figure A-192: Southwell Plot for SP1-05PT-11-CON

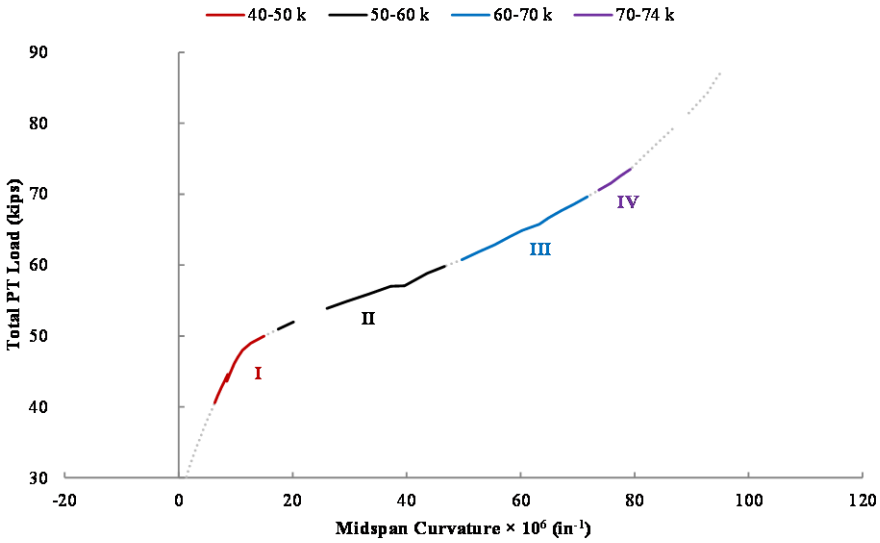

Figure A-193: Load vs. Lateral Curvature for SP1-05PT-11-CON

Table A-2: Southwell Plot Parameters for SP1-05PT-11-CON

Series	Load Increment (k)	Slope	Y-Intercept	R^2 value	Buckling Load P_{cr} (k)	Initial Imperfection (in)
I	30-40	0.0243	0.0001	0.9990	**41.2**	0.004
II	40-50	0.0184	0.0008	0.9982	**54.3**	0.043
III	50-55	0.0175	0.0012	0.9966	**57.1**	0.069
IV	55-60	0.009	0.0063	0.9913	**111.1**	0.700

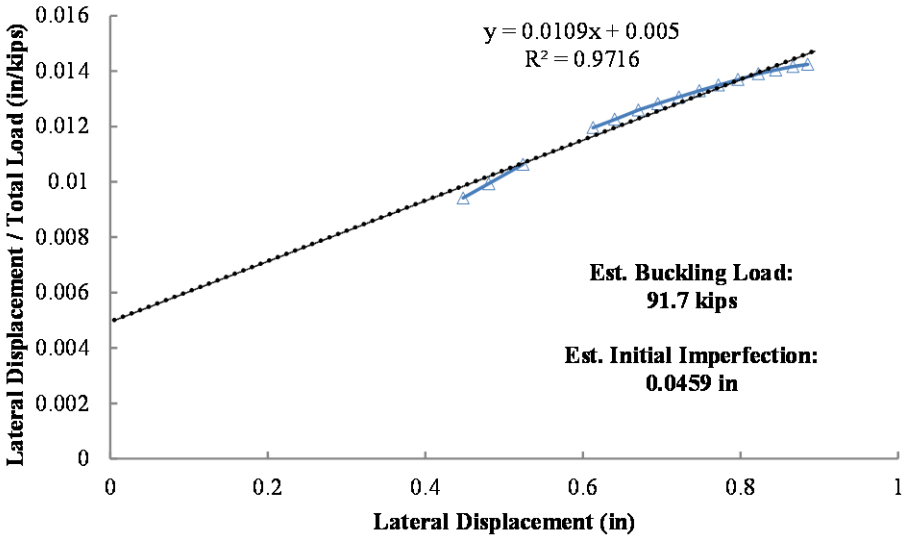

Figure A-194: Southwell Plot for SP1-05PT-12-CON

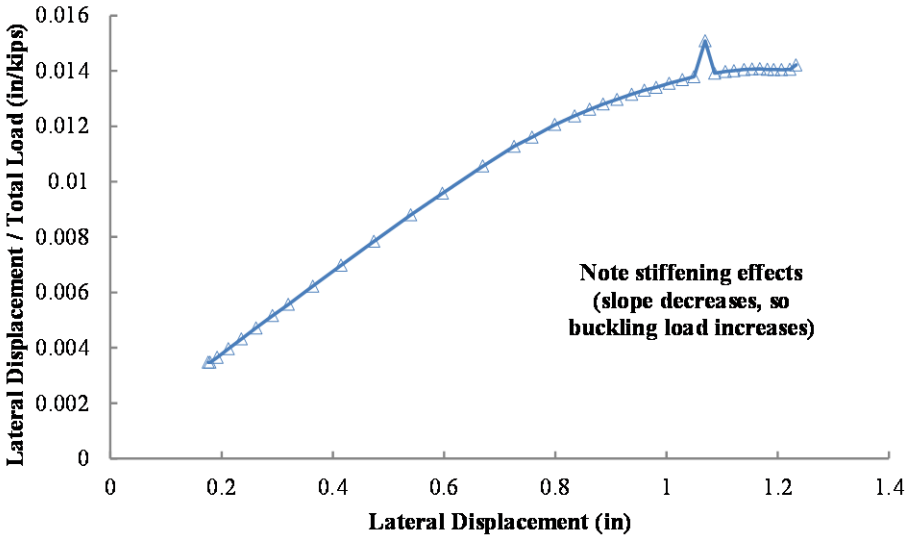

Figure A-195: Southwell Plot for SP1-06PT-1-CON

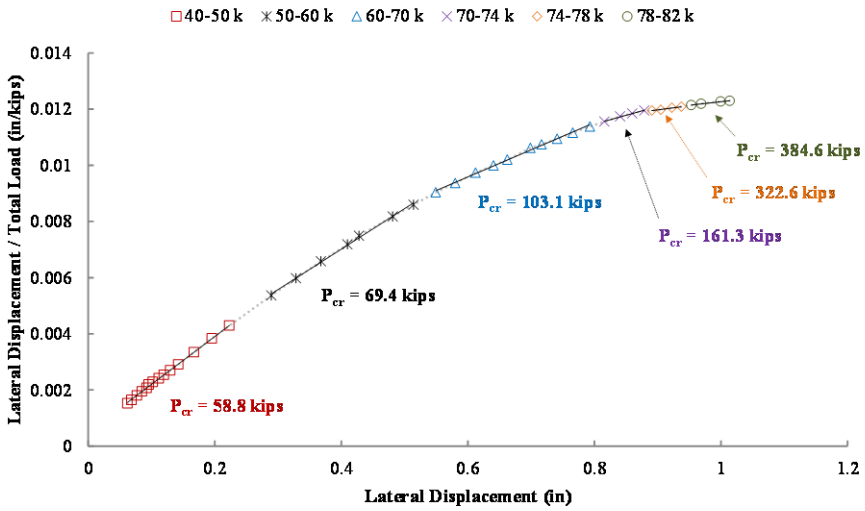

Figure A-196: Southwell Plot for SP1-06PT-2-CON

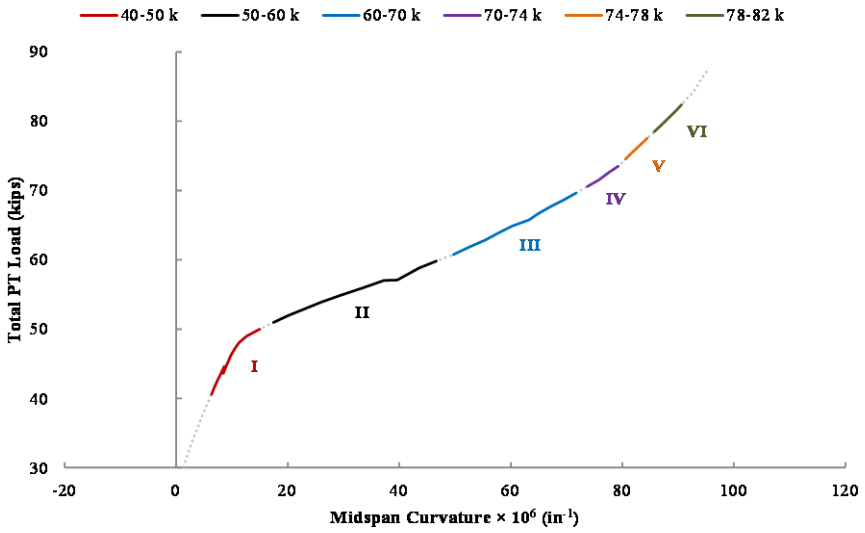

Figure A-197: Load vs. Lateral Curvature for SP1-06PT-2-CON

Table A-3: Southwell Plot Parameters for SP1-06PT-2-CON

Series	Load Increment (k)	Slope	Y-Intercept	R^2 value	Buckling Load P_{cr} (k)	Initial Imperfection (in)
I	40-50	0.017	0.0005	0.9990	**58.8**	0.029
II	50-60	0.0144	0.0013	0.9982	**69.4**	0.090
III	60-70	0.0097	0.0038	0.9966	**103.1**	0.392
IV	70-78	0.0062	0.0065	0.9913	**161.3**	1.048
V	74-78	0.0031	0.0092	0.9912	**322.6**	2.968
VI	78-82	0.0026	0.0097	0.9930	**384.6**	3.731

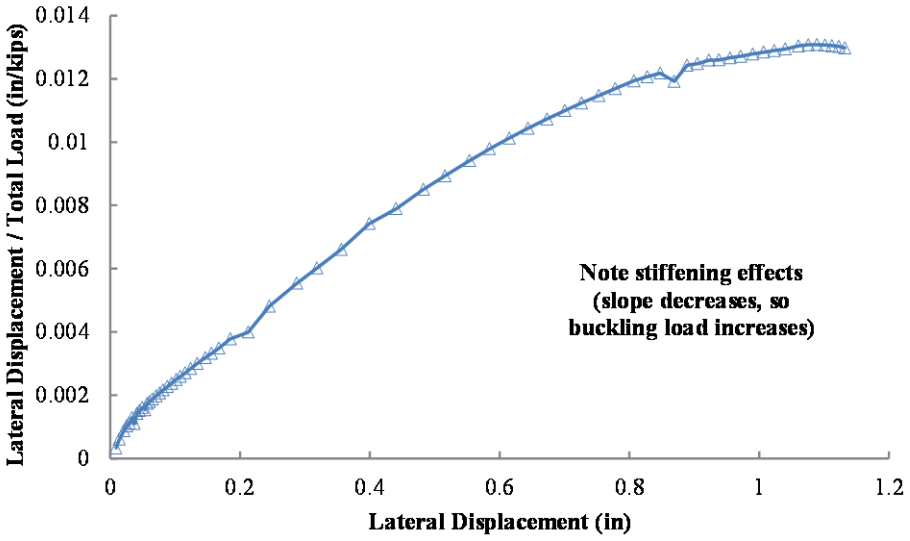

Figure A-198: Southwell Plot for SP1-06PT-3-CON

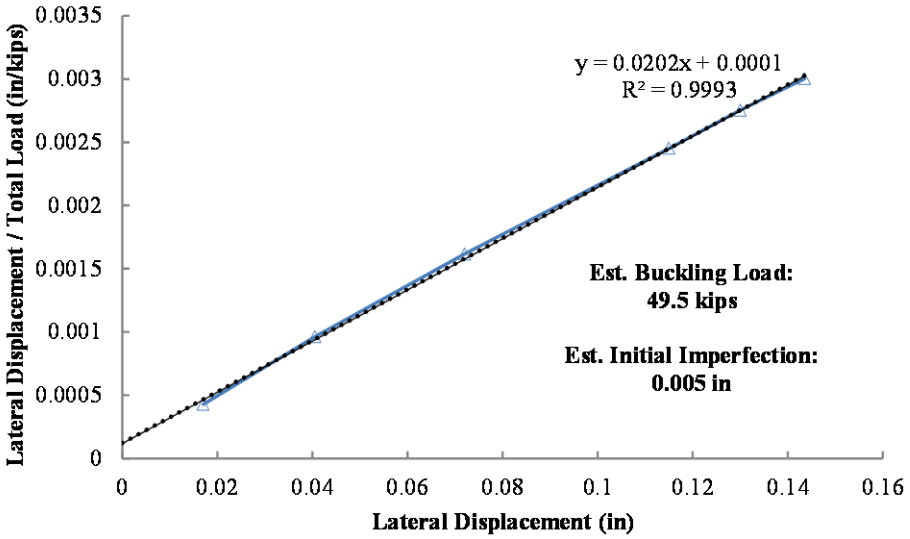

Figure A-199: Southwell Plot for SP1-06PT-6-CON

A.5.1.2 SP1 Combined Load Tests

The only combined load test in SP1 was performed after the specimen was cracked extensively due to a buckling failure. The post-failure buckled shape was not consistent with the initial assumptions of the Southwell plots. As such, construction of Southwell plots was not applicable in this load case for SP1.

A.5.1.3 SP1 External Load Tests

This section includes the Southwell plots constructed from the external load tests on SP1. There were a total of four external load tests performed. The first two tests occurred prior to cracking, and as such, demonstrate a much higher buckling capacity than do the two post-failure tests.

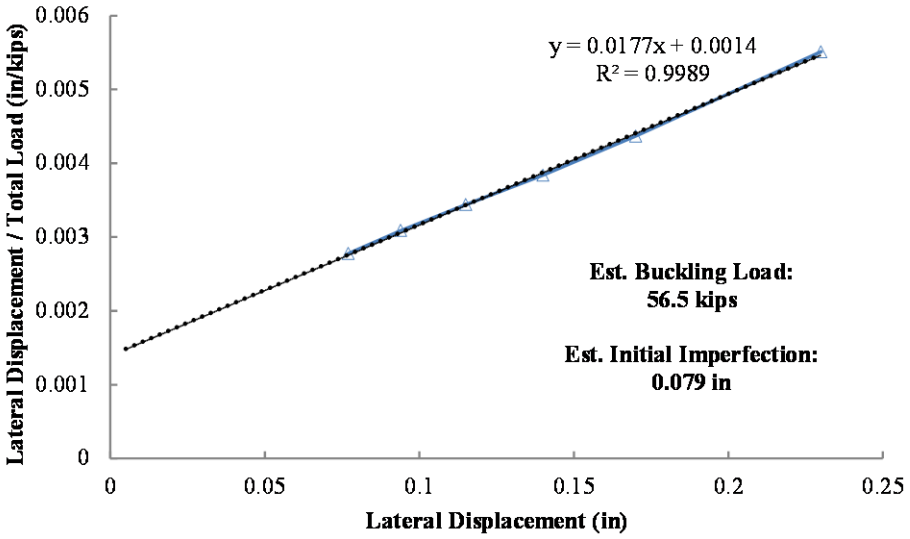

Figure A-200: Southwell Plot for SP1-PT0-EX-1

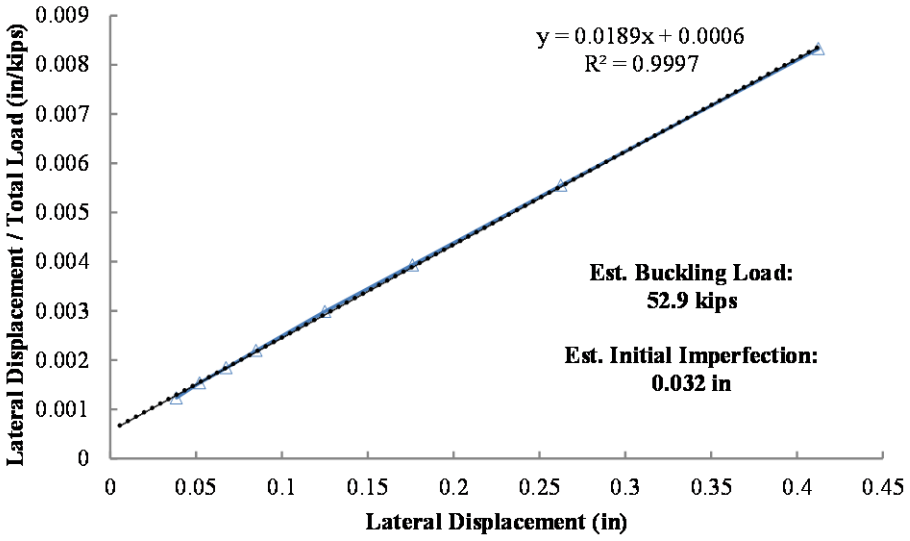

Figure A-201: Southwell Plot for SP1-PT0-EX-2 (Specimen buckled suddenly at approximately 51 kips in this test. Discussion is included in Chapter 5.)

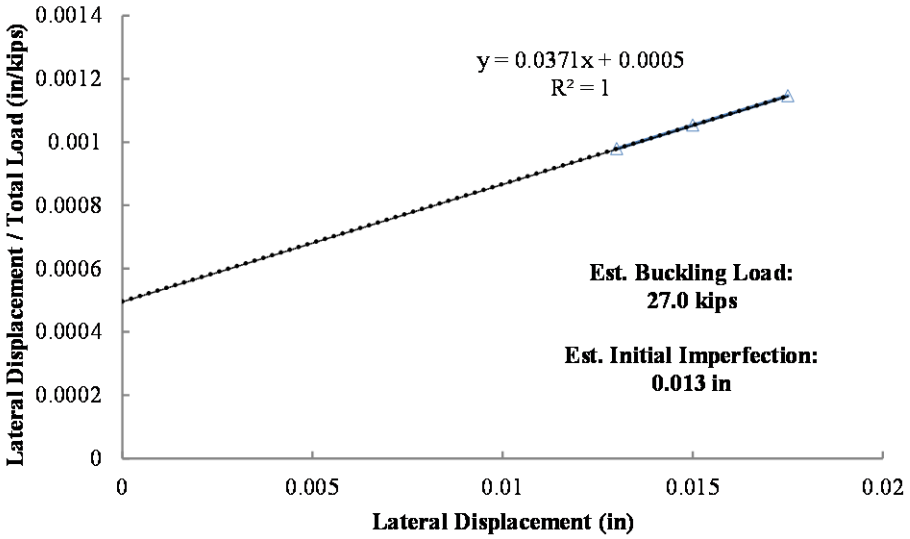

Figure A-202: Southwell Plot for SP1-PT0-EX-3 (Note: Plot is not highly meaningful due to lack of lateral deflection. Deflection increased in subsequent tests once the source of additional friction was identified and eliminated.)

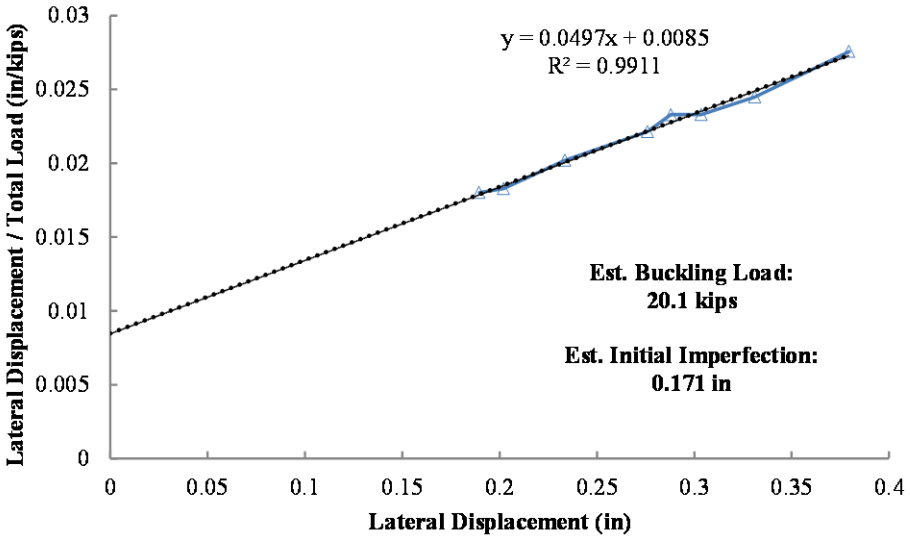

Figure A-203: Southwell Plot for SP1-PT0-EX-4

A.5.2 Specimen 2 (SP2)

This subsection includes Southwell plots for a total of 20 load tests on the second specimen (SP2). Notes on individual tests are included in the figure captions where applicable.

A.5.2.1 SP2 Post-tensioned Tests

This subsection includes the Southwell plots constructed from the pre-failure PT tests on SP2. There were a total of 22 pre-failure PT load tests performed. Southwell plots were constructed for 11 of the 22 tests.

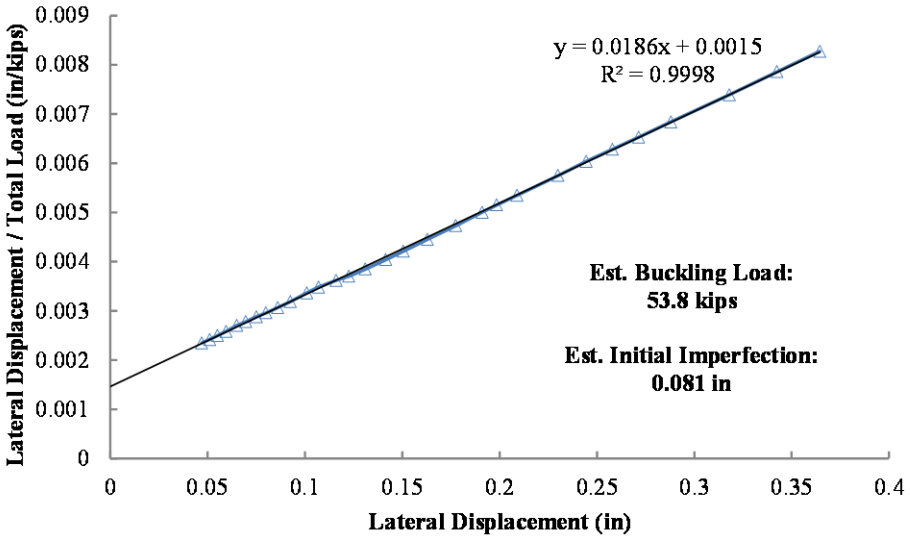

Figure A-204: Southwell Plot for SP2-05PT-1-CON

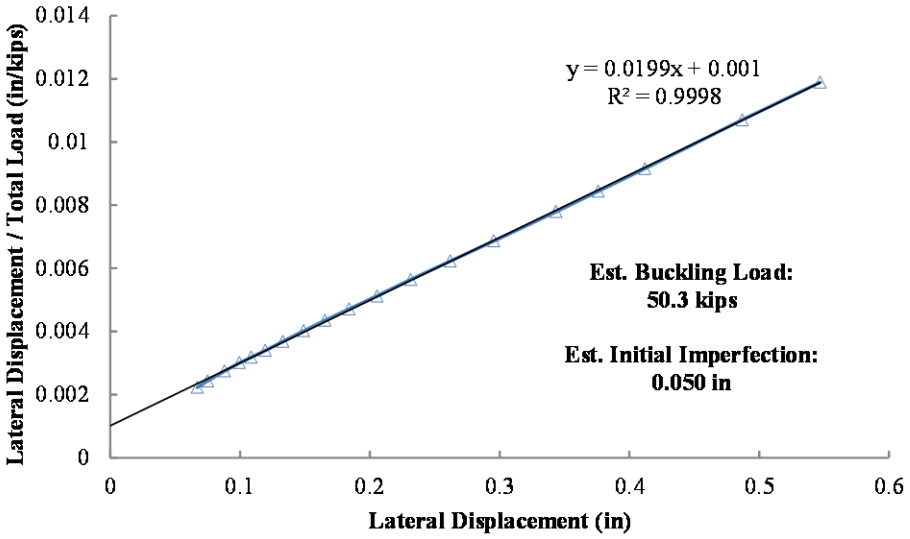

Figure A-205: Southwell Plot for SP2-05PT-3-CON

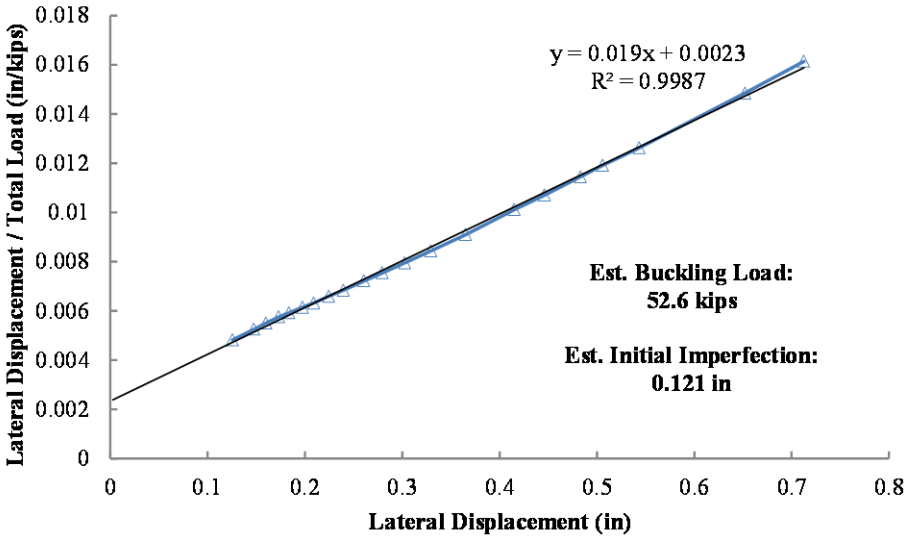

Figure A-206: Southwell Plot for SP2-05PT-6-CON

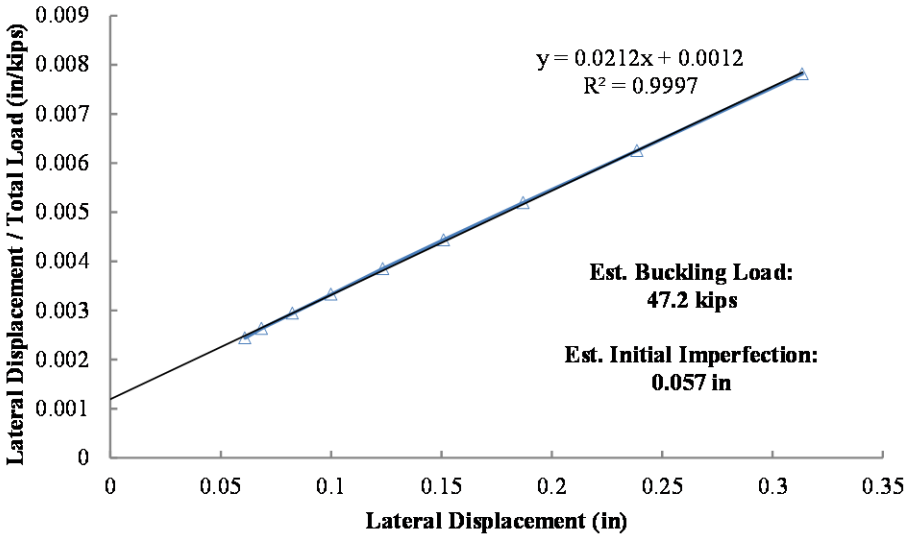

Figure A-207: Southwell Plot for SP2-06PT-1-CON

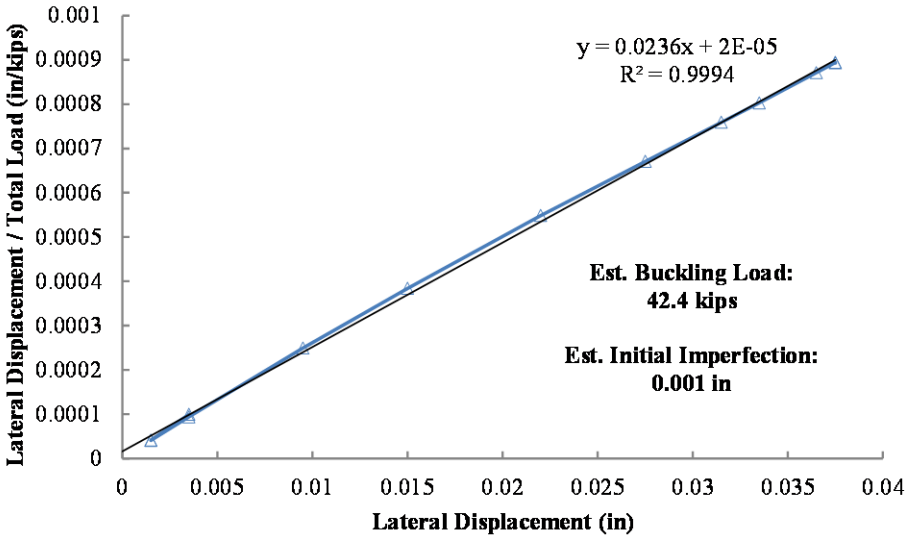

Figure A-208: Southwell Plot for SP2-06PT-4-CON (Note: Plot is not highly meaningful due to lack of lateral deflection. Deflection increased in subsequent tests once the source of additional end fixity was identified and eliminated.)

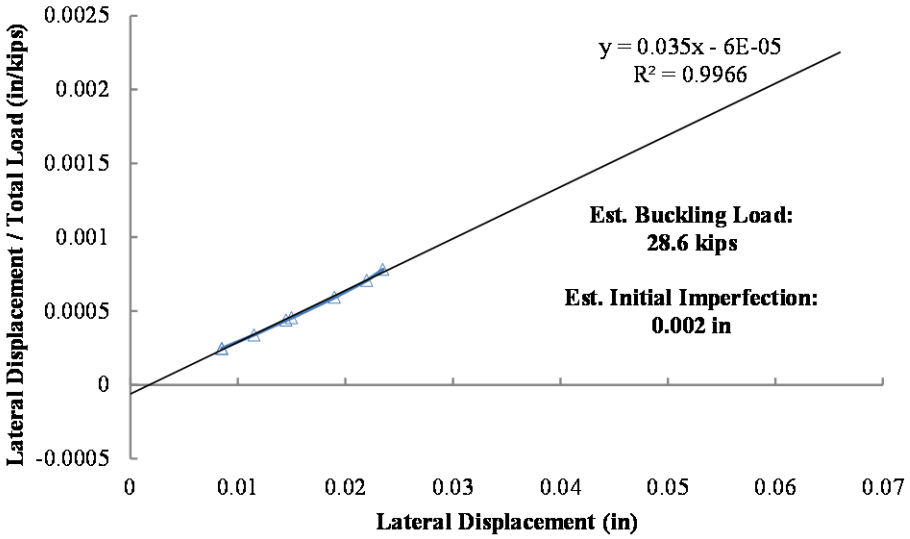

Figure A-209: Southwell Plot for SP2-06PT-5-CON (Note: Plot is not highly meaningful due to lack of lateral deflection. Deflection increased in subsequent tests once the source of additional end fixity was identified and eliminated.)

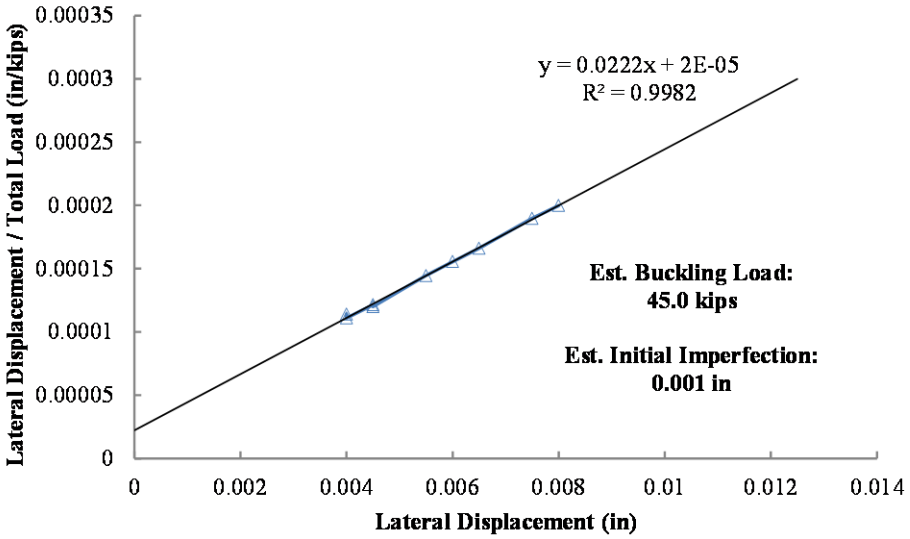

Figure A-210: Southwell Plot for SP2-06PT-6-CON (Note: Plot is not highly meaningful due to lack of lateral deflection. Deflection increased in subsequent tests once the source of additional end fixity was identified and eliminated.)

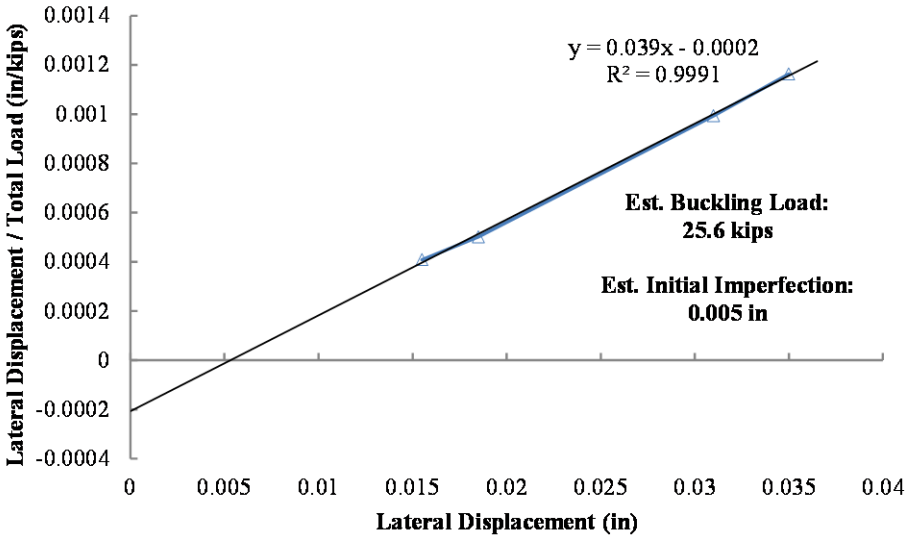

Figure A-211: Southwell Plot for SP2-06PT-7-CON (Note: Plot is not highly meaningful due to lack of lateral deflection. Deflection increased in subsequent tests once the source of additional end fixity was identified and eliminated.)

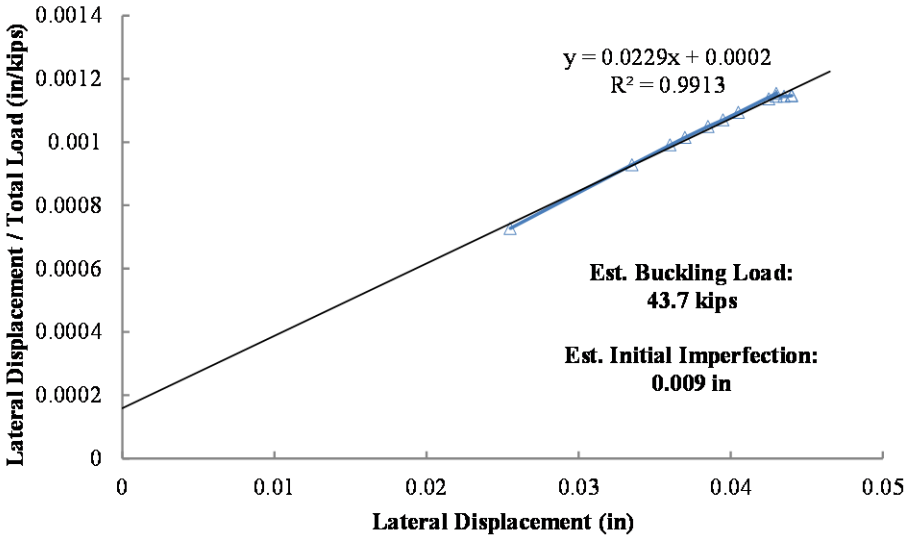

Figure A-212: Southwell Plot for SP2-06PT-8-CON (Note: Plot is not highly meaningful due to lack of lateral deflection. Deflection increased in subsequent tests once the source of additional end fixity was identified and eliminated.)

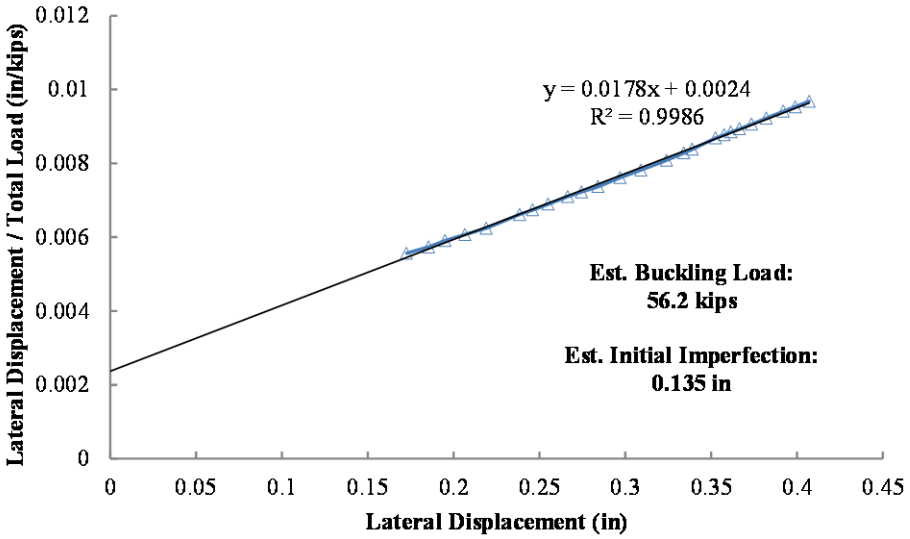

Figure A-213: Southwell Plot for SP2-06PT-9-CON

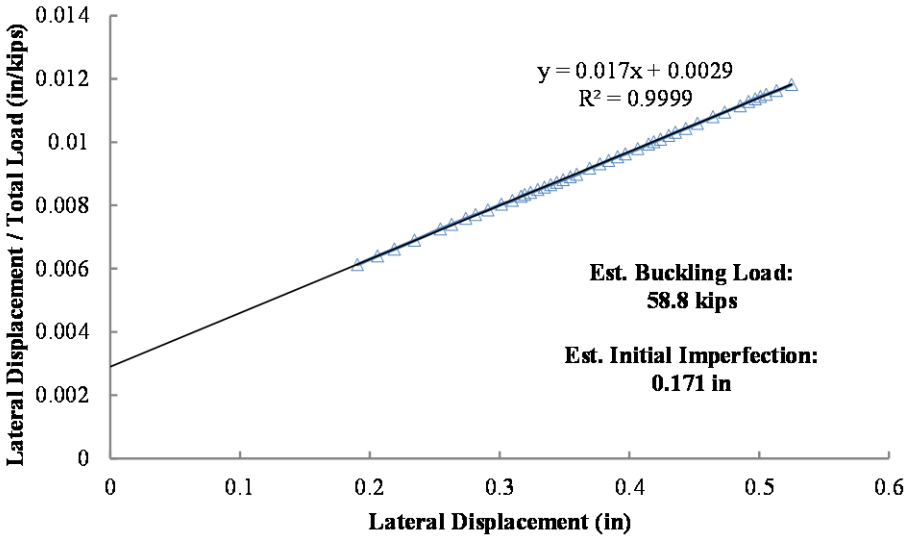

Figure A-214: Southwell Plot for SP2-06PT-10-CON

A.5.2.2 SP2 Combined Load Tests

This subsection includes the Southwell plots constructed from the combined load tests on SP2. There were a total of twelve combined load tests performed. Southwell plots were constructed for eight of the twelve tests. In some cases where stiffening or softening behavior was noted, a load versus lateral curvature plot is included. A table summarizing the change in the predicted buckling capacity of the member as stiffening or softening occurred is also provided. As discussed in the text, these estimates should not be interpreted as the actual buckling capacity of the member, but rather as an illustration of the effects of strand engagement on the stability of the member.

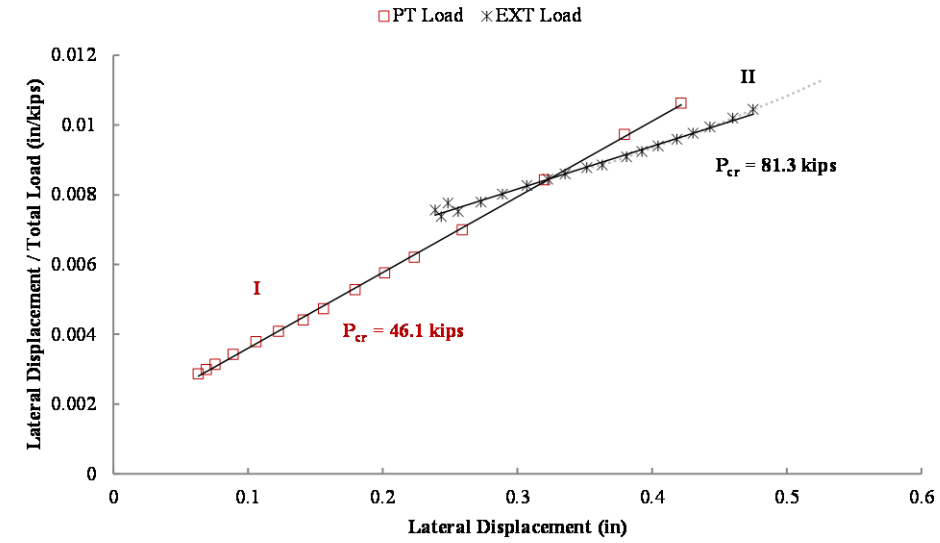

Figure A-215: Southwell Plot for SP2-05PT30-EX-1-DS

Table A-4: Southwell Plot Parameters for SP2-05PT30-EX-1-DS

Series	Load Increment (k)	Slope	Y-Intercept	R^2 value	Buckling Load P_{cr} (k)	Initial Imperfection (in)
I	PT: 20-40	0.0217	0.0014	0.9916	**46.1**	0.065
II	EXT: 32-45	0.0123	0.0045	0.9994	**81.3**	0.366

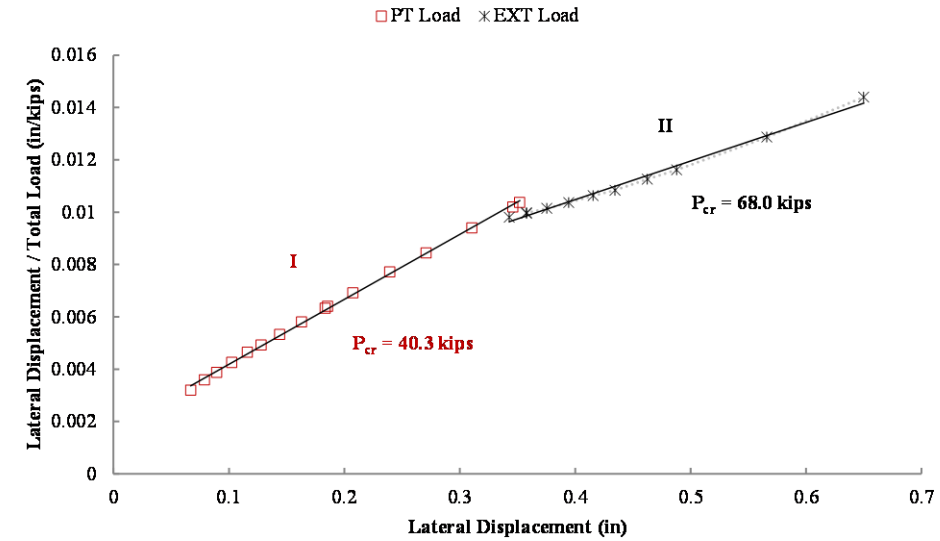

Figure A-216: Southwell Plot for SP2-05PT25-EX-2-DS

Table A-5: Southwell Plot Parameters for SP2-05PT25-EX-2-DS

Series	Load Increment (k)	Slope	Y-Intercept	R^2 value	Buckling Load P_{cr} (k)	Initial Imperfection (in)
I	PT: 20-34	0.0248	0.0017	0.9990	**40.3**	0.069
II	EXT: 35-45	0.0147	0.0046	0.9911	**68.0**	0.313

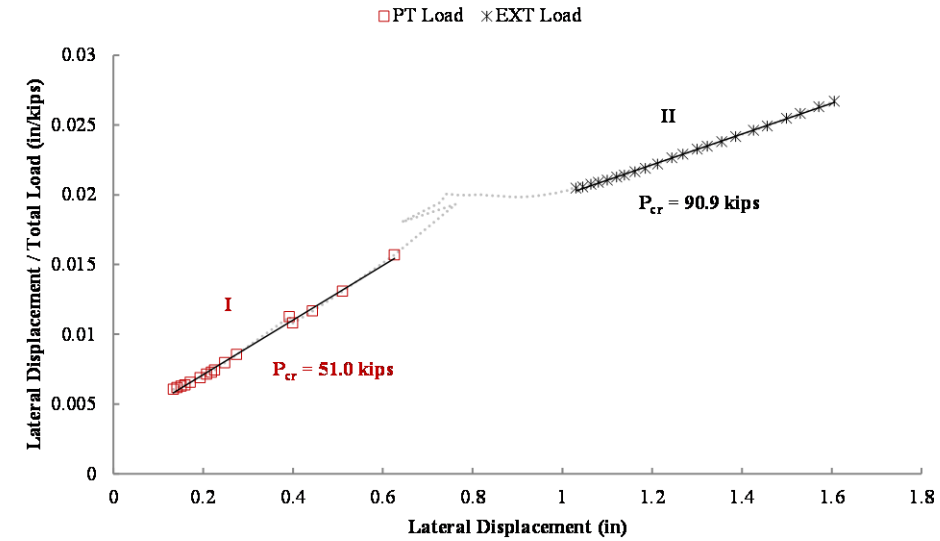

Figure A-217: Southwell Plot for SP2-05PT35-EX-3-DS

Table A-6: Southwell Plot Parameters for SP2-05PT35-EX-3-DS

Series	Load Increment (k)	Slope	Y-Intercept	R^2 value	Buckling Load P_{cr} (k)	Initial Imperfection (in)
I	PT: 20-40	0.0196	0.0032	0.9959	**51.0**	0.163
II	EXT: 45-60	0.011	0.009	0.9987	**90.9**	0.818

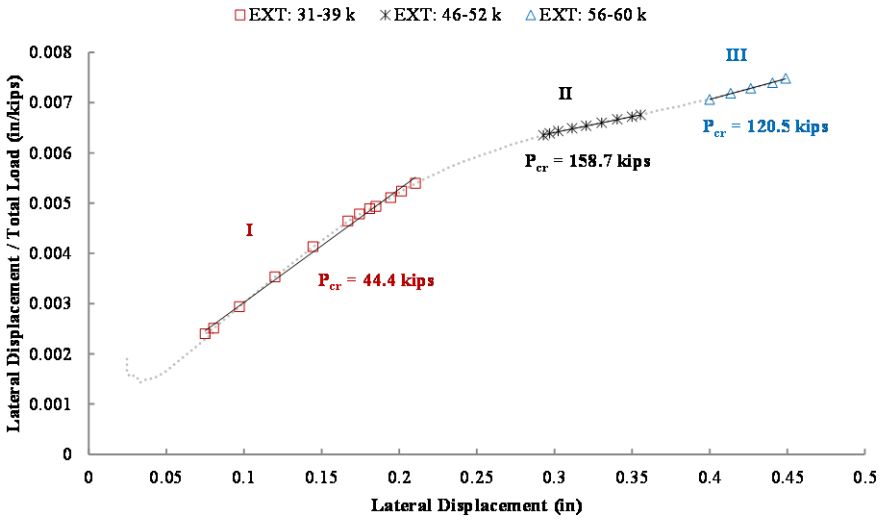

Figure A-218: Southwell Plot for SP2-06PT30-EX-2-DS

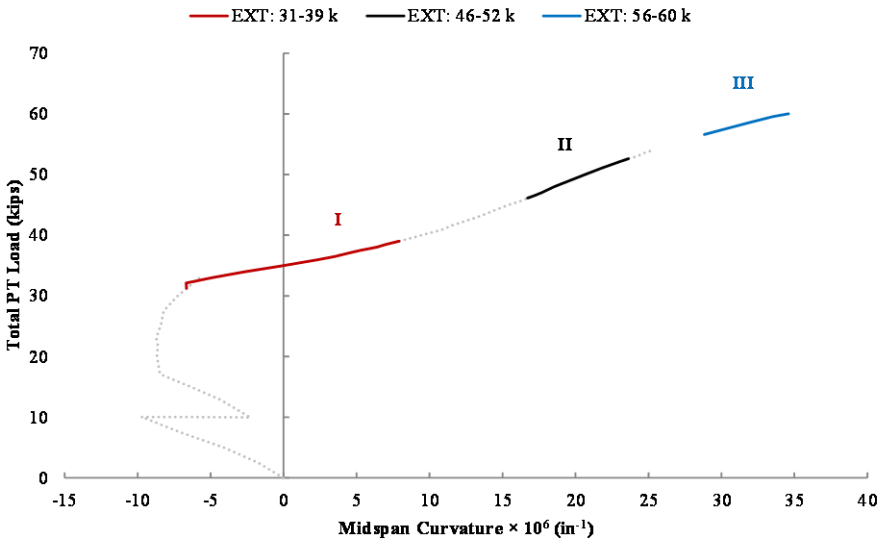

Figure A-219: Load vs. Lateral Curvature for SP2-06PT30-EX-2-DS

Table A-7: Southwell Plot Parameters for SP2-06PT30-EX-2-DS

Series	Load Increment (k)	Slope	Y-Intercept	R^2 value	Buckling Load P_{cr} (k)	Initial Imperfection (in)
I	EXT: 31-39	0.0225	0.0008	0.9950	**44.4**	0.036
II	EXT: 46-52	0.0063	0.0045	0.9975	**158.7**	0.714
III	EXT: 56-60	0.0083	0.0037	0.9984	**120.5**	0.446

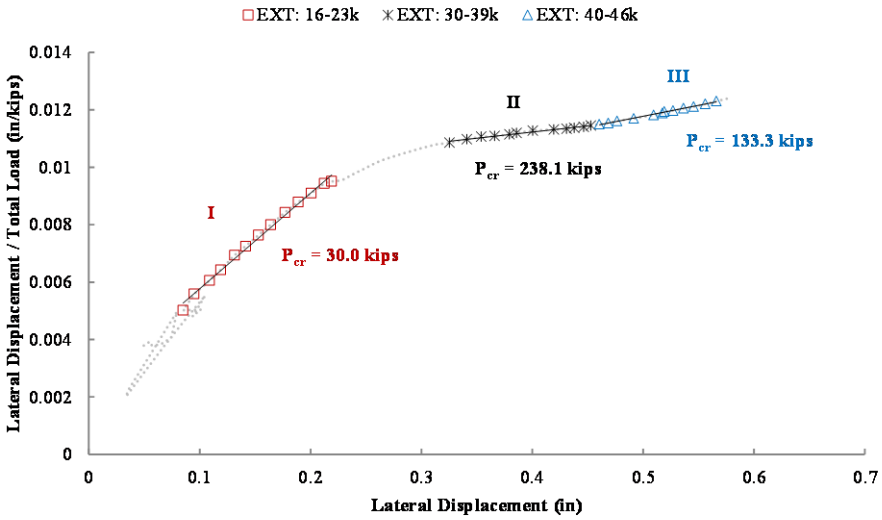

Figure A-220: Southwell Plot for SP2-06PT15-EX-5-DS

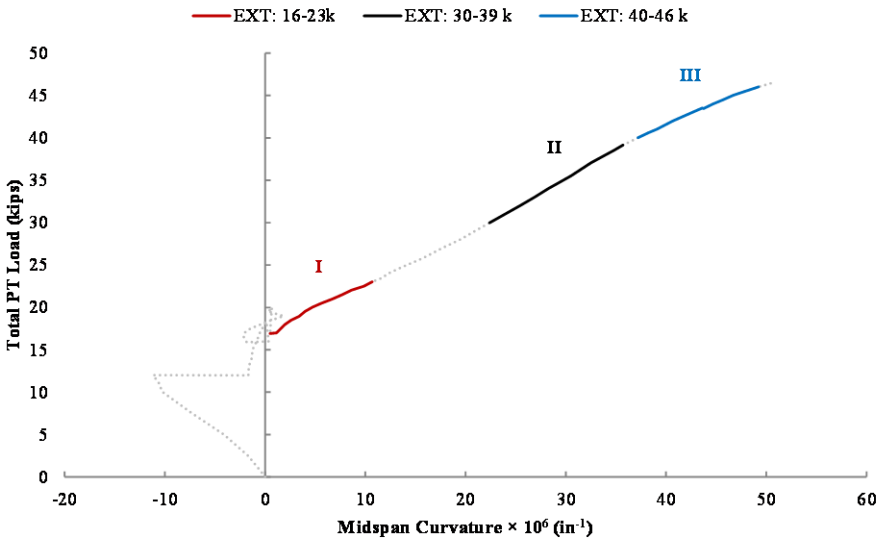

Figure A-221: Load vs. Lateral Curvature for SP2-06PT15-EX-5-DS

Table A-8: Southwell Plot Parameters for SP2-06PT15-EX-5-DS

Series	Load Increment (k)	Slope	Y-Intercept	R^2 value	Buckling Load P_{cr} (k)	Initial Imperfection (in)
I	EXT: 16-23	0.0333	0.0024	0.9934	**30.0**	0.072
II	EXT: 30-39	0.0042	0.0095	0.9762	**238.1**	2.262
III	EXT: 40-46	0.0075	0.008	0.9954	**133.3**	1.067

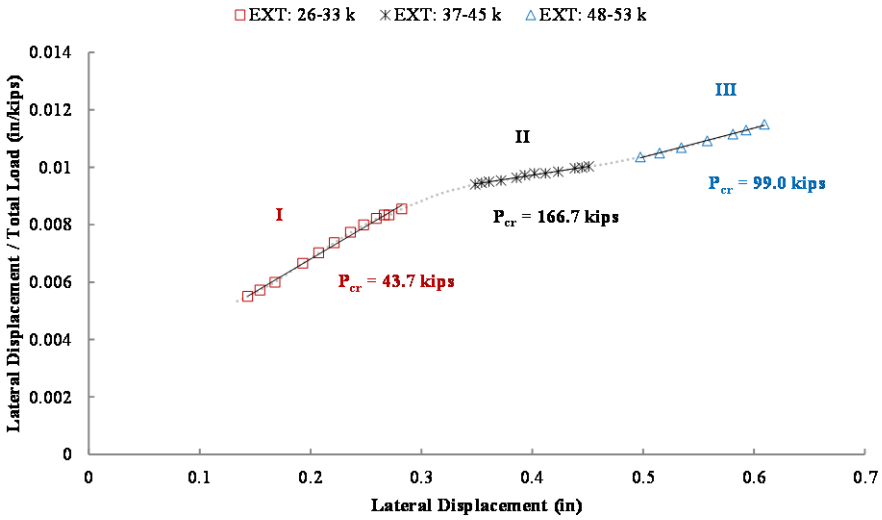

Figure A-222: Southwell Plot for SP2-06PT25-EX-6-DS

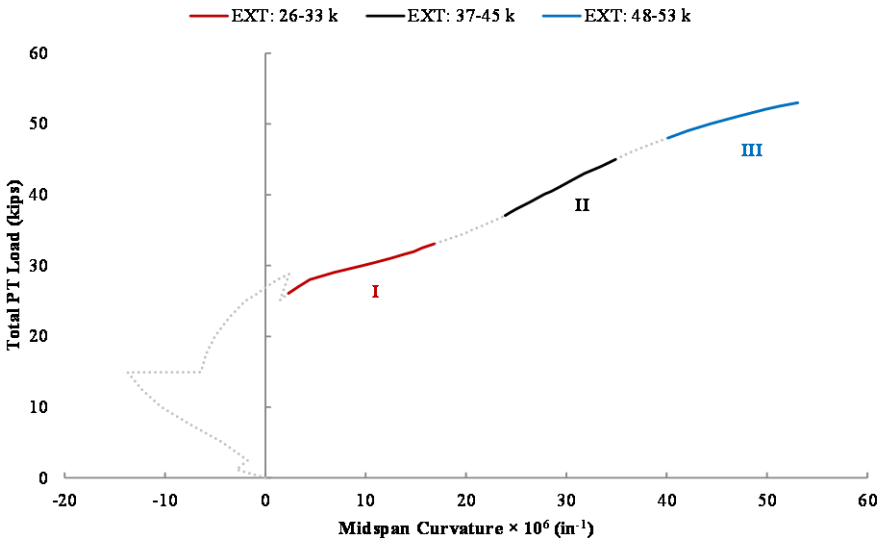

Figure A-223: Load vs. Lateral Curvature for SP2-06PT25-EX-6-DS

Table A-9: Southwell Plot Parameters for SP2-06PT25-EX-6-DS

Series	Load Increment (k)	Slope	Y-Intercept	R^2 value	Buckling Load P_{cr} (k)	Initial Imperfection (in)
I	EXT: 26-33	0.0229	0.0022	0.9951	**43.7**	0.096
II	EXT: 37-45	0.006	0.0071	0.9904	**166.7**	1.183
III	EXT: 48-53	0.0101	0.0053	0.9968	**99.0**	0.525

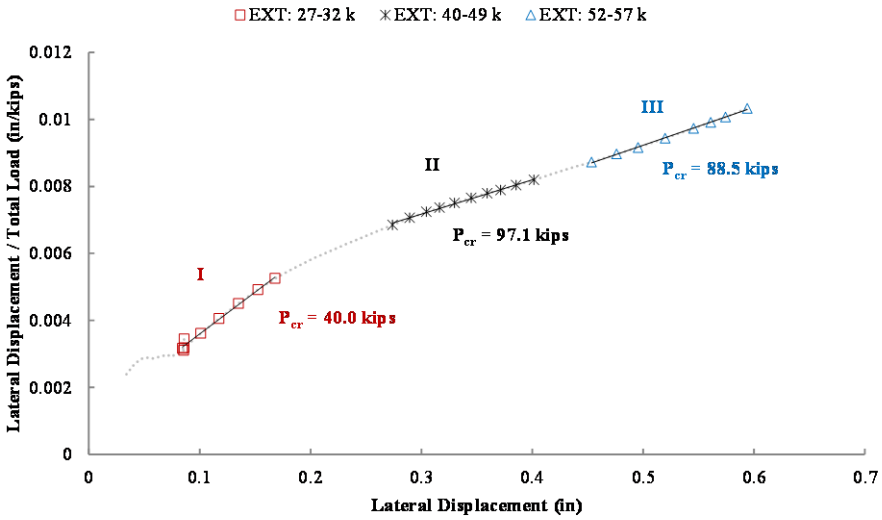

Figure A-224: Southwell Plot for SP2-06PT25-EX-7-SS

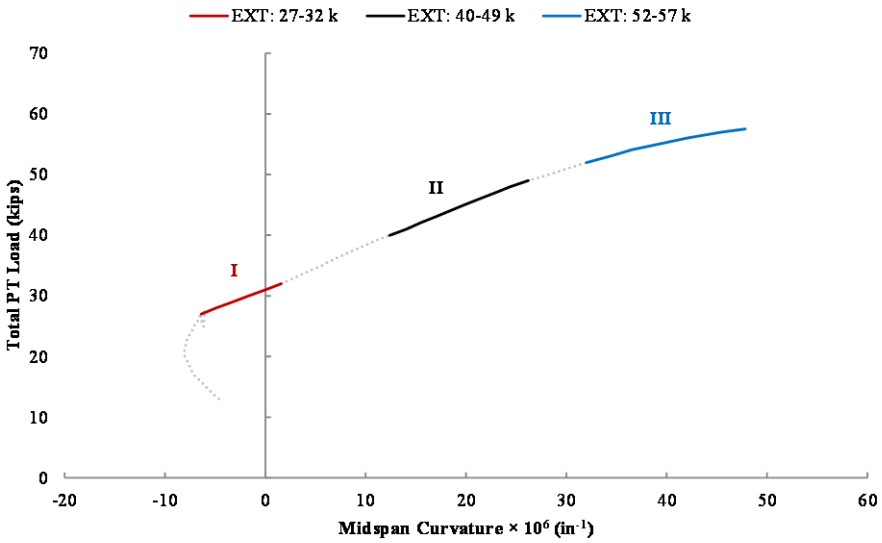

Figure A-225: Load vs. Lateral Curvature for SP2-06PT25-EX-7-SS

Table A-10: Southwell Plot Parameters for SP2-06PT25-EX-7-SS

Series	Load Increment (k)	Slope	Y-Intercept	R^2 value	Buckling Load P_{cr} (k)	Initial Imperfection (in)
I	EXT: 27-32	0.025	0.0011	0.9874	**40.0**	0.044
II	EXT: 40-49	0.0103	0.0041	0.9965	**97.1**	0.398
III	EXT: 52-57	0.0113	0.0036	0.9989	**88.5**	0.319

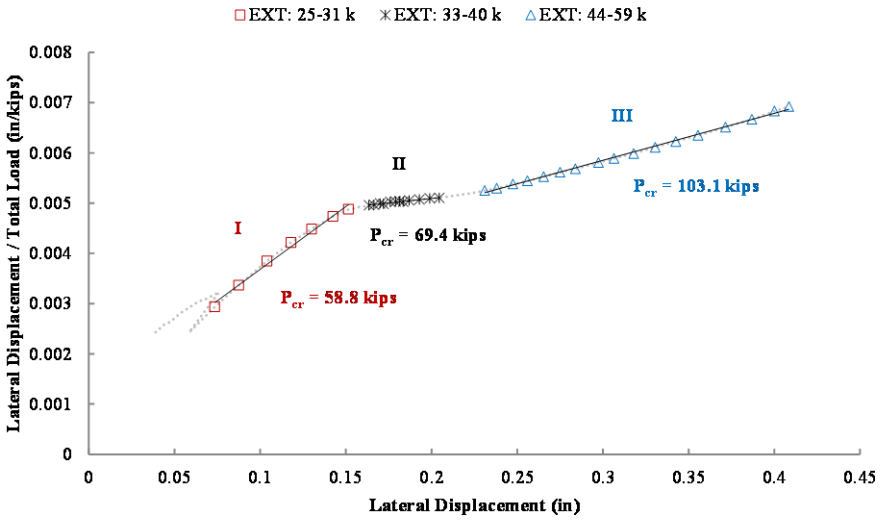

Figure A-226: Southwell Plot for SP2-06PT20-EX-8-SS

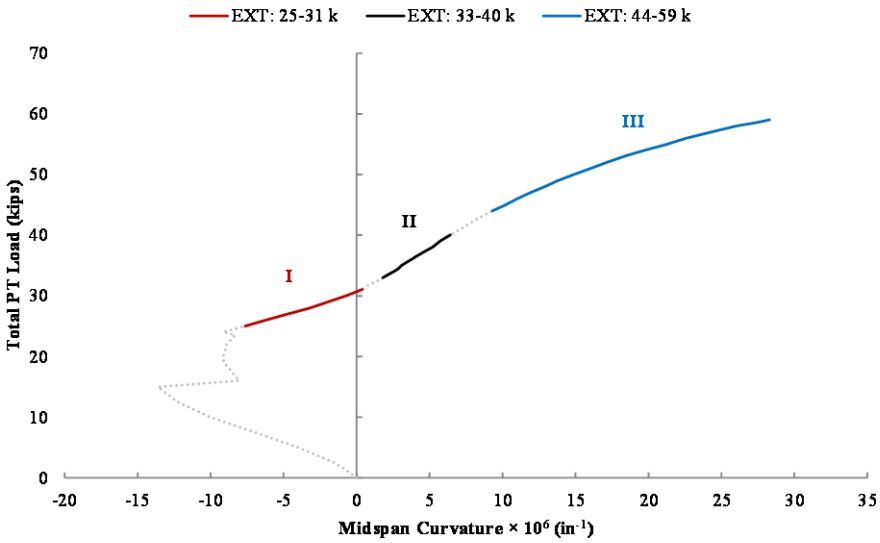

Figure A-227: Load vs. Lateral Curvature for SP2-06PT20-EX-8-SS

Table A-11: Southwell Plot Parameters for SP2-06PT20-EX-8-SS

Series	Load Increment (k)	Slope	Y-Intercept	R^2 value	Buckling Load P_{cr} (k)	Initial Imperfection (in)
I	EXT: 25-31	0.025	0.0012	0.9904	**40.0**	0.048
II	EXT: 33-40	0.0036	0.0044	0.9629	**277.8**	1.222
III	EXT: 44-59	0.0094	0.003	0.9975	**106.4**	0.319

A.5.2.3 SP2 External Load Tests

This subsection includes the Southwell plot constructed from the single external load test on SP2. The test ended in a full buckling failure which resulted in extensive cracking in the member.

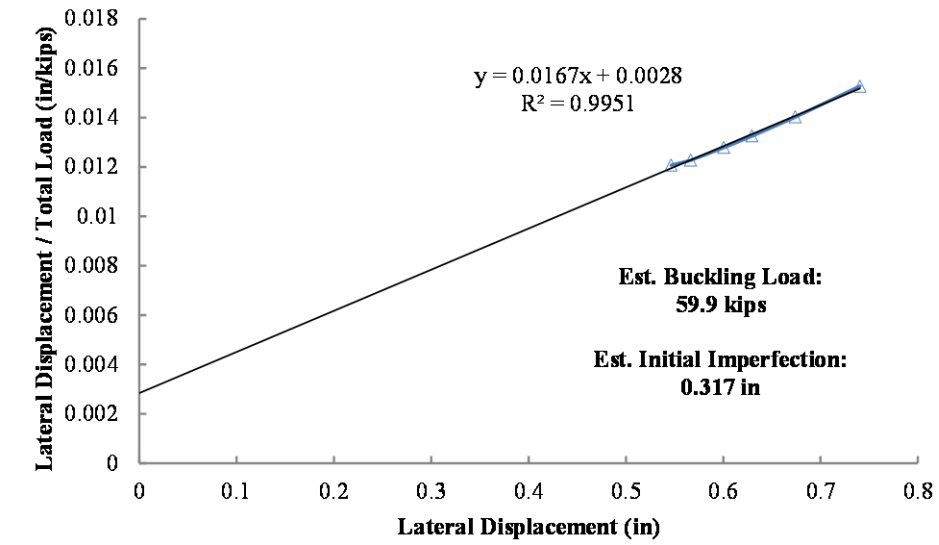

Figure A-228: Southwell Plot for SP2-PT0-EX-1(Specimen buckled suddenly at approximately 48.5 kips in this test. Discussion is included in Chapter 5.)

References

Ahlborn, T. M., French, C. E., & Shield, C. K. (2000). *High-Strength Concrete Prestressed Bridge Girders: Long-Term and Flexural Behavior.* Report to the Minnesota Department of Transportation, The University of Minnesota, St. Paul, MN. Retrieved March 3, 2012

Aktan, A. E., Catbas, F. N., Grimmelsman, K. A., & Pervizpour, M. (2001). *Development of a Model Health Monitoring Guide of Major Bridges.* Report to Federal Highway Administration, Drexel University.

Barr, P. J., Stanton, J. F., & Eberhard, M. O. (2005). Effects of Temperature Variation on Precast, Prestressed Concrete Bridge Girders. *Journal of Bridge Engineering*, *10*(2), 186-194. Retrieved September 21, 2011

Bazant, Z., & Cedolin, L. (2010). *Stability of Structures.* Hackensack, NJ: World Scientific Publishing Co.

Belis, J., Louter, C., Verfaillie, K., Van Impe, R., & Callewaert, D. (2006). *The Effect of Post-Tensioning On the Buckling Behaviour of a Glass T-Beam.* Delft University of Technology. Retrieved February 3, 2012

Benaim, R. (2008). *The Design of Prestressed Concrete Bridges.* New York: Taylor & Francis.

Bosworth, K. J. (2007). *Health Monitoring of the Veterans' Glass City Skyway: Vibrating Wire Strain Gage Testing, Study of Temperature Gradients and a Baseline Truck Test.* Master's Thesis, The University of Toledo. Retrieved April 6, 2011

Brownjohn, J. W., & Moyo, P. (2000). Monitoring of Singapore-Malaysia Second Link during Construction. *International Conference on Experimental Mechanics - Proceedings of SPIE*, *4317*, pp. 528-533. Retrieved July 20, 2011

Choquet, P., Juneau, F., Debreuille, P. J., & Bessette, J. (1999). Reliability, Long-term Stability and Gage Performance of Vibrating Wire Sensors with Reference to Case Histories. *Proceedings of the 5th International Symposium on Field Measurements in Geomechanics*, (pp. 49-54). Retrieved March 11, 2011

Collins, M. P., & Mitchell, D. (1991). *Prestressed Concrete Structures.* Prentice-Hall.

Connor, R. J., & Santosuosso, B. J. (2002). *Field measurements and controlled load testing on the Lehigh River Bridge (SR-33).* ATLSS Report Number 02-07, Lehigh University Center for Advanced Technology for Large Structural Systems (ATLSS).

Dickson, G. (2012, January 15). Work on Fort Worth's West Seventh bridge starts soon. *Fort Worth Star-Telegram*. Retrieved February 3, 2012

Espinoza, O. (2006). *A Guide to Data Acquisition via the CR5000 Data Logger with the Assistance of the AM416 Multiplexer.* Tutorial, The University of Texas at Austin.

Frangopol, D. M., Strauss, A., & Kim, S. (2008). Bridge Reliability Assessment Based on Monitoring. *Journal of Bridge Engineering, 13*(3), 258-260. Retrieved December 2, 2011

Hurff, J. B. (2010). *Stability of Precast Prestressed Concrete Bridge Girders Considering Imperfections and Thermal Effects.* Ph.D. Dissertation, Georgia Institute of Technology. Retrieved November 3, 2011

Instruction Manual - Model 4200 Series. (n.d.). Retrieved March 6, 2011, from Geokon.

Lin, T. Y., & Burns, N. H. (1981). *Design of Prestressed Concrete Structures* (3rd ed.). New York: Wiley.

Magnel, G. (1954). *Prestressed Concrete* (3rd ed.). London: Concrete Publications Limited.

Meck, H. R. (1977, March/April). Experimental Evaluation of Lateral Buckling Loads. *Journal of the Engineering Mechanics Division, 103*(2), 331-337.

Smith, L. M., Brodt, G. L., & Stafford, B. (2001). Performance Assessment and Reinstatement of Vibrating wire Strain Gauges in Nuclear Power Plant Structures. *Transactions, SMiRT 16.* Washington, D.C. Retrieved February 3, 2012

Southwell, R. V. (1932). On the Analysis of Experimental Observations in Problems of Elastic Stability. *Proceedings of the Royal Society of London. Series A, Containing Papers of a Mathematical and Physical Character. 135*, pp. 601-616. The Royal Society.

Stratford, T. J., & Burgoyne, C. J. (1999). Lateral stability of long precast concrete beams. *Proceedings of the ICE - Buildings and Stuctures, 124*, pp. 169-180.

Tveit, P. (2006, August). *An Introduction to the Network Arch: Lectures at NTNU Trondheim on August 15th, 2006.* (P. Tveit, Ed.) Retrieved October 14, 2011, from The Network Arch.

Tveit, P. (2007, May). An Introduction to the Network Arch. *Structural Engineering International, 17*(2), pp. 184-187. Retrieved October 14, 2011

Tveit, P. (2011, February). *The Network Arch: Bits of Manuscript in February 2011 after Lectures in 50 Countries.* (P. Tveit, Ed.) Retrieved February 3, 2012, from The Network Arch.

West 7th Street Fact Sheet. (n.d.). Retrieved February 3, 2012, from City of Fort Worth.

Wilby, C. B. (1963). *Elastic Stability of Post-tensioned Prestressed Concrete Members.* New York: American Elsevier Publishing Company.

Wongjeeraphat, R. (2011). *Stability Bracing Behavior for Truss Systems.* Ph.D. Dissertation, The University of Texas at Austin.

Yang, Y., & Meyers, J. J. (2003). Live-Load Test Results of Missouri's First High-Performance Concrete Superstructure Bridge. *Transportation Research Record*(1845), 96-103. Retrieved August 6, 2011